1-1-2022

SPECTROSCOPIC INVESTIGATIONS OF PHOTOINDUCED ELECTRON TRANSFER PROCESSES AT INTERFACES AND IN SOLUTION

leigh Anna Hunt

SPECTROSCOPIC INVESTIGATIONS OF PHOTOINDUCED ELECTRON TRANSFER PROCESSES AT INTERFACES AND IN SOLUTION

A DISSERTATION SUBMITTED IN PARTIAL FULFILLMENT OF

REQUIREMENTS FOR THE DEGREE OF

DOCTOR OF PHILOSOPHY IN THE DEPARTMENT OF

CHEMISTRY AND BIOCHEMISTRY

THE UNIVERSITY OF MISSISSIPPI

By

LEIGH ANNA HUNT

May 2022

ABSTRACT

Photoinduced electron transfer is an essential reaction in artificial solar energy conversion applications. The challenge for decades of research has been to demonstrate a long-lived charge separated state with high energy that in principle can be used for chemical or solar-to-electric energy conversion.[1] For example, the primary energy conversion process in a dye-sensitized solar cell (DSC) is a photoinduced charge separation at the metal oxide-dye interface, making the formation and decay lifetime of the charge separated state an important aspect of these systems.[2, 3] Upon photon absorption, a surface-bound chromophore is promoted to a higher energy excited state, whereby it can undergo forward electron transfer (electron injection) to the conduction band or acceptor states in TiO_2. The resultant charge separation consists of the injected electron and the oxidized dye. Following the initial charge separation step, DSCs are reliant upon regeneration of the oxidized dye by a soluble reductant present in the electrolyte. This reaction is often termed dye regeneration and is typically not optimized under operational conditions. However, pre-organized interactions between the immobilized dye and redox-active species in the electrolyte offer a method for enhancing the regeneration reaction in DSCs. Within this dissertation, several synthetic design approaches are introduced, and the corresponding electron dynamics are explored.

DEDICATION

To my dad. I often imagine how proud you would have been.

ACKNOWLEDGEMENTS

I am sincerely grateful to many people in my life, without whom this dissertation would not have been written. Many years ago, I walked into Dr. Hammer's office and requested research hours, oblivious to the impact it would eventually have on my life. I wouldn't have made it this far without first having someone take a chance on me as a student. That was Dr. Hammer. My time in his lab has been nothing short of memorable and I have learned much about self-motivation, self-discipline, and, above all, the invaluable skill of problem-solving. Dr. Hammer was the first person to believe in my abilities in this field, long before I believed in my own.

I also owe a great debt of thanks to my second advisor, Dr. Delcamp. I have a very specific memory of being a complete idiot in his office many years ago, the details of which I will not be disclosing, but nonetheless has provided some much-needed humor in these dark dissertation times. I think his impact on my career is best summarized by mentioning the @DelcampGroup Twitter bio, where it says, "The only thing we are afraid of is our own potential". While obviously hilarious, it's also a bit ironic because without his support I don't know that I would have truly recognized my own. For that, I will always be grateful.

Aside from my two advisors, I would also like to thank my committee members, Dr. Ryan Fortenberry, Dr. Nikki Reinemann, and Dr. Steven Davis, for their assistance and support throughout my time here.

To my Hammer lab cohorts, both former and present, I thank you for making this dissertation possible, not in the writing of it, but in the living of it. Many years of my life went into the making of this document. To Shane, Cameron, Abdul, Ethan, Louis, and many more—thank you for your friendship. It has been a joy (most days) to know and work with each of you. I look forward to seeing the incredible things you accomplish in your lives. Also, if anyone is wondering who broke the Princeton Instruments camera that cost $10,000 to repair, it wasn't me, but I do know who did it.

Two people have my everlasting gratitude and respect for both their friendship and enthusiasm in guiding my progress to where it is now—Ashley Williams and Austin Dorris. Austin will likely question why he wasn't listed first, but it is in chronological order.

Ashley was the first person I became friends with in the group and I am happy to report she still puts up with my nonsense, for whatever reason. I will never forget the *many* days spent aligning, misaligning, and realigning a dye laser only to get a ~5 mW output. Ashley dedicated her own dissertation to women in STEM, with the hope that we "break glass ceilings". She shattered them. I am immensely proud to know you and consider myself lucky to call you a friend.

Austin was generous with both his time and his quips, reading multiple drafts of my work throughout the years, suggesting his own commentary, and throughout all of it, drinking many of my beers. He is the little brother I never asked for and a friend that I did not deserve. I am proud of you and look forward to seeing what you accomplish at Auburn.

TABLE OF CONTENTS

ABSTRACT ii

DEDICATION iii

ACKNOWLEDGEMENTS iv

LIST OF FIGURES ix

LIST OF TABLES xiv

CHAPTER 1: MOLECULAR SPECTROSCOPY 1

1.1 INTRODUCTION 1

1.2 ELECTRONIC SPECTROSCOPY 1

1.2.1. ABSORPTION AND PHOTOLUMINESCENCE 2

1.2.1. TRANSIENT ABSORPTION 5

CHAPTER 2: MOTIVATION 9

2.1 ENERGY DEMAND 9

2.2.1. SOLAR CELLS 10

CHAPTER 3: DYE-SENSITIZED SOLAR CELLS 12

3.1 INTRODUCTION 12

3.1.1. WORKING PRINCIPLE 13

3.1.2 KINETIC COMPETITION 14

3.1.3. BACK ELECTRON TRANSFER 15

3.1.4. DYE REGENERATION 15

3.1.5. NONEXPONENTIAL KINETICS 16

3.2 SELF-ASSEMBLY STRATEGIES 17

3.2.1. LEWIS ACID-LEWIS BASE INTERACTIONS 19

3.2.2. HALOGEN BONDING 20

3.3 SURFACE MODIFICATION STRATEGIES 22

CHAPTER 4: EXPERIMENTAL METHODS 25

4.1 TIME-CORRELATED SINGLE PHOTON COUNTING 25

4.2 NANOSECOND TRANSIENT ABSORPTION SPECTROSCOPY 27

CHAPTER 4: HALOGEN BONDING AT THE INTERFACE 30

CHAPTER 5: LEWIS ACID–LEWIS BASE INTERACTIONS PROMOTE FAST INTERFACIAL ELECTRON TRANSFERS 62

CHAPTER 6: PREFERENTIAL DIRECTION OF ELECTRON TRANSFER REACTIONS AT THE INTERFACE 86

BIBLIOGRAPHY 111

APPENDICES I-IV 130

LIST OF FIGURES

CHAPTER 1 PAGE

FIGURE 1.1.1. Jablonksi diagram, where the initial excitation is represented by a blue arrow. Fluorescence (green arrow) occurs after vibrational relaxation (gray, curved arrows) as the sample relaxes radiatively. Intersystem crossing (orange arrow) to a triplet state can also occur. Phosphorescence (red arrow) occurs from a triplet to a singlet.....3

FIGURE 1.2.1. Representative differential absorption spectrum of $[Ru(bpy)_3]^{2+}$ and ascorbic acid in H_2O, where the positive absorption bands correspond to excited state absorption and the negative band corresponds to the ground state bleach region. Each plotted point is representative of an individual kinetic trace at a single wavelength used to visualize the ΔOD spectrum. 7

CHAPTER 3

FIGURE 3.1.1. A schematic representation of a DSC depicted with a representative dye (S) and redox shuttle (M). Operating principles consist of (1) light excitation, (2) excited-state electron injection to TiO_2, (3) generation of photocurrent through external circuit to perform work, (4) reduction of the redox mediator, and (5) regeneration of the oxidized sensitizer. Recombination pathways are denoted by red, dashed arrows (A) excited-state relaxation, (B) back electron transfer (BET), and (C) charge recombination to the redox shuttle.....13

FIGURE 3.2.1. Representation of a typical DSC environment where the regeneration reaction is diffusion-controlled. From left to right: Photoexcitation of an adsorbed sensitizer dye and subsequent excited-state electron injection to TiO_2, diffusional association of the redox shuttle, regeneration of the oxidized sensitizer, and diffusion of the RS back to the counter electrode. ...18

FIGURE 3.2.2. Representation of a DSC environment where the regeneration reaction is diffusion-controlled. From left to right: Photoexcitation of an adsorbed sensitizer dye and subsequent excited-state electron injection to TiO_2, diffusional association of the redox shuttle, regeneration of the oxidized sensitizer, and diffusion of the RS back to the counter electrode. 21

FIGURE 3.3.1. Representative graphic of TiO_2 surface before (left) and after (right) a post-modification surface treatment such as a fluorinated self-assembled monolayer, where the rectangles represent anchored PFTS chains that fill vacant sites between dye molecules 23

CHAPTER 4

FIGURE 4.1.1. Schematic of the Time-correlated Single Photon Counting (TCSPC) experiment, including a pulsed diode laser, trigger sources, and the avalanche photodiode detector. A histogram of photon counts per unit time is generated in reference to the trigger, which is tied to the firing signal for the laser. Inset: A dichroic or other optical filter separates the excitation from the epifluorescence 26

FIGURE 4.2.1. Schematic of the LP980 spectrometer, including a pulsed Nd:YAG laser, trigger source, and a photomultiplier tube for detection. Synchronization of the pulses is controlled by the L900 software 27

CHAPTER 5

FIGURE 5.1. Non-covalent interaction between a cobalt-based RS (Co(*N*-tpy)$_2$) and a halogen atom on a dye 34

FIGURE 5.2. Electron transfer pathways of AB4-AB7 to the TiO_2 CB and from Co(*N*-tpy)$_2$ 35

FIGURE 5.3. Molecular orbital (MO) diagrams of the neutral and positively charged AB7 49

FIGURE 5.4. Synthetic route for target dyes AB4, AB5, AB6 and AB7.....50

FIGURE 5.5. Synthetic route to [Co(*N*-tpy)$_2$][TFSI]$_2$ and [Co(*N*-tpy)$_2$][TFSI]$_3$.....51

FIGURE 5.6. Molar absorptivity of dyes AB4-AB7 in a DCM solution 52

FIGURE 5.7. Molar absorptivity of RSs [Co(*N*-tpy)$_2$][TFSI]$_2$ and [Co(*N*-tpy)$_2$][TFSI]$_3$ 53

FIGURE 5.8. Cyclic voltammograms of [Co(*N*-tpy)$_2$][TSFI]$_2$ and [Co(tpy)$_2$][TSFI]$_2$ 53

FIGURE 5.9. Molecular electrostatic potential (MEP) for the neutral and cationic dyes 55

FIGURE 5.10. Optimized geometries of AB7 with Co(*N*-tpy)$_2$.....56

FIGURE 5.11. Transient spectrum of AB7 on TiO_2 with 0.1 M LiTFSI in MeCN 58

FIGURE 5.12. Decay plots from TAS for AB7 with and without Co(*N*-tpy)$_2^{3+/2+}$ RS 58

FIGURE 5.13. Relative value comparison with each halogenated dye across several interrogation techniques with Co(*N*-tpy)$_2^{3+/2+}$ as a RS 62

CHAPTER 6

FIGURE 6.1. LA-LB interaction between a TiO_2 bound organic dye (DN1) and the Co(PY5Me$_2$) redox shuttle. Dye (A1)[4] and RS (Co(bpy)$_3$) as no LA-LB interaction control materials.....65

FIGURE 6.2. Synthetic route to DN1 67

FIGURE 6.3. UV−vis absorption spectra of DN1 in DCM, on TiO_2, and on TiO_2 after adding [Co(PY5Me$_2$)(MeCN)]$^{2+}$ to the solution 69

FIGURE 6.4. Potential energy diagram of DN1 relative to the conduction band of TiO_2 and [Co(PY5Me$_2$)(L)]$^{3+/2+}$ in the presence of TBP.....69

FIGURE 6.5. Transient decay signals at 720 nm corresponding to TiO_2 bound DN1, TiO_2 bound DN1 with added [CoPY5Me$_2$)(MeCN)]$^{3+/2+}$, and TiO_2 bound DN1 with added [Co(bpy)$_3$]$^{3+/2+}$. Middle: TA spectrum of DN1 on TiO_2 with no RS present. Bottom: TA spectrum of DN1 on TiO_2 with [Co(PY5Me$_2$)(MeCN)]$^{3+/2+}$.....72

FIGURE 6.6. Stern-Volmer quenching plot for DN1-ester at 5 μM concentration in acetonitrile with high (top) and low (bottom) concentrations of the RSs.....74

FIGURE 6.7. Optimized geometries of pyridyl-bound (left) and cyano-bound (right) DN1-ester with [Co(PY5Me$_2$)]$^{2+}$. Hydrogen atoms are omitted for clarity 77

FIGURE 6.8. Steady-state emission spectrum (left) and time-correlated single photon counting curves (right) of DN1 with and without redox shuttles present in the same concentration as in functional DSC devices. IRF stands for instrument response function 79

FIGURE 6.9. J−V curves of DSCs based on DN1 at 1000 W/m^2 with a solar simulator (top) and 10.8 W/m^2 (6000 lux) with fluorescent lighting (bottom) 80

FIGURE 6.10. Current dynamics of DN1 with $[Co(bpy)_3]^{3+/2+}$ (top) and $[Co(PY5Me_2)(L)]^{3+/2+}$ (bottom). Sun intensities are 100%, 78%, 50%, 32%, and 10% from left to right on each graph with the lamp shuttered on/off 83

CHAPTER 7

FIGURE 7.1. Illustration of the desired (black) and undesired (gray) electron transfer pathways with nomenclature listed beside each arrow 89

FIGURE 7.2. Structures of B11 (where TBA is tetrabutylammonium), $[Co(bpy)_3][PF_6]_{3/2}$, and 1*H*,1*H*,2*H*,2*H*-perfluorooctyltrimethoxysilane (PFTS) 90

FIGURE 7.3. Insulation strategies being probed in this work compared to the case of no added insulator.....92

FIGURE 7.4. *J-V* curves (top) and IPCE curves (bottom) for varying PFTS concentrations on B11/$[Co(bpy)_3]^{3+/2+}$ DSC device performances 93

FIGURE 7.5. Changes in photovoltage, photocurrent, and PCE with respect to PFTS concentration. All values are normalized to the highest performing cell values 94

FIGURE 7.6. SMPVT measurement with B11/$[Co(bpy)_3]^{3+/2+}$ devices varying concentration of PFTS 96

FIGURE 7.7. A) Time-resolved emission decays of B11 on ZrO_2 (blue), TiO_2 with no surface treatment (green), TiO_2 with an MgO surface treatment (red), and TiO_2 with a PFTS surface treatment (purple). The acquisition time for each sample was 300 seconds with excitation at 485 nm. B) Steady-state emission spectra of B11 on insulating ZrO_2 and semiconducting TiO_2 collected at room temperature 100

FIGURE 7.8. Transient absorption kinetics in logarithmic scale monitoring the rate of: (left) the back electron transfer reaction and (middle) the regeneration reaction for: a TiO_2-B11 sensitized films, a TiO_2-B11 sensitized film with an MgO surface treatment, and a TiO_2-B11 sensitized film with a PFTS surface treatment. Transient absorption difference spectra for a TiO_2-B11 sensitized film with a PFTS surface treatment 104

FIGURE 7.9. A diagram of electron lifetimes for each electron transfer reaction with and without an added insulator (no insulator = black; MgO = red; PFTS = blue). The most desirable value is in bold and italics for each electron transfer reaction. The PCE obtained with each condition is shown in the legend 106

FIGURE 7.10. Molecular electrostatic potential maps of hydroxyl terminated PFTS molecules surrounding B11 on a TiO_2 surface. A) The ground state partial charge configuration, B) the photoexcited MLCT state with electrostatically attracted partial charges on PFTS to the B11 molecule, C) the interfacial charge separated state with an electron injected into TiO_2 and B11 cation electrostatically attracted to a PFTS molecule, and D) a general charge layer cartoon with PFTS (red and blue) surrounding a B11 cationic dye (blue and green).....109

LIST OF TABLES

CHAPTER 5 PAGE

TABLE 5.1. Optical and electrochemical properties of dyes in DCM and RSs in MeCN.....52

TABLE 5.2. Calculated binding energy and distances between the RSs and dyes 56

TABLE 5.3. Summary TAS data for **AB5**, **AB6** and **AB7**.....59

CHAPTER 6

TABLE 6.1. Lifetimes and rates of photogenerated dye cation signal decays from TAS experiments.....73

TABLE 6.2. Current dynamics of **DN1** with $[Co(bpy)_3]^{3+/2+}$ (top) and $[Co(PY5Me_2)(L)]^{3+/2+}$ (bottom).....80

CHAPTER 7

TABLE 7.1. Effect of varying PFTS concentrations on **B11**/$[Co(bpy)_3]^{3+/2+}$ DSC device performance 95

TABLE 7.2. Effect of varying $Mg(OMe)_2$ concentrations on **B11**/$[Co(bpy)_3]^{3+/2+}$ device performances.....97

TABLE 7.3. Excited-state emission measurements for insulating ZrO_2 and semiconducting TiO_2 films sensitized with dye **B11**.....100

TABLE 7.4. Summary of kinetic data obtained for **B11** devices 104

CHAPTER 1

MOLECULAR SPECTROSCOPY

1.1. INTRODUCTION

The research presented within this dissertation is concerned with what molecular spectroscopy can contribute to the fundamental understanding of electron transfer dynamics in solar energy conversion systems. However, to fully understand the implications, it is essential to first discuss the nature of spectroscopy, the properties of light itself, and the interactions that may occur with matter. In its broadest sense, spectroscopy is concerned with the absorption, emission or scattering of electromagnetic radiation by atoms or molecules. Electromagnetic radiation encompasses a wide range of wavelengths, and systems of interest may be in the gas, liquid, or solid phase or, of great importance to the body of this dissertation, adsorbed on a surface. However, for the research discussed herein, discussion will focus on molecular spectroscopy, specifically absorption and emission, both steady state and time-resolved.

1.2. ELECTRONIC SPECTROSCOPY

Electronic excitation of a molecule typically promotes electrons from the highest occupied molecular orbital (HOMO) to the lowest unoccupied molecular orbital (LUMO) upon the absorption of ultraviolet (UV), visible, or near infrared (NIR) light. The study of these electronic transitions can provide useful information regarding both electronic structure and molecular

reactivity. Electronic states are termed according to the nature of the induced transitions as well as the spin total of the excited state. For instance, in $[Ru(bpy)_3]^{2+}$, the lowest energy excited state is well-documented to be a $^3MLCT^*$ state, where the superscripts denote an excited state with two unpaired electrons of parallel spin (triplet), formed via a metal to ligand charge transfer transition. The characterization of electronic states can be performed in a variety of ways. However, the research presented in this dissertation is specifically concerned with photoluminescence spectroscopy and transient absorption spectroscopy.

1.3. ABSORPTION AND PHOTOLUMINESCENCE

At room temperature, according to the Boltzmann distribution, most molecules in an ensemble will exist in the lowest energy vibrational sublevel of the ground electronic state. Thus, absorption occurs from the lowest energy ground vibrational state. However, what goes up must also come down, and the excited electronic state will lose the excess imparted energy by one of the pathways illustrated in Figure 1.2.1, which can be either a radiative or non-radiative transition.[5] After promotion to an excited electronic state, energy is lost through a dissipation process known as vibrational relaxation (VR). In this process, excess vibrational energy is lost until the lowest vibrational sublevel of the electronic state is reached. Following VR, a molecule in a higher energy excited state may also undergo an additional nonradiative transition termed internal conversion (IC) to a lower lying electronic state followed by VR to the lowest energy vibrational level of the newly accessed state. Another pathway for the dissipation of absorbed energy from the singlet excited state to the singlet ground state is by emission of a photon, i.e.

fluorescence, which is a radiative transition. Fluorescence occurs from the lowest vibrational sublevel of the singlet excited state following VR and/or IC, which is the basis of Kasha's Rule.[6]

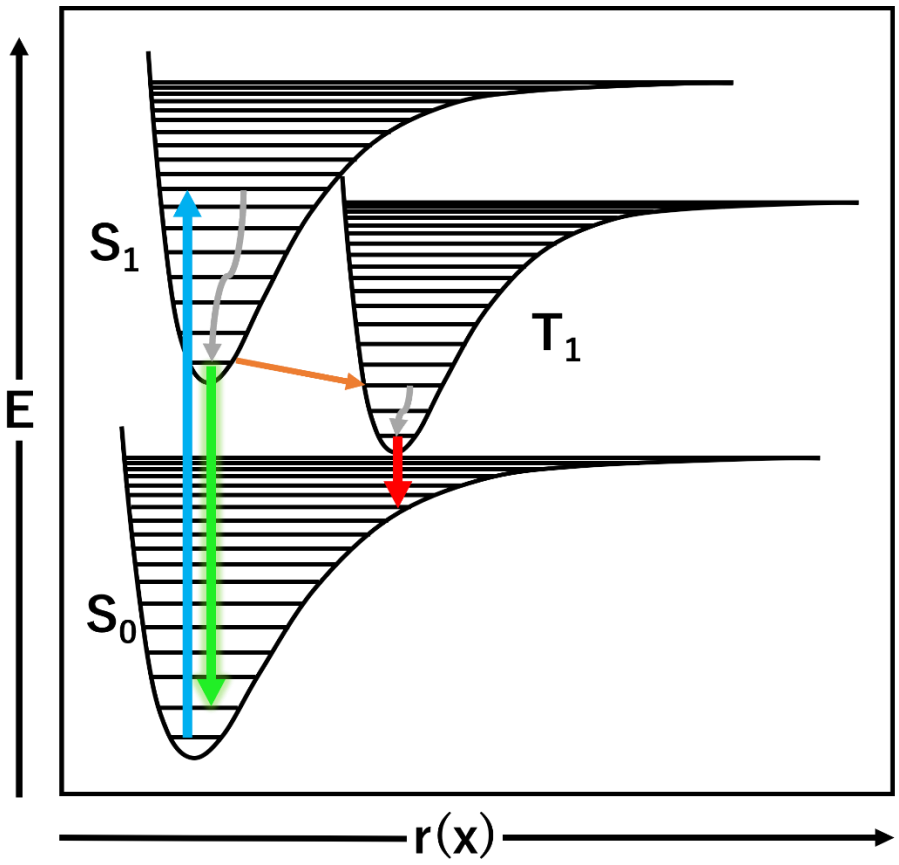

Figure 1.1.1. Jablonksi diagram, where the initial excitation is represented by a blue arrow. Fluorescence (green arrow) occurs after vibrational relaxation (gray, curved arrows) as the sample relaxes radiatively. Intersystem crossing (orange arrow) to a triplet state can also occur. Phosphorescence (red arrow) occurs from a triplet to a singlet.

Some molecules can also make the nonradiative transition to the ground state by a process known as intersystem crossing (ISC), where molecules in an excited singlet state undergo a forbidden spin transition from a singlet to a triplet excited state. A change in the spin state is quantum mechanically forbidden due to the conservation of spin angular momentum, but spin-orbit coupling can lead to a spin flip. The rate of ISC increases with the strength of spin-orbit

coupling. For instance, if a heavy atom such as ruthenium is present, the singlet-triplet transition will be rapid and occur with high probability due to increased spin-orbit coupling. Following ISC, the molecule will immediately undergo VR to the ground vibrational level of the triplet excited state. A radiative transition from the triplet excited state to the ground singlet state is known as phosphorescence, which is also a spin-forbidden transition and occurs on timescales longer than that of spin-allowed fluorescence.

The electronic characterization of radiative transitions can be categorized into two types of measurements—steady state and time-resolved. Steady state photoluminescence is a common technique, where the intensity of emission at different wavelengths is recorded after photoexcitation to generate an emission spectrum. Steady state photoluminescence is often used in excited state quenching experiments, where quenchers decrease the intensity of emission systematically, usually as a function of concentration. Steady state experiments are also useful for classifying systems based on emission range and peak shifting under varied local environments.

Time-resolved photoluminescence is a method for detecting the intensity of emission as a function of time after an initial excitation pulse, which can be characterized by a unique time-dependent radiative decay lifetime. For a large ensemble of molecules, the radiative decay is exponential in nature and can be described by exponential functions to give a lifetime value, denoted as τ (tau). In many molecular systems, the available pathways are unimolecular, or intrinsic to the system, while some are bimolecular, or extrinsic, and contributions from external perturbations can also affect the lifetime, increasing the number of exponentials necessary to describe the relaxation process. Additional processes, which will not be discussed, can also take

place for extremely high irradiation intensities, but are not relevant for the experimental data presented in this dissertation.

1.3.1. TRANSIENT ABSORPTION SPECTROSCOPY

Transient absorption spectroscopy, sometimes termed laser flash photolysis, is a pump-probe spectroscopic technique used to explore the rise and decay behavior of excited state absorption populations following photoinduction. The technique was developed by George Porter and Ronald G. W. Norrish, following the realization that large flashtubes constructed for aerial photography in World War II could also be used to initiate chemical reactions. [7-9]

In his doctoral studies at Cambridge, Porter was tasked with developing a technique capable of detecting short-lived free radicals generated in photochemical reactions. His initial work focused on the methylene radical using an army search light as a continuous light source. While at a Seimens factory collecting a replacement arc lamp for the search light, Porter was introduced to flash lamps, which were being developed for nighttime aerial reconnaissance photographs. Rather than using a continuous white light source to extract information about transient species, Porter realized that using a flash lamp to increase the photon flux applied to a sample could be actinic and generate the free radicals he wished to study. Subsequent flashes from the same source could then be used to monitor the decay of the generated radicals with appropriate detection and timing of the flashes.[10] After the invention of the ruby laser, Porter pushed the limits of flash photolysis into the nanosecond and picosecond time regimes. In 1967, Porter, Norrish, and Manfred Eigen were awarded the Nobel Prize in Chemistry for their contributions to the study of “extremely fast chemical reactions, effected by disturbing the equilibrium by means of very short pulses of

energy." Transient absorption has continued to develop with increasing time resolution, reaching the femtosecond scale in the 1990s thanks to advances by Nobel prize winner Ahmed Zewail. [11]

In TAS, a short, monochromatic pulse of light, or "pump" pulse, generates a transient species in a sample; e.g., a free radical, short-lived excited state, or charge transfer intermediate. A second, broadband pulse of light, typically from a xenon arc lamp, arrives after the first pulse to measure how the absorption of the sample was altered by the initial pump pulse. Practically, pump-probe or transient absorption experiments consist of measuring the intensity of the probe beam transmitted by the sample with and without the pump pulse. In a typical TAS experiment, the probe beam is on before the pump pulse arrives, which allows for characterization of the experiment background. The "probe-only" spectrum represents the ground state absorption of the sample while the "pump + probe" spectrum corresponds to a mixture of contributions from the ground and excited states of the sample (equation #).

$$\Delta OD(t,\lambda) = log\frac{I_{100}}{I_T(t,\lambda)}$$

Spectral data is then represented as the change in absorption, ΔOD, which corresponds to the difference between the "pump + probe" and "probe-only" signal. In spectral representation of the data, a positive ΔOD value corresponds to excited state absorption of the sample following excitation from the pump pulse. This is attributed to the altered wavefunction of the excited electron, which can be further promoted to higher electronic levels via interaction with photons in the probe pulse. Conversely, a negative ΔOD value can be described as a photoinduced transparency, which signifies the depletion of the ground state population (ground state bleaching). Here, the electrons that were interacting with photons in the ground state have been excited by the

pump pulse, i.e., they have departed from the ground state. As such, the photons in this part of the spectrum are transmitted more readily through the sample as the electrons are now described by a wavefunction characteristic to the excited state, which does not wholly overlap with the absorption of the ground state.

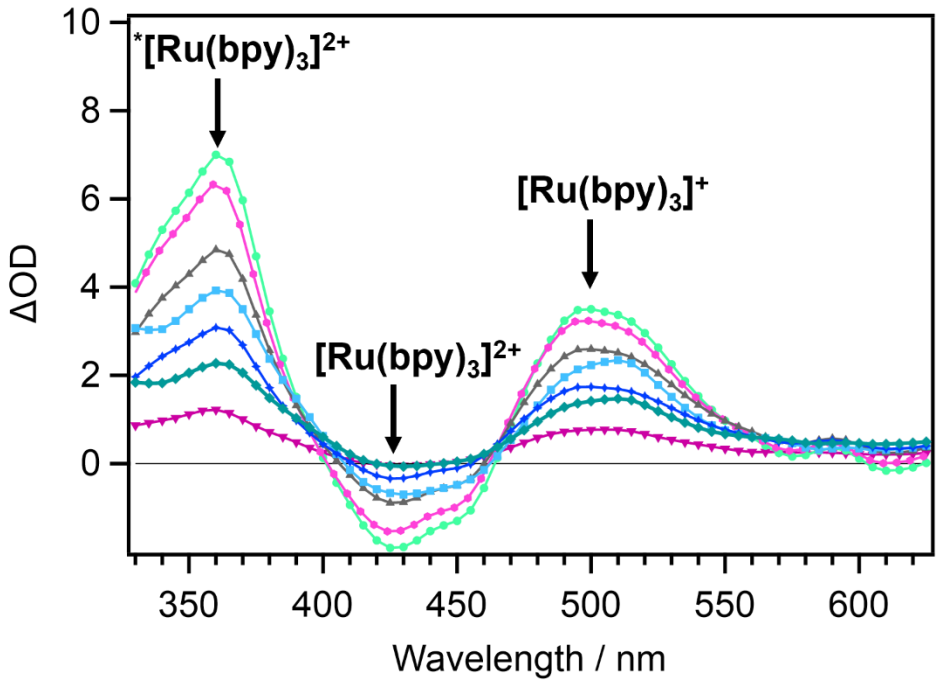

Figure 1.2.2. Representative differential absorption spectrum of $[Ru(bpy)_3]^{2+}$ and ascorbic acid in H_2O, where the positive absorption bands correspond to excited state absorption and the negative band corresponds to the ground state bleach region. Each plotted point is representative of an individual kinetic trace at a single wavelength used visualize the ΔOD spectrum.

The ΔOD data can be acquired and visualized by repeating kinetic measurements at different wavelengths. From this data, a two-dimensional array, ΔOD (t, λ), can be used to generate time-resolved differential absorption spectra. Thus, the ΔOD values can be plotted as a function of time and/or wavelength to describe the evolution of the transient species as it decays

exponentially to the ground state via radiative or nonradiative decay. The Beer-Lambert law, which illustrates the dependence of absorption on the concentration of the species being analyzed, can be used to describe the progression of the system as it relaxes. Immediately after excitation, the largest population of the excited state exists. Thus, the highest concentration of transient species investigated corresponds to the maximum ΔOD signal observed. As the transient species decays, the differential absorption trends towards the baseline generated from probing the ground state before excitation and the ΔOD signal decreases over time. The kinetic traces can be fit with exponential functions to estimate the rate constants associated with these relaxations. Coupled with spectral data, this allows for the interrogation of multiple transient species with unique decay profiles and their associated rate constants in different regions of the spectrum of the probe pulse.

CHAPTER 2

MOTIVATION

2.1. ENERGY DEMAND

The average global energy demand increases each year by an estimated 1.3%.[12] Consequently, increase in global population, economic factors, and continued technological advances contribute to an increasing demand for energy. Fossil fuels such as oil and natural gas are the predominant sources of energy and are predicted to until 2050.[13] However, the consumption of fossil fuels is environmentally taxing due to greenhouse gas emissions, which also contribute to global climate change. Nearly 85% of the global energy demand is met with carbon-based fuel production. An estimated 36 billion tons of CO_2 are emitted into Earth's atmosphere each year, of which more than 90% is produced by fossil fuel consumption. Further, global fossil fuel reserves are finite, and supplies cannot be replenished after use. As a result, many countries are targeting energy consumption and carbon emission reduction efforts. [12] Further, the combustion of fossil fuels contributes to atmospheric pollution and generates significant amounts of CO_2, which is heavily implicated in global warming. Essentially, humans have introduced more CO_2 into the environment than the earth's trees have been able to recycle since the industrial revolution, resulting in an increase in the global temperature. This has motivated the scientific community to seek alternative energy sources that are cleaner and more abundant like renewable energy sources.[14]

2.1.2. SOLAR CELLS

Photovoltaics (PVs) have the potential to play a major role in worldwide energy harvesting and the realization of a low carbon society. Solar cell technology dates to the 1830s when A.E. Becquerel discovered that, upon illumination, an electrode coated in platinum or silver chloride generated voltage when in contact with an electrolyte.[15] The photoelectric effect was later described by Einstein, but several decades passed before the first p-n junction solid state cell was created.[16] Shortly after, the first silicon solar cell was developed using silicon as a raw material and yielded a 6% efficiency, which was quickly improved to an efficiency of 10%.[17] The production cost of these silicon cells was high and, thus, photovoltaics were not recognized as a viable alternative energy resource. However, this changed in the 1970s when oil prices began to climb and alternative energy sources such as solar, wind, and nuclear started to gain public attention in the following decades.

Photovoltaics remain one of the most attractive alternatives to fossil fuels, but for photovoltaics to play a dominant role in the global energy supply a major requirement is the cost reduction of production. Dye-sensitized solar cells (DSCs) have arisen as a technically and economically viable alternative to standard p-n junction photovoltaic devices especially considering the emergence of lightweight computing technologies such as the Internet of Things. The powering of such devices, which operate mostly indoors, is an additional energy issue. Thus, it is sensible to have a self-sustainable power source, such as a photovoltaic cell that can harvest indoor light. While unlikely to completely replace fossil fuels in the foreseeable future, DSCs have shown the capacity to satisfy the energy demands for indoor electronics and could provide a means to reduce the consumption of non-renewables.

CHAPTER 3

DYE-SENSITIZED SOLAR CELLS

3.1 INTRODUCTION

Dye-sensitized solar cells (DSCs) are one emerging solar technology that has attracted substantial attention in recent years due to their relative economic advantage and tunability of individual components.[2, 3] This was initiated by the 1991 report from O'Regan and Grätzel of an efficient photovoltaic device based on a mesoporous, nanocrystalline titania electrode sensitized to visible light by the adsorption of a ruthenium bipyridyl dye in the presence of an iodide/iodine redox electrolyte.[18] Since their seminal report, great progress has been made in materials composition to enhance device efficiency and improve stability and processability.[19-22] Additionally, significant advances have been made in understanding the electron transfer processes underlying overall device performance, which, in turn, provides opportunity for advancing the fundamental understanding of light driven electron transfer reactions at semiconductor interfaces.[23-26]

3.1.1. WORKING PRINCIPLE

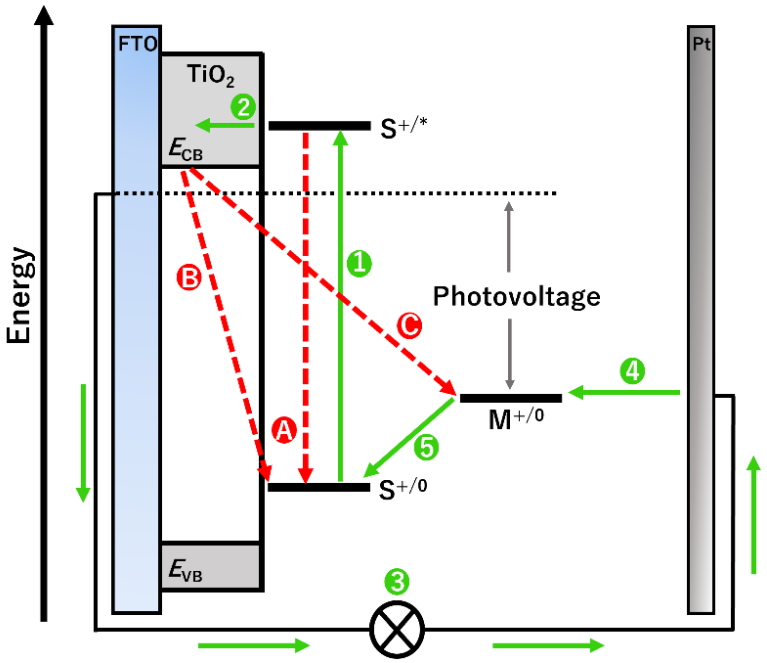

Figure 1. A schematic representation of a DSC depicted with a representative dye (S) and redox shuttle (M). Operating principles consist of (1) light excitation, (2) excited-state electron injection to TiO_2, (3) generation of photocurrent through external circuit to perform work, (4) reduction of the redox mediator, and (5) regeneration of the oxidized sensitizer. Recombination pathways are denoted by red, dashed arrows (A) excited-state relaxation, (B) back electron transfer (BET), and (C) charge recombination to the redox shuttle.

In a typical dye-sensitized solar cell, mesoporous thin films of TiO_2 nanocrystallites are functionalized with molecular chromophores, which are often termed “sensitizers” due to their role in extending the spectral response into the visible region.[3] Upon photon absorption by the sensitizer, a surface-bound chromophore is promoted to a higher energy excited state, whereby it can undergo forward electron transfer (electron injection) to the conduction band or acceptor states in TiO_2. The resultant charge separation consists of the injected electron and the oxidized chromophore. The injected electron then diffuses through TiO_2 until it reaches the back contact

and traverses an external circuit to perform work before collection at the counter electrode. The original state of the dye is restored via electron donation from a redox shuttle (RS) present in the electrolyte, which then transports the oxidizing equivalent, or “hole”, to the counter electrode. The reduction of the oxidized sensitizer by the RS is often termed “dye regeneration” and competes with the back electron transfer from the electron in the TiO_2 conduction band to the oxidized dye.[3]

3.1.2. KINETIC COMPETITION IN DSCs

In addition to the desired processes in a DSC, there are several detrimental processes that can contribute to a decrease in overall cell performance. Upon absorption of a photon, the excited chromophore can undergo relaxation through unproductive radiative pathways rather than undergoing excited-state electron injection. Furthermore, the injected electron can recombine with the redox mediator at the TiO_2 interface (termed recombination) or the oxidized chromophore in a process often termed back electron transfer (BET). Competition between the collection of the injected electron and recombination reactions is considered a significant factor in decreased efficiency of DSCs and the electron must move through the mesoporous TiO_2 layer without interception by an oxidized sensitizer or RS. Numerous TAS studies have sought to understand these reactions, but complex interfacial electron transfer reactions are not fully understood.[27-34] One significant difficulty with interpretation is the dispersive nature of the kinetics abstracted from time-resolved absorption techniques. Interfacial kinetics often span multiple time scales, from nanoseconds to milliseconds, and the underlying rate constants abstracted from exponential fitting are difficult to relate the actual interfacial electron transfer step.[35-38]

3.1.3. BACK ELECTRON TRANSFER (BET)

The electron transfer between reduced TiO_2 and oxidized sensitizers has been investigated extensively using transient absorption spectroscopy (TAS) in order to examine dye cation decay kinetics in devices with no RS present.[39-43] With no RS present, the oxidized sensitizer undergoes back electron transfer (BET) from the reduced TiO_2. An estimated rate constant for this reaction can be determined from monitoring the evolution of the transient absorption signal at its maximum over time, corresponding to the oxidized sensitizer when no RS is present (Figure 2). However, kinetic data abstracted from TAS measurements rarely follows simple first order behavior, stretching from a time scale of nanoseconds to milliseconds. Investigations by the Meyer group and the Durrant group suggest BET kinetics are determined by diffusion-limited encounters between electrons in TiO_2 and oxidized dye molecules.[35-38]

3.1.4. DYE REGENERATION

Dye regeneration is an interfacial electron transfer reaction between oxidized dyes adsorbed to TiO_2 and a RS present in the electrolyte.[44] It is well understood that the regeneration reaction must be fast in comparison to the competing BET reaction for efficient solar-to-energy conversion and TAS measurements offer valuable insight into the efficiency of the reaction when a RS is present in a system. If a RS is present in the electrolyte, the dye cation returns to its ground state by the regeneration reaction with the RS. However, the oxidized dye can also be reduced to its ground state by the competitive BET reaction described above. The rate of the regeneration reaction is commonly estimated by monitoring the decay of the transient absorption signal of the dye cation in the presence of a RS. With efficient regeneration, the transient absorption kinetics

are dominated by the regeneration reaction and the estimated rate constant corresponds to the regeneration of the dye by the RS.

3.1.5. NONEXPONENTIAL KINETICS

Kinetics obtained from TAS measurements used to describe the electron transfer reactions in complex systems like DSCs are often convoluted due to multiple processes. The Kohlrausch−Williams−Watts (KWW) stretched exponential function is most widely used where *k* is the rate constant, A_0 is the initial amplitude of the single wavelength absorption change, and β is inversely related to the width of an underlying distribution of rate constants.[45]

$$A_0(t) = A_0 e^{-(kt)^{\beta}}$$

Stretched exponential decay behavior can be considered as a linear combination of single exponential functions with a continuous distribution of lifetimes.[46-48] Therefore, the stretched exponential function is representative of a system with multiple relaxation pathways that each present single exponential behavior.[49, 50] An advantage of this function is that kinetic data is fit to only two parameters, *k* and β, that quantify the characteristic rate of the transient absorption decay. A β value of 1 corresponds to a single relaxation pathway that exhibits first-order kinetics, i.e., single exponential behavior is observed. As β approaches values closer to 0, the kinetics become more dispersive. Numerous interpretations of stretched exponential behavior exist in the literature. In DSC literature, the most widely accepted interpretation uses a random walk model to derive the stretched exponential behavior of dye-sensitized TiO_2 where electron diffusion occurs via multiple trap/de-trapping from an exponential density of trap states in the conduction band of TiO_2.[51-53] In simplest terms, stretched exponential behavior for the oxidized dye is predicted

when there is an excess of electrons in TiO_2. Therefore, transient absorption kinetics are largely influenced by the concentration of electrons in TiO_2 and subsequently, the excitation intensity used in TAS experiments.[53, 54] A recent study used Monte Carlo simulations to further interpret β values recovered from dye regeneration kinetics. For small β values, the reaction was found to be diffusion-limited and reactions dominated by electron transfer presented β values close to 1.[55]

3.2 SELF-ASSEMBLY STRATEGIES

As mentioned previously, the interfacial electron transfer from the semiconductor back to the oxidized sensitizer dye (back electron transfer, BET) is detrimental to the overall efficiency of DSCs. The DSC is reliant on the reduction of the oxidized dye by a soluble reductant present in the electrolyte, i.e. dye regeneration. In order to extract useful work from a DSC, the regeneration step must possess a larger rate constant than that of the BET reaction. Or to put it more simply, the regeneration reaction must proceed faster than the BET reaction for a DSC to be efficient. For many years, the observation of nearly quantitative conversion efficiencies led many researchers to believe that the regeneration reaction needed no further optimization.[56] Each photoexcited molecule that injected an electron into the semiconductor was believed to be regenerated by the reduced redox species, such as iodide.[57] This assumption appears to hold true for DSCs measured at short circuit conditions, but several studies have shown that BET to the oxidized sensitizer represents a significant loss mechanism at the maximum power point. To put it more simply, the regeneration reaction is not believed to be quantitative when power is extracted from the device.[58] Thus, optimization of the regeneration reaction is necessary to further rationalize DSC device performance.

Typical optimization approaches rely on diffusion-controlled regeneration; however, self-assembled systems have shown dramatic improvements in regeneration rates in addition to enhanced overall DSC device performances. Recent efforts by the Meyer group have shown that interactions between the reductant present in the electrolyte and the reactive donor portion of the immobilized sensitizer dye can significantly affect the rates of the observed regeneration reaction. Further, their studies have also shown that the efficiency of the regeneration step can significantly impact the open-circuit voltage and a decrease in the overall power conversion efficiency of DSC devices may be attributed to nonquantitative regeneration.[56, 59] These studies inspired a significant amount of the work presented within this dissertation.

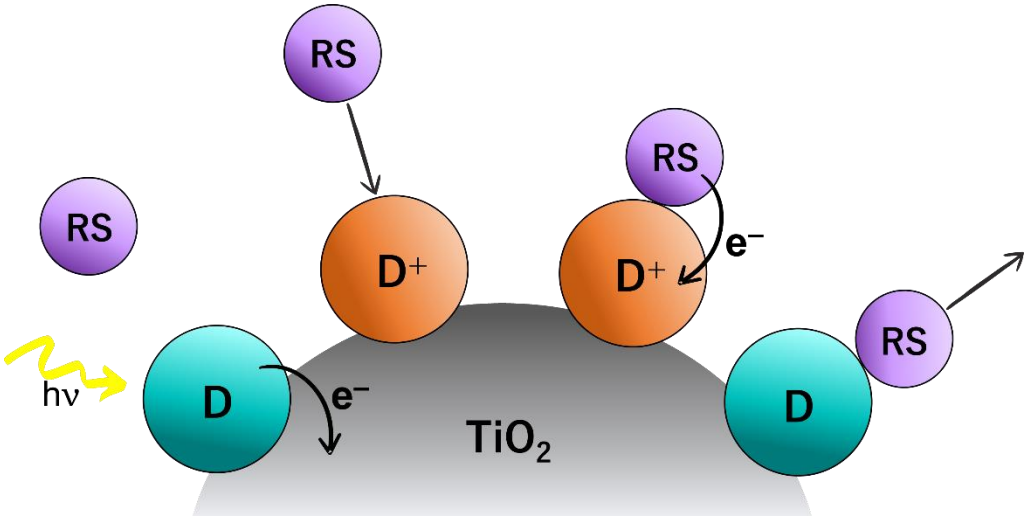

Figure 3.2.1. Representation of a typical DSC environment where the regeneration reaction is diffusion-controlled. From left to right: Photoexcitation of an adsorbed sensitizer dye and subsequent excited-state electron injection to TiO_2, diffusional association of the redox shuttle, regeneration of the oxidized sensitizer, and diffusion of the RS back to the counter electrode.

Several other studies by Meyer and others have attempted to control associations between the donor portion of the dye and the redox shuttle, such as with halogen bonding.[60] This is an

interesting approach towards controlling reactivity using molecular design principles. The remainder of this dissertation will focus on how self-assembly strategies can potentially affect the efficiency of the dye regeneration step and, in turn, the overall conversion efficiency of DSC devices.

3.2.1. LEWIS ACID-LEWIS BASE INTERACTIONS

In his seminal report, Gilbert N. Lewis introduced the concept of electron-pair donor-acceptor complexes, which formed the basis of the current understanding of Lewis acid-Lewis base interactions. [61] Lewis defined acids as any species which can accept an electron pair and bases as species which can donate an electron pair. Interaction of the two chemical species results in the formation of a coordinate covalent bond, i.e., one reactant donates a pair of electrons to another reactant. In this model, it is predicted that a dative bond forms upon reaction of a Lewis acid and a Lewis base to form an adduct by electron donation from the highest occupied molecular orbital (HOMO) of a Lewis base to the lowest unoccupied molecular orbital (LUMO) of a Lewis acid. [62] For example, this is observed in the coordination complex of ammonia borane (H_3NBH_3) where the lone pair on the nitrogen in ammonia is donated to an empty p-orbital on the boron in BH_3. Regardless of the simplicity of the model, the concept of Lewis acid/base interactions is critical in modern transition metal and main group inorganic chemistry.

Until recently, these interactions had yet to be explored as a method for controlling interfacial electron transfer reactions between a sensitizer dye and a redox shuttle in dye-sensitized solar cell (DSC) applications. The research presented in Chapter 6 explores the electron transfer dynamics of a transient redox shuttle-dye coordination complex pre-organized by a Lewis acid-Lewis base interaction.

3.2.1. HALOGEN BONDING

Halogen bonding (X-bonding) can be described as a non-covalent interaction between a covalently bound halogen atom with a Lewis base. In order to understand the implications of halogen bonding as a means to control reactivity, it is essential to describe the nature of halogen bonding. When a halogen forms a covalent bond with another atom such as carbon, an electron from the valence of the halogen atom participates in the formation of the molecular orbital, creating polarization. As a result, electrons opposite the sigma bond are depopulated, creating an anisotropic distribution of charge across the halogen's surface, a positive electrostatic region opposite the sigma bond, and a ring of negative charge around the halogen's equator. Several more detailed accounts of halogen bonding have been published elsewhere.[63-65] In short, the distribution of electron density about the halogen substituent forms an electropositive region termed the σ-hole [CITE]. The size of the σ-hole is expected to increase as the size and polarizability of the halogen increases. Further, increasing electron withdrawing strength of covalently bound functional groups will also result in an increase in the size of the σ-hole. Halogen bonding is a weak interaction but increasing the electron withdrawing strength of covalently bound functional groups has been shown to enhance the electropositive charge of the σ-hole. In this regard, halogen bonding becomes an attractive opportunity for controlling reactivity at the interface.

In a study by Neuburger et al., a series of copper-based sensitizers containing two halogens of differing identities was synthesized and characterized. Their results suggest that the iodine-based sensitizer exhibited greater overall efficiency due to enhanced regeneration between the oxidized dye and redox shuttle.[66] Similarly, studies by the Meyer group investigated a

homologous series of donor-pi-acceptor (D-π-A) dyes that differed only in the identity of the halogen substituents (F, Cl, Br, I) on the triphenylamine (TPA) donor unit of the molecule. Their work suggests that the rate of the dye regeneration reaction increases across the halogen series as the size of the sigma hole increased, which also correlated with improved device performance values for the iodine-substituted donor unit.

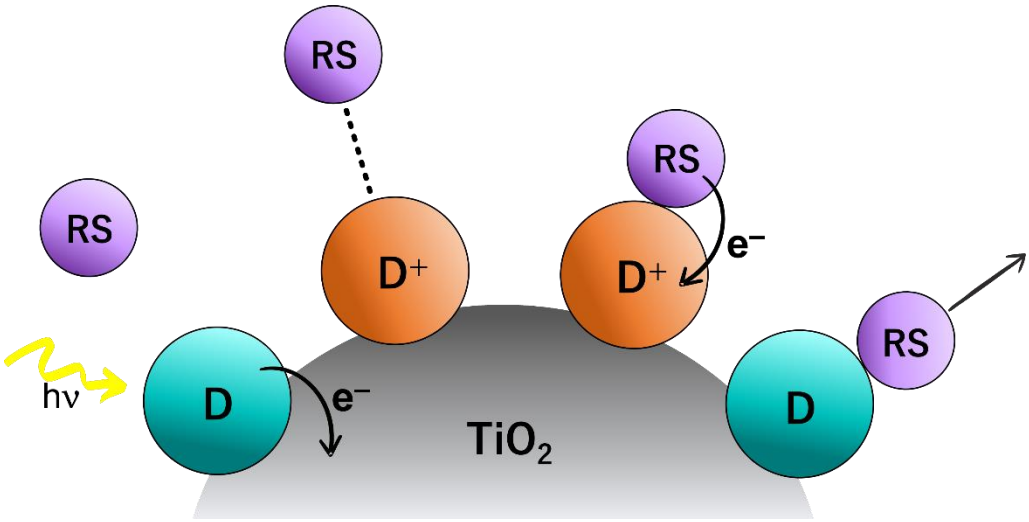

Figure 3.2.2. Representation of a DSC environment where the regeneration reaction is **. From left to right: Photoexcitation of an adsorbed sensitizer dye and subsequent excited-state electron injection to TiO_2, pre-organized interactions between the redox mediator and the reactive donor portion of the oxidized dye, regeneration of the oxidized sensitizer, and diffusion of the RS to the counter electrode.

Specifically, the analysis of single wavelength absorption changes monitored by transient absorption spectroscopy (TAS) supported a halogen bonding interaction following the trend I>Br>Cl>F, in order of decreasing regeneration rate. A follow-up publication used x-ray absorption spectroscopy to further interrogate the interactions and found that halogen bonding only occurred between Cl^- and the oxidized sensitizer and no interactions were found between the

ground state of the sensitizers with the redox shuttle.[60] Expanding upon this approach, Chapter 5 explores the possibility of halogen bonding interactions between sensitizers designed with electron rich cyclopentadithiophene (CPDT) donor groups with attached halogen atoms (Cl, Br, I) at one terminal position and Lewis basic transition metal-based redox shuttle.

3.3 SURFACE MODIFICATION STRATEGIES

As discussed in the previous sections, a key requirement for improved efficiency of DSCs is the enhancement of forward electron transfer processes, such as electron transfer from the reductant to the oxidized dye. However, an alternative approach to improving DSC efficiency involves methods for reducing detrimental electron transfer reactions, such as recombination of electrons in the TiO_2 conduction band with the redox species in the electrolyte. One of the simplest methods among these approaches is modification of the surface of the photoanode, which has previously been reported to have beneficial effects on both light harvesting ability and reduction in recombination pathways.[67]

For DSC applications, the most commonly used photoanode material is TiO_2 nanoparticles, which are sintered together establish electronic conduction. Efforts to reduce recombination of electrons in TiO_2 and electron acceptors in the electrolyte has been explored with various approaches: blocking layers on the TiO_2 surface, $TiCl_4$ treatment, acid treatments, co-adsorbents, and electrolyte additives.[68, 69] These strategies are particularly important because they offer methods to improve overall efficiency without tuning sensitizer structure so they reduce synthetic design demands and potentially allow for the use of existing sensitizer dyes. [70-79] [69-78] [68-77] [68-77] [67-76] [67-76] [67-76] [66-75] [65-74] Recently, fluorinated molecules with silyl anchors have been employed as fluorinated self-assembled monolayers (F-SAM) that co-adsorb to

the semiconductor in the presence of a sensitizer dye to reduce recombination sites and lower surface tension.

The pre-sensitization approach explored in this dissertation involves the treatment of the photoanode with a wide bandgap metal oxide, which forms a thin overlayer at the TiO_2 surface and acts as an insulating layer to inhibit backward electron transfers. The use of insulating metal oxides such as MgO and Al_2O_3 between the dye and semiconductor to reduce recombination rates has been an active area of research within the DSC field. However, in many studies, this blocking effect has also been shown to decrease the efficiency of electron injection from the dye to TiO_2. The pre-sensitization treatment investigated herein uses an $Mg(OMe)_2$ solution incorporated in the semiconductor matrix (underneath the adsorbed dye layer).

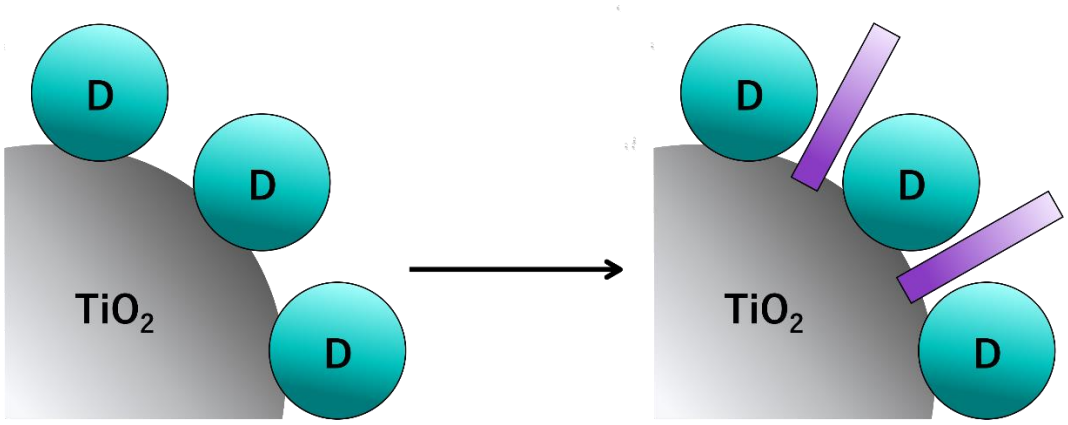

Figure 3.3.1. Representative graphic of TiO_2 surface before (left) and after (right) a post-modification surface treatment such as a fluorinated self-assembled monolayer, where the ** represent anchored PFTS chains that fill vacant sites between dye molecules.

The post-sensitization treatment explores the formation of a fluorinated self-assembled monolayer (F-SAM) on the TiO_2 surface. With this approach, the fluorinated PFTS chains anchor

to the surface between dye molecules, which is thought to reduce aggregation between dye molecules and prevent recombination by filling vacant sites on the surface. Chapter 7 explores how these pre- and post-sensitization treatments can affect recombination, BET, and the dye regeneration rate of a broadly absorbing **B11**/$Co(bpy)_3^{3+/2+}$ system for dye-sensitized applications.

CHAPTER 4

EXPERIMENTAL METHODS

4.1 TIME-CORRELATED SINGLE PHOTON COUNTING

Time-resolved luminescence spectroscopy is a powerful method for the determination of a molecule's emissive properties. Many molecules are emissive and given the dependence of local environment on a molecule's emissive properties, time-resolved measurements often provide valuable information. In principle, information can be derived from a single excitation emission cycle, but practical problems can prevent the extrapolation of valuable information from these measurements such as the rapid timescale of excited state deactivation. Implementation of it in such fast time domains requires recording the time dependent intensity profile of the emitted light upon excitation by a short flash of light, typically a laser pulse. For the TCSPC data presented in this dissertation, a schematic of the experimental setup is presented in Figure 4.1.1. The basic principles of TCSPC have been the subject of many reviews.[80-82] Briefly, the method relies on the concept that following photoexcitation, the probability distribution for emission of a single photon gives an intensity against time distribution of all photons emitted, thus by sampling the time-dependent single photon emission following several excitation pulses, a probability distribution is created.

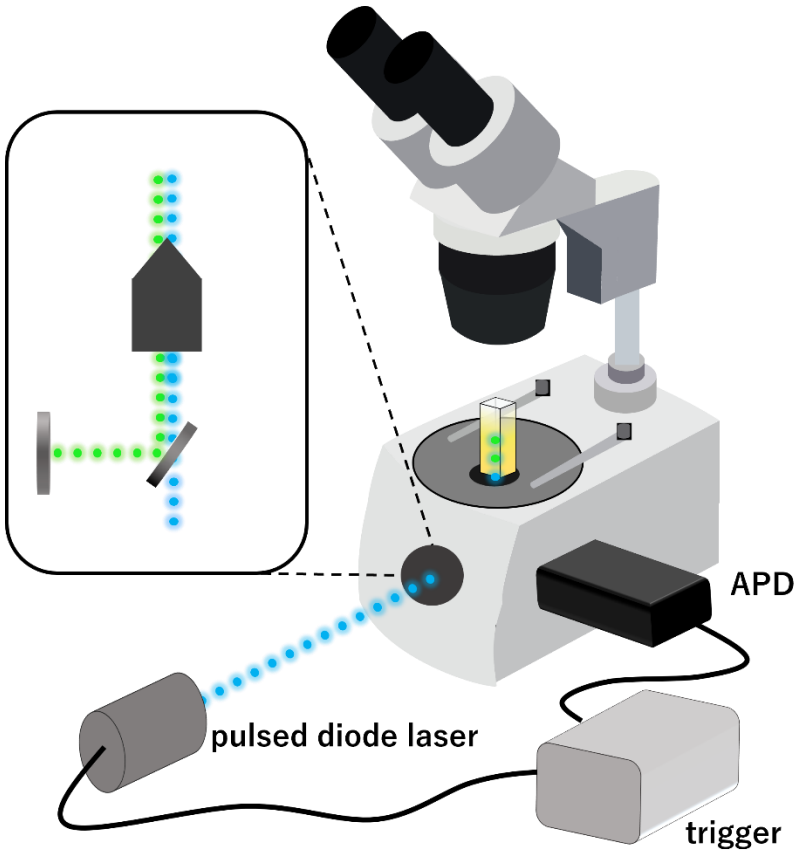

Figure 4.1.1. Schematic of the Time-correlated Single Photon Counting (TCSPC) experiment, including a pulsed diode laser, trigger sources, and the avalanche photodiode detector. A histogram of photon counts per unit time is generated in reference to the trigger, which is tied to the firing signal for the laser. Inset: A dichroic or other optical filter separates the excitation from the epifluorescence.

For the data presented herein, the excitation source, a pulsed diode laser, has a pulse width of <150 ps and a variable rep rate. As shown in Figure 4.1.1, the excitation beam is focused into the sample through a microscope. The light emitted from the sample then passes through a filter (or multiple filters), to eliminate artifacts from the excitation source as well as other experimental artifacts. These optical filters should be chosen based on the laser line used as well as the steady state emission profile of the sample of interest. The emitted light is redirected into a single photon

counting avalanche photodiode (APD). The photocurrent generated at the diode is processed by a Picoquant® photon counting card with ~60 ps of jitter and the observed emission decay traces are displayed using a program coded in LabView. The TCSPC data presented in this dissertation was acquired with a 485 nm pulsed diode laser. Because the experiment utilizes an APD, no information regarding the range of emitted wavelengths is acquired. Steady state fluorescence spectra can be obtained by switching the output to a CCD camera.

4.2 TRANSIENT ABSORPTION SPECTROSCOPY

As discussed in Chapter 1, transient absorption spectroscopy (TAS) is a valuable technique to extract kinetic information of short-lived excited state species that are important for several applications such as dye-sensitized solar cells (DSCs) and photocatalysis. The transient absorption spectroscopy data presented in this dissertation was recorded with a commercial flash photolysis spectrometer from Edinburgh Instruments (LP980). A representative schematic is shown in Figure 4.2.2.

The pump (or excitation) source is a pulsed Neodymium-doped Yttrium Aluminum Garnet (Nd:YAG) laser (Continuum, Surelite II), which has a fundamental output wavelength of 1064 nm. However, for the measurements described herein, the 1064 nm output was typically frequency doubled to 532 nm by means of a second harmonic generator. Briefly, this is a nonlinear process in which two photons of the same frequency interact with a nonlinear material and are doubled in energy to generate a photon with half the wavelength of the incident photons.[83]

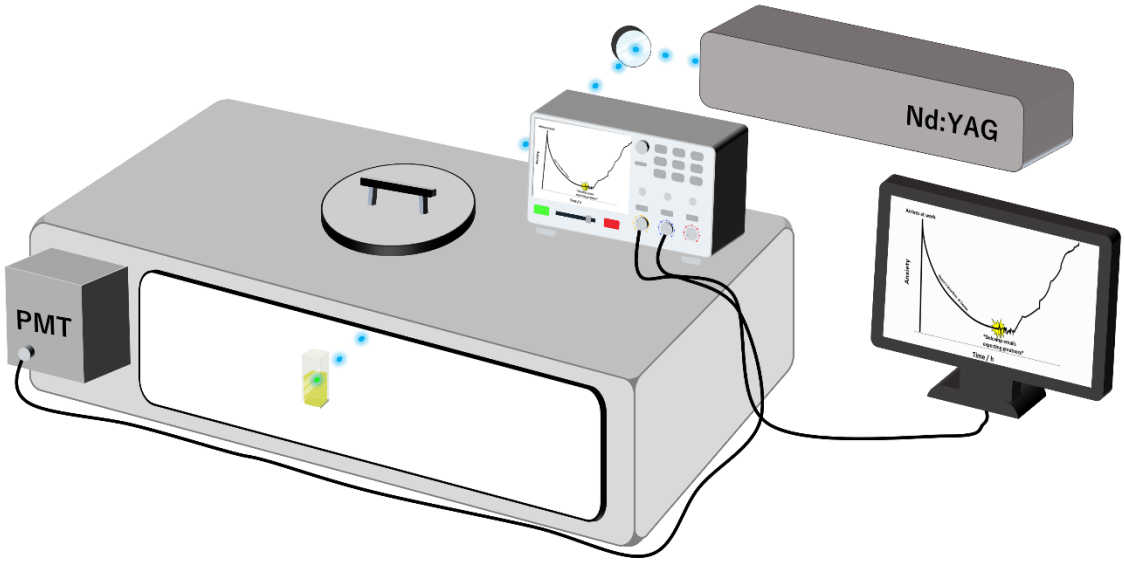

Figure 4.2.2. Schematic of the LP980 spectrometer, including a pulsed Nd:YAG laser, trigger source, and a photomultiplier tube for detection. Synchronization of the pulses is controlled by the L900 software.

Absorption changes induced by the excitation pulse are recorded with broadband xenon lamp (150 W) that is operational in pulsed or continuous wave mode, dependent upon the timescale of the experiment and the systems under study. The probe source can be operated in pulsed mode when a higher photon flux is desired or necessary, specifically in short time domains (ns to low μs) or when systems are intensity independent. However, the use of such large lamps in pulsed mode can be actinic and careful consideration should be given when determining the applicability of a pulsed probe source for an experiment. Thus, the data reported in this dissertation were acquired with a CW probe source due to the well-documented irradiation sensitivity of surface-adsorbed systems, two photon absorption effects,[84] and the prolonged timescales of the monitored absorption changes. An electronically controlled shutter placed between the probe and the sample prevents photodegradation of samples under study.

Time-dependent absorption changes are recorded at a single wavelength by means of a monochromator, a photomultiplier tube, and a digital storage oscilloscope, which can also be termed a “kinetic” mode, i.e., no gated spectral detector. Spectral data can be achieved in this acquisition mode by scanning a software-defined spectral range and subsequent “slicing” of the compiled kinetic data. In looser terms, single wavelength kinetics are obtained at specified wavelengths and the corresponding O.D. values are representative of transient species both spectrally and temporally. This method of spectral data acquisition is reliable but does require the user to have extensive knowledge of both the instrument and the system under study.

CHAPTER 5

HALOGEN BONDING AT THE INTERFACE

The work in this chapter is based on a publication in the *Journal of Physical Chemistry C*, "Probing interfacial halogen bonding effects with halogenated organic dyes and a Lewis base decorated transition metal-based redox shuttles at a metal oxide interface in dye-sensitized solar cells". This work was collaborative with contributions from Christine Curiac,[a,†] Md Abdus Sabuj, [b,†] Qing Li,[a] Alexandra Baumann,[a] Hammad Cheema,[a] and Yanbing Zhang[a]. The dyes were synthesized and characterized by Alexandra Baumann and Qing Li. The redox shuttles were synthesized and characterized by Christine Curiac. Computations were performed by Md Abdus Sabuj. The TAS data collection and data analysis was performed by the author.

[a.] Department of Chemistry and Biochemistry; University of Mississippi; University, MS 38677, USA

[b.] Dave C. Swalm School of Chemical Engineering and Center for Advanced Vehicular Systems; Mississippi State University; Mississippi State, MS, 39762, USA

[†]*Denotes equal contribution.*

INTRODUCTION

Photoinduced electron transfer systems with molecular organic dyes at interfaces are critically important to numerous applications including dye-sensitized photoelectrochemical cells (DS-PECs),[85-89] dye-sensitized solar cells,[19, 90-97] and solar redox batteries.[98-105] Metal oxide semiconductor (e.g. TiO_2) bound chromophore devices are common in the literature and typically rely on a photoinduced charge transfer event from the dye to the metal oxide followed by regeneration to the ground state of the dye from a redox shuttle (RS). Studies on TiO_2-dye-RS systems with pre-organized transiently stable non-covalent interactions between the dye and RS can improve electron transfer reaction kinetics and improve device performances. Ideally, the dye-RS non-covalent bond could be used to increase the effective concentration of RS at the dye interface and be broken allowing for diffusion of the RS from the TiO_2-dye interface.

Halogen bonds typically refer to non-covalent interactions involving a halogen atom,[106] which to the best of our knowledge, have not yet been probed with transition metal-based redox shuttles (RSs) to a halogen on an organic dye at a metal oxide surface. Literature has shown significant precedent for using of Lewis base or halogen functionality on dyes coordinating to X_2 and X^- groups in solution [106, 107] and at surfaces.[108-113] Expanding from X^- coordination to transition metal based RSs with Lewis base functionality coordination could modulate electron transfer kinetics. Designing systems with faster electron regeneration kinetics by using transition metal-based RSs via self-assembly through non-covalent interactions is therefore an intriguing direction.[114-116] This study employs a RS with an accessible peripheral Lewis base site ($Co(\textit{N}\text{-tpy})_2$, where *N*-tpy is 2,6-di(pyrid-2-yl)pyrazine), targeted for studies with a series of organic dyes having a single atom change (Cl, Br, and I) at a TiO_2 semiconductor interface (Figure 1).

The target dyes use electron rich cyclopentadithiophene (CPDT) donor groups with attached halogen atoms at one terminal position (Figure 1). A control with a hydrogen atom at the terminal position is also targeted as a comparison material for some studies. The use of thiophene-based donors provides an opportunity to examine the effects of having a halogen in conjugation with an intramolecular charge transfer (ICT) π-system when an acceptor group is placed at the opposite terminal to the halide. The cyanoacrylic acid (CAA) group is used as a TiO_2 anchoring acceptor known to undergo facile electron injection into TiO_2. This molecular engineered construct exposes the halogen to the environment above the TiO_2 film surface functionalization with the dye. A Lewis base decorated transition metal-based redox shuttle in a solution can then be used to probe halogen bonding effects at the TiO_2-dye-X surface experimentally and computationally.

A series of electron transfer reactions can occur upon photoexcitation of the TiO_2-dye-X-RS system, including: (1, ICT) the photoexcitation of the dye bound to the surface of TiO_2 to promote an ICT event, (2, injection) electron injection into the TiO_2 conduction band (CB) yielding a dye cationic species, (3, regeneration) electron transfer to an oxidized dye by a reduced RS in solution, and (4, recombination) electron transferring back to the oxidized RS from the TiO_2 CB under open circuit conditions (Figures 1 and 2, arrows correspond to the numbers listed). If an external circuit is connected to a counter electrode, an electron transfer from the counter electrode to the oxidized RS will complete the circuit. The RS-dye pair has a significant impact on the electron transfer reactions indicated in arrows 3-5. Arrow 3 (or regeneration) in this scheme is particularly important to photoelectrochemical cells, solar cells, solar batteries, and dye-sensitized photodetectors since a competitive parasitic pathway, arrow 5 or back electron transfer (BET), exists for the transfer of electrons from the TiO_2 CB to the oxidized dye which limits the overall

quantum yield of these devices. Arrows 3 and 5 are both readily monitored by transient absorption spectroscopy in the presence or absence of a RS, respectively. The dye cation signature diminishing over time and provides a method of analyzing the influence of halogen bonding on the kinetics of electron transfer when RSs with and without Lewis basic functionality are compared. Positive charge build-up near the halide after electron transfer from a dye to TiO_2 is likely,[117] and positive charge build up has been shown to increase halogen bond donor strength resulting in a stronger halogen bond for more dramatic effects.[118] The use of two CPDT groups results in extended conjugation of the system which allows for both broader and increased visible light absorption past the absorption of the RSs.[119] Additionally, arrow 4 (recombination) can be probed with small modulated photovoltage transient (SMPVT) techniques or electrochemical impedance spectroscopy (EIS). The series of spectroscopic techniques allow for the analysis of halogen bonding effects on arrows 3-5.

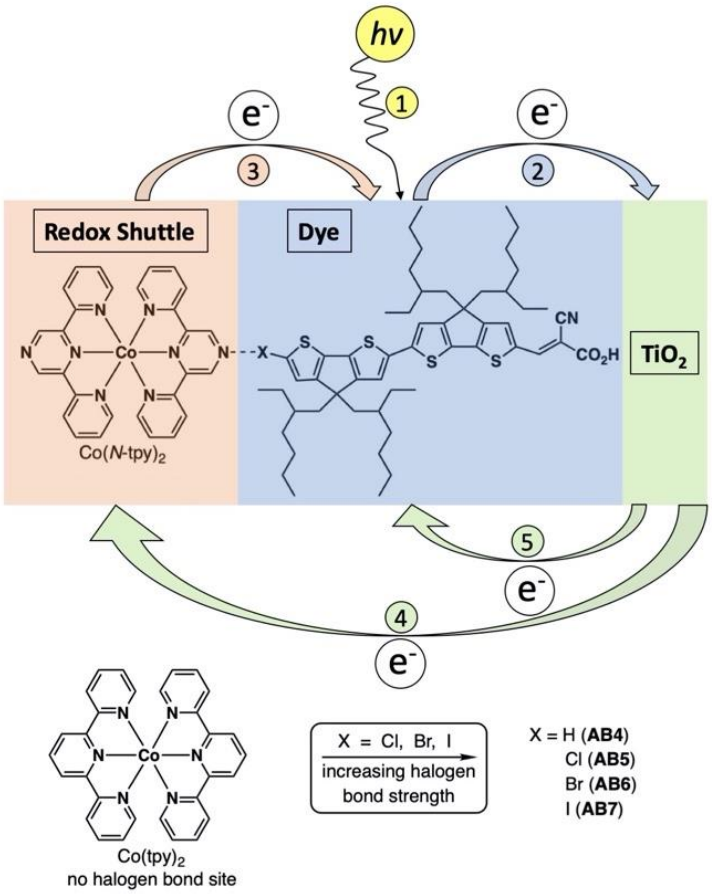

Figure 5.1. Non-covalent interaction between a cobalt-based RS (Co(*N*-tpy)$_2$) and a halogen atom on a dye.

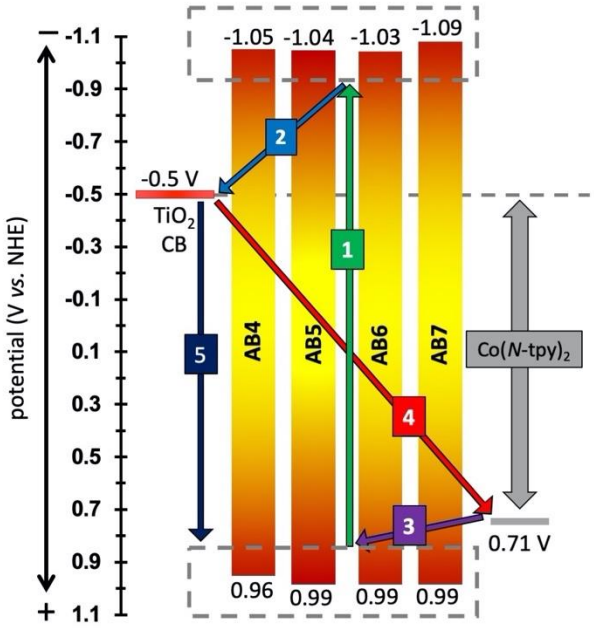

Figure 5.2. Electron transfer pathways of dyes **AB4-AB7** to the TiO_2 CB and from Co(*N*-tpy)$_2$.

MATERIALS

All commercially obtained regents were used as received. 4H-cyclopenta[2,1-b:3,4-b']dithiophene and 2-ethylhexyl bromide were purchased from Matrix Scientific. Thin-layer chromatography (TLC) was conducted with Sorbtech silica XHL TLC plates and visualized with UV. Flash column chromatography was performed with Sorbent Tech P60, 40-63 um (230-400 mesh). ^{1}H and ^{13}C NMR spectra were recorded on a Bruker Avance-300 (300 MHz), Bruker Avance-400 (400 MHz) and Bruker Avance-500 (500 MHz) spectrometer and are reported in ppm using solvent as an internal standard ($CDCl_3$ at 7.26 ppm and CD_3CN at 1.94 ppm). Data reported as s = singlet, d = doublet, t = triplet, q = quartet, p = pentet, m = multiplet, br = broad, ap = apparent, dd = doublet of doublets; coupling constant(s) in Hz. UV spectra were measured with a Cary 5000 UV-Vis-NIR spectrometer with dichloromethane solution. Cyclic voltammetry curves were measured with a C-H Instruments electrochemical analyzer CHI600E. 0.1 M

tetrabutylammonium hexafluorophosphate was used as the electrolyte. The working electrode is glassy carbon, reference is a silver wire, and the counter is platinum with a scan rate of 100 mV/s. Ferrocene is used as an internal standard (taken as 0.64 V vs NHE in MeCN, 0.70 V vs NHE in DCM) and decamethyl ferrocene (taken as 0.05 V vs NHE in MeCN) was used as an internal standard for Co(*N*-tpy)$_2$ due to overlap of signals with ferrocene. Tributyl-(4,4-diethylhexyl-4a,7a-dihydro-4H-cyclopenta[2,1-b;3,4-b']dithiophen-2-yl)-stannane (**1**),[119, 120] 6'-bromo-4,4-diethylhexyl-4H-cyclopenta[2,1-b:3,4-b']dithiophene-2-carbaldehyde (**2**),[121] [Co(tpy)$_2$][TSFI]$_2$,[122] [Co(tpy)$_2$][TSFI]$_3$,[122] and 2,6-di(pyrid-2-yl)pyrazine (*N*-tpy)[123] are previously reported (see Schemes 1 and 2 for numbering). Analogues of the following compounds are reported with hexyl chains in place of the ethylhexyl chains with slightly modified synthetic procedures for these compounds reported below: 4,4,4',4'-tetraethylhexyl-4a,7a,4',7'b-tetrahydro-4H,3'aH-[2,2']bi[cyclopenta[2,1-b;3,4-b']dithiophenyl]-6-carbaldehyde (**3**),[119] 6'-bromo-4,4,4',4'-tetraethylhexyl-4a,7a,4',7'b-tetrahydro-4H,3'aH-[2,2']bi[cyclopenta[2,1-b;3,4-b']dithiophenyl]-6-carbaldehyde (**5**),[119] and 2-cyano-3-(4,4,4',4'-tetraethylhexyl-4a,7a,4',7'b-tetrahydro-4H,3'aH-[2,2']bi[cyclopenta[2,1-b;3,4-b']dithiophenyl]-6-yl)-acrylic acid (**AB4**).[119] ^{13}C NMR data is reported for **3-6** and **AB4-AB7** despite being a mixture of multiple diastereomers due to the four ethyl hexyl chains having stereocenters which causes a number of the carbon atoms to have unique shifts depending on the diastereomer complicating the ^{13}C NMR spectrum.

SYNTHESIS

4,4,4',4'-Tetraethylhexyl-4a,7a,4',7'b-tetrahydro-4H,3'aH-[2,2']bi[cyclopenta[2,1-b;3,4-b']dithiophenyl]-6-carbaldehyde (**3**): In a 100 mL round bottom flask, 6'-bromo-4,4-diethylhexyl-

4H-cyclopenta[2,1-b:3,4-b']dithiophene-2-carbaldehyde (**2**)[121] (0.528 g, 1.04 mmol) and tributyl-(4,4-diethylhexyl-4a,7a-dihydro-4H-cyclopenta[2,1-b;3,4-b']dithiophen-2-yl)-stannane (**1**)[119, 120] (0.663 g, 1.04 mmol) were dissolved in chloroform (31 mL). The solution was then degassed for about 30 minutes with N_2 and $Pd(PPh_3)_4$ (0.120 g, 0.104 mmol) was added. The solution was sealed in a pressure flask and heated to 80^{o}C until completion. The mixture was then extracted with dichloromethane and water, then dried with sodium sulfate. The crude product **3** was purified with silica gel chromatography with 25% dicholormethane/hexanes to give pure **3** (0.588 g, 68%). ^{1}H NMR (400 MHz, $CDCl_3$) δ 9.82 (s, 1H), 7.57-7.52 (m, 1H), 7.17 (ap d, J = 4.8 Hz, 1H), 7.08-7.06 (m, 1H), 7.02 (m, 1H), 6.95-6.93 (m, 1H), 2.00-1.80 (m, 8H), 1.20-.50 (m, 60H) ppm. ^{13}C NMR (400 MHz, $CDCl_3$) δ 182.5, 163.1, 158.5, 157.3, 143.2, 142.7, 137.0, 136.6, 136.6, 130.8, 125.3, 122.5, 119.3, 119.2, 119.1, 117.7, 117.6, 54.2, 53.9, 43.2, 35.4, 35.2, 34.3, 28.7, 27.7, 27.4, 22.9, 14.2, 10.9, 10.7 ppm. HRMS (ESI positive mode) m/z calc'd for $C_{51}H_{74}OS_4$ $[M]^+$: calculated 830.4622, found 830.4615.

6'-chloro-4,4,4',4'-tetraethylhexyl-4a,7a,4',7'b-tetrahydro-4H,3'aH-[2,2']bi[cyclopenta[2,1- b;3,4-b']dithiophenyl]-6-carbaldehyde (**4**): In a 10 mL round bottom flask, 4,4,4',4'-Tetraethylhexyl-4a,7a,4',7'b-tetrahydro-4H,3'aH-[2,2']bi[cyclopenta[2,1-b;3,4-b']dithiophenyl]-6-carbaldehyde (**3**) (0.100 g, 0.120 mmol) was dissolved in 2.9 mL of tetrahydrofuran. The solution was then degassed for about 10 minutes with N_2 and cooled to 0^{o}C. Recrystallized NCS (*N*-chlorosuccinimide, 0.018 g, 0.132 mmol) was then added. The reaction was kept under N_2 and stirred at 0^{o}C for 1 hour, then allowed to warm to room temperature for 16 hours. The mixture was then extracted with diethyl ether and water, and dried with sodium sulfate. The crude product **4** was purified with silica gel chromatography with 25%

dicholormethane/hexanes to give pure **4** (0.102 g, 98%). ^{1}H NMR (400 MHz, $CDCl_3$) δ 9.86-9.81 (m, 1H), 7.60-7.53 (m, 1H), 7.11-6.97 (m, 2H), 6.84 (ap t, J = 3.8 Hz, 1H), 2.01-1.77 (m, 8H), 1.14-0.51 (m, 60H ppm. ^{13}C NMR (400 MHz, $CDCl_3$) δ 182.6, 163.0, 157.5, 157.3, 155.5, 148.1, 142.9, 142.8, 137.1, 136.3, 134.1, 130.8, 129.3, 129.2, 122.1, 119.0, 117.9, 54.9, 54.2, 43.1, 35.4, 35.3, 34.4, 34.2, 29.9, 28.7, 28.6, 27.7, 27.6, 27.5, 27.5, 27.4, 22.9, 14.2, 10.9, 10.7 ppm. ESI HRMS m/z calc'd for $C_{51}H_{73}ClOS_4Cs$ $[M + Cs]^+$: calculated 997.3287, found 997.3277.

6'-bromo-4,4,4',4'-tetraethylhexyl-4a,7a,4',7'b-tetrahydro-4H,3'aH-[2,2']bi[cyclopenta[2,1-b;3,4-b']dithiophenyl]-6-carbaldehyde (**5**): In a 10 mL round bottom flask, 4,4,4',4'-tetraethylhexyl-4a,7a,4',7'b-tetrahydro-4H,3'aH-[2,2']bi[cyclopenta[2,1-b;3,4-b']dithiophenyl]-6-carbaldehyde (**3**) (0.100 g, 0.120 mmol) was dissolved in 2.9 mL tetrahydrofuran. The solution was then degassed for about 10 minutes with N_2 and cooled to 0°C. Recrystallized NBS (*N*-bromosuccinimide, 0.024 g, 0.132 mmol) was then added. The reaction was kept under N_2 and stirred at 0°C for 1 hour, then allowed to warm to room temperature for 16 hours. The mixture was then extracted with diethyl ether and water, and dried with sodium sulfate. The crude product **5** was purified with silica gel chromatography with 25% dicholormethane/hexanes to give **5** (0.109 g, 91%). ^{1}H NMR (400 MHz, $CDCl_3$) δ 9.82 (s, 1H), 7.55 (ap t, J = 3.7 Hz, 1H), 7.08-7.00 (m, 2H), 6.96 (ap t, J = 4.1 Hz, 1H), 2.02-1.76 (m, 8H), 1.19-0.41 (m, 60H) ppm. ^{13}C NMR (400 MHz, $CDCl_3$) δ 182.6, 163.1, 157.7, 157.2, 156.7, 148.1, 142.9, 142.8, 137.2, 137.0, 136.3, 134.1, 130.8, 125.5, 119.0, 117.8, 111.4, 54.7, 54.2, 43.1, 35.3, 34.4, 34.3, 34.2, 28.7, 28.6, 27.7, 27.6, 27.5, 27.4, 22.9, 22.9, 22.9, 14.2, 10.9, 10.8, 10.7 ppm. HRMS (ESI positive mode) m/z calc'd for $C_{51}H_{73}BrOS_4Cs$ $[M + Cs]^+$: calculated 1041.2782, found 1041.2772.

6'-iodo-4,4,4',4'-tetraethylhexyl-4a,7a,4',7'b-tetrahydro-4H,3'aH-[2,2']bi[cyclopenta[2,1-b;3,4-b']dithiophenyl]-6-carbaldehyde (**6**): In a 10 mL round bottom flask, 4,4,4',4'-tetraethylhexyl-4a,7a,4',7'b-tetrahydro-4H,3'aH-[2,2']bi[cyclopenta[2,1-b;3,4- b']dithiophenyl]-6-carbaldehyde (**3**) (0.050 g, 0.060 mmol) was dissolved in 1.4 mL of tetrahydrofuran. The solution was then degassed for about 10 minutes with N_2 and cooled to 0^{o}C. Recrystallized NIS (*N*-iodosuccinimide, 0.015 g, 0.066 mmol) was then added. The reaction kept under N_2 and stirred at 0^{o}C for 1 hour, then allowed to warm to room temperature for 16 hours. The mixture was then extracted with diethyl ether and water, and dried with sodium sulfate. The crude product **6** was purified with silica gel chromatography with 25% dicholormethane/hexanes to give pure **6** (0.034 g, 60%). ^{1}H NMR (400 MHz, $CDCl_3$) δ 9.82 (s, 1H), 7.55 (ap t, J = 4.0 Hz, 1H), 7.12 (ap t, J = 4.1 Hz, 1H), 7.09-6.98 (m, 2H), 2.12-1.69 (m, 8H), 1.16-0.18 (m, 60H) ppm. ^{13}C NMR (400 MHz, $CDCl_3$) δ 182.6, 163.1, 158.6, 158.2, 158.1, 157.4, 148.1, 142.9, 142.7, 141.7, 137.3, 136.2, 134.2, 131.9, 130.8, 129.3, 119.1, 119.0, 118.0, 117.9, 71.9, 71.8, 54.2, 53.9, 43.17, 43.1, 35.3, 34.5, 34.4, 34.2 39.8, 28.7, 28.6, 27.8, 27.7, 27.6, 27.5, 27.4, 27.3, 22.9, 14.3, 14.2, 10.9, 10.8, 10.7 ppm. ESI HRMS m/z calc'd for $C_{51}H_{73}IOS_4Cs$ $[M + Cs]^+$: calculated 1089.2643, found 1089.2625.

2-Cyano-3-(4,4,4',4'-tetraethylhexyl-4a,7a,4',7'b-tetrahydro-4H,3'aH-[2,2']bi[cyclopenta[2,1-b;3,4-b']dithiophenyl])-acrylic acid (**AB4**): In a 8.0 mL vial, 4,4,4',4'-tetraethylhexyl-4a,7a,4',7'b-tetrahydro-4H,3'aH-[2,2']bi[cyclopenta[2,1- b;3,4-b']dithiophenyl])-6-carbaldehyde (**3**) (0.100 g, 0.120 mmol) was dissolved in 2.4 mL chloroform. The mixture was then degassed with N_2 for approximately 30 minutes. Cyanoacetic acid (0.031 g, 0.360 mmol) and piperidine (0.083 mL, 0.840 mmol) were added to the vial, which was then sealed with an open top cap sealed with a PTFE coated rubber septum, heated to 90^{o}C and allowed to stir

for 16 hours. The reaction mixture was diluted with dichloromethane and purified through a plug of silica gel with the following elution solvents sequentially: 100% dichloromethane, then 10% methanol/dichloromethane, and finally 12% methanol/3% acetic acid/dichloromethane. The solvent of the third fraction was evaporated under reduced pressure. The dye (**AB4**) was then extracted with hexanes and water and purified further with a CombiFlash R_f^+ chromatography system (RediSep R_f Gold high performance silica gel, 0% methanol/dichloromethane gradually increasing to 10% methanol/dichloromethane) to give the final pure dye (0.070 g, 65%). ^{1}H NMR (400 MHz, $CDCl_3$) δ 8.30 (br s, 1H), 7.70-7.56 (br m, 1H), 7.20 (ap d, J = 4.9 Hz, 1H), 7.15-7.08 (m, 1H), 7.08-7.00 (m, 1H), 6.99-6.92 (m, 1H), 2.10-1.79 (m, 8H), 1.21-0.54 (m, 60H) ppm. HRMS (ESI negative mode) m/z calc'd for $C_{54}H_{75}NO_2S_4$ $[M]^-$: calculated 897.4681, found 897.4676.

2-Cyano-3-(6'-chloro-4,4,4',4'-tetraethylhexyl-4a,7a,4',7'b-tetrahydro-4H,3'aH-[2,2']bi[cyclopenta[2,1- b;3,4-b']dithiophenyl])-acrylic acid (**AB5**): In a 8.0 mL vial, 6'-chloro-4,4,4',4'-tetraethylhexyl-4a,7a,4',7'b-tetrahydro-4H,3'aH-[2,2']bi[cyclopenta[2,1-b;3,4-b']dithiophenyl])-6-carbaldehyde (**4**) (0.05 g, 0.058 mmol) was dissolved in 1.2 mL of chloroform. The mixture was then degassed with N_2 for approximately 30 minutes. Cyanoacetic acid (0.015 g, 0.173 mmol) and piperidine (0.040 mL, 0.406 mmol) were added to the vial, which was then sealed with an open top cap sealed with a PTFE coated rubber septum, heated to 90°C, and allowed to stir for 16 hours. The reaction mixture was diluted with dichloromethane and purified through a plug of silica gel with the following solvents sequentially: 100% dichloromethane, then 10% methanol/dichloromethane, and finally 12% methanol/3% acetic acid/dichloromethane. The solvent of the third fraction was evaporated under reduced pressure. The dye (**AB5**) was then

extracted with hexanes and water and purified further with a CombiFlash R_f^+ chromatography system (RediSep R_f Gold high performance silica gel, 0% methanol/dichloromethane gradually increasing to 10% methanol/dichloromethane) to give the final pure dye (0.050 g, 92%). ^{1}H NMR (400 MHz, $CDCl_3$) δ 8.30 (s, 1H), 7.71-7.54 (br m, 1H), 7.09 (br s, 1H), 7.03 (br s, 1H), 6.85 (br s, 1H), 2.12-1.74 (m, 8H), 1.20-.40 (m, 60H ppm. IR (neat) ν = 3340, 2944, 2923, 2854, 2333, 2114, 1602, 1593 cm^{-1}. ESI HRMS m/z calc'd for $C_{54}H_{73}ClNO_2S_4$ $[M - H]^-$: calculated 930.4213, found 930.4236.

2-Cyano-3-(6'-bromo-4,4,4',4'-tetraethylhexyl-4a,7a,4',7'b-tetrahydro-4H,3'aH-[2,2']bi[cyclopenta[2,1- b;3,4-b']dithiophenyl])-acrylic acid (**AB6**): In a 8.0 mL vial, 6'-bromo-4,4,4',4'-tetraethylhexyl-4a,7a,4',7'b-tetrahydro-4H,3'aH-[2,2']bi[cyclopenta[2,1-b;3,4-b']dithiophenyl])-6-carbaldehyde (**5**) (0.05 g, 0.055 mmol) was dissolved in 1.1 mL chloroform. The mixture was then degassed with N_2 for approximately 30 minutes. Cyanoacetic acid (0.014 g, 0.165 mmol) and piperidine (0.038 mL, 0.385 mmol) were added to the vial, which was then sealed with an open top cap sealed with a PTFE coated rubber septum, heated to 90^{o}C, and allowed to stir for 16 hours. The reaction mixture was diluted with dichloromethane and purified through a plug of silica gel with the following solvents sequentially: 100% dichloromethane, then 10% methanol/dichloromethane, and finally 12% methanol/3% acetic acid/dichloromethane. The solvent of the third fraction was evaporated under reduced pressure. The dye (**AB6**) was then extracted with hexanes and water and purified further with a CombiFlash R_f^+ chromatography system (RediSep R_f Gold high performance silica gel, 0% methanol/dichloromethane gradually increasing to 10% methanol/dichloromethane) to give the final pure dye (0.05 g, 95%). ^{1}H NMR (300 MHz, $CDCl_3$) δ 8.30 (s, 1H), 7.70-7.55 (br m, 1H), 7.09 (s, 1H), 7.03 (s, 1H), 6.97 (ap t, J =

3.1 Hz, 1H), 2.10-1.76 (m, 8H), 1.17-0.49 (m, 60H) ppm. IR (neat) ν = 3340, 2944, 2923, 2854, 2333, 2114, 1602, 1593 cm^{-1}. ESI HRMS m/z calc'd for $C_{54}H_{74}BrNO_2S_4Cs$ $[M + Cs]^+$: calculated 1108.2840, found 1108.2832.

2-Cyano-3-(6'-iodo-4,4,4',4'-tetraethylhexyl-4a,7a,4',7'b-tetrahydro-4H,3'aH-[2,2']bi[cyclopenta[2,1- b;3,4-b']dithiophenyl])-acrylic acid (**AB7**): In a 8.0 mL vial, 6'-iodo-4,4,4',4'-tetraethylhexyl-4a,7a,4',7'b-tetrahydro-4H,3'aH-[2,2']bi[cyclopenta[2,1- b;3,4-b']dithiophenyl])-6-carbaldehyde (**6**) (0.0173 g, 0.0181 mmol) was dissolved in 0.4 mL chloroform. The mixture was then degassed with N_2 for approximately 30 minutes. Cyanoacetic acid (0.005 g, 0.0542 mmol) and piperidine (0.013 mL, 0.127 mmol) were added to the vial, which was then sealed with an open top cap sealed with a PTFE coated rubber septum, heated to 90°C, and allowed to stir for 16 hours. The reaction mixture was diluted with dichloromethane and purified through a plug of silica gel with the following solvents sequentially: 100% dichloromethane, then 10% methanol/dichloromethane, and finally 12% methanol/3% acetic acid/dichloromethane. The solvent of the third fraction was evaporated under reduced pressure. The dye (**AB7**) was then extracted with hexanes and water and purified further with a CombiFlash R_f^+ chromotography system (RediSep R_f Gold high performance silica gel, 0% methanol/dichloromethane gradually increasing to 10% methanol/dichloromethane) to give the final pure dye (0.017 g, 90%). ^{1}H NMR (400 MHz, $CDCl_3$) δ 8.29 (br s, 1H), 7.70-7.55 (br m, 1H), 7.13 (ap t, J = 4.1 Hz, 1H), 7.09 (br s, 1H), 7.03 (br s, 1H), 1.93-1.87 (m, 8H), 1.16-0.49 (m, 60H) ppm. IR (neat) ν = 3340, 2944, 2923, 2854, 2333, 2114, 1602, 1593 cm^{-1}. ESI HRMS m/z calc'd for $C_{54}H_{74}INO_2S_4Cs$ $[M + Cs]^+$: calculated 1156.2702, found 1156.2683.

[Co(*N*-tpy)$_2$][TSFI]$_2$: In a 1000 mL round bottom flask, $CoCl_2$*6 H_2O (2.47 g, 10.4 mmol) was stirred in 520 mL of methanol until completely dissolved. *N*-tpy (4.85 g, 20.7 mmol) was then added to the solution and the reaction was sealed and refluxed for 16 hours. The solution was then cooled to room temperature. Excess LiTSFI (6.12 g, 20.7 mmol) was dissolved in minimal methanol then added to the solution and stirred for 1 hour. Half of the solvent was removed under reduced pressure and water was added until a precipitate formed. The solution was filtered and washed with a methanol/water solution to obtain the final product as a dark red powder (4.16 g, 47% yield). ^{1}H NMR (400 MHz, $CDCl_3$) δ 90.67 (br s, 1H), 49.66 (s, 1H), 34.14 (s, 1H), 30.43 (s, 1H), 10.39 (s, 1H) ppm. ^{19}F NMR (400 MHz, $CDCl_3$) δ 80.2 ppm. IR (neat) ν = 3088, 1601 cm^{-1}. MS (MALDI): calculated for $C_{30}H_{20}CoN_9O_4S_2F_6$ $[M\text{-}2TFSI]^+$ 807.0, found: 807.1. CHN Elemental Analysis (EA) calculated for $C_{32}H_{20}CoF_{12}N_{10}O_8S_4$: C, 35.34%; H, 1.85%; N, 12.88%. Found: C, 35.41%; H, 1.72%; N, 12.90%.

[Co(*N*-tpy)$_2$][TSFI]$_3$: In a 100 mL round bottom flask, [Co(*N*-tpy)$_2$][TSFI]$_2$ (1.05 g, 1.23 mmol) was stirred in 31 mL of acetonitrile until completely dissolved. The solution was then bubbled with N_2 for 10 minutes. $NOBF_4$ (0.160 g, 1.35 mmol) was then added to the solution, and the reaction was kept under N_2 and stirred at room temperature for 1 hour. Excess LiTSFI (0.80 g, 1.35 mmol) was added dissolved in minimal acetonitrile, then added to the solution, and stirred for 1 hour. Half of the solvent was removed under reduced pressure, and water was added until a precipitate formed. The remaining solution was filtered and washed with water to obtain the final product as a yellow powder (0.60 g, 43% yield). ^{1}H NMR (400 MHz, $CDCl_3$) δ 10.19 (s, 1H), 8.71 (dd, J = 8.0 Hz, 1.6 Hz, 1H), 8.30 (dt, J = 8.0 Hz, 1.6 Hz, 1H), 7.48 (dt, J = 5.6 Hz, 1.2 Hz, 1H), 7.31 (dd, J = 5.6 Hz, J = 1.2 Hz, 1H) ppm. ^{13}C NMR (400 MHz, $CDCl_3$) δ 155.0, 154.5, 151.6,

148.7, 144.6, 132.7, 129.4 ppm. ^{19}F NMR (400 MHz, $CDCl_3$) δ 80.25 (s) ppm. IR (neat) ν = 3117, 1607 cm^{-1}. HRMS (ESI positive mode): calculated for $C_{28}H_{20}CoN_8$ $[M\text{-}3TFSI]^+$ 527.1143, found: 527.1115. MS (MALDI): calculated for $C_{30}H_{20}CoN_9O_4S_2F_6$ [M-2TFSI]+ 807.0, found: 807.1. CHN Elemental Analysis (EA) calculated for $C_{34}H_{20}CoF_{18}N_{11}O_{12}S_6$: C, 29.85%; H, 1.47%; N, 11.26%. Found: C, 29.86%; H, 1.31%; N, 11.08%.

COMPUTATIONAL METHODOLOGY

The geometry optimizations, binding energy, and time-dependent density functional theory (TDDFT) calculations were performed with Gaussian 16 program package.[124] To account for the long-range interactions, wB97XD[125] functional was used with D2 dispersion corrections.[126] The residual force and density matrix were converged with tight convergence criteria and ultrafine grid was used for the numerical integration. LANL2TZ*(f)* and LANL2DZ*dp* basis sets with effective core potential[127, 128] were used for the cobalt (Co) and halogens, respectively. For all other atoms, 6-31G(*d, p*) basis set was used.[129] The geometry optimizations and binding energy calculations were performed with two different charge states of the dyes: neutral and oxidized state. First, the dyes and the cobalt-complex were optimized separately, and the optimized geometries were placed together for the final optimization. All the geometry optimization, and binding energy calculations were performed with +2 charge on cobalt-complex and for the charged dyes, the total charge of the system was +3. For a difficult convergence case where the SCF cycles were not converged within 200 cycles, a quadratically convergence procedure[130] for SCF was utilized. Integral Equation Formalism (IEFPCM) of the Polarizable Continuum Model (PCM)[131-133] was used with acetonitrile as the implicit solvent. A fragment

guess calculation was used to generate the initial guess for the individual fragments with a full geometry optimization afterwards. To reduce the computational cost, the -C_6H_{13} group was replaced with -C_2H_5 and all geometries were considered optimized once the forces on all atoms were converged to zero.[134] Geometry optimizations were performed without any symmetry constraint. Frequency calculations were performed on each geometry to confirm the local minima.

The analysis of binding energies (E_{BE}) involved the energy difference between the dye-cobalt-complex (E_{total}) with energy of the dye ($E_{fragment-1}$) and cobalt-complex ($E_{fragment-2}$). For the $E_{Fragment-1}$ and $E_{Fragment-2}$ energy, a single point energy calculation was performed on the total system (cobalt-complex + dyes) by replacing the other fragments with a ghost-atom.

$$E_{BE} = E_{total} - E_{fragment-1} - E_{fragment-2} \qquad \text{(equation 1)}$$

For the excited states, TDDFT[135, 136] calculation was performed with Tamm-Dancoff approximation.[134] The vertical excitation of the lowest 25 singlet excited states was calculated to determine key transitions in the complex. TDDFT calculations were performed at the same level of theory and basis set as DFT calculations using acetonitrile as an implicit solvent.

TAS MEASUREMENTS

Time-resolved absorption spectra were collected using an Edinburgh LP980 optical system. Excitation (532 nm) light was generated from a pulsed Nd:YAG laser (Continuum, Surelite II) equipped with a doubling crystal (<3 mJ/pulse; ~1 ns pulsewidth) and probed with a 150 W pulsed xenon arc lamp. Time-resolved absorption decays were collected at a single wavelength of 720 nm by use of a Czerny-Turner monochromator and photomultiplier tube and averaged over 300 laser shots. The ΔOD versus t curve is typically modeled using a Kohlrausch−Williams−Watts (KWW)[137-140] stretched exponential decay function:

$$\Delta OD(t) = \Delta OD_{t=0} e^{-\left(\frac{t}{\tau_{KWW}}\right)^{\beta}} \qquad \text{(equation 2)}$$

where $\Delta OD_{t=0}$ represents the signal amplitude at time zero, τ_{KWW} is the stretched exponential lifetime, and β is the stretch parameter, which ranges in value from 0 to 1. The observed lifetime is calculated from the fitting parameters by using a gamma function distribution of β^{-1} (equations 3 and 4),

$$\Gamma(x) = \int_0^{\infty} u^{(x-1)} e^{-x}\, du \qquad \text{(equation 3)}$$

$$\tau_{obs} = \frac{\tau}{\beta}\Gamma\left(\frac{1}{\beta}\right) \qquad \text{(equation 4)}$$

The mean lifetime is then used to calculate the observed rate values obtained in the absence, k_{rec}, and presence, k_{reg}, of the redox active species (equation 5). The overall redox shuttle electron transfer efficiency relative to back electron transfer from the TiO_2 CB is calculated using equation 6.

$$k_{obs,i} = \frac{1}{\tau_{obs,i}} \qquad \text{(equation 5)}$$

$$\varphi_{reg} = \frac{k_{reg}}{k_{reg}+k_{rec}} \times 100 \qquad \text{(equation 6)}$$

nsTAS TiO_2–DYE FILM PREPARATION

Chenodeoxycholic acid (CDCA) was purchased from Chem-Impex International. TEC 10 glass was purchased from Hartford Glass and cut into 2x2 cm squares, 0.2% Deconex 21 aqueous solution and sonicated for 10 min at room temperature, then rinsed with water, acetone and lastly ethanol. The electrodes were comprised of a single 5 µm mesoporous TiO_2 layer (particle size, 30 nm, Dyenamo, DN-GPS-30TS). All the layers were screen printed from a Sefar screen (54/137–64W). Following the print, the substrate was heated for 7 minutes at 125°C and the thickness was measured with a profilometer (Alpha-Step D-500 KLA Tencor). Once the layer was deposited, the substrate was then sintered with progressive heating from 125°C (5-minute ramp from r.t., 5 minute hold) to 325°C (15 minute ramp from 125°C, 5 minute hold) to 375°C (5 minute ramp from 325°C, 5 minute hold) to 450°C (5 minute ramp from 375°C, 15 minute hold) to 500°C (5 minute ramp from 450°C, 15 minute hold) using a programmable furnace (Vulcan® 3-Series Model 3-550). The cooled electrode was prepared by immersing the TiO_2 film into the dye solution for 3 hours. The solution is 0.3 mM of dye in MeCN:t-BuOH:THF mixture (1:1:1) with a 20:1 CDCA:dye ratio unless otherwise indicated. The electrodes were washed with acetonitrile and the dried substrates were then partially sealed with a pre-cut semicircle of 25 µm thick hot melt film (Surlyn, Solaronix, "Meltonix 1170-25") and a thin glass cover slip by heating the system at 130°C under 0.1 psi pressure for 30 seconds. Devices were completed by filling the cells with electrolyte solution by injecting it into the open portion of the coverslip with a micro syringe. Electrolyte without cobalt RS comprised of 0.1 M LiTFSI and 0.5 M TBP in MeCN. Electrolyte with cobalt RS for both Co(tpy) and Co(*N*-tpy) comprised of 0.25M Co^{2+}, 0.05M Co^{3+}, 0.1 M LiTFSI, and 0.5 M TBP in MeCN. The device is then sealed with a light-cured adhesive (Permabond UV6231) and curing under 450 nm light for 45 seconds with the cell active dye area shielded from light.

TARGET DYE PREDICTED PROPERTIES AND SYNTHESIS

Computational studies were undertaken on all four dyes in both the neutral and cation states at the ωB97XD/6-31G(*d*,*p*) level of theory and basis set.**[126-129]** Analysis of the frontier molecular orbitals (MOs) indicates that the highest occupied MO (HOMO) is delocalized across the two CPDT groups for all of the neutral dyes with some HOMO orbital contribution on the halides (Figures 3 and S19). No significant change in the HOMO orbital position is observed based on halide choice. The lowest unoccupied MO (LUMO) is primarily localized on the CPDT π-bridge group attached to the CAA group and the CAA acceptor. No significant change based on halide is observed for the LUMO as well. These orbitals are well-positioned spatially for efficient electron injection into the TiO_2 CB from the CAA group upon photoinduced intramolecular electron transfer from the HOMO to the LUMO.

All of the neutral dyes are behaving as intramolecular charge transfer (ICT) dyes based on the orbital positions, analysis of charge transfer (CT) amounts, and CT distances (Table S1). Upon photoinduced electron transfer from the dye to TiO_2, a cationic dye is generated. The dye cation singly occupied molecular orbital (SOMO) and neutral dye HOMO orbitals are very similar in positioning on the dyes with contributions on the halides (Figures 3 and S19). This suggests that a RS with Lewis base functionality on the periphery could coordinate with the halide of a cationic dye for a close dye orbital interaction. No significant changes in free energy for electron transfers are predicted between the dyes based on orbital energies (Table S2), which allows for a direct evaluation of halogen bonding effects.

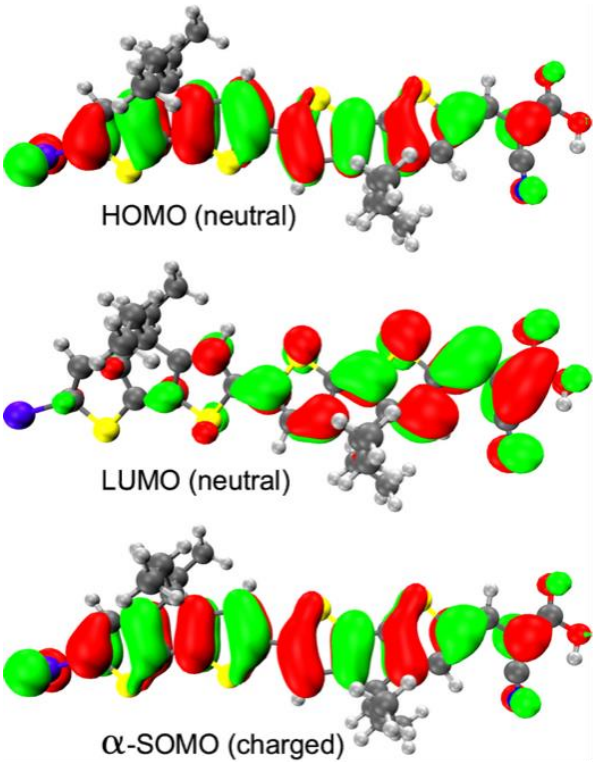

Figure 5.3. Molecular orbital (MO) diagrams of the neutral and positively charged **AB7**. The green and red surface represents the positive and negative signs of MO at isovalue = 0.02 a.u, respectively. See SI for images of additional orbitals and **AB4-AB6**.

The synthesis of the desired dyes and RSs is described in the experimental section. Briefly, the synthesis began with the Stille coupling of known stannylated CPDT **1[119, 120]** and known bromo-CPDT-aldehyde **2[121]** to give bis-CPDT-aldehyde **3** in 68% yield (Scheme 1). N-halogenated succinimide electrophiles could be used to then halogenate **3** to give the chloro (**4**), bromo (**5**), and iodo (**6**) derivatives in 75-94% yield. Finally, Knoevenagel condensation of aldehydes **3-6** with cyanoacetic acid gave the target dyes in 85-89% yield. The Lewis base decorated RS $[Co(N\text{-tpy})_2][TFSI]_2$ was synthesized beginning from known *N*-tpy ligand**[123]** by

metalation with $CoCl_2*6H_2O$ and salt metathesis with LiTFSI to give the desired product in 47% yield (Scheme 2). The oxidized redox shuttle [Co(*N*-tpy)$_2$][TFSI]$_3$ was synthesized from [Co(*N*-tpy)$_2$][TFSI]$_2$ by $NOBF_4$ oxidation and counter anion exchange with LiTFSI to probe halogen bonding effects under a more practical environment with both RS oxidation states present. The RS without the peripheral Lewis base group ([Co(tpy)$_2$][TFSI]$_x$, where tpy is 2,2':6',2"-terpyridine) was synthesized in both oxidation states as described in the literature to serve as a negative control which will not halogen bond to the dyes.**[122]**

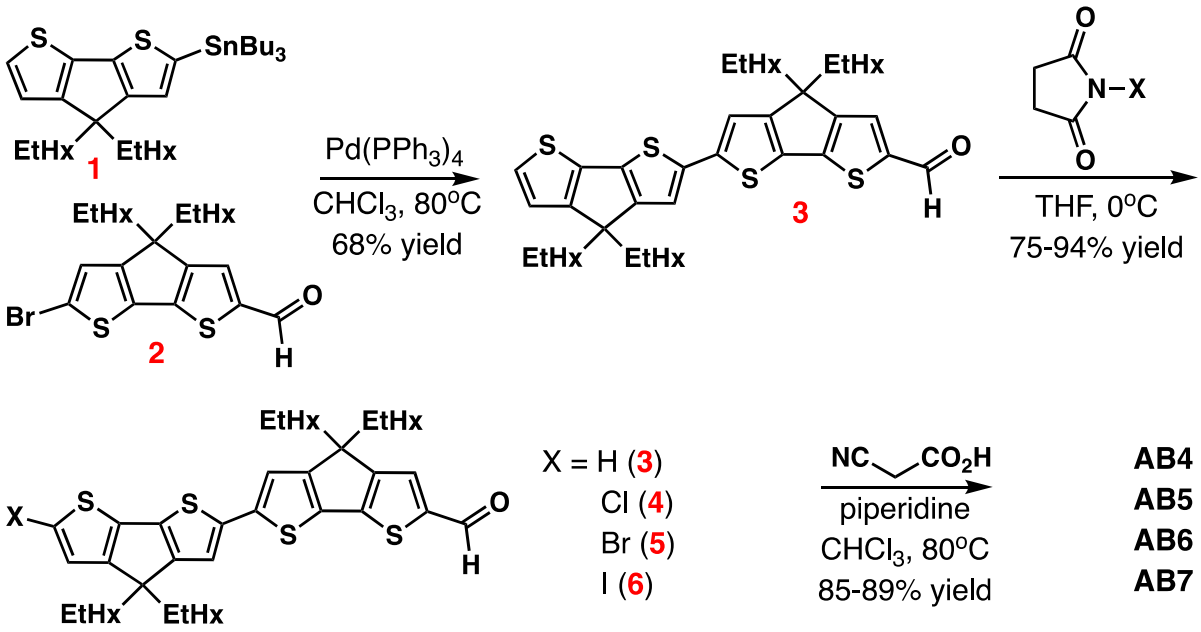

Figure 5.4. Synthetic route for target dyes **AB4**, **AB5**, **AB6** and **AB7**.

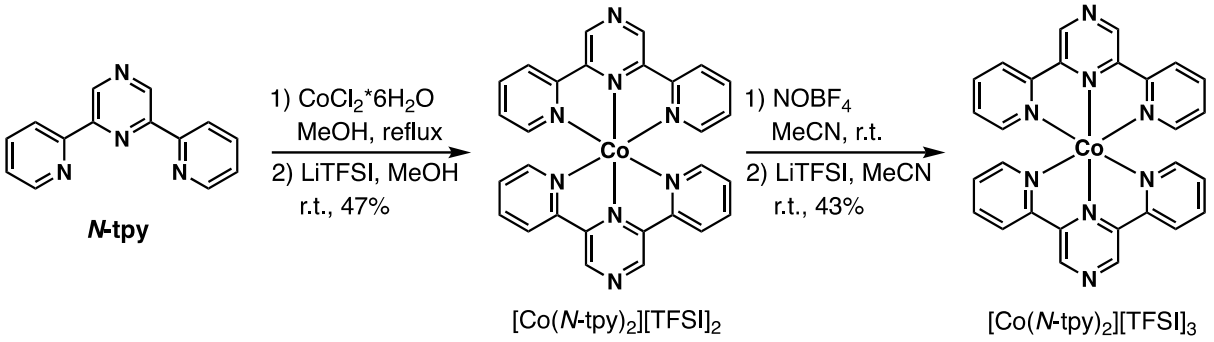

Figure 5.5. Synthetic route to [Co(*N*-tpy)$_2$][TFSI]$_2$ and [Co(*N*-tpy)$_2$][TFSI]$_3$.

SOLUTION MEASUREMENTS

The optical properties of the dyes and cobalt RSs were evaluated with steady-state absorption spectroscopy to assess the suitability of this system for nanosecond transient absorption spectroscopy (nsTAS). The dyes were found to have absorption maxima (λ_{max}) ranging from 488-503 nm with absorption curve onsets (λ_{onset}) closely grouped at 595-618 nm in dichloromethane (DCM) (Table 1, Figure 4). The λ_{max} values differ by 0.08 eV or less with higher energy values being observed as the halide increases in size. A trend is also observed for the dye molar absorptivities (ε) with a modest increase in molar absorptivity from 27,000 $M^{-1}cm^{-1}$ to 31,000 $M^{-1}cm^{-1}$ according to the following order: Cl < Br < I. TD-DFT analysis shows similar results for the vertical transitions and oscillator strength (Table S3). The Co(*N*-tpy)$_2$ RS was found to have minimal absorption in the visible region (>400 nm) for both the Co^{2+} and Co^{3+} oxidation states in acetonitrile (MeCN), which indicates this RS could be used for TAS measurements with **AB4-AB7** (Figure 5).

Table 5.1. Optical and electrochemical properties of dyes in DCM and RSs in MeCN.

Dye/RS	λ_{max} (nm)	ε_{max} ($M^{-1}cm^{-1}$)	λ_{onset} (nm)[a]	$E_{(S+/S)}$ (V)	$E_{(S+/S*)}$ (V)[b]	E_g^{opt} (eV)[a,c]
AB4	489	25000	618	0.96	-1.05	2.01
AB5	503	27000	612	0.99	-1.04	2.03
AB6	499	28000	613	0.99	-1.03	2.02
AB7	488	31000	595	0.99	-1.09	2.08
Co(*N*-tpy)$_2^{2+}$	345	45000	375	0.71	---	---
Co(*N*-tpy)$_2^{3+}$	372	15000	400	---	---	---

[a]Determined via 0nset program. [141], [b]Calculated according to the equation: $E_{(S+/S*)} = E_{(S+/S)} - E_g^{opt}$. [c]Estimated from the onset of the absorption curve using the equation $E_g^{opt} = 1240/\lambda_{onset}$.

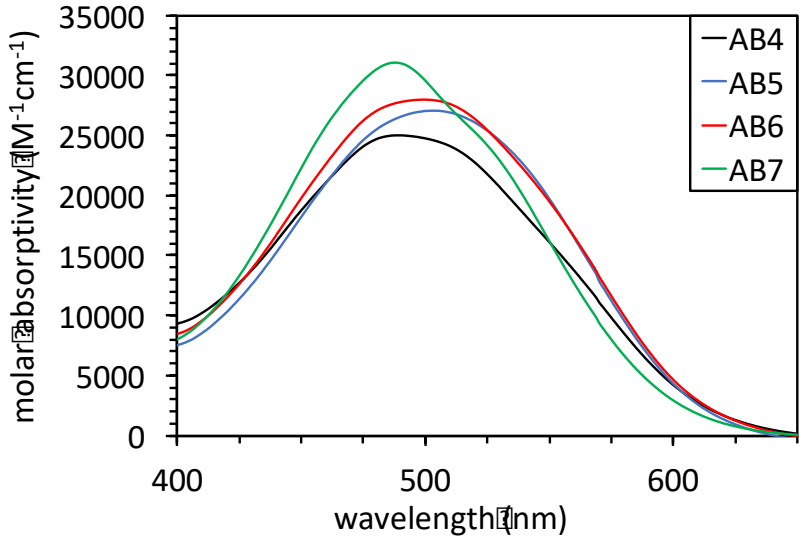

Figure 5.6. Molar absorptivity of dyes **AB4-AB7** in a DCM solution.

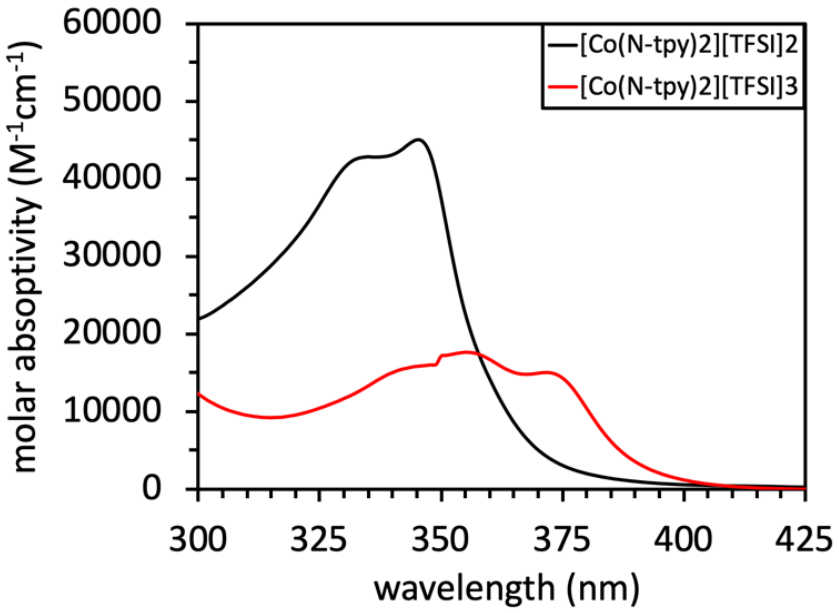

Figure 5.7. Molar absorptivity of redox shuttles [Co(*N*-tpy)$_2$][TFSI]$_2$ and [Co(*N*-tpy)$_2$][TFSI]$_3$ in MeCN.

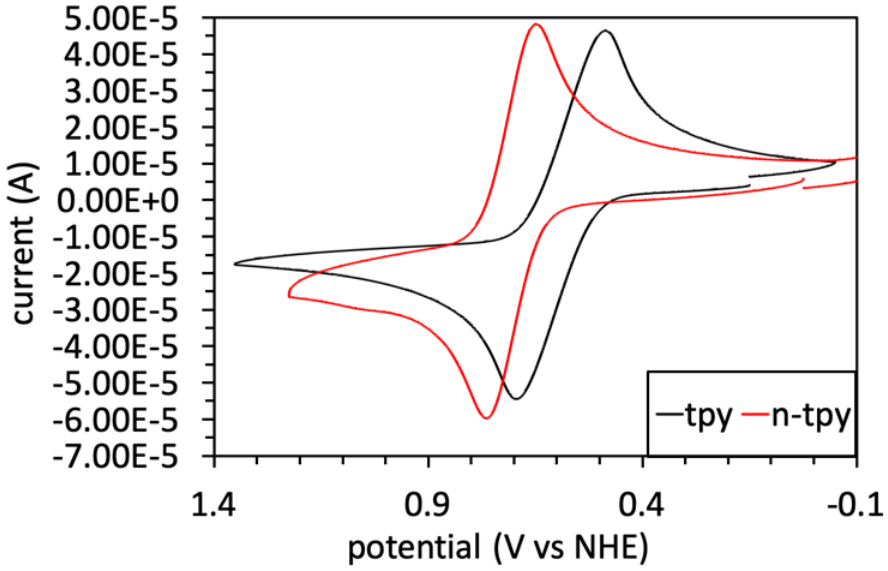

Figure 5.8. Cyclic voltammograms of [Co(*N*-tpy)$_2$][TSFI]$_2$ and [Co(tpy)$_2$][TSFI]$_2$ in MeCN.

Next, the free energies for electron transfer from the RSs to the dye cations were probed by cyclic voltammetry (CV). The dye ground state oxidation potentials ($E_{(S+/S)}$) were measured to be

identical for the halogenated dyes at 0.99 V versus normal hydrogen electrode (NHE) (Table 1). The RS half-wave potentials were measured at 0.60 V and 0.71 V for $Co(tpy)_2^{3+/2+}$ and $Co(N\text{-}tpy)_2^{3+/2+}$, respectively which indicates a free energy for electron transfer to the dye cations from the RSs of at least 390 mV and 280 mV (Table 1, Figure 6). The dye excited state oxidation potentials ($E_{(S+/S^*)}$) were evaluated energetically with respect to the TiO_2 CB taken at –0.5 V versus NHE. A close grouping of $E_{(S+/S^*)}$ values from –1.03 V to –1.09 V is observed without correlation to the halide group. Thus, all of the dyes can inject electrons into the TiO_2 CB with favorable free energies for electron transfer by at least 530 mV.

COMPUTATIONAL ANALYSIS

The molecular electrostatic potential (MEP) surfaces were analyzed for each of the dyes to assess the possibility of halogen bonding to the $Co(N\text{-}tpy)_2^{2+}$ RS (Figure 7). In both the neutral and cationic states of the dyes, the halide group shows a significantly positive σ-hole region. The positive potential value at the σ-hole is significantly higher for the cation than the neutral dye (0.01 versus 0.08 Hartree), which indicates a potentially stronger interaction of the Lewis basic nitrogen on $Co(N\text{-}tpy)_2$ to the dye cation. The size and charge of the σ-hole increases as the halides increases in size, suggesting that $Co(N\text{-}tpy)_2^{2+}$ should bind **AB7** the strongest.[111] A favorable interaction and geometry is observed computationally between the $Co(N\text{-}tpy)_2^{2+}$ RS and the dye (Figures 8 and S21). The binding energy obtained from this interaction gave the following halide trend from low to high binding strength: Cl < Br < I with a range of –6.37 kcal/mole for **AB5** to –9.44 kcal/mole for **AB7** (Table 2, Table S4). Notably, the binding geometry of the dyes with halides differ slightly

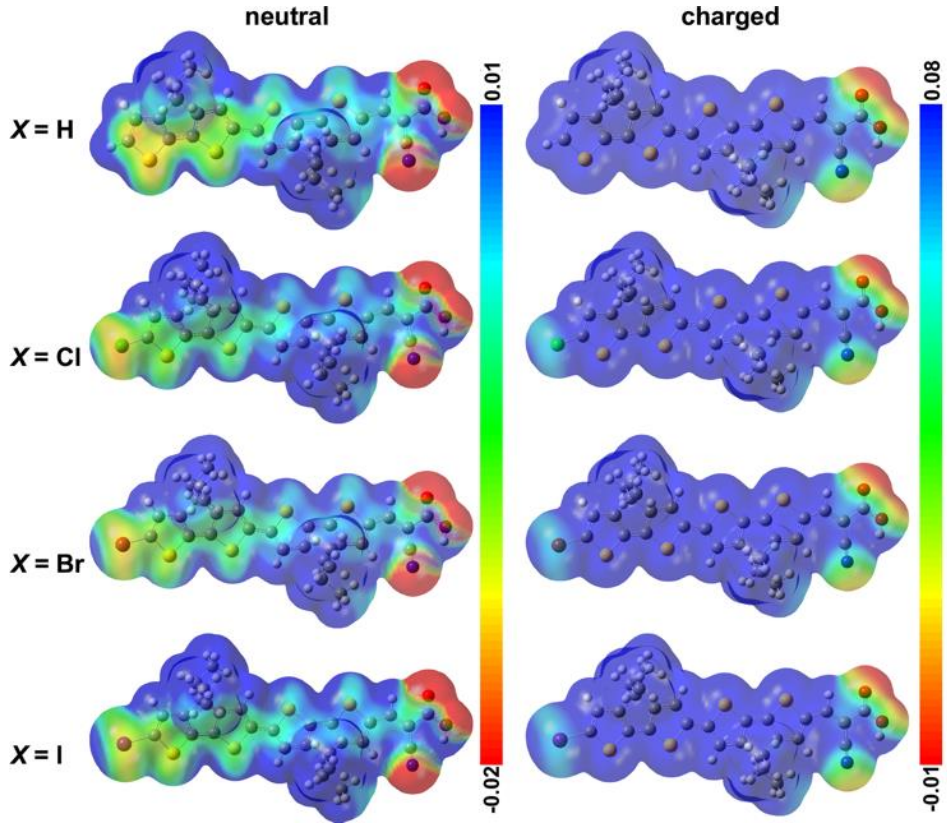

Figure 5.9. Molecular electrostatic potential (MEP) surface for the neutral and cationic dyes. The isosurface value for the total electron density is 0.001 au with the potential value (Hartree) shown in the scales. The blue and red surface represents the highest (less electrons) and lowest (more electrons) electrostatic potential, respectively.

to the dye with a hydrogen atom which limits direct comparisons of **AB4** to **AB5-AB7**. Similar binding energies are observed in the cationic dye states with bond distances from 2.28 Å to 3.00 Å, which are typical halogen bonding distances.[106, 118] The bonding distance is observed to be approximately 0.07 Å closer on average for Co(*N*-tpy)$_2^{2+}$ to the cationic dye relative to the neutral dye. No favorable binding of the Co(tpy)$_2^{2+}$ RS to any of the neutral dyes was observed. These results suggest a significant halogen bonding event can take place with the dyes and Co(*N*-tpy)$_2^{2+}$.

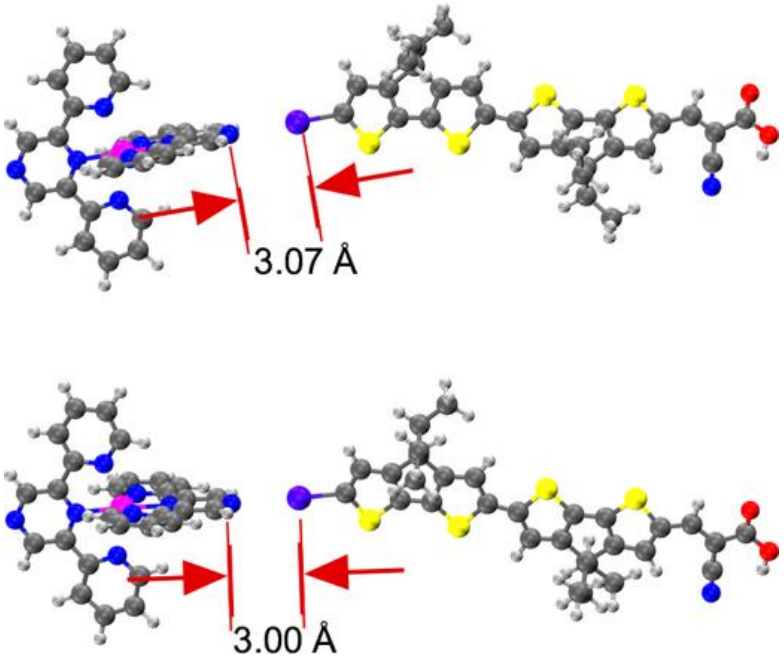

Figure 5.10. Optimized geometries of **AB7** with Co(*N*-tpy)$_2$. (A) Neutral **AB7** (top) and cationic **AB7** (bottom).

Table 5.2. Calculated binding energy and distances between the RSs and dyes.

RS	X-Dye	BE dye (kcal/mol)	BE dye$^+$ (kcal/mol)	RS-Dye dist. (Å)	RS-Dye$^+$ dist. (Å)
Co(*N*-tpy)$_2^{2+}$	Cl	-6.37	-6.22	3.14	3.07
Co(*N*-tpy)$_2^{2+}$	Br	-7.69	-7.39	3.07	3.00
Co(*N*-tpy)$_2^{2+}$	I	-9.44	-9.30	3.07	3.00

SURFACE STUDIES

The dyes were loaded onto TiO_2 films with similar dye loading densities of 7.33 x 10^{-8} to 1.37 x 10^{-7} mol/cm^2 at described in the SI (Table S8). The dye loading density trend follows the

halide trend with: **AB7** > **AB6** > **AB5**. The TiO_2-dye were subjected to nanosecond transient absorption (nsTAS) measurements to monitor the absorption profile of the dye cation on the surface of TiO_2. When measuring the kinetics on a microsecond timescale, electron transfer from the dye to the CB of TiO_2 is assumed to be completed and therefore the main signals observed are those arising from the oxidized dye. Transient decay measurements were collected to analyze the rates of the electron transfer reaction from TiO_2 to the oxidized dye (i.e. back electron transfer) and the rates of electron transfer to the oxidized dye from the redox shuttle (i.e. dye regeneration). The transient cationic dye species generated is represented by an observable change in the electronic spectrum for the dyes (Figures 9 and S22-S34). The negative change in optical density (ΔOD) in the 400-575 nm region represents the disappearance of ground-state dye species (ground state bleaching) and the positive ΔOD in the 600-800 nm region represents absorption from the dye cation. The dye cation absorption was monitored as a function of time at 720 nm in the absence of a RS to measure the rate of back electron transfer between 8.40×10^4 and 1.08×10^5 s^{-1} (Figures 9 and S35-S38, Table 3). Kinetic traces were fit with a stretched exponential decay function and the corresponding rate values were calculated according to the procedure in the experimental section.[137-140]

Dynamics measured with the dyes in the presence of a RS are representative of the rate of the dye neutral state regeneration from the RS (blue and red traces) and the back electron transfer from the electron in TiO_2. The changes in decay rate when a RS is added relative to the no RS decay traces (green traces) represents faster consumption of the dye cation due to electron transfer from the RS.

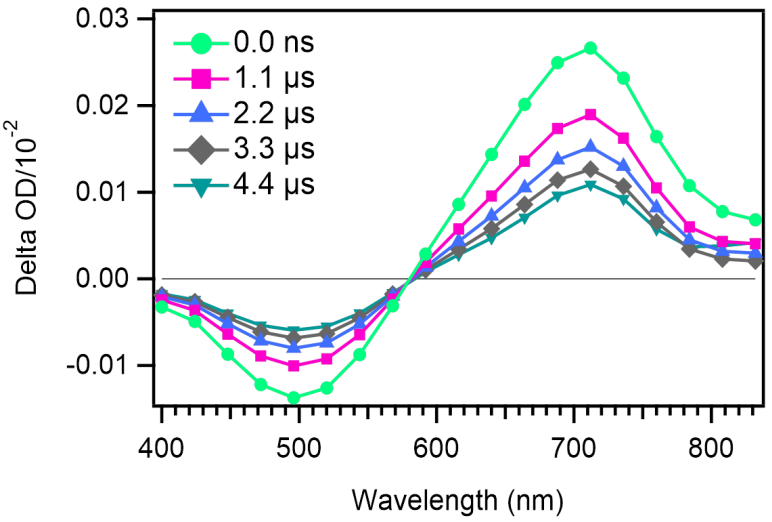

Figure 5.11. Transient spectrum of **AB7** on TiO_2 with 0.1 M LiTFSI in MeCN.

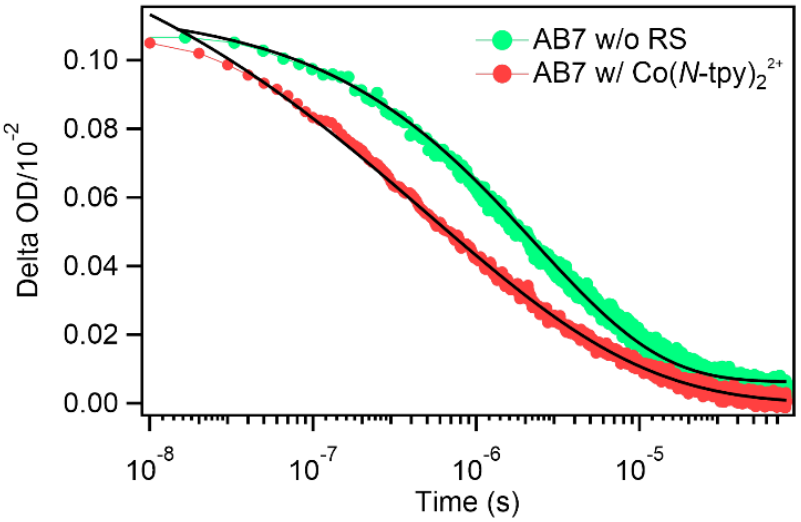

Figure 5.12. Decay plots resulting from TAS for **AB7** with and without Co(*N*-tpy)$_2^{3+/2+}$ RS.

Table 5.3. Summary TAS data for **AB5**, **AB6** and **AB7**.[a]

Dye	k_{reg} (s^{-1})	k_{rec} (s^{-1})	□ (%)
AB5	5.85 x 10^5	1.08 x 10^5	84.4
AB6	3.45 x 10^5	8.60 x 10^4	80.0
AB7	1.82 x 10^5	8.40 x 10^4	68.4

[a] All measurements were taken under open-circuit conditions, with the pump power = <3.0 mJ/pulse and the probe wavelength set to 720 nm. The electrolyte is 0.25M Co(*N*-tpy)$_2^{2+}$ and 0.1 M LiTFSI.

All of the systems show a significant increase in dye cation decay rate in the presence the RS (k_{reg}) when compared to the dye cation decay rate in the absence of a RS (k_{rec}) (Tables 4 and S7). The back electron transfer reaction rates (k_{rec}) are similar ranging from 1.08 x 10^5 to 8.60 x 10^4 s^{-1} and no trend with respect to halide. Upon addition of Co(*N*-tpy)$_2^{2+}$, k_{reg} values of 5.85 x 10^5 to 1.82 x 10^5 s^{-1} are observed which track with the a halogen trend. As the halogen atom size increased across the dye series, the k_{reg} value decreases. This suggests halogen bonding is occurring and insulating the dye cation-RS electron transfer reaction. The regeneration efficiency (□) factors in the two competing electron transfer pathways to the dye cation via equation 6. □ is calculated to be 84.4%, 80.0% and 68.4% for **AB5**, **AB6** and **AB7**, respectively (see equation 6), which again shows halogen bonding slowing the regeneration of the neutral dye.

Co(tpy)$_2^{2+}$ was also evaluated via TAS (Table S7) with each of the dyes and the k_{reg} rates were found to be more than an order of magnitude faster than with Co(*N*-tpy)$_2^{2+}$. The slower kinetics for the halogen bonding RS, Co(*N*-tpy)$_2^{2+}$, as compared to the non-binding RS, Co(tpy)$_2^{2+}$, may be due to a preorganization of the dye and the RS resulting from halogen bonding resulting in a

geometry that is poor for electron transfer reactions. Additionally, Co(*N*-tpy)$_2^{2+}$ may also bind to the TiO_2 surface which could limit productive dye-RS interactions.

DSC devices were constructed with the Co(*N*-tpy)$_2^{3+/2+}$ redox shuttle system as described in the experimental section. The device performance efficiencies were evaluated via current density-voltage (*J*-*V*) curves according to the equation PCE = (J_{SC} x V_{OC} x FF)/I_0, where PCE is the power conversion efficiency, J_{SC} is the short-circuit current density, V_{OC} is the open circuit voltage, FF is the fill factor, and I_0 is the incident sun intensity (Table S9, Figures S39-S40). Additionally, the DSC devices were studied via small modulated photovoltage transient (SMPVT) and electrochemical impedance spectroscopy (EIS) in the dark to probe electron lifetime and recombination resistances within the DSC device (Figures S41-S42, Table S10). These techniques have been described elsewhere with added details in the SI.[142, 143] Figure 11 summarizes the outcomes of all of these studies with the values scaled relative to the lowest value in the series for a measurement. This allows for the rapid comparison of five parameters on a single bar graph. Interestingly, the DSC device PCE was found to increase as the halide increased in size with **AB7** (iodine-based) having the highest performance. Via EIS, recombination resistance for the transfer of electrons for the TiO_2-dye interface to the electrolyte was found to also track with halide size with this parasitic reaction having the least resistance in the presence of the iodinated dye. This is likely due to indiscriminate halogen bonding of the dye to the oxidized RS near the TiO_2 surface leading to an increase in local concentration of the oxidizing RS near the TiO_2 surface.

Interestingly, SMPVT shows long electron lifetimes in TiO_2 that are similar between Br and I-terminated dyes with the Cl-terminated dye giving DSC devices with much shorter lifetimes. Notably, minimal difference in electron lifetimes are observed when non-halogen bonding

$Co(tpy)_2^{3+/2+}$ is used (Figures S41 and S43). The halogen bonding results track much closer to the DSC device performance observations with respect to photovoltage and PCE trends than dark EIS measurements or TAS measurements. Computational binding studies show a direct correlation to device PCE values and similar to the SMPVT measurements. Notably, an inverse correlation of binding energy is observed with TAS and EIS measurements. Combined, these results suggest that halogen bonding increases recombination without increasing the regeneration rate when dark measurements and pulsed illumination techniques are used. It is important to note that the non-steady state and steady state illumination experiments do use different electrolyte environments with the full DSC device electrolytes being much more complex. However, with steady-state and light intensity modulated techniques (*J*-*V* and SMPVT measurements), halogen bonding is observed to have a beneficial effect toward device performances. This may be related to the need to increase the concentration of the RS under steady state conditions which is often depleted under continued irradiation.[144] The halogen bonding approach may enable an increased effective concentration at the dye-TiO_2 interface despite steady-state depletion.

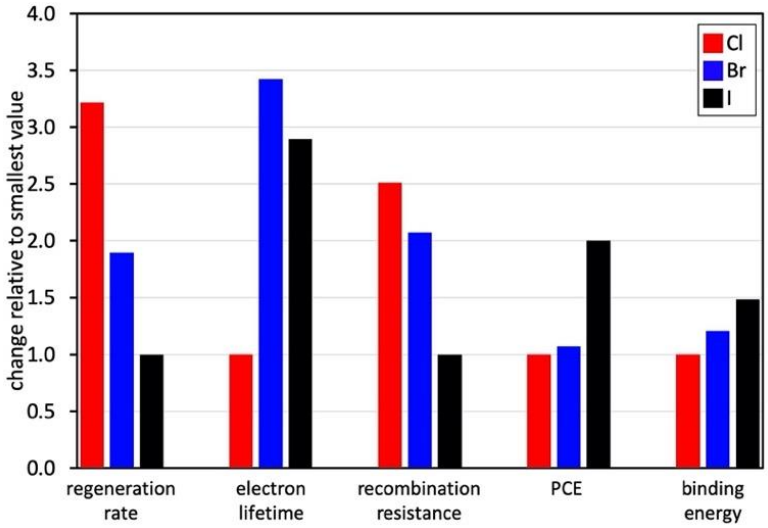

Figure 5.13. Relative value comparison with each halogenated dye across several interrogation techniques with Co(*N*-tpy)$_2^{3+/2+}$ as a RS.

CONCLUSIONS

Three dyes differing only in the identity of a single atom were synthesized with hydrogen or halogen terminal groups. Steady-state absorption and electrochemical data shows favorable energetics and spectral regions where the dye can be selectively photoexcited in the presence of the RSs tested. Computational analysis shows a significant build-up of positive charge at the σ-hole on the halides of the cationic dyes. A halide trend is observed with binding to iodine being 3 kcal/mole stronger than binding to Cl. Interestingly, TAS measurements show decay of the oxidized dye signal significantly decelerates as the size of the attached halogen atom increases when in the presence of a halogen binding RS, Co(*N*-tpy)$_2^{2+}$. In contrast, the TAS measurements showed no significant rate changes based on halogen effects with the non-halogen bonding Co(tpy)$_2^{2+/3+}$ RS, as expected. EIS again reveals a negative impact on recombination resistance that can be correlated to halogen bonding. However, SMPVT and DSC devices show a positive

correlation with relation to halogen bonding events. This suggests all techniques have correlation to halogen bonding with dark and pulsed light interrogation techniques showing negative results, but steady-state illumination techniques showing a desirable influence attributed to halogen bonding.

CHAPTER 6

LEWIS ACID-LEWIS BASE INTERACTIONS PROMOTE FAST INTERFACIAL ELECTRON TRANSFER

The work in this chapter is based on a publication in *ACS Applied Energy Materials*, "Lewis Acid-Lewis Base Interactions Promote Fast Interfacial Electron Transfers with a Pyridine-Based Donor Dye in Dye-Sensitized Solar Cells". This work was collaborative with contributions from Dinesh Nugegoda,[†] Anthony Devdass, Hammad Cheema, Ryan C. Fortenberry. The dyes were synthesized and characterized by Dinesh Nugegoda. The redox shuttles were synthesized and characterized by Anthony Devdass. Computations were performed by Dr. Ryan Fortenberry. The TAS data collection and data analysis was performed by the author.

[a]Department of Chemistry and Biochemistry, University of Mississippi, University, Mississippi 38677, United States

[†]Denotes equal contribution.

INTRODUCTION

Dye-sensitized solar cells (DSCs) are a relatively low-cost photovoltaic technology with exception performances in practical low light settings.[145-149] These low-light tailored devices are attractive for building integrated photovoltaics[150-154] and for use as indoor photovoltaics which are needed to self-power Internet of Things devices.[122, 155, 156] DSCs operate with a series of electron transfer events by: (1) photoexcitation of the sensitizer and injection of an electron into TiO_2, (2) electron transfer from a redox shuttle (RS) to the oxidized dye, and (3) collection of electrons from a counter electrode by the oxidized RS.[97] Increasing the rate of these productive pathways is an attractive approach toward avoiding performance losses due to competitive back electron transfer pathways.[157] Methods to increase the rate of electron transfer reaction from the RS to the oxidized dye (referred to as "regeneration") are needed to improve the overall performance of DSC devices. Typical approaches rely on diffusion-controlled regeneration; however, transiently bonded self-assembled systems through approaches such as halogen bonding have shown dramatic improvements to regeneration rates with enhanced DSC device performances.[111-113, 158] This work seeks to probe the effects of weak Lewis acid-Lewis base (LA-LB) interactions between a TiO_2 anchored dye with a Lewis basic functionality and a Lewis acidic transition metal RS (Figure 1).

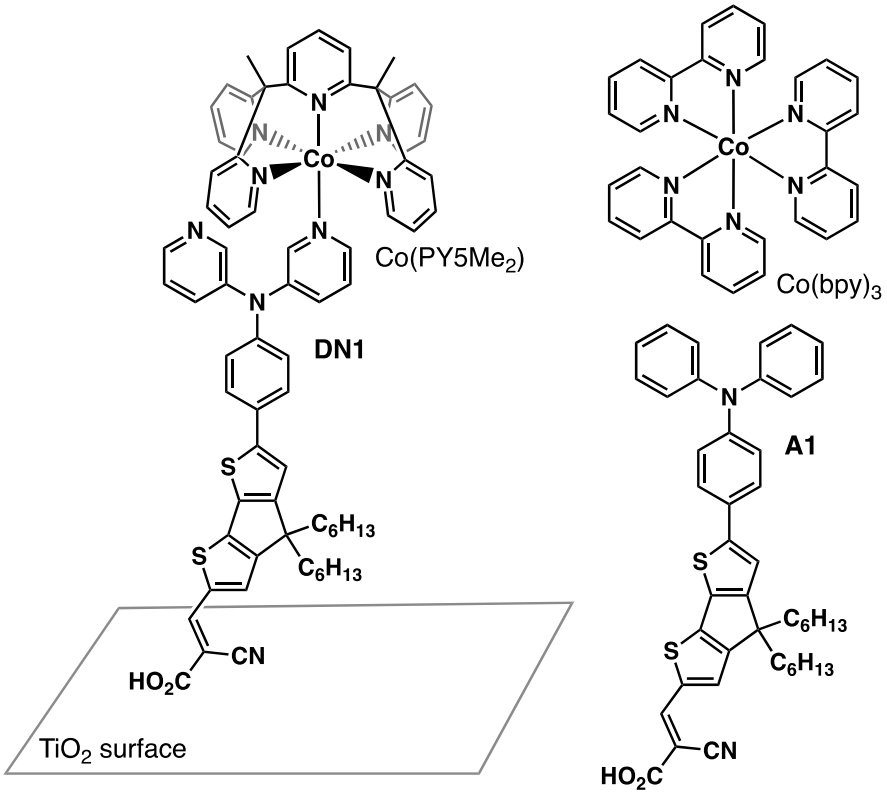

Figure 6.1. LA-LB interaction between a TiO_2 bound organic dye (**DN1**) and the Co(PY5Me$_2$) redox shuttle (left). Dye (**A1**)[4] and RS (Co(bpy)$_3$) as no LA-LB interaction control materials.

The **DN1** dye design incorporates amine-substituted pyridine rings on a triarylamine donor group with a cyclopentadithiophene (CPDT) bridge and cyanoacrylic acid (CAA) acceptor. The dye follows the high performing donor-π bridge-acceptor (D-π-A) organic dye design, which is known to promote facile electron transfers with significant interfacial charge separation times.[159-162] After photoexcitation, the D-π-A design relies on an intramolecular charge transfer (ICT) event leaving a hole on the donor region of the dye. **DN1** is designed with the Lewis basic pyridine groups on the donor region to hold a redox shuttle in close proximity to the photogenerated hole to promote rapid regeneration. The pyridyl groups are substituted at the 3-position to avoid weakening of the ICT event from the amine donor to the CAA acceptor. The

CPDT bridge was chosen since it has two surface protecting alkyl chains and has shown exceptional performance with transition metal-based RSs in the literature.[159-162] The CAA acceptor is known to promote facile electron injection into TiO_2.[97] We note that pyridyl groups are known to bind TiO_2; however, it is anticipated that the bidentate binding carboxylic acid group is a better binding group.[163] Likewise, the $[Co(PY5Me_2)(L)]^{3+/2+}$ RS has been shown to be an effective RS for DSCs with organic dyes.[164] The prior report demonstrates the tunability of this RS with added Lewis bases such as 4-*tert*-butylpyridine (TBP) and methyl benzimidazole in the electrolyte, which indicates that the RS readily accepts a monodentate imine ligand (L) under operational device conditions. We hypothesize that pyridyl groups on a dye could serve as the monodentate ligand, L, in $[Co(PY5Me_2)(L)]^{3+/2+}$ resulting in enhanced electron transfer reaction rates at the TiO_2-dye-electrolyte interface. Note that throughout this manuscript, (L) is used when the ligand associated to $[Co(PY5Me_2)]^{3+/2+}$ is undefined whereas $[Co(PY5Me_2)(MeCN)]^{3+/2+}$ is written for the complex as synthesized when it is either added to an experiment or when L is known to be MeCN.

RESULTS AND DISCUSSION

The synthesis of **DN1** begins with the bromination of known *N*-phenyl-*N*-(pyridin-3-yl)pyridin-3-amine (**1**)[165] with *N*-bromosuccinimide in THF to give brominated dipyridylarylamine (**2**) in 64% yield (Scheme 1). Known stannylated CPDT (**3**)[120] was coupled to **2** via a Stille coupling in 81% yield to give CPDT-amine intermediate **4**. A Vilsmeier-Haack reaction at the CPDT site of **4** gives the formylated intermediate **5** in 44% yield. Finally, a

Knoevenagel reaction on aldehyde **5** affords **DN1** in 84% yield in four steps from known materials in 19% overall yield.

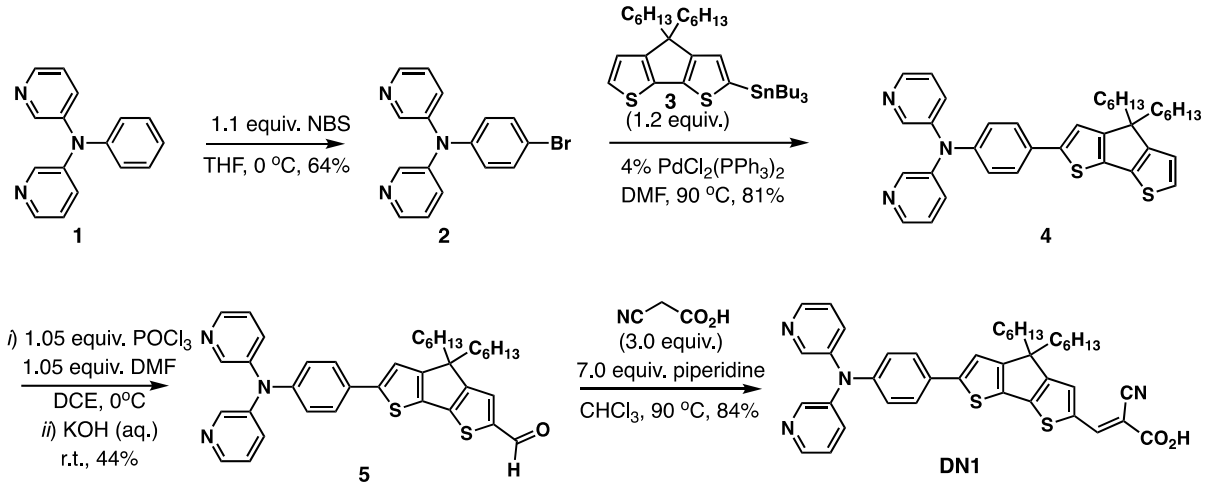

Figure 6.2. Synthetic route to **DN1**.

The optical properties of **DN1** were analyzed with steady-state absorption spectroscopy. **DN1** exhibits a broad absorption band from approximately 400 nm to 600 nm in dichloromethane solution which is assigned as an ICT band. A maximum absorption (λ_{max}) is observed at 515 nm with a molar absorptivity (ε) of 17,500 $M^{-1}cm^{-1}$ (Figure 2). When the dye is adsorbed onto TiO_2, the dye absorbance has a near identical onset value with a broadening of the absorption band relative to solution measurements (Figure 2). Notably, the absorption maxima blue-shifts on TiO_2 films as is commonly observed in the literature with ICT based dyes.[166] In the presence of the RS, a near identical onset value is obtained with narrowing of the low energy absorbance band with respect to dye absorbed to TiO_2. The narrowing of the absorption curve upon addition of the RS could be due to a RS-dye interaction (consistent with a LA-LB interaction) taking place at the TiO_2-dye-electrolyte interface resulting in less conformational freedom of the dye with the bulky RS coordinated. While these studies do not confirm this hypothesis, it is clear empirically that

addition the RS does narrow the absorption band of the dye on the TiO_2 surface. The onset of absorption (λ_{onset}) is used to calculate the excited state oxidation potential ($E_{(S^+/S^*)}$) via the equation $E_{(S^+/S^*)} = E_{(S^+/S)} - E_g^{opt}$, where $E_{(S^+/S)}$ is the ground state oxidation potential found via cyclic voltammetry (CV) and E_g^{opt} is the optical gap found by converting λ_{onset} from nm to eV. The λ_{onset} was mathematically derived to be 581 nm via the "0nset" program.[141] The $E_{(S^+/S)}$ value of **DN1** was found from CV to be 1.22 V versus the normal hydrogen electrode (NHE) in dichloromethane solution with tetrabutylammonium hexafluorophosphate as the supporting electrolyte (Figure S1). The oxidation potential of $[Co(PY5Me_2)(L)]^{3+/2+}$ is reported to be 0.78 V versus NHE in the presence of common DSC device additive *tert*-butylpyridine (TBP)[164] (or at 0.82 V in the absence of TBP where L is MeCN, Figure S2). Thus, the $E_{(S^+/S)}$ value of **DN1** is sufficiently positive to drive a favorable electron transfer reaction to between the oxidized dye and $[Co(PY5Me_2)(L)]^{2+}$. The $E_{(S^+/S)}$ and absorption curve onset lead to a $E_{(S^+/S^*)}$ value of –0.91 V, which is sufficiently negative for favorable electron injection into the TiO_2 conduction band taken as –0.5 V as is commonly used in the DSC literature.[97, 167, 168] From the optical and electrochemical data, it is apparent that **DN1** is well-positioned energetically for facile electron injection into the TiO_2 conduction band with a driving force of injection (ΔG_{inj}) of 410 mV and for a facile electron transfer reaction from $[Co(PY5Me_2)(L)]^{2+}$ at a regenerative driving force (ΔG_{reg}) of 440 mV (Figure 3).

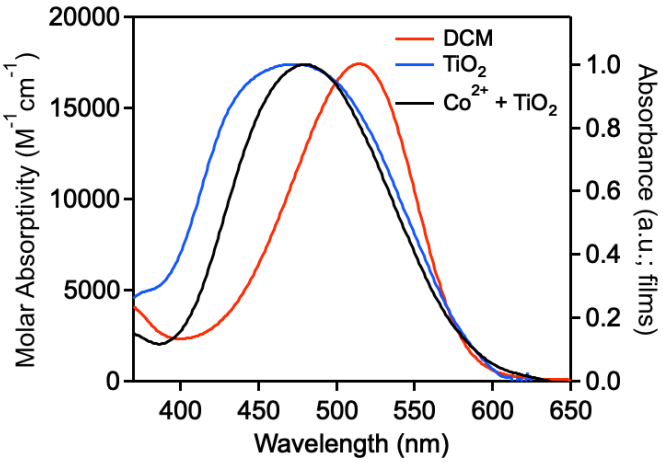

Figure 6.3. UV−vis absorption spectra of **DN1** in DCM, on TiO_2, and on TiO_2 after adding $[Co(PY5Me_2)(MeCN)]^{2+}$ to the solution.

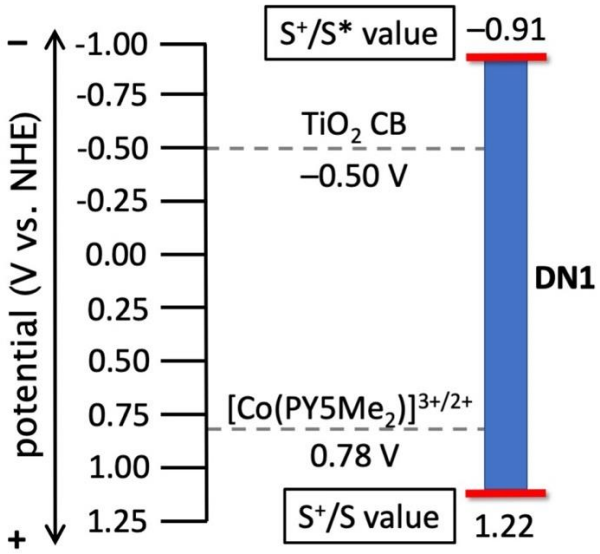

Figure 6.4. Potential energy diagram of **DN1** relative to the conduction band of TiO_2 and $[Co(PY5Me_2)(L)]^{3+/2+}$ in the presence of TBP.

Transient absorption spectroscopy (TAS) experiments were conducted on TiO_2 bound **DN1** films to observe both the duration of photoinduced charge separation after electron injection in the

absence of the RS and the rate of electron transfer from $[Co(PY5Me_2)(L)]^{2+}$ to the oxidized dye. The TAS studies herein are done on a microsecond time scale where electron injection is assumed to be completed so that the main signals observed are from the oxidized dye. For the LA-LB approach to have a significant influence on DSC device performances, an LA-LB rate enhancement must be evident in the presence of a complex electrolyte system as used in DSC solar cells which includes the oxidized RS, the reduced RS, LiTFSI (lithium bis(trifluoromethane)sulfonimide), and TBP – an additive that serves several key functions in the device.[142, 169] The full regenerative electrolyte in this study is comprised of 0.25 M Co^{2+}, 0.05 M Co^{3+}, 0.1 M LiTFSI, and 0.5 M TBP. We note that this electrolyte environment is complex; however, the full electrolyte is required for more realistic measurements when assessing the regeneration efficiency of a DSC device (*vide infra*). TAS studies using complex electrolytes are common in the DSC field for this reason.[147, 148, 170] Thus, in these studies, 0.1 M LiTFSI and 0.5 M TBP are held constant while the charge separation duration and regeneration rates are probed without and with the Co-complexes being present, respectively.

TAS measurements in the absence of the RS show a strong absorbance at 720 nm which is assigned to the dye cation along with a ground state bleach (GSB) near 450 nm (Figure 4, Table 1). The TAS signal decay kinetics at 720 nm were fit with a stretched exponential Kohlrausch–Williams–Watts (KWW) function.[138-140, 171] The use of a KWW fitting approach is commonly used in the DSC literature, in part, because it can accommodate the complexity of signals with multiple rate components within complex DSC environments.[172-175] A photoinduced interfacial charge separated state lifetime of 1.2×10^{-3} s is observed between reduced TiO_2 and the oxidized dye ($TiO_2(e)^-|dye^+$). This corresponds to a back electron transfer (BET) rate

of 8.6×10^{2} s^{-1}. Upon introduction of the RS (both Co^{2+} and Co^{3+} states), a similar TAS spectrum is observed of the dye cation with a substantially shorter dye cation lifetime of 1.8×10^{-6} s, which can be attributed to rapid electron transfer from the Co^{2+} species to the oxidized dye. Notably, neither oxidation state of the [Co(PY5Me$_5$)(L)] RS absorbs past ~650 nm which allows for direct monitoring of the dye cation signal (Figure S3).[176] The corresponding rate of dye cation signal decay is 5.5×10^{5} s^{-1} (Figure 4). The regeneration rate (k_{reg}) is substantially faster than the BET rate (k_{BET}), which leads to a regeneration efficiency (Φ_{reg}) of 99.8% using the equation $\Phi_{reg} = (k_{reg}/(k_{reg}+k_{BET}))\times100\%$ (Table 1).[170, 175] As has been previously noted, this commonly used approach to estimating Φ_{reg} likely overestimates the often complex-to-obtain absolute Φ_{reg} value acquired from the electron transfer reactions; however, this approach works well for the comparison of Φ_{reg} obtained under similar experimental conditions.[177-179]

As a control, $[Co(bpy)_3]^{3+/2+}$ was used as a RS which does not have an open or labile coordination site available to bind to **DN1**. The lifetime of the dye cation is observed at 5.8×10^{-4} s for a signal decay rate of 1.7×10^{3} s^{-1}, which is more than 2 orders of magnitude slower than the dye cation signal decay rate when $[Co(PY5Me_2)(L)]^{3+/2+}$ is employed (Figures 4 and S7). The dramatic change in rates can be attributed to the generation of a transient LA-LB bonding interaction between the surface-bound dye and $[Co(PY5Me_2)(L)]^{3+/2+}$, which is unlikely to be formed with $[Co(bpy)_3]^{3+/2+}$. The Φ_{reg} of **DN1** with the $[Co(bpy)_3]^{3+/2+}$ electrolyte is calculated to be 66.4%, which is significantly lower than the 99.8% value obtained with $[Co(PY5Me_2)(L)]^{3+/2+}$. As an additional control, dye **A1** with no pyridyl groups was synthesized according to literature procedures (Figure 1).[4] Interestingly, the dye cation decay

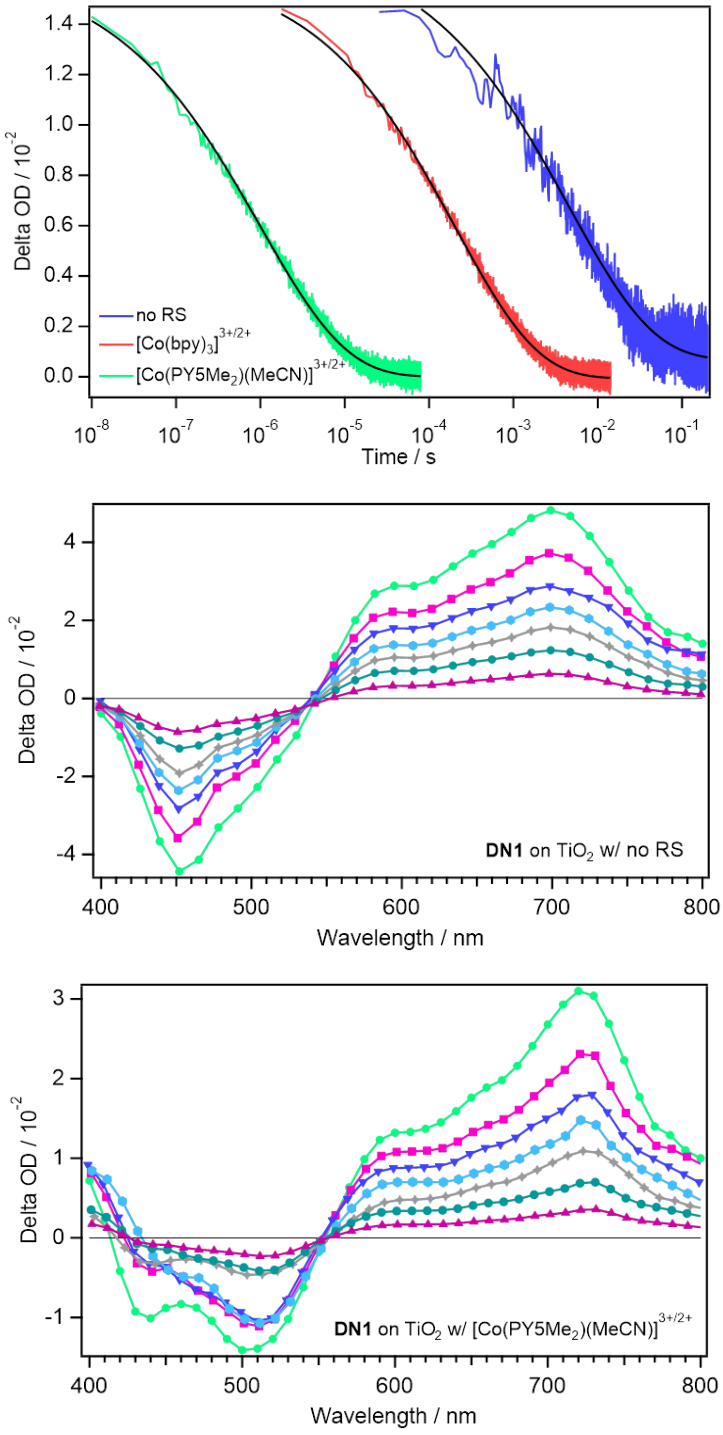

Figure 6.5. Top: Transient decay signals at 720 nm corresponding to TiO_2 bound **DN1**, TiO_2 bound **DN1** with added $[CoPY5Me_2)(MeCN)]^{3+/2+}$, and TiO_2 bound **DN1** with added $[Co(bpy)_3]^{3+/2+}$. Middle: TA spectrum of **DN1** on TiO_2 with no RS present. Bottom: TA spectrum of **DN1** on TiO_2 with $[Co(PY5Me_2)(MeCN)]^{3+/2+}$.

rate was faster with the $[Co(bpy)_3]^{3+/2+}$ electrolyte than the $[Co(PY5Me_2)(L)]^{3+/2+}$ electrolyte with **A1** (1.0×10^6 s^{-1} versus 1.1×10^4 s^{-1}, Table 1, Figures S10-S11). This suggests a favorable interaction between **DN1** and $[Co(PY5Me_2)(L)]^{3+/2+}$ is occurring since this system shows the inverse trend.

Table 6.1. Lifetimes and rates of photogenerated dye cation signal decays found via TAS experiments.

Entry	Dye	RS	τ_{obs} (s)	k_{obs} (s^{-1})	Φ_{reg} (%)
1	**DN1**	none	1.2×10^{-3}	8.6×10^2	---
2	**DN1**	$[Co(PY5Me_2)(L)]^{3+/2+}$	1.8×10^{-6}	5.5×10^5	99.8
3	**DN1**	$[Co(bpy)_3]^{3+/2+}$	5.8×10^{-4}	1.7×10^3	66.4
4	**DN1-ester**	$[Co(bpy)_3]^{2+}$	2.0×10^{-7}	5.0×10^6	---
5	**DN1-ester**	$[Co(bpy)_3]^{3+}$	$>1.0\times10^{-2}$	$<1.0\times10^2$	---
6	**DN1-ester**	$[Co(PY5Me_2)]^{2+}$	9.4×10^{-7}	1.1×10^6	---
7	**DN1-ester**	$[Co(PY5Me_2)]^{3+}$	2.5×10^{-4}	4.0×10^3	---
8	**A1**	none	4.0×10^{-4}	2.5×10^3	---
9	**A1**	$[Co(PY5Me_2)(L)]^{3+/2+}$	9.2×10^{-5}	1.1×10^4	81.5
10	**A1**	$[Co(bpy)_3]^{3+/2+}$	1.0×10^{-6}	1.0×10^6	99.8

The binding of the dye to the $[Co(PY5Me_2)(MeCN)]^{2+}$ RS was further probed in homogeneous solution studies through the synthesis of the methyl ester derivative of **DN1** (**DN1-ester**). **DN1-ester** was synthesized to eliminate any potential hydrogen bonding of the CAA group on the acceptor region with the pyridine groups on the donor region of the dye which could complicate the results (Scheme S1). To probe the dye-RS interactions, Stern-Volmer plots with emission quenching were generated with the dye in the presence of added $[Co(PY5Me_2)(MeCN)]^{2+}$ with a comparison to $[Co(bpy)_3]^{2+}$ (Figures 5 and S4-S5).[180, 181] Non-linear emission quenching was observed when $[Co(PY5Me_2)(MeCN)]^{2+}$ was added at

concentrations of the RS significantly lower than those present in an operational DSC device. Co RSs are typically present in DSC devices at a concentration of ~0.25 M for high performance devices; however, these concentrations lead to complete quenching. The highest concentration of the RS shown on the graph (40 mM) resulted in a substantial quenching of

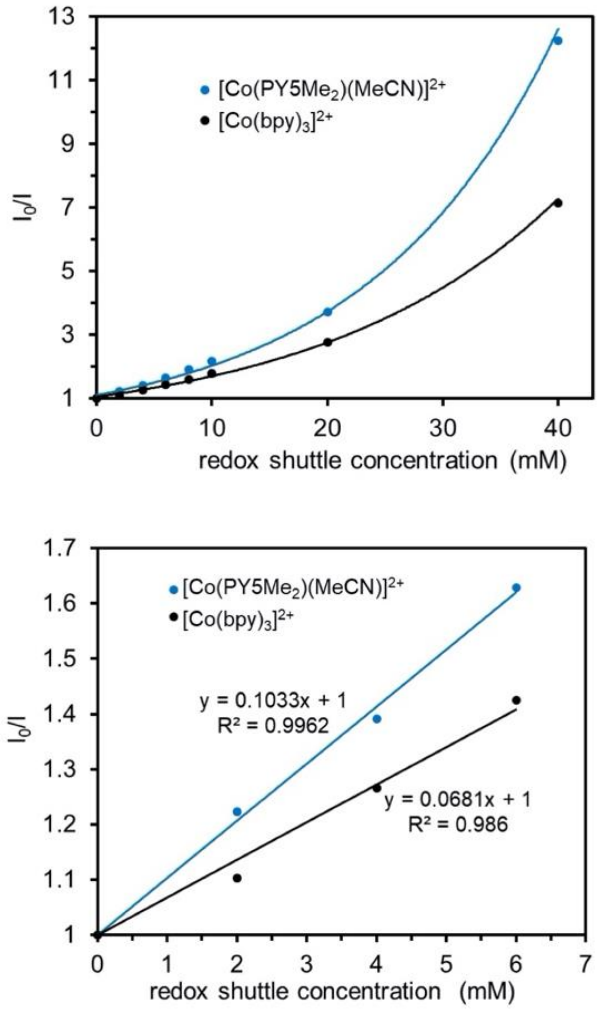

Figure 6.6. Stern-Volmer quenching plot for **DN1-ester** at 5 μM concentration in acetonitrile with high (top) and low (bottom) concentrations of the RSs.

emission with higher concentrations of the RS giving no appreciable emission (Figure S4). A similar non-linear emission quenching profile is observed for $[Co(bpy)_3]^{2+}$ at approximately half

the quenching ratio observed for $[Co(PY5Me_2)(MeCN)]^{2+}$ at the highest concentration probed (40 mM, Figures 5 and S5). The non-linearity of both the Co^{2+} RSs in quenching the emission of **DN1-ester** suggests non-diffusional behavior for the dye and both RS quencher pairs. The non-linear quenching with added $[Co(PY5Me_2)(MeCN)]^{2+}$ is predicted due to LA-LB binding; however, the origin of non-linear quenching with added $[Co(bpy)_3]^{2+}$ is not obvious. However, the reduced quenching with $[Co(bpy)_3]^{2+}$ is correlated to the reduced signal suppression in the ^{1}H NMR, which could be due to a diminished interaction with the dye. Emission quenching is significantly more effective with added $[Co(PY5Me_2)(MeCN)]^{2+}$ presumably due to LA-LB binding which is consistent with the TAS experimental results. At low concentrations (2-6 mM) of the RSs, a near linear relationship is observed in the Stern-Volmer plot with Stern-Volmer quenching constants (K_{SV}) of 0.103 and 0.068 for the $[Co(PY5Me_2)(MeCN)]^{2+}$ and $[Co(bpy)_3]^{2+}$ RSs, respectively (Figure 5). The higher quenching constant upon addition of the $[Co(PY5Me_2)(MeCN)]^{2+}$ complex is correlated to a faster electron transfer reaction from $[Co(PY5Me_2)(L)]^{2+}$ to the dye cation as observed via surface TAS studies. It is important to note that there are multiple emission quenching pathways available such as paramagnetic quenching, and the quenching constants may contain other emission loss pathways beyond electron transfer reactions.[182]

^{1}H NMR studies were undertaken in an attempt to examine binding of $[Co(PY5Me_2)(MeCN)]^{2+}$ to **DN1-ester** (Figures S24-S26). A broadening of the **DN1-ester** signals is observed as $[Co(PY5Me_2)(MeCN)]^{2+}$ is added. This does not confirm binding of **DN1-ester** to $[Co(PY5Me_2)(MeCN)]^{2+}$, but it is interesting to note that the tetramethylsilane in the ^{1}H NMR experiments retains a sharp peak shape regardless of $[Co(PY5Me_2)(MeCN)]^{2+}$ concentration. The selective broadening of the **DN1** peaks in the presence of $[Co(PY5Me_2)(MeCN)]^{2+}$ suggests an

interaction between these two species. Additionally, a ratio of **DN1-ester** fluorescence intensity without and with $[Co(PY5Me_2)(MeCN)]^{2+}$ plotted against mole fraction of total analyte (dye plus redox shuttle) shows no significant quenching of the emission intensity from the dye at 1×10^{-5} M regardless of mole fraction (Figures S27-S28). This suggests that if a binding interaction of the redox shuttle to the dye is taking place, the binding is a weak interaction with an equilibrium possibly favoring non-binding of the cobalt complex to the dye at these concentrations. Higher concentrations of the cobalt complex were needed to observe fluorescence quenching, such as those used in the Stern-Volmer studies above.

The **DN1-ester** binding to $[Co(PY5Me_2)]^{2+}$ was also probed computationally at the ω-B97XD[125]/6-31+G(d)[129, 183] level of theory for all atoms except the Co atom which utilizes the LANL2TZ(f) basis set (see the Methods section for additional details).[127] The cobalt complex was placed within bonding distance to each of the nitrogen and sulfur heteroatoms of **DN1-ester**, and the structure was then allowed to optimize geometrically. No low energy geometry was found for the binding of the cobalt complex to either sulfur atom of **DN1-ester**. The cobalt complex, instead, moves to either the pyridyl nitrogens or the cyano nitrogen as a minimum energy geometry. The choice depends upon which sulfur atom the cobalt complex was initially attempted to bond at the beginning of the optimization computation. Additionally, no low energy geometry was found with respect to the triarylamine nitrogen, presumably due to the steric environment around the amine, and the cobalt complex moved to the pyridyl nitrogens as a low energy complex. The two low energy geometries are effectively degenerate with one another since the relative energies are within ~9 kcal/mol of each other. These structures are shown in Figure 6 with binding of the cobalt complex to either a pyridyl nitrogen or the cyano nitrogen. In a functional DSC device

where the carboxylic acid group is bound to a TiO_2 surface, the binding of the cobalt complex to a cyano group is not likely due to steric constraints. Thus, only the pyridyl nitrogens lead to a reasonable binding of the cobalt complex to **DN1**. A computed bond distance of 1.85 Å is observed from the **DN1**-pyridyl nitrogen to the Co center. The Co-N_{ligand} bond length trans to the dye-N-Co bond is 1.88 Å, and all the remaining Co-N_{ligand} bond lengths are ~1.82 Å. Thus, the bond length from the Co center to the dye is similar to the $PY5Me_2$ ligand Co-N bond lengths. A potential cause of the weak binding observed in the fluorescence quenching studies described above could be due to the steric environment at the pyridyl groups. The non-binding pyridyl group has a carbon atom within 3.2 Å of another carbon atom of the pentadentate ligand on the cobalt atom. This type of steric congestion likely weakens the dye-cobalt complex binding, which could be beneficial in a DSC device where the redox shuttle should be transiently bound.

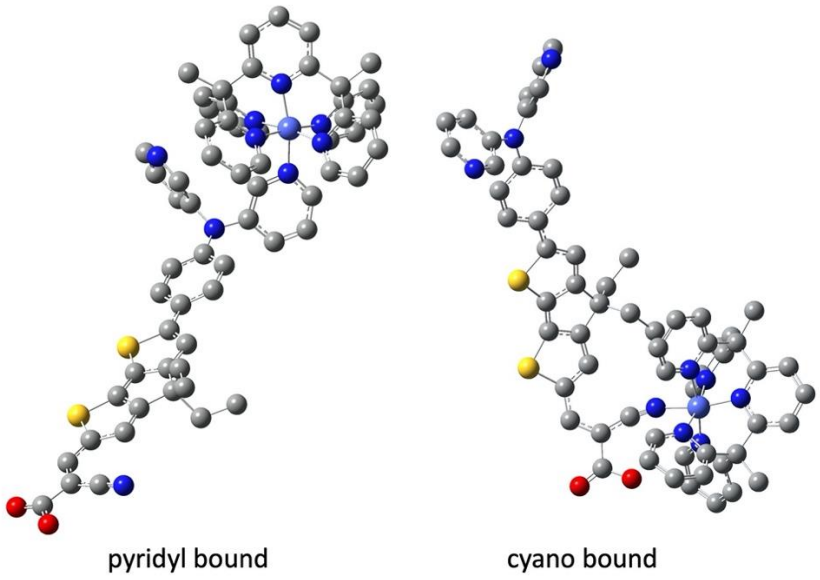

Figure 6.7. Optimized geometries of pyridyl-bound (left) and cyano-bound (right) **DN1-ester** with $[Co(PY5Me_2)]^{2+}$. Hydrogen atoms are omitted for clarity.

Additional solution-phase TAS studies were undertaken with **DN1-ester** and the Co^{2+} complexes with significantly simplified conditions relative to the film studies (Figures S8-S9,

Tables 1). Upon photoexcitation with only dye and RS present in solution, an electron transfer reaction may occur according to equation 1:

$$\textbf{DN1-ester} + Co^{3+} + h\nu \rightarrow [\textbf{DN1-ester}]^{+} + Co^{2+} \qquad \text{(equation 1)}$$

$$[\textbf{DN1-ester}]^{+} + Co^{2+} \rightarrow \textbf{DN1-ester} + Co^{3+} \qquad \text{(equation 2)}$$

$$\textbf{DN1-ester} + Co^{2+} + h\nu \rightarrow [\textbf{DN1-ester}]^{+} + Co^{1+} \qquad \text{(equation 3)}$$

The transient absorption spectra are very similar to that observed for **DN1** on TiO_2 and via spectroelectrochemistry (SEC) measurements on **DN1-ester** (Figure S6). The electron transfer reaction in equation 2 is similar to the electron transfer reaction occurring at the TiO_2 surface referred to as regeneration. With **DN1-ester**, the electron transfer reaction between photogenerated **DN1-ester** cation and $[Co(PY5Me_2)(L)]^{2+}$ is observed to be faster than with $[Co(bpy)_3]^{2+}$ (dye cation decay rates of 4.0×10^3 s^{-1} versus $<1.0\times10^2$ s^{-1}), which can be explained by a LA-LB interactions of the **DN1-ester** cation and $[Co(PY5Me_2)(L)]^{2+}$. A LA-LB interaction would keep the dye and cobalt complex in close proximity for increased electron transfer reaction rates. Since the oxidative quenching of photoexcited **DN1-ester** is thermodynamically favorable with $[Co(PY5Me_2)(L)]^{2+}$ by 80 mV,[184] TAS experiments with **DN1-ester** and added $[Co(PY5Me_2)(MeCN)]^{2+}$ were undertaken as well, which show the formation of the **DN1-ester** cation with a relatively rapid decay rate of 1.1×10^6 s^{-1} (equation 3, Table 1). Notably, this electron transfer reaction is not desirable within a DSC device since the photoexcited dye would ideally be oxidatively quenched by TiO_2. This suggests a potential DSC device performance limitation which could be circumvented through the future design of dyes and RSs that do not thermodynamically favor oxidative quenching of the photoexcited dye. Similarly, **DN1** was examined on insulating ZrO_2 films via emission quenching studies both under steady-state and time-resolved conditions

(Figure 7). Under these conditions with the redox shuttles present in the same amounts as in functional DSC devices (0.25 M Co^{2+} and 0.05 M Co^{3+}), **DN1** emission is quenched at near equal amounts with both $[Co(bpy)_3]^{3+/2+}$ and $[Co(PY5Me_2)]^{3+/2+}$. A slightly stronger quenching in the presence of $[Co(PY5Me_2)]^{3+/2+}$ is observed. Time-correlated single photon counting experiments suggest a similar trend with

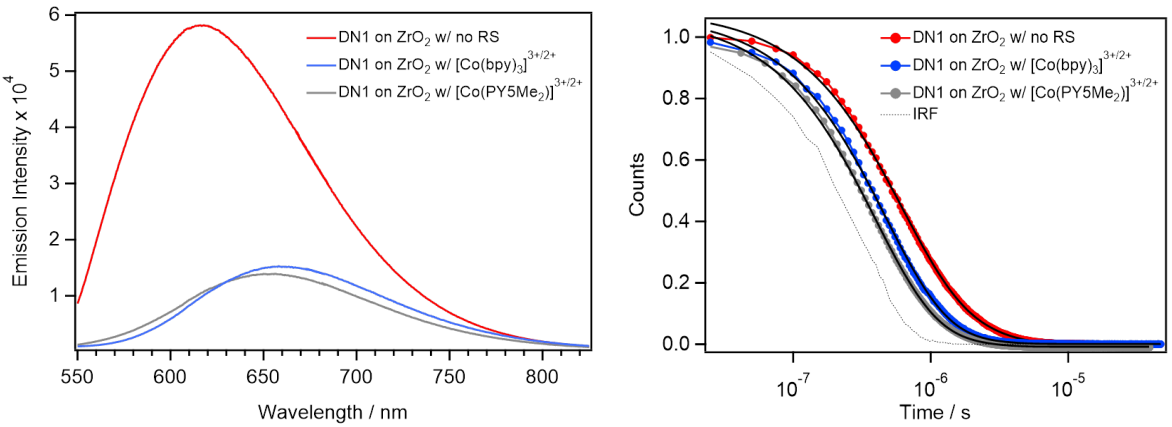

Figure 6.8. Steady-state emission spectrum (left) and time-correlated single photon counting curves (right) of **DN1** with and without redox shuttles present in the same concentration as in functional DSC devices. IRF stands for instrument response function.

emissive lifetimes of 0.9 ns without RS, 0.5 ns with $[Co(bpy)_3]^{3+/2+}$, and 0.4 ns with $[Co(PY5Me_2)]^{3+/2+}$.

DSC devices were fabricated with **DN1** and photovoltaic performances were measured under AM 1.5G solar simulated conditions and under fluorescent lighting conditions (Figure 8, Table 2). Power conversion efficiencies (PCEs) of each device were obtained from the equation $PCE = (J_{SC}*V_{OC}*FF)/I_0$, where J_{SC} is the short-circuit current density, V_{OC} is the open-circuit voltage, FF is the fill factor, and I_0 is the irradiation intensity. Devices with the

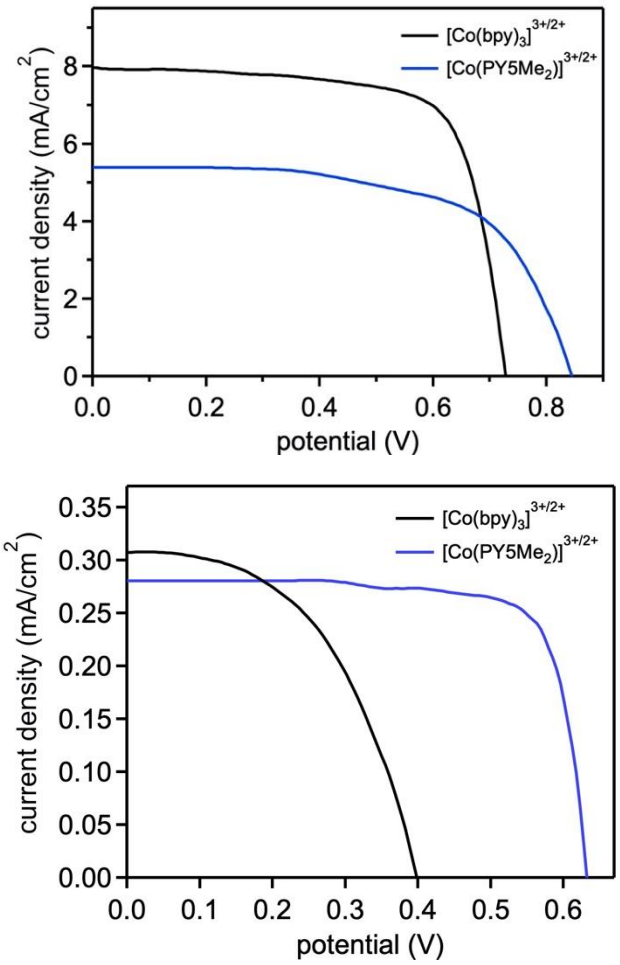

Figure 6.9. *J*–*V* curves of DSCs based on **DN1** at 1000 W/m^2 with a solar simulator (top) and 10.8 W/m^2 (6000 lux) with fluorescent lighting (bottom).

Table 6.2. DSC device data with **DN1**.

RS	irradiation intensity	irradiation source	V_{oc} (mV)	J_{sc} (mA/cm^2)	*FF* (%)	PCE (%)
$[Co(PY5Me_2)(L)]^{3+/2+}$	1000 W/m^2	solar simulator	835	5.5	63	2.9
$[Co(bpy)_3]^{3+/2+}$	1000 W/m^2	solar simulator	731	8.1	73	4.3
$[Co(PY5Me_2)(L)]^{3+/2+}$	100 W/m^2	solar simulator	752	0.58	60	3.0
$[Co(bpy)_3]^{3+/2+}$	100 W/m^2	solar simulator	625	0.76	53	3.0
$[Co(PY5Me_2)(L)]^{3+/2+}$	25.4 W/m^2 (13000 lux)	fluorescent	645	0.65	74	12.4
$[Co(bpy)_3]^{3+/2+}$	25.4 W/m^2 (13000 lux)	fluorescent	481	0.71	55	7.3
$[Co(PY5Me_2)(L)]^{3+/2+}$	10.8 W/m^2	fluorescent	625	0.28	73	13.0

	(6000 lux)					
$[Co(bpy)_3]^{3+/2+}$	10.8 W/m^2 (6000 lux)	fluorescent	400	0.31	49.4	5.6
$[Co(PY5Me_2)(L)]^{3+/2+}$	5.3 W/m^2 (2300 lux)	fluorescent	565	0.07	82.5	9.4

Electrolyte is comprised of 0.25 M Co^{2+}, 0.05 M Co^{3+}, 0.1 M LiTFSI, and 0.5 M TBP in acetonitrile. A PEDOT counter electrode was used in all devices. Values are the average of at least two devices with a < ±0.3 variance of PCE.

$[Co(PY5Me_2)(L)]^{3+/2+}$ RS have a V_{OC} of 835 mV, a J_{SC} of 5.5 mA/cm^2, a FF of 63% for a PCE of 2.9% under full sun illumination (1000 W/m^2). Notably, a higher photocurrent is observed for devices with $[Co(bpy)_3]^{3+/2+}$ despite a higher regeneration efficiency being observed for the electron transfer reaction from $[Co(PY5Me_2)(L)]^{2+}$ to oxidized **DN1**. Presumably, the oxidative quenching of photoexcited **DN1** by a bound $[Co(PY5Me_2)(L)]^{3+}$ complex as shown by TAS studies (*vide supra*) leads to non-productive photoinduced electron transfer reactions which lower the peak incident photon-to-current conversion efficiency (IPCE) value and reduces photocurrent (Figure S14). A maximum V_{OC} (V_{OC}^{max}) of 1.28 V is possible based on the $[Co(PY5Me_2)(L)]^{3+/2+}$ RS potential when the conduction band of TiO_2 is taken to be –0.5 V. The V_{OC} loss (V_{OC}^{loss}) of this system is calculated according to the equation $V_{OC}^{loss} = V_{OC}^{max} - V_{OC}$ to be 440 mV.[185] A lower V_{OC} is observed when $[Co(bpy)_3]^{3+/2+}$ is used as the RS with a V_{OC}^{loss} of 330 mV. The lower V_{OC}^{loss} value with a lower observed V_{OC} is due to the less positive potential of $[Co(bpy)_3]^{3+/2+}$ when compared with $[Co(PY5Me_2)(MeCN)]^{3+/2+}$. Notably, electrochemical impedance spectroscopy suggests the two DSC devices with each RS system have similar electron lifetimes in TiO_2, which indicates that any LA-LB interactions occurring at the TiO_2-dye surface are not leading to appreciably faster recombination reactions (electron transfer reactions from the TiO_2-dye interface to the oxidized RS) despite a presumably higher RS concentration at that TiO_2-dye interface for

$[Co(PY5Me_2)(L)]^{3+/2+}$ (see SI Figures S12-S13 and Table S1). The higher photocurrent and fill factor when $[Co(bpy)_3]^{3+/2+}$ is used relative to $[Co(PY5Me_2)(MeCN)]^{3+/2+}$ results in an overall higher PCE of 4.3% at full sun (1000 W/m^2) irradiation. However, when the irradiation intensity is reduced to 10% sun (100 W/m^2), the PCE values of DSC devices with $[Co(PY5Me_2)(MeCN)]^{3+/2+}$ and $[Co(bpy)_3]^{3+/2+}$ are the same at 3.0%. The decrease in relative PCE value for $[Co(bpy)_3]^{3+/2+}$ is due to a faster decrease in photocurrent and fill factor than is observed with $[Co(PY5Me_2)(MeCN)]^{3+/2+}$ as the irradiation intensity is changed from full sun intensity to 10% sun intensity.

Current dynamic measurements at variable light intensities were undertaken to better understand the change in performance as a function of light intensity for the two systems (Figure 9). For these current dynamic measurements, the light source is shuttered on and off with varied light filters. The current response toward on/off light cycling can show mass transport limitations within the system if an initial spike is observed upon opening the shutter.[186, 187] This initial spike occurs due to the rapid consumption of the reduced RS species at the TiO_2 surface with slow diffusion which depletes the needed reducing RS concentration near dye cations. $[Co(bpy)_3]^{3+/2+}$ shows no evidence of mass transport issues at any irradiation intensity; however $[Co(PY5Me_2)(MeCN)]^{3+/2+}$ has clear evidence of current limited mass transport with a 30% decrease in current from the initial high current spike to the steady-state plateau of photocurrent at 100% sun irradiation intensity. Upon changing sunlight intensities to lower values, the magnitude of the decrease in photocurrent output from the spike to the steady state plateau decreases significantly from a 30% drop at 100% sun intensity to a 10% drop at 10% sun intensity. This indicates that as irradiation intensity is decreased, $[Co(PY5Me_2)(L)]^{3+/2+}$

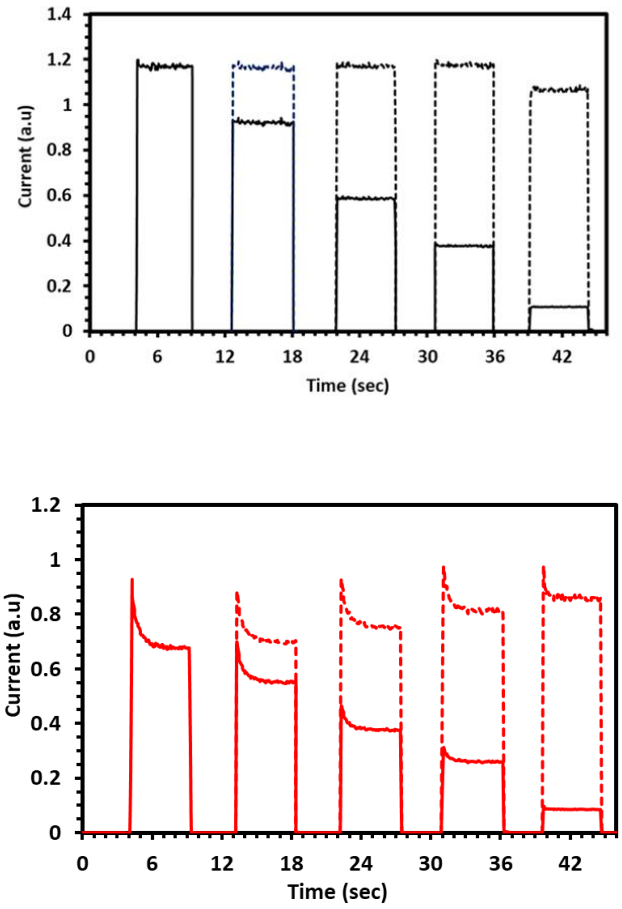

Figure 6.10. Current dynamics of **DN1** with $[Co(bpy)_3]^{3+/2+}$ (top) and $[Co(PY5Me_2)(L)]^{3+/2+}$ (bottom). Sun intensities are 100%, 78%, 50%, 32%, and 10% from left to right on each graph with the lamp shuttered on/off. The dashed lines are found by normalizing the data to sun intensity so that relative efficiency of current generated can be easily compared across the varied intensities.[186, 187]

becomes more kinetically competent at reaching steady-state redox cycling in the DSC device allowing for higher quantum yields for the completed device circuit. Current dynamics measurements at varied light intensity also provide information about the current response at varied light intensity. In Figure 9, the dashed lines are the current responses normalized based on light intensity. For the case of $[Co(PY5Me_2)(L)]^{3+/2+}$, the photocurrent response is highest when normalized to light intensity at 10% sun intensity. The opposite is observed in the case of

$[Co(bpy)_3]^{3+/2+}$ with 10% sun intensity providing the least amount of photocurrent. These trends suggest that the LA-LB approach using $[Co(PY5Me_2)(MeCN)]^{3+/2+}$ could be valuable for indoor photovoltaics in fluorescent light-to-electric applications.

Fluorescent light generated *J-V* curve measurements on the DSC devices were undertaken with a OSRAM 930 warm-white fluorescent light source (bulb 011318) which has a commonly used emission range at near 750 nm onset and has been used in prior reports on fluorescent light studies.[147] DSC devices with $[Co(PY5Me_2)(L)]^{3+/2+}$ have a peak performance of 13.0% PCE at 6000 lux with similar performance at 13000 lux. The PCE of these devices begins to decrease at 2300 lux to 9.4%. DSC devices with $[Co(bpy)_3]^{3+/2+}$ show dramatically lower PCE values at all indoor lighting intensities. A 13000 lux intensity leads to a 7.3% PCE which decreases to 5.6% at 6000 lux and does not give a *J-V* curve on our instrumentation at 2300 lux. Under these low light conditions, diffusion (or mass transport) is no longer current limiting under steady-state conditions for the $[Co(PY5Me_2)(L)]^{3+/2+}$ RS. In this environment, the LA-LB approach has a clear advantage leading to higher performing devices (13.0% versus 5.6% at 6000 lux) than $[Co(bpy)_3]^{3+/2+}$ which was non-operable at extremely low light intensity. Thus, dye-RS self-assembly design approaches are valuable toward improving indoor photovoltaics performances.

CONCLUSIONS

A dye with Lewis base functionality was designed and synthesized with pyridine groups on the donor portion of the donor-π bridge-acceptor dye. The dye optical and electronic properties were examined via absorption spectroscopy and cyclic voltammetry. Evidence suggesting a redox shuttle with a Lewis acid site may be binding to the dye was observed using absorption

spectroscopy and fluorescence spectroscopy via Stern-Volmer plots. Transient absorption spectroscopy reveals the redox shuttle with a labile coordination site that functions as a Lewis acid site, $[Co(PY5Me_2)(L)]^{2+}$, underwent a faster electron transfer reaction with the dye when photoexcited at a TiO_2 surface by >2 orders of magnitude when compared to a redox shuttle without an obvious Lewis acid site, $[Co(bpy)_3]^{2+}$. Similar electron transfer reaction kinetic observations were made via TAS measurements on an esterified dye in solution. DSC devices were fabricated with the dye and the two redox shuttles. At full sun conditions, $[Co(PY5Me_2)(L)]^{3+/2+}$ based devices gave inferior PCE values at full sun (about 2× lower) when compared to $[Co(bpy)_3]^{3+/2+}$ based devices. Current dynamic studies reveal a mass transport limitation with $[Co(PY5Me_2)(L)]^{3+/2+}$ at full sun, which is likely due to slow diffusion of the redox shuttle because of Lewis acid-Lewis base interactions at the surface. However, fluorescent lighting studies reveal significantly higher PCE values with $[Co(PY5Me_2)(L)]^{3+/2+}$ based devices relative to those with $[Co(bpy)_3]^{3+/2+}$ (13.0% versus 5.6%, respectively). Under these low light conditions, mass transport was not current limiting, which allowed for the improved electron transfer reaction rates of the Lewis acid-Lewis base self-assembly approach to demonstrate higher performances. This approach is valuable for low light conditions such as those used for indoor photovoltaics and in tandem or multijunction DSC systems. Intriguingly, this approach has led to reasonable performances with a cobalt redox shuttle under low light conditions where the commonly utilized $[Co(bpy)_3]^{3+/2+}$ underperforms. Notably, recombination rates as measured by electrochemical impedance spectroscopy do not seem to increase with the use of the Lewis acid-Lewis base coordination approach pursued with $[Co(PY5Me_2)(L)]^{3+/2+}$ despite the presumably higher local concentration of the redox shuttle near the TiO_2 surface. Future studies focused on designing a dye

with electronically and sterically altered Lewis basic functionality to vary binding strength and better fluorescent lighting spectral overlap is underway since the current dye ceases to absorb photons approximately 150 nm (about 42% of the spectrum) before common fluorescent lighting systems stop emitting.

CHAPTER 7

PREFERENTIAL DIRECTION OF ELECTRON TRANSFER REACTIONS AT THE INTERFACE

The work in this chapter is based on a publication in *Journal of Physical Chemistry C*, "Preferential Direction of Electron Transfers at a Dye-Metal Oxide Interface with an Insulating Fluorinated Self-Assembled Monolayer". This work was collaborative with contributions from Roberta R. Rodrigues, Kayla Foell, Dinesh Nugegoda, and Hammad Cheema. The dye and surface treatment characterization were done by Kayla Foell, Dinesh Nugegoda, and Hammad Cheema. The TCSPC and TAS data collection and data analysis was performed by the author.

INTRODUCTION

Dye-sensitized solar cells (DSCs) offer a convenient way to analyze interfacial electron transfer reactions within a well-understood framework.[19, 96, 97, 142, 153, 168, 188-193] In general, DSCs are continuing to attract intense research interest due to the ability to use these devices as building-integrated photovoltaics,[150, 151, 153, 154, 194] a relatively low production cost compared to many inorganic technologies,[95, 150, 153, 195] high performance in low light environments such as those commonly used for consumer electronics,[146, 147, 155] and a continued rise of power conversion efficiencies.[196-200] Power conversion efficiencies (PCEs) as high as 14.3% for organic dye-based devices have been demonstrated,[197] which has surpassed the highest PCEs of the traditionally dominant ruthenium-based sensitizers at approximately 11.9%.[201]

n-Type DSCs operate by photoexcitation of a sensitizer followed by an interfacial electron transfer reaction at a metal oxide interface (injection, Figure 1). The electron then traverses an external circuit to a counter electrode and is collected by a redox shuttle (RS). The RS then returns the electron to the oxidized dye (regeneration) to complete the circuit. Two non-productive competing pathways are: (1) electron transfer from TiO_2 to the oxidized dye after electron injection (back electron transfer, BET), and (2) transfer of electrons in TiO_2 to the electrolyte (recombination).

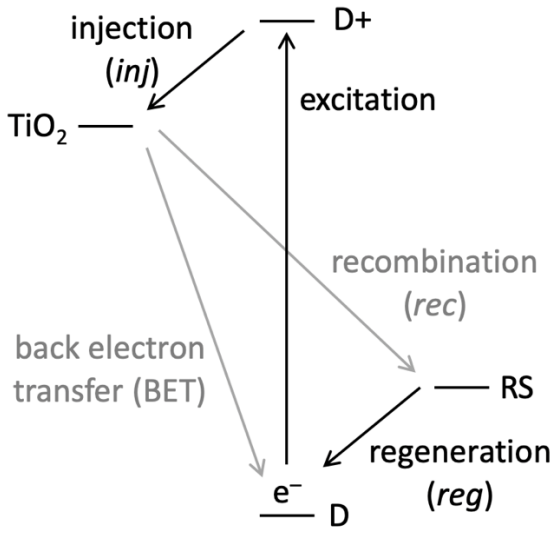

Figure 7.1. Illustration of the desired (black) and undesired (gray) electron transfer pathways with nomenclature listed beside each arrow.

The higher performance of organic sensitizers relative to metal-based dyes is due in part to organic sensitizers being more easily engineered to give slower recombination rates in many cases. This allows for the use of positively charged one-electron RSs with organic sensitizers that would otherwise have PCE inhibitive fast recombination rates with metal-based dyes.[90, 91, 93, 202, 203] The highest efficiency ruthenium sensitizers with I_3^-/I^- often rely on ligands such as thiocyanate (NCS^-) which are not easily amendable to the introduction of long alkyl chain groups often used to slow recombination rates with one electron redox shuttles.[97, 204-207] A popular strategy to overcome this limitation is through the molecular engineering of ruthenium sensitizers without NCS^- ligands for better semiconductor surface protection which has improved the PCE of ruthenium sensitizers to above 9% with cobalt-based redox shuttles.[207-213] However, these approaches have generally resulted in blue-shifted absorption spectra, which has limited these sensitizers from reaching the high photocurrent values traditionally associated with ruthenium dyes.[201, 214, 215] An alternate approach to the re-engineering of ruthenium sensitizers to be

compatible with transition metal-based redox shuttles is the use of surface insulation strategies that are irrespective of the sensitizer structure.[70, 75-78, 216-220] Strategies working irrespective of sensitizer structure are particularly attractive as they reduce synthetically difficult dye design demands and could allow for the use of existing, broadly absorbing dyes such as **B11** with transition metal-based redox shuttles such as $Co(bpy)_3^{3+/2+}$ (Figure 2).[221] Through kinetic improvements such as slowing recombination and back electron transfer rates, there is the potential to enhance the performance of a broadly absorbing **B11**/$Co(bpy)_3^{3+/2+}$ system to have wide applicability for many dye-sensitized applications.

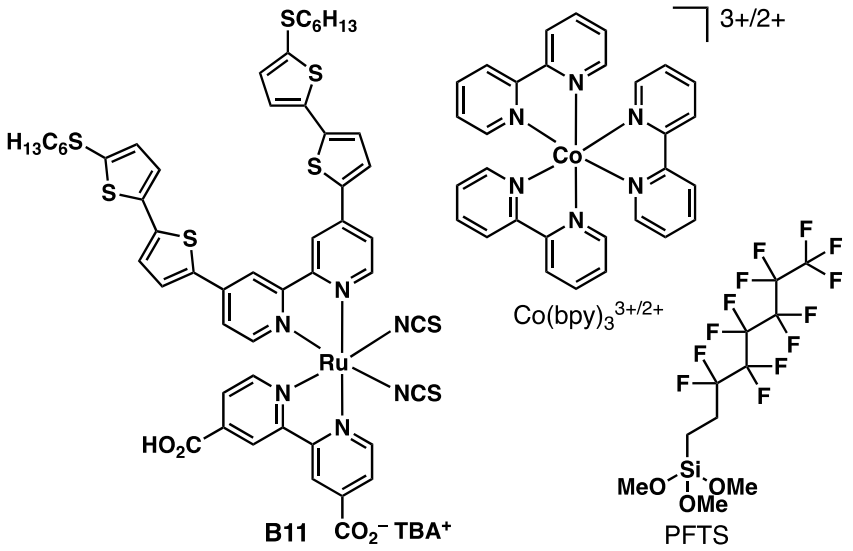

Figure 7.2. Structures of **B11** (where TBA is tetrabutylammonium), $[Co(bpy)_3][PF_6]_{3/2}$, and 1*H*,1*H*,2*H*,2*H*-perfluorooctyltrimethoxysilane (PFTS).

The use of insulating metal oxides such as MgO and Al_2O_3 between the dye and semiconductor to reduce recombination rates has been an active area of research within the DSC field.[70-79] More recently, fluorinated molecules with silyl anchors have been employed as

fluorinated self-assembled monolayers (F-SAM) that co-adsorb to the semiconductor in the presence of dyes to reduce recombination sites and lower surface tension (i.e. give a reduction in non-covalent bonding or electrolyte adhesion to the TiO_2 surface).[78, 222-225] This study seeks to compare these two approaches using a transition metal-based redox shuttle ($[Co(bpy)_3]^{3+/2+}$) used widely in high performing devices and a ruthenium sensitizer (**B11**) that is one of the highest PCE ruthenium dyes known using I_3^-/I^- (Figure 3).[221] Notably, with the MgO insulating approach, significant effects on the rates of the injection, back electron transfer reaction, and recombination reactions are expected since each of these electron transfers crosses the insulating barrier. With the F-SAM approach, only the recombination reactions would have to cross the insulating barrier while the remaining electron transfer reactions would not have to directly cross the insulating barrier. The majority of the prior studies on these two insulating approaches focus on monitoring recombination rates typically with ruthenium-based sensitizers and the iodide/triiodide redox shuttle through light modulated voltage techniques or electrochemical impedance spectroscopy (see Table S1 for a more detailed analysis of prior studies that were referenced above). A common observation in these studies is a reduction in charge recombination rates. The study of ruthenium-based sensitizers with cobalt redox shuttles to analyze regeneration rates and injection rates in the presence of insulator functionality at the TiO_2 surface is understudied and a focus of this work. Combining ruthenium photosensitizers with a cobalt redox shuttle and comparing F-SAM to MgO while studying electron transfer reactions via transient absorption spectroscopy (TAS) and time-correlated single photon counting (TCSPC) is a new approach to the best of our knowledge. Additionally, the back electron transfer reaction and

recombination reaction are also studied in this work to give a more complete picture of how these insulating approaches are effecting the four primary electron transfer reactions in the DSC device.

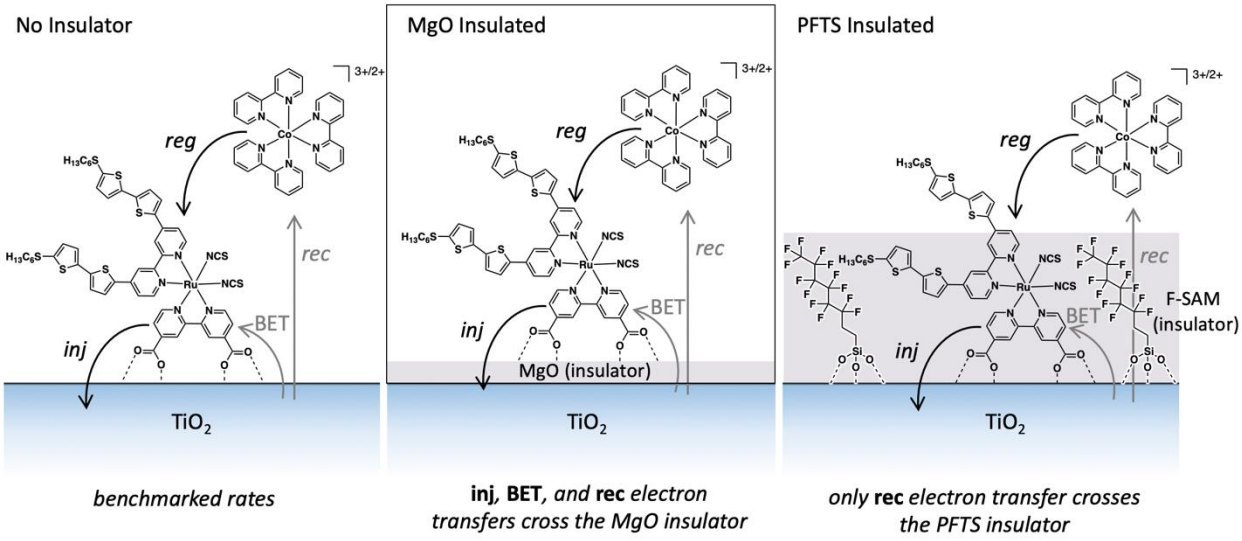

Figure 7.3. Added insulation strategies being probed in this work compared to the case of no added insulator. Arrows represent electron transfer reactions with black arrows representing productive electron transfer reactions and grey arrows representing non-desirable electron transfer reactions.

RESULTS AND DISCUSSION

DSC devices with **B11** as the dye and $Co(bpy)_3^{3+/2+}$ as the RS were fabricated by treating TiO_2-dye electrodes with varying concentrations of a F-SAM generating reagent, 1*H*,1*H*,2*H*,2*H*-perfluorooctyltrimethoxysilane (PFTS, Figures 2, 4 & 5, Table 1). In the absence of PFTS, the **B11**/$Co(bpy)_3^{3+/2+}$ RS DSC device gives a baseline PCE of 5.7% according to the equation PCE = (J_{SC} x V_{OC} x *FF*)/I_0, where J_{SC} is the short-circuit current density, V_{OC} is the open circuit voltage, *FF* is the fill factor, and I_0 is the incident photon intensity set to 1 sun for these studies (Table 1, entry 1; Figure 4). Upon submerging the TiO_2-**B11** sensitized electrode into a 0.0125 M PFTS

solution in hexanes for 90 minutes at 30 °C then assembling the DSC device, the PCE increased to 6.3% primarily due to an increase in V_{OC} from 717 mV to 752 mV (Table 1, entry 2; Figure 4). The increase in photovoltage is likely due to a reduction in the recombination of electrons at

Table 7.1. Effect of varying PFTS concentrations on **B11**/$[Co(bpy)_3]^{3+/2+}$ DSC device performance.

entry	PFTS	V_{OC} (mV)	J_{SC} (mA/cm^2)	FF	PCE (%)
1	None	717±12	11.7±0.8	0.66±0.05	5.7±0.2
2	0.0125 M	752±8	11.9±0.1	0.68±0.01	6.3±0.1
3	0.025 M	779±7	13.5±0.4	0.70±0.01	7.7±0.3
4	0.05 M	760±19	13.0±0.7	0.68±0.03	6.8±0.2
5	0.1 M	748±45	9.9±0.5	0.71±0.01	5.3±0.2
6	0.2 M	732±11	10.3±0.4	0.70±0.00	5.4±0.3

*Each entry is an average of at least 5 devices.

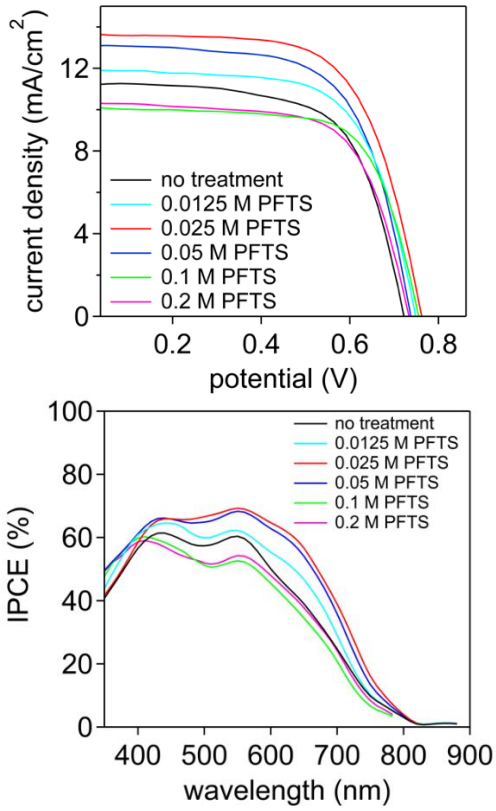

Figure 7.4. *J-V* curves (top) and IPCE curves (bottom) for varying PFTS concentrations on **B11**/$[Co(bpy)_3]^{3+/2+}$ DSC device performances.

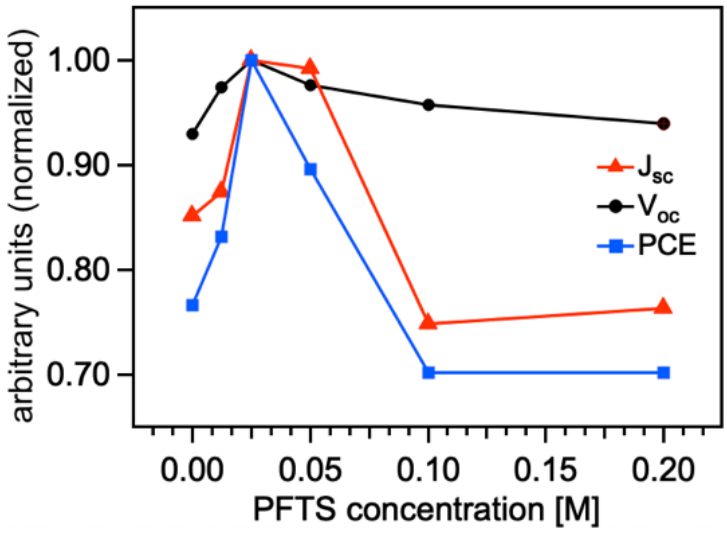

Figure 7.5. Changes in photovoltage, photocurrent, and PCE with respect to PFTS concentration. All values are normalized to the highest performing cell values.

the TiO_2 surface with $[Co(bpy)_3]^{3+}$ and is further discussed below. A modest increase in J_{SC} is also noted from 11.7 mA/cm^2 to 11.9 mA/cm^2. Increasing the PFTS solution concentration to 0.025 M further increased the V_{OC} to 779 mV and gave a significant increase in J_{SC} to 13.5 mA/cm^2 for a PCE of 7.7% (Table 1, entry 3). The observed PCE value corresponds to a 35% increase in PCE over the no-PFTS device. The increase in J_{SC} is apparent from the incident photon-to-current conversion efficiency (IPCE) measurement which shows an increased height throughout the spectrum with a higher peak IPCE value at 70% versus 60% for the no-PFTS device (Figure 4). The increase in J_{SC} may be due to the reduction of surface tension (defined above) allowing for a faster flowing electrolyte in addition to slowing recombination, slowing back electron transfer, or increasing injection efficiencies to improve improving charge collection efficiencies (see discussion below).[222] Increasing the PFTS solution concentration further gave lower V_{OC}, J_{SC}, and PCE values relative to the 0.025 M treatment (Table 1, entries 4-6; Figure 5). Surface absorption curves were taken with **B11** on TiO_2, **B11** on MgO treated TiO_2 (discussed below), and

B11 on PFTS treated TiO_2 to evaluate relative dye loadings (Figure S1). **B11** on TiO_2 or on MgO treated TiO_2 films show similar film absorbances with no appreciable change. However, upon PFTS treatment (0.025 M), a 40% reduction in film absorption is observed. Upon analyzing the PFTS treatment solution after the film is submerged, no significant absorption is found in the liquid layer corresponding to **B11** which suggests the dye is not desorbing from the surface (Figure S2). Increasing the concentration of PFTS correlates to decreasing film absorption (Figure S3), which could be due to a difference in dielectric environment around **B11** being induced by PFTS. Analogous device data was also obtained for an additional ruthenium-based sensitizer, **N719** (Figure S5-S7; Table S2). A similar trend for **N719** devices was observed which indicates this approach is likely general since two ruthenium-based sensitizers with significantly different structures demonstrated an increase in PCE values at low PFTS solution concentrations when compared to no-PFTS devices and devices prepared with higher PFTS solution concentrations (Figures S3-S4, Table S1). Additionally, F-SAM treatments with three different fluorinated materials varying the number of perfluorinated carbons were also analyzed in DSC devices with longer chain lengths favoring higher V_{OC} values (Table S3; Figures S20-S21). The highest photocurrent is observed at the intermediate chain length. These chain length dependent trends are discussed in regard to the kinetics of electron transfer reactions below; however, the PFTS treatment is consistently used for the remaining comparative studies.

Devices with no PFTS, 0.025 M PFTS, and 0.05 M PFTS were probed further to better understand the role of PFTS on electron lifetimes with small modulated photovoltage transient (SMPVT) measurements (Figure 6).[142, 190] The three concentrations were selected with no PFTS being the baseline measurement, 0.025 M PFTS being the peak PCE conditions, and 0.05

M PFTS showing a decline in device performance. SMPVT data correlates to the photovoltage trend observed via current density-voltage (*J-V*) curve measurements with electron lifetime in TiO_2 increasing as follows: no PFTS < 0.05 M PFTS < 0.025 M PFTS (Figure 6). This data suggests that recombination in the DSC device decreases initially as PFTS is added, and then begins to increase modestly as a larger amount of PFTS is added to the TiO_2 surface. The reason for the modest increase in recombination rates at higher PFTS loading is not apparent from the SMPVT measurements since increased amounts of PFTS would presumably serve to better block TiO_2 surface sites.

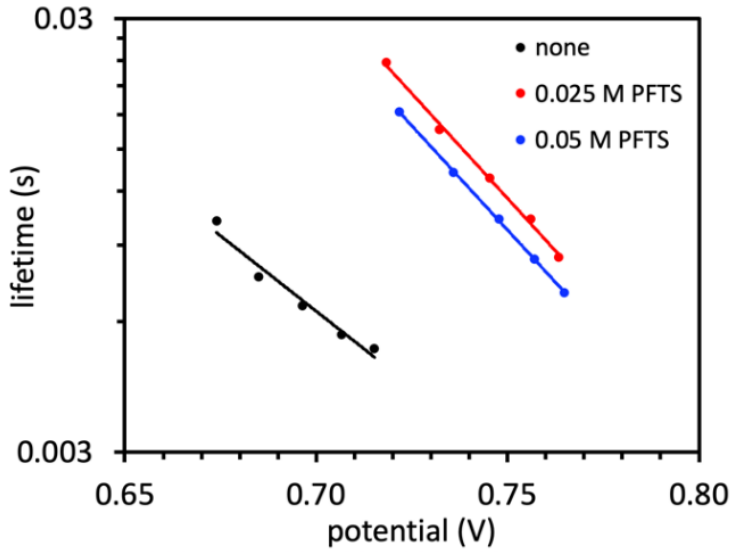

Figure 7.6. SMPVT measurement with **B11**/$[Co(bpy)_3]^{3+/2+}$ DSC devices varying concentration of PFTS.

MgO as an outer shell surface insulating approach to the TiO_2 nanoparticles was analyzed by applying an MgO layer from a solution of varying concentrations of $Mg(OMe)_2$ in methanol at room temperature for 30 minutes to non-stained TiO_2 films. These films were prepared as previously described in the literature.[70, 220] Films were rinsed with MeOH and heated to 500

^{o}C before staining the MgO insulated electrode surface with the sensitizer. This approach shows an increase in PCE for the lowest concentration applied (0.001 M $Mg(OMe)_2$) relative to the untreated surface (5.7% versus 6.9%, Table 2, Figures S8-S9). A smaller peak PCE performance is observed with the MgO treatment compared to the PFTS treatment approach (6.9% versus 7.7%). The increase in PCE when MgO is used compared to non-MgO treated films is due to an increase in both V_{OC} (717 mV versus 773 mV) and J_{SC} (11.7 mA/cm^2 versus 13.2 mA/cm^2) for the MgO treated surface due to a lowering of recombination rate which is supported by SMPVT measurements that demonstrate an increase in electron lifetimes when MgO is applied (Figure S10). Attempts to further lower the $Mg(OMe)_2$ concentration beyond 0.001 M led to aberrant results with low reproducibility. Addition of higher amounts of MgO led to lower performing devices due to a rapid loss in J_{SC} that was partially offset by the continually rising V_{OC} values (Table 2, entries 3-7). Notably, attempts to combine the two surface treatment approaches (MgO and PFTS) did not lead to a combined performance enhancement in the DSC devices compared to either of the individual treatments (Table 2, entries 8-11). The effects of MgO and PFTS on electron transfer kinetics (electron injection, back electron transfer, and regeneration) was further probed with time correlated single photon counting (TCSPC) and transient absorption spectroscopy (TAS) below.

Table 7.2. Effect of varying $Mg(OMe)_2$ concentrations on **B11**/$[Co(bpy)_3]^{3+/2+}$ device performances.

Entry	$Mg(OMe)_2$ (conc.)	PFTS	VOC (mV)	J_{SC} (mA/cm^2)	FF	PCE (%)
1	none	none	717	11.7	0.66	5.7
2	0.001 M	none	773	13.2	0.68	6.9

3	0.005 M	none	764	12.2	0.61	5.7
4	0.01 M	none	809	8.3	0.71	4.9
5	0.05 M	none	841	7.2	0.74	4.6
6	0.1 M	none	859	7.9	0.76	5.2
7	0.15 M	none	836	6.8	0.75	4.3
8	0.001 M	0.0125 M	758	10.9	0.63	5.3
9	0.001 M	0.025 M	764	11.6	0.71	6.5
10	0.001 M	0.05 M	809	11.6	0.70	6.6
11	0.001 M	0.1 M	782	13.5	0.49	5.3

*Each entry is an average of at least 2 devices with a PCE standard deviation of ≤ ±0.3.

The excited state dynamics of **B11** were probed using steady-state and time-resolved emission spectroscopy (Figure 7 & Table 3). Time-resolved emission experiments were performed in order to evaluate the kinetics of electron injection based on different surface treatments (see the experimental section for spectroscopy equipment details). Excited state lifetimes were measured for **B11** anchored on an insulating zirconium oxide (ZrO_2) film, a TiO_2 film, a TiO_2 film with a MgO surface treatment prepared from a 0.001 M $Mg(OMe)_2$ solution, and a TiO_2 film with a PFTS surface treatment prepared from a 0.025 M PFTS solution. All films were submerged in a 0.1 M LiTFSI solution in MeCN. Electron injection efficiencies (η_{eff}) were determined according to equation 1 where τ_{TiO_2} represents the approximate excited state lifetime on TiO_2 and τ_{ZrO_2} represents the approximate excited state lifetime on ZrO_2.

$$\eta_{eff} = \left[1 - \frac{\tau_{TiO2}}{\tau_{ZrO_2}}\right] \times 100 \qquad \text{(equation 1)}$$

The excited state lifetime measured for **B11** sensitized on ZrO_2 was used as a reference measurement since ZrO_2 is an insulator that prevents electron injection and allows for the monitoring of dye excited state kinetics at a solid surface.[226, 227] The emission lifetime of **B11**

on ZrO_2 was estimated to be 12.5 ns, which is consistent with previously reported studies of the decay dynamics of Ru triplet excited states using ZrO_2 as a reference material under similar environmental conditions (Table 3; Figure 7).[226, 227] In contrast, the excited state lifetime on TiO_2 is predicted to be significantly shorter due to emission quenching upon injection of an electron from the photoexcited dye to the TiO_2 conduction band (CB). For the TiO_2 electrode without a surface treatment, the emission lifetime of **B11** was found to be 4.2 ns which corresponds to a η_{eff} of 66%. This is notably shorter than the lifetime measured on ZrO_2 and is assigned to quenching of the **B11** triplet excited state by electron injection. Steady-state emission measurements on the TiO_2-**B11** film show a quenching of the emission intensity relative to ZrO_2-**B11** films as expected (Figure 7). With the addition of an MgO surface insulating treatment between TiO_2 and **B11**, the excited state lifetime was observed to increase to 5.2 ns, which decreased η_{eff} from 66% to 58% when TiO_2 films and MgO treated TiO_2 films were compared (Table 3). This suggests that the presence of a thin insulating layer between TiO_2 and the dye results in a decrease injection quantum yields from the photoexcited dye. Interestingly, when PFTS was used as a surface treatment, the emission lifetime of **B11** on TiO_2 *decreased* to 1.8 ns, which improved η_{eff} from 66% to 86%. This result suggests that the PFTS surface treatment not only acts as an insulating layer, but may also introduce a method for improving charge transfer efficiency from photoexcited dyes to TiO_2. Upon analyzing F-SAM materials with varied number perfluorinated carbons, an injection efficiency trend is observed with $4 < 6 < 8$ perfluorinated carbons on the F-SAM reagent giving devices ranging from 85% to 87% injection efficiency (Figures S32-S33; Table S6). Notably, combining the MgO and PFTS treatments lead to injection efficiencies between MgO only and PFTS only treated films (Figures S32-S33; Table S6).

Table 7.3. Excited-state emission measurements for insulating ZrO_2 and semiconducting TiO_2 films sensitized with dye **B11**.

Sample	τ (ns)	η_{eff} (%)
B11 on ZrO_2	12.5	---
B11 on TiO_2	4.2	66
B11 on TiO_2 w/ MgO	5.2	58
B11 on TiO_2 w/ F-SAM	1.8	86
B11 on TiO_2 w/ MgO & F-SAM	2.5	80

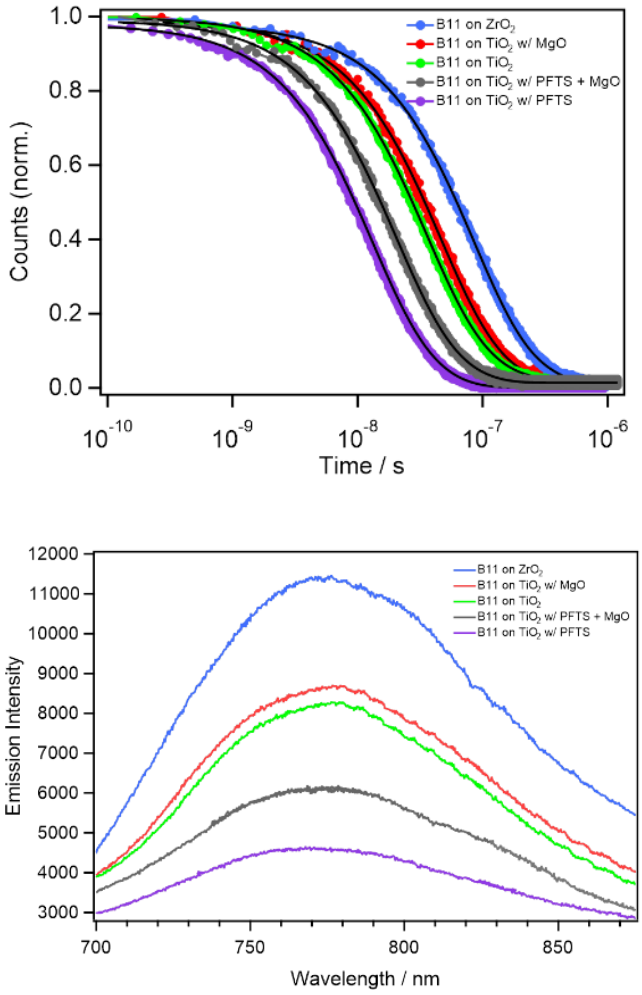

Figure 7.7. A) Time-resolved emission decays of **B11** on ZrO_2 (blue), TiO_2 with no surface treatment (green), TiO_2 with an MgO surface treatment (red), and TiO_2 with a PFTS surface treatment (purple). The acquisition time for each sample was 300 seconds with excitation at 485 nm. B) Steady-state emission spectra of **B11** on insulating ZrO_2 and semiconducting TiO_2 collected at room temperature.

Next, transient absorption spectroscopy was used to probe the rate of back electron transfer to the dye and the rate of regeneration of the ground state dye from $[Co(bpy)_3]^{2+}$ after photoinduced interfacial charge separation. Following photoexcitation of **B11**, electrons are injected into the CB of TiO_2, which produces an oxidized **B11** dye and reduced TiO_2. When measuring device kinetics on a microsecond timescale, electron injection is assumed to be completed and therefore the main signal observed can be attributed to the oxidized dye. Figure 8 shows the transient absorption spectrum of a TiO_2-**B11** sensitized film, which consists of a negative absorption band that corresponds to the ground state bleach (GSB) region and a positive, lower energy, absorption band that corresponds to the absorption spectrum of oxidized **B11**. Time-resolved absorption measurements were monitored in the oxidized **B11** absorption region to analyze the effects of the two surface treatments on regeneration and back electron transfer reactions. The transient absorption kinetics were monitored at a constant wavelength (750 nm) near the maxima of the oxidized **B11** absorption signal despite some modest drift in the observed absolute maxima value on the broad oxidized **B11** absorption signal.

Transient decays were nonexponential in nature and well-described by a Kohlrausch−Williams−Watts (KWW) [138-140, 171, 172, 226-228] stretched exponential function according to equation 2,

$$\Delta OD(t) = \Delta OD_{t=0} e^{-\left(\frac{t}{\tau_{KWW}}\right)^{\beta}} \qquad \text{(equation 2)}$$

where $\Delta OD_{t=0}$ is equal to the signal magnitude at time zero and β is the stretching parameter, which is inversely related to the width of the underlying Lévy distribution of rate constants and ranges in value from 0 to 1. Correlation between the calculated lifetime constant and the stretching parameter can lead to significantly different distributions of the underlying rate constants that fit the kinetics objectively well.[229] To ensure the most appropriate fits, time constants and β values chosen to normalize the transient absorption kinetics were sampled from a range of values and assigned on the basis of best fit and minimal error. The average lifetime can be calculated from these fitting parameters by using a gamma function distribution of β^{-1} (equations 3 and 4),

$$\Gamma(x) = \int_0^{\infty} u^{(x-1)} e^{-x}\, du \qquad \text{(equation 3)}$$

$$\tau_{obs} = \frac{\tau}{\beta}\Gamma\left(\frac{1}{\beta}\right) \qquad \text{(equation 4)}$$

where Γ denotes the gamma function distribution and *u* is the integrand $\beta^{\alpha} \times \Gamma(x)^{-1}$. The parameter α is known as the shape parameter and it defines the shape of the distribution and β is the inverse scale (or stretch) parameter that defines the width of the distribution. This mean lifetime can then be used to calculate the observed rate values obtained in the absence, k_{BE}, and presence, k_{reg}, of a redox active species (equation 5). The regeneration efficiency is then calculated using equation 6.

$$k_{obs,i} = \frac{1}{\tau_{obs,i}} \qquad \text{(equation 5)}$$

$$\varphi_{reg} = \frac{k_{reg}}{k_{reg}+k_{BE}} \times 100 \qquad \text{(equation 6)}$$

We stress that assigning absolute regeneration efficiencies is challenging with several approaches noted in the literature in addition to the commonly used approach above.[177-179, 230] We note that this comparison likely over estimates the absolute regeneration efficiency as has been noted in the literature, but this method does allow for a simple comparison of regeneration efficiencies within this study.[179]

If the dye-sensitized device contains an electrolyte void of a redox-active species, the oxidized **B11** will undergo back electron transfer from the reduced TiO_2. The rate of this back electron transfer reaction, k_{BE}, can be determined from the time-resolved absorption profile of a sample without a RS present. If a RS is present in the electrolyte, the neutral **B11** ground state dye can be formed by either back electron transfer with reduced TiO_2 or by the regeneration reaction with the RS. In this case, the term "neutral" is the initial dye prior to photoinduced electron transfer not the absolute charge state of the complex. Efficient dye regeneration (φ_{reg}) requires that the rate of the reduction of the oxidized dye by the RS (k_{reg}) be sufficiently fast to effectively compete with the back electron transfer reaction rate (k_{BE}). When regeneration is efficient, the absorption-time profile is dominated by the regeneration reaction and the corresponding rate constant, k_{reg}, is representative of the rate of neutral dye regeneration by the RS.[23]

In all cases examined, the rate of the dye cation decay is observably faster for devices containing the $[Co(bpy)_3]^{3+/2+}$ redox shuttle than for the redox shuttle free devices, which suggests that the rate of dye regeneration is sufficiently competitive with the rate of the back electron transfer reaction irrespective of surface treatment (Figure 8, Table 4). Without a surface treatment,

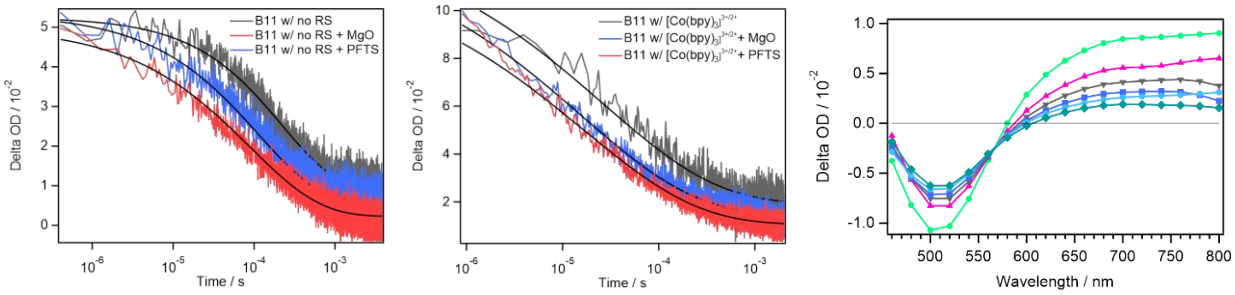

Figure 7.8. Transient absorption kinetics in logarithmic scale monitoring the rate of: (left) the back electron transfer reaction and (middle) the regeneration reaction for: a TiO_2-**B11** sensitized films, a TiO_2-**B11** sensitized film with an MgO surface treatment, and a TiO_2-**B11** sensitized film with a PFTS surface treatment. (Right) Transient absorption difference spectra for a TiO_2-**B11** sensitized film with a PFTS surface treatment. Decays are x-axis scaled to emphasize kinetic comparisons.

Table 7.4. Summary of kinetic data obtained for **B11** devices.[a]

Sample	τ_{KWW} (µs)	β	Γ	τ_{obs} (µs)	κ_{obs} (s^{-1})	Φ (%)
B11	70.2	0.50	1.0	150	6.70×10^3	
B11/$[Co(bpy)_3]^{3+/2+}$	13.6	0.35	1.3	68.0	1.50×10^4	70
B11/MgO	90.2	0.50	1.0	180	5.30×10^3	
B11/MgO/$[Co(bpy)_3]^{3+/2+}$	0.55	0.32	2.3	4.0	2.50×10^5	98
B11/PFTS	98.0	0.50	1.0	200	5.00×10^3	
B11/PFTS/$[Co(bpy)_3]^{3+/2+}$	0.58	0.32	2.3	4.2	2.40×10^5	98

[a]Back electron transfer kinetics were measured with an electrolyte containing 0.1 M LiTFSI and 0.5 M 4-*tert*-butylpyridine (TBP) in MeCN. Regeneration kinetics were measured with an electrolyte containing 0.25 M Co^{2+}, 0.05 M Co^{3+}, 0.1 M LiTFSI and 0.5 M TBP in MeCN. All TAS measurements were taken under open-circuit conditions, with the pump power = <2.0 mJ/pulse and the probe wavelength set to 750 nm.

the rate of oxidized dye consumption is an order of magnitude faster in the presence of $[Co(bpy)_3]^{3+/2+}$ at 1.50×10^4 s^{-1} versus 6.70×10^3 s^{-1} in the absence of the redox shuttle. This leads to a dye regeneration efficiency of 70% according to equation 6. Comparatively, the use of an insulating MgO surface treatment leads to a dye cation consumption rate of 5.30×10^3 s^{-1} with no RS present, which modestly slower than the interfacial charge separated lifetime in the absence of

MgO. The electron transfer reaction from $[Co(bpy)_3]^{3+/2+}$ is surprisingly faster in the presence of an MgO treatment when compared to the no treatment system (2.50×10^5 s^{-1} versus 1.50×10^4 s^{-1}). Thus, the faster regeneration reaction rate in the presence of an MgO surface treatment leads to a significant increase in the overall regeneration efficiency (98%). Concerning electron transfer reactions across the TiO_2|MgO|**B11** interfaces, MgO primarily affects the rate of the regeneration reaction (beneficially) and electron injection reaction (detrimentally). A similar, yet more dramatic effect was observed when a PFTS surface treatment was applied. Addition of PFTS led to a back electron transfer reaction rate of 5.00×10^3 s^{-1}, which is slower than that observed for untreated TiO_2 devices or MgO-treated devices. Additionally, F-SAM materials with a lower number of perfluorinated carbons led to slower back electron transfer rates (Figures S28-S29, S31; Table S5). The PFTS findings coupled with emission lifetime studies show a dramatic increase in both the rate and duration of charge separation at TiO_2-dye interfaces as is desired for many dye-sensitized applications with a co-adsorbent adjacent to the dye rather than between the dye and the metal oxide. Notably, addition of a PFTS surface treatment also increases the rate of the electron transfer reaction from $[Co(bpy)_3]^{3+/2+}$ to the oxidized dye relative to untreated TiO_2 films, and the overall regeneration efficiency is improved to 98% versus 70% for untreated TiO_2. The reason for the increase in rate of electron transfer from $[Co(bpy)_3]^{2+}$ to the oxidized dye when F-SAM is used is not directly obvious, but may have to do the installation of a fluorous phase at the TiO_2-dye surface that allows for faster electrolyte diffusion across the TiO_2-dye surface due to a reduction in attractive non-covalent interactions. An increased diffusion rate would allow for an increased rate of collision between the dye cation and the reducing redox shuttle for an overall faster regeneration. Importantly, the directional charge transfer control imparted by PFTS (faster injection, faster

regeneration, slower back electron transfer, and slower recombination) is important for achieving efficient and prolonged charge separation durations. Notably, combining PFTS with MgO did not significantly improve the electron transfer reactions further when compared to PFTS treated devices (Figure S30; Table S5).

Based on the first principles model shown in Figure 3, the rate of recombination was expected to be perturbed for both surface treatment approaches as is observed in Figure 9. The lifetime of electrons in TiO_2 was found to go up for both MgO and PFTS, with PFTS showing a modestly longer electron lifetime (slowed recombination) based on SMPVT measurements at open circuit potentials. No significant effect on regeneration was predicted based on the first principles model; however, much faster regeneration is observed via TAS when MgO or PFTS is used. Only MgO is predicted to have a

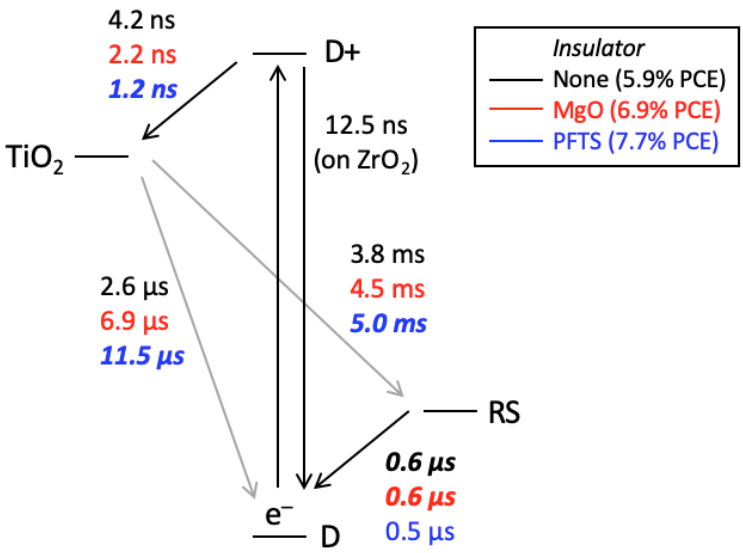

Figure 7.9. A diagram of electron lifetimes for each electron transfer reaction with and without an added insulator (no insulator = black; MgO = red; PFTS = blue). The most desirable value is in bold and italics for each electron transfer reaction. The PCE obtained with each condition is shown in the legend.

significant effect on electron injection rates and back electron transfer reaction rates based on the first principles model. Surprisingly, both electron injection and back electron transfer reaction rates were affected to a larger degree by the PFTS insulator than MgO. The lifetime of electrons in the dye excited state were shortened by more than 2x (indicative of faster electron injection via TCSPC studies) with PFTS when compared with MgO. Similarly, the lifetime of electrons in TiO_2 in the presence of the oxidized dye as the only oxidizing species shows a longer electron lifetime for the PFTS-treated electrode than MgO (slower back electron transfer reaction rate for PFTS systems). Combined, this shows that as expected PFTS slows the detrimental recombination reaction, while unexpectedly increasing the rate of the desirable electron injection reaction, unexpectedly increasing the rate of the regeneration reaction, and slowing the rate of the detrimental back electron transfer reaction. Thus, desirable electron transfer reaction events are favored herein with faster photoinduced charge separation and prolonged charge separation. This one-way valved or gated electron flow behavior induced by PFTS is highly desirable, and has led to a 35% increase in PCE (5.7% without PFTS, 7.7% with PFTS) with the **B11**/$[Co(bpy)_3]^{3+/2+}$ DSC devices studied here with all other components being held constant.

A plausible model which explains the unexpected behavior observed in PFTS treated systems with regard to electron injection and the back electron transfer reaction is shown in Figure 10. The Mulliken charges (Figures S34 and S35) and molecular electrostatic potential (MEP) maps

(Figures 10 and S36) of PFTS and the hydroxyl terminated analogue 1*H*,1*H*,*2*H,*2*H-perfluorooctylsilanetriol were computationally analyzed via density functional theory at the B3LYP/6-311G (*d*,*p*) level of theory.[231-233] The hydroxyl terminated analogue is shown in Figure 10 since the OMe groups are anticipated to have hydrolyzed upon surface binding. The MEP surface map shows a region of negative electrostatic charge extending from the surface due to the fluorine atoms (red colored surface region, Figure 10). A region of positive electrostatic charge is observed near the silicon atom due to the hydrogen atoms at the two methylene groups attached to the silicon. This generates a layer of partial negative charge away from the TiO_2 surface and a region of partial positive charge near the TiO_2 surface. Upon photoexcitation of the dye, electron density is moved towards TiO_2 during the metal-to-ligand charge transfer (MCLT) event. This negative charge on the dye near the surface can be stabilized by the partial positive charge of the PFTS treated surface near the TiO_2. The remaining dye cation is located further away from the surface in the partial negative region of the PFTS treated surface, serving to further stabilize the oxidized chromophore (Figure 10B). Upon electron injection, the negative charge is moved from the dye to TiO_2 which is stabilized by the partial positive charge from the PFTS treated surface (Figure 10C). This presumably leads to more favorable charge injection and a more favorable sustained charge separation duration due to electrostatic effects which results in surface treatment induced rectification (Figure 10D). Electrostatic attraction of the negative charge from the fluorine atoms with the positively charged RS may also aid in an increased rate of ground state dye regeneration by increasing the effective concentration of RS near the film.

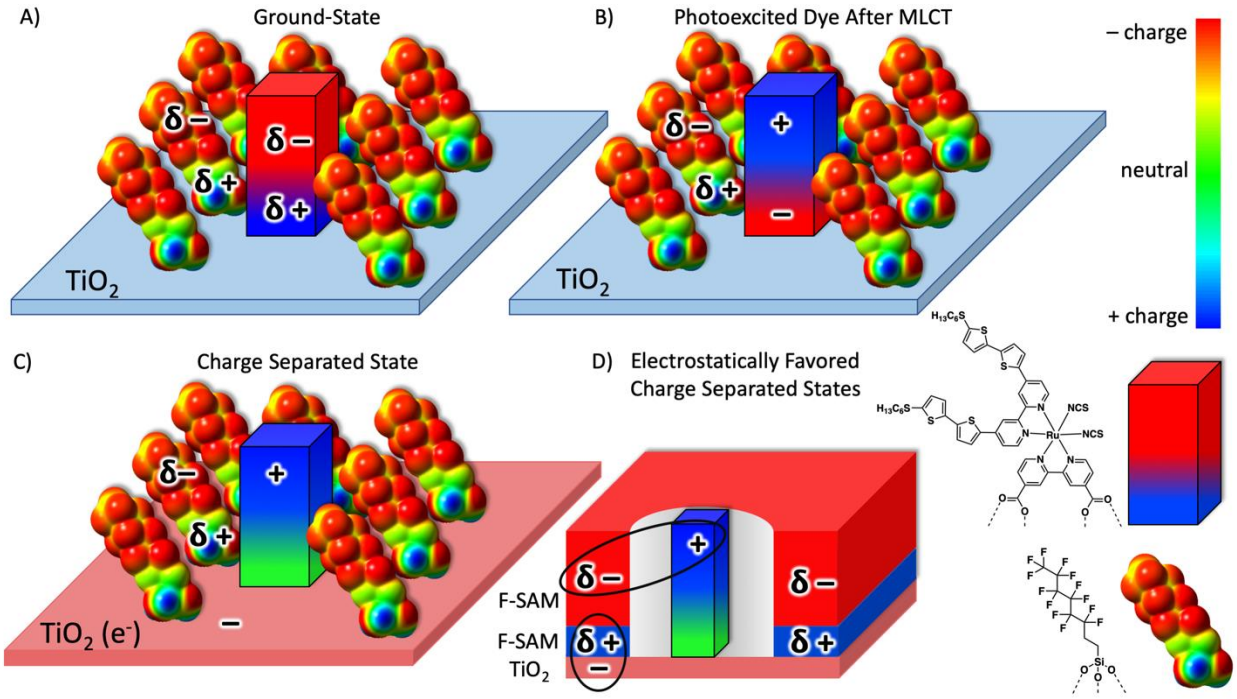

Figure 7.10. Molecular electrostatic potential maps of hydroxyl terminated PFTS molecules surrounding **B11** on a TiO_2 surface. A) The ground state partial charge configuration, B) the photoexcited MLCT state with electrostatically attracted partial charges on PFTS to the **B11** molecule, C) the interfacial charge separated state with an electron injected into TiO_2 and **B11** cation electrostatically attracted to a PFTS molecule, and D) a general charge layer cartoon with PFTS (red and blue) surrounding a **B11** cationic dye (blue and green). Note the small blue region at the bottom of the perfluorinated molecules in the MEP surface map is representative of a hydrogen that may not be present upon surface binding.

CONCLUSIONS

Two surface modification strategies, PFTS and MgO, were evaluated within DSC devices based on **B11** and $[Co(bpy)_3]^{3+/2+}$. Initial studies show an improved device efficiency from 5.7% to 7.7% with the addition of a PFTS surface treatment, which suggests desired electron transfer reaction pathways are improved with this F-SAM treatment. A similar, yet lesser effect is observed when MgO is used as a surface treatment. Additionally, SMPVT measurements reveal longer

electron lifetimes when a PFTS surface treatment is applied, which indicates a slower rate of electron recombination between electrons in the TiO_2 conduction band with acceptors in the electrolyte. Emission lifetime studies on **B11**-sensitized films show reduced charge injection efficiency with an MgO treatment as expected from an insulating layer between the dye and TiO_2. Interestingly, the introduction of a PFTS surface treatment results in a *>2x increase* in the rate of charge injection. Nanosecond transient absorption studies show that the addition of an MgO or PFTS surface treatment results in a slower back electron transfer reaction from TiO_2 to the dye cation in comparison to devices without surface modification. Importantly, this study shows that electron transfer reaction rates can be preferentially accelerated in the desired forward direction (electron injection and regeneration) and preferentially slowed in the undesirable directions (back electron transfer and recombination) with the use of a co-adsorbent insulating surface protection strategy which does not space the dye from the semiconductor. Intriguingly, a more efficient electron transfer reaction between the dye cation and an electron transfer reaction reagent ($[Co(bpy)_3]^{3+/2+}$) in the electrolyte is observed to occur at the TiO_2 surface. This one-way electron transfer inducing approach also has broad application in areas such as dye-sensitized photoelectrochemical cells and dye-sensitized photodetectors. Future studies are aimed at evaluating the effect of alternative co-adsorbents to further enhance these desirable effects.

BIBLIOGRAPHY

[1] S. Fukuzumi, K. Ohkubo, T. Suenobu, Accounts of Chemical Research, 47 (2014) 1455-1464.
[2] J. Gong, J. Liang, K. Sumathy, Renewable and Sustainable Energy Reviews, 16 (2012) 5848-5860.
[3] A. Hagfeldt, G. Boschloo, L. Sun, L. Kloo, H. Pettersson, Chemical Reviews, 110 (2010) 6595-6663.
[4] D.Y. Chen, Y.Y. Hsu, H.C. Hsu, B.S. Chen, Y.T. Lee, H. Fu, M.W. Chung, S.H. Liu, H.C. Chen, Y. Chi, P.T. Chou, Chem. Commun., 46 (2010) 5256-5258.
[5] J. Zimmermann, A. Zeug, B. Röder, Physical Chemistry Chemical Physics, 5 (2003) 2964-2969.
[6] J.C. del Valle, J. Catalán, Physical Chemistry Chemical Physics, 21 (2019) 10061-10069.
[7] G.-N. Porter, R.G.W. Norrish, Proceedings of the Royal Society of London. Series A. Mathematical and Physical Sciences, 200 (1950) 284-300.
[8] G. Porter, Science, 160 (1968) 1299-1307.
[9] B.A. Thrush, Photochemical & Photobiological Sciences, 2 (2003) 453-454.
[10] A. Marsh, With this Ruby Laser, George Porter Sped up Photochemistry, in: IEEE Spectrum, 2022.
[11] The Nobel Prize in Chemistry 1999, in, NobelPrize.org, 1999.
[12] P.J. Megía, A.J. Vizcaíno, J.A. Calles, A. Carrero, Energy & Fuels, 35 (2021) 16403-16415.
[13] B.E. Logan, R. Rossi, G. Baek, L. Shi, J. O'Connor, W. Peng, ACS Energy Letters, 5 (2020) 3514-3517.
[14] O.B. Awodumi, A.O. Adewuyi, Energy Strategy Reviews, 27 (2020) 100434.
[15] M. Gul, Y. Kotak, T. Muneer, Energy Exploration & Exploitation, 34 (2016) 485-526.
[16] P. Rappaport, Solar Energy, 3 (1959) 8-18.
[17] M.A. Green, Progress in Photovoltaics: Research and Applications, 13 (2005) 447-455.
[18] M. Grätzel, Journal of Photochemistry and Photobiology C: Photochemistry Reviews, 4 (2003) 145-153.
[19] B.E. Hardin, H.J. Snaith, M.D. McGehee, Nature Photonics, 6 (2012) 162-169.
[20] K. Hu, R.N. Sampaio, J. Schneider, L. Troian-Gautier, G.J. Meyer, Journal of the American Chemical Society, 142 (2020) 16099-16116.
[21] M. Kokkonen, P. Talebi, J. Zhou, S. Asgari, S.A. Soomro, F. Elsehrawy, J. Halme, S. Ahmad, A. Hagfeldt, S.G. Hashmi, Journal of Materials Chemistry A, 9 (2021) 10527-10545.
[22] K. Sharma, V. Sharma, S.S. Sharma, Nanoscale Research Letters, 13 (2018) 381.
[23] A. Listorti, B. O'Regan, J.R. Durrant, Chemistry of Materials, 23 (2011) 3381-3399.
[24] B.C. O'Regan, J.R. Durrant, Accounts of Chemical Research, 42 (2009) 1799-1808.
[25] C.I. Oprea, A. Ndiaye, A. Trandafir, F. Cimpoesu, M.A. Gîrţu, Electron Transfer and Dye Regeneration in Dye-Sensitized Solar Cells, in: 2018 International Semiconductor Conference (CAS), 2018, pp. 273-276.
[26] D.F. Watson, G.J. Meyer, Annual Review of Physical Chemistry, 56 (2005) 119-156.
[27] Y. Cao, Y. Saygili, A. Ummadisingu, J. Teuscher, J. Luo, N. Pellet, F. Giordano, S.M. Zakeeruddin, J.E. Moser, M. Freitag, A. Hagfeldt, M. Grätzel, Nature Communications, 8 (2017) 15390.
[28] U.B. Cappel, S.M. Feldt, J. Schöneboom, A. Hagfeldt, G. Boschloo, Journal of the American Chemical Society, 132 (2010) 9096-9101.
[29] N. Fuke, R. Katoh, A. Islam, M. Kasuya, A. Furube, A. Fukui, Y. Chiba, R. Komiya, R. Yamanaka, L. Han, H. Harima, Energy & Environmental Science, 2 (2009) 1205-1209.

[30] J. Li, X. Yang, Z. Yu, G.G. Gurzadyan, M. Cheng, F. Zhang, J. Cong, W. Wang, H. Wang, X. Li, L. Kloo, M. Wang, L. Sun, RSC Advances, 7 (2017) 4611-4615.
[31] C. Martín, M. Ziółek, A. Douhal, Journal of Photochemistry and Photobiology C: Photochemistry Reviews, 26 (2016) 1-30.
[32] V. Saavedra Becerril, E. Sundin, M. Mapar, M. Abrahamsson, Physical Chemistry Chemical Physics, 19 (2017) 22684-22690.
[33] Y. Saygili, M. Söderberg, N. Pellet, F. Giordano, Y. Cao, A.B. Muñoz-García, S.M. Zakeeruddin, N. Vlachopoulos, M. Pavone, G. Boschloo, L. Kavan, J.-E. Moser, M. Grätzel, A. Hagfeldt, M. Freitag, Journal of the American Chemical Society, 138 (2016) 15087-15096.
[34] J.-H. Yum, E. Baranoff, F. Kessler, T. Moehl, S. Ahmad, T. Bessho, A. Marchioro, E. Ghadiri, J.-E. Moser, C. Yi, M.K. Nazeeruddin, M. Grätzel, Nature Communications, 3 (2012) 631.
[35] R.E. Bangle, G.J. Meyer, The Journal of Physical Chemistry C, 123 (2019) 25967-25976.
[36] T.J. Barr, G.J. Meyer, ACS Energy Letters, 2 (2017) 2335-2340.
[37] B.N. DiMarco, L. Troian-Gautier, R.N. Sampaio, G.J. Meyer, Chemical Science, 9 (2018) 940-949.
[38] K. Hu, A.D. Blair, E.J. Piechota, P.A. Schauer, R.N. Sampaio, F.G.L. Parlane, G.J. Meyer, C.P. Berlinguette, Nature Chemistry, 8 (2016) 853-859.
[39] M.J. Katz, M.J. DeVries Vermeer, O.K. Farha, M.J. Pellin, J.T. Hupp, The Journal of Physical Chemistry B, 119 (2015) 7162-7169.
[40] P.R. Nitha, V. Jayadev, S.C. Pradhan, V.V. Divya, C.H. Suresh, J. John, S. Soman, A. Ajayaghosh, Chemistry – An Asian Journal, 15 (2020) 3503-3512.
[41] L. Troian-Gautier, R.N. Sampaio, E.J. Piechota, M.D. Brady, G.J. Meyer, The Journal of Chemical Physics, 150 (2019) 041719.
[42] J. Villanueva-Cab, H. Wang, G. Oskam, L.M. Peter, The Journal of Physical Chemistry Letters, 1 (2010) 748-751.
[43] N. Yao, J. Huang, K. Fu, X. Deng, M. Ding, S. Zhang, X. Xu, L. Li, Sci Rep, 6 (2016) 31123.
[44] J. Wu, Z. Lan, J. Lin, M. Huang, Y. Huang, L. Fan, G. Luo, Chemical Reviews, 115 (2015) 2136-2173.
[45] G.J. Meyer, ACS Nano, 4 (2010) 4337-4343.
[46] R. Kohlrausch, Annalen der Physik, 167 (1854) 56-82.
[47] G. Williams, Polymer, 35 (1994) 1915-1922.
[48] G. Williams, D.C. Watts, S.B. Dev, A.M. North, Transactions of the Faraday Society, 67 (1971) 1323-1335.
[49] D. Apitz, P. Johansen, Journal of Applied Physics, 97 (2005) 063507-063507.
[50] T.J. Miao, J. Tang, The Journal of Chemical Physics, 152 (2020) 194201.
[51] J. Nelson, Physical Review B, 59 (1999) 15374-15380.
[52] J. Nelson, R.E. Chandler, Coordination Chemistry Reviews, 248 (2004) 1181-1194.
[53] J. Nelson, S.A. Haque, D.R. Klug, J.R. Durrant, Physical Review B, 63 (2001) 205321.
[54] M. Pazoki, A. Hagfeldt, G. Boschloo, Electrochimica Acta, 179 (2015) 174-178.
[55] M. Ansari-Rad, The Journal of Physical Chemistry C, 120 (2016) 9000-9006.
[56] K.C.D. Robson, K. Hu, G.J. Meyer, C.P. Berlinguette, Journal of the American Chemical Society, 135 (2013) 1961-1971.
[57] T. Daeneke, A.J. Mozer, Y. Uemura, S. Makuta, M. Fekete, Y. Tachibana, N. Koumura, U. Bach, L. Spiccia, Journal of the American Chemical Society, 134 (2012) 16925-16928.
[58] J.G. Rowley, B.H. Farnum, S. Ardo, G.J. Meyer, The Journal of Physical Chemistry Letters, 1 (2010) 3132-3140.
[59] F. Li, J.R. Jennings, Q. Wang, ACS Nano, 7 (2013) 8233-8242.

[60] S.J.C. Simon, F.G.L. Parlane, W.B. Swords, C.W. Kellett, C. Du, B. Lam, R.K. Dean, K. Hu, G.J. Meyer, C.P. Berlinguette, Journal of the American Chemical Society, 138 (2016) 10406-10409.
[61] R.J. Gillespie, E.A. Robinson, Journal of Computational Chemistry, 28 (2007) 87-97.
[62] P.C. Stair, Journal of the American Chemical Society, 104 (1982) 4044-4052.
[63] G. Cavallo, P. Metrangolo, R. Milani, T. Pilati, A. Priimagi, G. Resnati, G. Terraneo, Chemical Reviews, 116 (2016) 2478-2601.
[64] L.C. Gilday, S.W. Robinson, T.A. Barendt, M.J. Langton, B.R. Mullaney, P.D. Beer, Chemical Reviews, 115 (2015) 7118-7195.
[65] J.Y.C. Lim, P.D. Beer, Chem, 4 (2018) 731-783.
[66] F.J. Malzner, S.Y. Brauchli, E.C. Constable, C.E. Housecroft, M. Neuburger, RSC Advances, 4 (2014) 48712-48723.
[67] V. Saxena, D.K. Aswal, Semiconductor Science and Technology, 30 (2015) 064005.
[68] Q. Sun, Y. Li, J. Dou, M. Wei, Science China Materials, 59 (2016) 867-883.
[69] A. Jain, P. Veerender, V. Saxena, A. Gusain, P. Jha, S.P. Koiry, A.K. Chauhan, D.K. Aswal, S.K. Gupta, AIP Conference Proceedings, 1512 (2013) 774-775.
[70] T. Taguchi, X.-t. Zhang, I. Sutanto, K.-i. Tokuhiro, T.N. Rao, H. Watanabe, T. Nakamori, M. Uragami, A. Fujishima, Chem. Commun., (2003) 2480-2481.
[71] E. Palomares, J.N. Clifford, S.A. Haque, T. Lutz, J.R. Durrant, J. Am. Chem. Soc., 125 (2003) 475-482.
[72] H. Alarcón, M. Hedlund, E.M.J. Johansson, H. Rensmo, A. Hagfeldt, G. Boschloo, J. Phys. Chem. C, 111 (2007) 13267-13274.
[73] J.-Y. Kim, S.H. Kang, H.S. Kim, Y.-E. Sung, Langmuir, 26 (2010) 2864-2870.
[74] H. Ozawa, Y. Okuyama, H. Arakawa, Dalton Transactions, 41 (2012) 5137-5139.
[75] M. Asemi, M. Ghanaatshoar, Applied Physics A, 122 (2016) 842.
[76] H.J. Snaith, C. Ducati, Nano Lett, 10 (2010) 1259-1265.
[77] B.M. Klahr, T.W. Hamann, J. Phys. Chem. C, 113 (2009) 14040-14045.
[78] H. Cheema, J.H. Delcamp, ACS Appl. Mater. Interfaces, 9 (2017) 3050-3059.
[79] T. Peng, K. Fan, D. Zhao, J. Chen, J. Phys. Chem. C, 114 (2010) 22346-22351.
[80] D.A. Smith, G. McKenzie, A.C. Jones, T.A. Smith, Methods and Applications in Fluorescence, 5 (2017) 042001.
[81] P. Peronio, G. Acconcia, I. Rech, M. Ghioni, Rev Sci Instrum, 86 (2015) 113101-113101.
[82] D. Phillips, R.C. Drake, D.V. O'Connor, R.L. Christensen, Instrumentation Science & Technology, 14 (1985) 267-292.
[83] D.A. Kleinman, Physical Review, 128 (1962) 1761-1775.
[84] M. Lorenc, M. Ziolek, R. Naskrecki, J. Karolczak, J. Kubicki, A. Maciejewski, Applied Physics B, 74 (2002) 19-27.
[85] Z. Yu, F. Li, L. Sun, Energy Environ. Sci., 8 (2015) 760-775.
[86] X. Liu, S. Inagaki, J. Gong, Angew. Chem. Int. Ed., 55 (2016) 2-29.
[87] J.L. White, M.F. Baruch, J.E. Pander Iii, Y. Hu, I.C. Fortmeyer, J.E. Park, T. Zhang, K. Liao, J. Gu, Y. Yan, T.W. Shaw, E. Abelev, A.B. Bocarsly, Chem. Rev., 115 (2015) 12888-12935.
[88] G. Luciani, C. Imparato, G. Vitiello, Catalysts, 10 (2020).
[89] D. Antón-García, J. Warnan, E. Reisner, Chem. Sci., (2020).
[90] P. Brogdon, H. Cheema, J.H. Delcamp, ChemSusChem, 11 (2018) 86-103.
[91] Y. Saygili, M. Stojanovic, N. Flores-Díaz, S.M. Zakeeruddin, N. Vlachopoulos, M. Grätzel, A. Hagfeldt, Inorganics, 7 (2019) 30.
[92] J.M. Cole, G. Pepe, O.K. Al Bahri, C.B. Cooper, Chem. Rev., 119 (2019) 7279-7327.
[93] J.-M. Ji, H. Zhou, H.K. Kim, J. Mater. Chem. A, 6 (2018) 14518-14545.

[94] Y. Wu, W.H. Zhu, S.M. Zakeeruddin, M. Gratzel, ACS Appl. Mater. Interfaces, 7 (2015) 9307-9318.
[95] A. Fakharuddin, R. Jose, T.M. Brown, F. Fabregat-Santiago, J. Bisquert, Energy Environ. Sci., 7 (2014) 3952-3981.
[96] S. Zhang, X. Yang, Y. Numata, L. Han, Energy Environ. Sci., 6 (2013) 1443-1464.
[97] A. Hagfeldt, G. Boschloo, L. Sun, L. Kloo, H. Pettersson, Chem. Rev., 110 (2010) 6595-6663.
[98] D. Schmidt, M.D. Hager, U.S. Schubert, Adv. Energy Mater., 6 (2016) 1500369.
[99] C. Friebe, U.S. Schubert, Adv. Energy Mater., 5 (2015).
[100] J. Winsberg, T. Hagemann, T. Janoschka, M.D. Hager, U.S. Schubert, Angew. Chem. Int. Ed., 56 (2017) 686-711.
[101] N.F. Yan, G.R. Li, X.P. Gao, J. Electrochem. Soc., 161 (2014) A736-A741.
[102] B. Lei, G.-R. Li, P. Chen, X.-P. Gao, ACS Appl. Energy Mater., 2 (2019) 1000-1005.
[103] M. Yu, W.D. McCulloch, D.R. Beauchamp, Z. Huang, X. Ren, Y. Wu, J. Am. Chem. Soc., 137 (2015) 8332-8335.
[104] W. Li, E. Kerr, M.A. Goulet, H.C. Fu, Y. Zhao, Y. Yang, A. Veyssal, J.H. He, R.G. Gordon, M.J. Aziz, S. Jin, Adv. Energy Mater., 9 (2019).
[105] W.D. McCulloch, M. Yu, Y. Wu, ACS Energy Lett., 1 (2016) 578-582.
[106] G. Cavallo, P. Metrangolo, R. Milani, T. Pilati, A. Priimagi, G. Resnati, G. Terraneo, Chem. Rev., 116 (2016) 2478-2601.
[107] G. Terraneo, G. Resnati, P. Metrangolo, Iodine Chemistry and Applications: Chapter 8 Iodine and Halogen Bonding, First ed., John Wiley & Sons, 2015.
[108] A. Baumann, H. Cheema, M.A. Sabuj, L.E. McNamara, Y. Zhang, A. Peddapuram, S.T. Nguyen, D.L. Watkins, N.I. Hammer, N. Rai, J.H. Delcamp, Phys. Chem. Chem. Phys., 20 (2018) 17859-17870.
[109] K. Hu, H.A. Severin, B.D. Koivisto, K.C.D. Robson, E. Schott, R. Arratia-Perez, G.J. Meyer, C.P. Berlinguette, J. Phys. Chem. C, 118 (2014) 17079-17089.
[110] S. Aghazada, P. Gao, A. Yella, T. Moehl, J. Teuscher, J.E. Moser, M. Gratzel, M.K. Nazeeruddin, ACS Appl. Mater. Interfaces, 8 (2016) 26827-26833.
[111] S.J.C. Simon, F.G.L. Parlane, W.B. Swords, C.W. Kellett, C. Du, B. Lam, R.K. Dean, K. Hu, G.J. Meyer, C.P. Berlinguette, J. Am. Chem. Soc., 138 (2016) 10406-10409.
[112] W.B. Swords, S.J. Simon, F.G. Parlane, R.K. Dean, C.W. Kellett, K. Hu, G.J. Meyer, C.P. Berlinguette, Angew. Chem. Int. Ed., 55 (2016) 5956-5960.
[113] F.G.L. Parlane, C. Mustoe, C.W. Kellett, S.J. Simon, W.B. Swords, G.J. Meyer, P. Kennepohl, C.P. Berlinguette, Nat Commun, 8 (2017) 1761.
[114] T.D. Nguyen, C.H. Lin, C.G. Wu, Inorg. Chem., 56 (2017) 252-260.
[115] L. Casarin, W.B. Swords, S. Caramori, C.A. Bignozzi, G.J. Meyer, Inorg. Chem., (2017).
[116] O.O. Ogunsolu, A.J. Braun, A.J. Robb, S.R. Salpage, Y. Zhou, K. Hanson, ACS Appl. Energy Mater., 2 (2018) 29-36.
[117] J.H. Delcamp, A. Yella, T.W. Holcombe, M.K. Nazeeruddin, M. Grätzel, Angew. Chem. Int. Ed., 52 (2013) 376-380.
[118] S.T. Nguyen, A.L. Rheingold, G.S. Tschumper, D.L. Watkins, Cryst. Growth Des., 16 (2016) 6648-6653.
[119] Y. Hu, A. Abate, Y. Cao, A. Ivaturi, S.M. Zakeeruddin, M. Grätzel, N. Robertson, J. Phys. Chem. C, 120 (2016) 15027-15034.
[120] B.P. Karsten, J.C. Bijleveld, L. Viani, J. Cornil, J. Gierschner, R.A.J. Janssen, J. Mater. Chem., 19 (2009) 5343-5350.
[121] S. Guo, W. Yan, J. Chen, C. Tang, Z. Wang, J. Jiang, H. Xin, Synt. Met., 245 (2018) 167-174.
[122] H.N. Tsao, M. Gratzel, ACS Appl Mater Interfaces, 10 (2018) 36602-36607.

[123] L.J. Cook, F. Tuna, M.A. Halcrow, Dalton Trans., 42 (2013) 2254-2265.
[124] M.J. Frisch, G.W. Trucks, H.B. Schlegel, G.E. Scuseria, M.A. Robb, J.R. Cheeseman, G. Scalmani, V. Barone, G.A. Petersson, H. Nakatsuji, X. Li, M. Caricato, A.V. Marenich, J. Bloino, B.G. Janesko, R. Gomperts, B. Mennucci, H.P. Hratchian, J.V. Ortiz, A.F. Izmaylov, J.L. Sonnenberg, D. Williams-Young, F. Ding, F. Lipparini, F. Egidi, J. Goings, B. Peng, A. Petrone, T. Henderson, D. Ranasinghe, V.G. Zakrzewski, J. Gao, N. Rega, G. Zheng, W. Liang, M. Hada, M. Ehara, K. Toyota, R. Fukuda, J. Hasegawa, M. Ishida, T. Nakajima, Y. Honda, O. Kitao, H. Nakai, T. Vreven, K. Throssell, J.A. Montgomery Jr., J.E. Peralta, F. Ogliaro, M.J. Bearpark, J.J. Heyd, E.N. Brothers, K.N. Kudin, V.N. Staroverov, T.A. Keith, R. Kobayashi, J. Normand, K. Raghavachari, A.P. Rendell, J.C. Burant, S.S. Iyengar, J. Tomasi, M. Cossi, J.M. Millam, M. Klene, C. Adamo, R. Cammi, J.W. Ochterski, R.L. Martin, K. Morokuma, O. Farkas, J.B. Foresman, D.J. Fox, Gaussian 16, Revision A.03, (2016) Gaussian, Inc., Wallingford CT.
[125] J.D. Chai, M. Head-Gordon, Phys. Chem. Chem. Phys., 10 (2008) 6615-6620.
[126] S. Grimme, J. Comp. Chem., 27 (2006) 1787-1799.
[127] D. Feller, J. Comp. Chem., 17 (1996) 1571-1586.
[128] K.L. Schuchardt, B.T. Didier, T. Elsethagen, L. Sun, V. Gurumoorthi, J. Chase, J. Li, T.L. Windus, J. Chem. Inf. Model., 47 (2007) 1045-1052.
[129] M.M. Francl, W.J. Pietro, W.J. Hehre, J.S. Binkley, M.S. Gordon, D.J. DeFrees, J.A. Pople, J. Chem. Phys., 77 (1982) 3654-3665.
[130] G.B. Bacskay, Chem. Phys., 61 (1981) 385-404.
[131] J. Tomasi, B. Mennucci, R. Cammi, Chem. Rev., 105 (2005) 2999-3093.
[132] S. Miertus, E. Scrocco, J. Tomasi, Chem. Phys., 55 (1981) 117-129.
[133] M. Cossi, V. Barone, R. Cammi, J. Tomasi, Chem. Phys. Lett., 255 (1996) 327-335.
[134] J.B. Foresman, A. Frisch, Exploring Chemistry with Electronic Structure Methods: A Guide to Using Gaussian, 2nd ed., Gaussian, Inc., Pittsburgh, PA, 2013.
[135] C. Adamo, D. Jacquemin, Chem Soc Rev, 42 (2013) 845-856.
[136] R. Bauernschmitt, R. Ahlrichs, Chem. Phys. Lett., 256 (1996) 454-464.
[137] R. Kohlrausch, Pogg. Ann. Phys., 167 (1854) 179-214.
[138] G. Williams, D.C. Watts, Trans. Faraday Soc., 66 (1970) 80-85.
[139] C.P. Lindsey, G.D. Patterson, J. Chem. Phys., 73 (1980) 3348-3357.
[140] A. Lukichev, Physics Letters A, 383 (2019) 2983-2987.
[141] A.M. Wallace, C. Curiac, J.H. Delcamp, R.C. Fortenberry, J. Quant. Spectrosc. Radiat. Transf., 265 (2021) 107544.
[142] G. Boschloo, L. Häggman, A. Hagfeldt, J. Phys. Chem. B, 110 (2006) 13144-13150.
[143] Q. Wang, J.E. Moser, M. Grätzel, J. Phys. Chem. B, 109 (2005) 14945-14953.
[144] F.A. Houle, Chem Sci, 12 (2021) 6117-6128.
[145] H. Cheema, J. Watson, J.H. Delcamp, ACS Appl. Electron. Mater., 3 (2021) 316-324.
[146] Y. Cao, Y. Liu, S.M. Zakeeruddin, A. Hagfeldt, M. Grätzel, Joule, 2 (2018) 1108-1117.
[147] M. Freitag, J. Teuscher, Y. Saygili, X. Zhang, F. Giordano, P. Liska, J. Hua, S.M. Zakeeruddin, J.-E. Moser, M. Grätzel, A. Hagfeldt, Nat. Photon., 11 (2017) 372-378.
[148] D. Zhang, M. Stojanovic, Y. Ren, Y. Cao, F.T. Eickemeyer, E. Socie, N. Vlachopoulos, J.E. Moser, S.M. Zakeeruddin, A. Hagfeldt, M. Gratzel, Nat. Commun., 12 (2021) 1777.
[149] A.B. Munoz-Garcia, I. Benesperi, G. Boschloo, J.J. Concepcion, J.H. Delcamp, E.A. Gibson, G.J. Meyer, M. Pavone, H. Pettersson, A. Hagfeldt, M. Freitag, Chem. Soc. Rev., 50 (2021) 12450-12550.
[150] S. Yoon, S. Tak, J. Kim, Y. Jun, K. Kang, J. Park, Build. Environ., 46 (2011) 1899-1904.
[151] B.P. Jelle, C. Breivik, Energy Procedia, 20 (2012) 78-87.

[152] E. Biyik, M. Araz, A. Hepbasli, M. Shahrestani, R. Yao, L. Shao, E. Essah, A.C. Oliveira, T. del Caño, E. Rico, J.L. Lechón, L. Andrade, A. Mendes, Y.B. Atlı, Eng. Sci. Technol., 20 (2017) 833-858.
[153] M. Saifullah, J. Gwak, J.H. Yun, J. Mater. Chem. A, 4 (2016) 8512-8540.
[154] A. Roy, A. Ghosh, S. Bhandari, P. Selvaraj, S. Sundaram, T.K. Mallick, J. Phys. Chem. C, 123 (2019) 23834-23837.
[155] H. Michaels, M. Rinderle, R. Freitag, I. Benesperi, T. Edvinsson, R. Socher, A. Gagliardi, M. Freitag, Chem. Sci., 11 (2020) 2895-2906.
[156] A. Aslam, U. Mehmood, M.H. Arshad, A. Ishfaq, J. Zaheer, A. Ul Haq Khan, M. Sufyan, Solar Energy, 207 (2020) 874-892.
[157] Z. Sun, M. Liang, J. Chen, Acc. Chem. Res., 48 (2015) 1541-1550.
[158] J. Jeon, Y.C. Park, S.S. Han, W.A. Goddard, 3rd, Y.S. Lee, H. Kim, J. Phys. Chem. Lett., 5 (2014) 4285-4290.
[159] H.N. Tsao, C. Yi, T. Moehl, J.H. Yum, S.M. Zakeeruddin, M.K. Nazeeruddin, M. Grätzel, ChemSusChem, 4 (2011) 591-594.
[160] S. Ahmad, T. Bessho, F. Kessler, E. Baranoff, J. Frey, C. Yi, M. Gratzel, M.K. Nazeeruddin, Phys. Chem. Chem. Phys., 14 (2012) 10631-10639.
[161] Y. Cao, Y. Saygili, A. Ummadisingu, J. Teuscher, J. Luo, N. Pellet, F. Giordano, S.M. Zakeeruddin, J.E. Moser, M. Freitag, A. Hagfeldt, M. Gratzel, Nat. Commun., 8 (2017) 15390.
[162] E. Gabrielsson, H. Ellis, S. Feldt, H. Tian, G. Boschloo, A. Hagfeldt, L. Sun, Adv. Energy Mater., 3 (2013) 1647-1656.
[163] L. Zhang, J.M. Cole, ACS Appl. Mater. Interfaces, 7 (2015) 3427-3455.
[164] M.K. Kashif, J.C. Axelson, N.W. Duffy, C.M. Forsyth, C.J. Chang, J.R. Long, L. Spiccia, U. Bach, J. Am. Chem. Soc., 134 (2012) 16646-16653.
[165] M.A. Topchiy, P.B. Dzhevakov, M.S. Rubina, O.S. Morozov, A.F. Asachenko, M.S. Nechaev, Eur. J. Org. Chem., 2016 (2016) 1908-1914.
[166] Z.S. Huang, X.F. Zang, T. Hua, L. Wang, H. Meier, D. Cao, ACS Appl. Mater. Interfaces, 7 (2015) 20418-20429.
[167] M. Urbani, M. Grätzel, M.K. Nazeeruddin, T. Torres, Chem. Rev., 114 (2014) 12330-12396.
[168] A.Y. Anderson, P.R.F. Barnes, J.R. Durrant, B.C. O'Regan, J. Phys. Chem. C, 115 (2011) 2439-2447.
[169] H. Long, D. Zhou, M. Zhang, C. Peng, S. Uchida, P. Wang, J. Phys. Chem. C, 115 (2011) 14408-14414.
[170] L.E. Polander, A. Yella, J. Teuscher, R. Humphry-Baker, B.F.E. Curchod, N. Ashari Astani, P. Gao, J.-E. Moser, I. Tavernelli, U. Rothlisberger, M. Grätzel, M.K. Nazeeruddin, J. Frey, Chem. Mater., 25 (2013) 2642-2648.
[171] R. Kohlrausch, Ann. Phys. (Pogg.), 167 (1854) 179-214 DOI: 110.1002/andp.18541670203.
[172] L. Casarin, W.B. Swords, S. Caramori, C.A. Bignozzi, G.J. Meyer, Inorg. Chem., 56 (2017) 7324-7327.
[173] B.N. DiMarco, L. Troian-Gautier, R.N. Sampaio, G.J. Meyer, Chem. Sci., 9 (2018) 940-949.
[174] A. Peddapuram, H. Cheema, R.E. Adams, R.H. Schmehl, J.H. Delcamp, J. Phys. Chem. C, 121 (2017) 8770-8780.
[175] H. Cheema, A. Peddapuram, R.E. Adams, L.E. McNamara, L.A. Hunt, N. Le, D.L. Watkins, N.I. Hammer, R.H. Schmehl, J.H. Delcamp, J. Org. Chem., 82 (2017) 12038-12049.
[176] A.E. King, Y. Surendranath, N.A. Piro, J.P. Bigi, J.R. Long, C.J. Chang, Chem. Sci., 4 (2013) 1578-1587.
[177] F. Li, J.R. Jennings, Q. Wang, ACS Nano, 7 (2013) 8233-8242.
[178] I. Cho, P. Wagner, P.C. Innis, S. Mori, A.J. Mozer, J. Am. Chem. Soc., 143 (2021) 488-495.
[179] J. Yang, P. Ganesan, J. Teuscher, T. Moehl, Y.J. Kim, C. Yi, P. Comte, K. Pei, T.W. Holcombe, M.K. Nazeeruddin, J. Hua, S.M. Zakeeruddin, H. Tian, M. Grätzel, J. Am. Chem. Soc., 136 (2014) 5722-5730.

[180] M. Freitag, F. Giordano, W. Yang, M. Pazoki, Y. Hao, B. Zietz, M. Grätzel, A. Hagfeldt, G. Boschloo, J. Phys. Chem. C, 120 (2016) 9595-9603.
[181] M.H. Gehlen, Journal of Photochemistry and Photobiology C: Photochemistry Reviews, 42 (2020) 100338.
[182] W. Yang, X. Chen, H. Su, W. Fang, Y. Zhang, Chem. Commun., 51 (2015) 9616-9619.
[183] W.J. Hehre, R. Ditchfield, J.A. Pople, J. Chem. Phys., 56 (1972) 2257-2261.
[184] Y. Sun, J.P. Bigi, N.A. Piro, M.L. Tang, J.R. Long, C.J. Chang, J. Am. Chem. Soc., 133 (2011) 9212-9215.
[185] W. Zhang, Y. Wu, H.W. Bahng, Y. Cao, C. Yi, Y. Saygili, J. Luo, Y. Liu, L. Kavan, J.-E. Moser, A. Hagfeldt, H. Tian, S.M. Zakeeruddin, W.-H. Zhu, M. Grätzel, Energy Environ. Sci., 11 (2018) 1779-1787.
[186] R. Garcia-Rodriguez, R. Jiang, E.J. Canto-Aguilar, G. Oskam, G. Boschloo, Phys. Chem. Chem. Phys., 19 (2017) 32132-32142.
[187] S.M. Feldt, E.A. Gibson, E. Gabrielsson, L. Sun, G. Boschloo, A. Hagfeldt, J. Am. Chem. Soc., 132 (2010) 16714-16724.
[188] A. Polman, M. Knight, E.C. Garnett, B. Ehrler, W.C. Sinke, Science, 352 (2016) aad4424.
[189] S.-H. Nam, K.H. Lee, J.-H. Yu, J.-H. Boo, Appl. Sci. Converg. Technol., 28 (2019) 194-206.
[190] J. Nissfolk, K. Fredin, A. Hagfeldt, G. Boschloo, J. Phys. Chem. B, 110 (2006) 17715-17718.
[191] K. Oum, P.W. Lohse, J.R. Klein, O. Flender, M. Scholz, A. Hagfeldt, G. Boschloo, T. Lenzer, Phys. Chem. Chem. Phys., 15 (2013) 3906-3916.
[192] M. Pazoki, U.B. Cappel, E.M.J. Johansson, A. Hagfeldt, G. Boschloo, Energy Environ. Sci., 10 (2017) 672-709.
[193] H.J. Snaith, Energy Environ. Sci., 5 (2012) 6513.
[194] P. Selvaraj, A. Ghosh, T.K. Mallick, S. Sundaram, Renewable Energy, 141 (2019) 516-525.
[195] M.F. Vildanova, A.B. Nikolskaia, S.S. Kozlov, O.I. Shevaleevskiy, J. Phys.: Conf. Ser., 643 (2015) 012106.
[196] L. Zhang, X. Yang, W. Wang, G.G. Gurzadyan, J. Li, X. Li, J. An, Z. Yu, H. Wang, B. Cai, A. Hagfeldt, L. Sun, ACS Energy Lett., 4 (2019) 943-951.
[197] K. Kakiage, Y. Aoyama, T. Yano, K. Oya, J.I. Fujisawa, M. Hanaya, Chem. Commun., 51 (2015) 15894-15897.
[198] Y.K. Eom, S.H. Kang, I.T. Choi, Y. Yoo, J. Kim, H.K. Kim, J. Mater. Chem. A, 5 (2017) 2297-2308.
[199] S. Mathew, A. Yella, P. Gao, R. Humphry-Baker, B.F. Curchod, N. Ashari-Astani, I. Tavernelli, U. Rothlisberger, M.K. Nazeeruddin, M. Grätzel, Nat. Chem., 6 (2014) 242-247.
[200] S.H. Kang, M.J. Jeong, Y.K. Eom, I.T. Choi, S.M. Kwon, Y. Yoo, J. Kim, J. Kwon, J.H. Park, H.K. Kim, Adv. Energy Mater., 7 (2016) 1602117.
[201] H. Ozawa, T. Sugiura, T. Kuroda, K. Nozawa, H. Arakawa, J. Mater. Chem. A, 4 (2016) 1762-1770.
[202] B. Pashaei, H. Shahroosvand, P. Abbasi, RSC Adv., 5 (2015) 94814-94848.
[203] A. Baumann, C. Curiac, J.H. Delcamp, ChemSusChem, (2020) DOI: 10.1002/cssc.202000409.
[204] Y. Liu, J.R. Jennings, Y. Huang, Q. Wang, S.M. Zakeeruddin, M. Grätzel, J. Phys. Chem. C, 115 (2011) 18847-18855.
[205] E. Mosconi, J.H. Yum, F. Kessler, C.J. Gomez Garcia, C. Zuccaccia, A. Cinti, M.K. Nazeeruddin, M. Gratzel, F. De Angelis, J. Am. Chem. Soc., 134 (2012) 19438-19453.
[206] K. Omata, S. Kuwahara, K. Katayama, S. Qing, T. Toyoda, K.M. Lee, C.G. Wu, Phys. Chem. Chem. Phys., 17 (2015) 10170-10175.
[207] S. Aghazada, M. Nazeeruddin, Inorganics, 6 (2018) 52.
[208] S. Aghazada, P. Gao, A. Yella, G. Marotta, T. Moehl, J. Teuscher, J.E. Moser, F. De Angelis, M. Gratzel, M.K. Nazeeruddin, Inorg. Chem., (2016).

[209] T. Kono, N. Masaki, M. Nishikawa, R. Tamura, H. Matsuzaki, M. Kimura, S. Mori, ACS Appl. Mater. Interfaces, (2016).
[210] K.L. Wu, A.J. Huckaba, J.N. Clifford, Y.W. Yang, A. Yella, E. Palomares, M. Gratzel, Y. Chi, M.K. Nazeeruddin, Inorg. Chem., (2016).
[211] S. Aghazada, Y. Ren, P. Wang, M.K. Nazeeruddin, Inorg. Chem., (2017).
[212] K.-L. Wu, Y. Hu, C.-T. Chao, Y.-W. Yang, T.-Y. Hsiao, N. Robertson, Y. Chi, J. Mater. Chem. A, 2 (2014) 19556-19565.
[213] L.E. Polander, A. Yella, B.F. Curchod, N. Ashari Astani, J. Teuscher, R. Scopelliti, P. Gao, S. Mathew, J.E. Moser, I. Tavernelli, U. Rothlisberger, M. Gratzel, M.K. Nazeeruddin, J. Frey, Angew. Chem. Int. Ed., 52 (2013) 8731-8735.
[214] T. Kinoshita, K. Nonomura, N. Joong Jeon, F. Giordano, A. Abate, S. Uchida, T. Kubo, S.I. Seok, M.K. Nazeeruddin, A. Hagfeldt, M. Grätzel, H. Segawa, Nat. Commun., 6 (2015) 8834.
[215] G. Li, A. Yella, D.G. Brown, S.I. Gorelsky, M.K. Nazeeruddin, M. Grätzel, C.P. Berlinguette, M. Shatruk, Inorg. Chem., 53 (2014) 5417-5419.
[216] M. Konstantakou, P. Falaras, T. Stergiopoulos, Polyhedron, 82 (2014) 109-115.
[217] Y. Liu, J.R. Jennings, X. Wang, Q. Wang, Phys. Chem. Chem. Phys., 15 (2013) 6170-6174.
[218] M.J. DeVries, M.J. Pellin, J.T. Hupp, Langmuir, 26 (2010) 9082-9087.
[219] J. Sobus, B. Gierczyk, G. Burdzinski, M. Jancelewicz, E. Polanski, A. Hagfeldt, M. Ziolek, Chem. Eur. J., 22 (2016) 15807-15818.
[220] H. Ozawa, Y. Okuyama, H. Arakawa, Dalton Trans., 41 (2012) 5137-5139.
[221] C.Y. Chen, M. Wang, J.Y. Li, N. Pootrakulchote, L. Alibabaei, C.H. Ngoc-le, J.D. Decoppet, J.H. Tsai, C. Gratzel, C.G. Wu, S.M. Zakeeruddin, M. Gratzel, ACS Nano, 3 (2009) 3103-3109.
[222] S. Wooh, T.-Y. Kim, D. Song, Y.-G. Lee, T.K. Lee, V.W. Bergmann, S.A.L. Weber, J. Bisquert, Y.S. Kang, K. Char, ACS Applied Materials & Interfaces, 7 (2015) 25741-25747.
[223] G.A. Sewvandi, Z. Tao, T. Kusunose, Y. Tanaka, S. Nakanishi, Q. Feng, ACS Appl. Mater. Interfaces, 6 (2014) 5818-5826.
[224] H. Cheema, J.H. Delcamp, Adv. Energy Mater., 9 (2019) 1900162.
[225] H. Cheema, R.R. Rodrigues, J.H. Delcamp, Energy Environ. Sci., 10 (2017) 1764-1769.
[226] Q. Shen, Y. Ogomi, B.W. Park, T. Inoue, S.S. Pandey, A. Miyamoto, S. Fujita, K. Katayama, T. Toyoda, S. Hayase, Phys. Chem. Chem. Phys., 14 (2012) 4605-4613.
[227] S.E. Koops, B.C. O'Regan, P.R.F. Barnes, J.R. Durrant, J. Am. Chem. Soc., 131 (2009) 4808-4818.
[228] K.C. Robson, K. Hu, G.J. Meyer, C.P. Berlinguette, J. Am. Chem. Soc., 135 (2013) 1961-1971.
[229] A.Y. Anderson, P.R.F. Barnes, J.R. Durrant, B.C. O'Regan, The Journal of Physical Chemistry C, 115 (2011) 2439-2447.
[230] C. Curiac, L.A. Hunt, M.A. Sabuj, Q. Li, A. Baumann, H. Cheema, Y. Zhang, N. Rai, N.I. Hammer, J.H. Delcamp, J. Phys. Chem. C, 125 (2021) 17647-17659.
[231] M.J. Frisch, J.A. Pople, J.S. Binkley, J. Chem. Phys., 80 (1983) 3265-3269.
[232] A.D. Becke, J. Chem. Phys., 98 (1993) 5648-5652.
[233] C. Lee, W. Yang, R.G. Parr, Phys. Rev. B, 37 (1988) 785-789.
[234] T. Le Bahers, C. Adamo, I. Ciofini, J Chem Theory Comput, 7 (2011) 2498-2506.
[235] P. Brogdon, L.E. McNamara, A. Peddapuram, N.I. Hammer, J.H. Delcamp, Synt. Met., 222 (2016) 66-75.
[236] H. Cheema, J. Watson, J.H. Delcamp, Solar Energy, 208 (2020) 747-752.
[237] H. Cheema, J.H. Delcamp, Chem. Eur. J., 25 (2019) 14205-14213.
[238] H. Cheema, A. Baumann, E.K. Loya, P. Brogdon, L.E. McNamara, C.A. Carpenter, N.I. Hammer, S. Mathew, C. Risko, J.H. Delcamp, ACS applied materials & interfaces, 11 (2019) 16474-16489.

LIST OF APPENDICES

APPENDICES FOR THE PUBLICATIONS PRESENTED WITHIN THIS DISSERTATION,

"SPECTROSCOPIC INVESTIGATIONS OF PHOTOINDUCED ELECTRON TRANSFER PROCESSES AT INTERFACES AND IN SOLUTION"

BY LEIGH ANNA HUNT

APPENDIX I: SUPPORTING INFORMATION FOR CHAPTER 4 "PROBING INTERFACIAL HALOGEN BONDING EFFECTS WITH HALOGENATED ORGANIC DYES AND A LEWIS BASE DECORATED TRANSITION METAL-BASED REDOX SHUTTLES AT A METAL OXIDE INTERFACE IN DYE-SENSITIZED SOLAR CELLS".....1

APPENDIX II: SUPPORTING INFORMATION FOR CHAPTER 5 "LEWIS ACID−LEWIS BASE INTERACTIONS PROMOTE FAST INTERFACIAL ELECTRON TRANSFERS WITH A PYRIDINE-BASED DONOR DYE IN DYE-SENSITIZED SOLAR CELLS".....1

APPENDIX III: SUPPORTING INFORMATION FOR CHAPTER 6 "PREFERENTIAL DIRECTION OF ELECTRON TRANSFERS AT A DYE−METAL OXIDE INTERFACE WITH AN INSULATING FLUORINATED SELF-ASSEMBLED MONOLAYER AND MGO".....1

Appendix I

Supporting Information for "PROBING INTERFACIAL HALOGEN BONDING EFFECTS WITH HALOGENATED ORGANIC DYES AND A LEWIS BASE DECORATED TRANSITION METAL-BASED REDOX SHUTTLES AT A METAL OXIDE INTERFACE IN DYE-SENSITIZED SOLAR CELLS"

Christine Curiac,[†,a] Leigh Anna Hunt,[†,a] Md Abdus Sabuj,[†,b] Qing Li,[a] Alexandra Baumann,[a]

Hammad Cheema,[a] Yanbing Zhang,[a] Neeraj Rai,[b,*] Nathan I. Hammer,[a,*] and Jared H.

Delcamp[a,*]

Table of Contents – Appendix I

1. Figure S1: ^{1}H NMR for Co(*N*-tpy)$_2$[TFSI]$_2$ in CD_3CN at room temperature with a 400 MHz NMR.

2. Figure S2: ^{13}C NMR for Co(*N*-tpy)$_2$[TFSI]$_2$ in CD_3CN at room temperature with a 400 MHz NMR where the signal is likely the TFSI carbon only due to the Co-complex of Co(*N*-tpy)$_2$[TFSI]$_2$ being paramagnetic spectrum.

3. Figure S3: ^{19}F NMR for Co(*N*-tpy)$_2$[TFSI]$_2$ in CD_3CN at room temperature with a 400 MHz NMR.

4. Figure S4: ^{1}H NMR for Co(*N*-tpy)$_2$[TFSI]$_3$ in CD_3CN at room temperature with a 400 MHz NMR.

Figure S5: ^{13}C NMR for Co(*N*-tpy)$_2$[TFSI]$_3$ in CD_3CN at room temperature with a 400 MHz NMR.

Figure S6: ^{19}F NMR for Co(*N*-tpy)$_2$[TFSI]$_3$ in CD_3CN at room temperature with a 400 MHz NMR.

Figure S7: ^{1}H NMR for compound 3 in $CDCl_3$ at room temperature with a 400 MHz NMR.

Figure S8: ^{13}C NMR for compound 3 in $CDCl_3$ at room temperature with a 400 MHz NMR.

Figure S9: ^{1}H NMR for compound 4 in $CDCl_3$ at room temperature with a 400 MHz NMR.

Figure S10: ^{13}C NMR for compound 4 in $CDCl_3$ at room temperature with a 400 MHz NMR.

Figure S11: ^{1}H NMR for compound 5 in $CDCl_3$ at room temperature with a 400 MHz NMR.

Figure S12: ^{13}C NMR for Compound 5 in $CDCl_3$ at room temperature with a 400 MHz NMR.

Figure S13: ^{1}H NMR for compound 6 in $CDCl_3$ at room temperature with a 400 MHz NMR.

Figure S14: ^{13}C NMR for compound 6 in $CDCl_3$ at room temperature with a 400 MHz NMR.

Figure S15: ^{1}H NMR for AB4 in $CDCl_3$ at room temperature with a 300 MHz NMR.

Figure S16: ^{1}H NMR for AB5 in $CDCl_3$ at room temperature with a 400 MHz NMR.

Figure S17: ^{1}H NMR for AB6 in $CDCl_3$ at room temperature with a 300 MHz NMR.

Figure S18: ^{1}H NMR for AB7 in $CDCl_3$ at room temperature with a 400 MHz NMR.

Figure S19: Molecular orbital (MO) diagrams of the neutral and positively charged dyes. The green and red surface represents the positive and negative signs of MO at isovalue = 0.02 a.u, respectively.

Table S1: Calculated charge transfer distance[234] due to excitation, the total amount of charge transfer, and wavelength associated with the excitation from the ground to the first singlet excited state (S_0-S_1) for the neutral and positively charged dyes.

Figure S20: The total density difference ($\Delta\rho$) between the ground and first singlet excited state (S_0-S_1) of the neutral and positively charged dyes. The purple and blue-green surface represents the depletion (where electrons came from) and increment (where electrons went) of density due to excitation at isovalue=0.0005 a.u, respectively.

Table S2: Computed frontier molecular orbital energies, energy gap, optical gap and partial charges on the substituents for neutral and positively charged dyes.

Table S3: Calculated optical properties of the neutral and charged dyes. The electronic transitions with orbital contributions, wavelength (λ) associated with that particular transition, and the oscillator strength (f) of the individual transitions. The orbital contributions of the charged dyes are not normalized.

Table S4: Calculated binding energy between the redox-shuttles and different dyes, the distance between the dye substituents (X) and redox-shuttles, and the dihedral angle connecting the substituents with the redox-shuttles.

Figure S21: Optimized geometries of the dyes with different redox shuttles. (a) Neutral (top) and charged (bottom) dyes with Co(N-tpy)$_2$ redox shuttle; and (b) charged dyes with Co(tpy)$_2$ redox shuttle.

Table S5. Summary of fit parameters for target dyes **AB4**, **AB5**, **AB6** and **AB7** with the Co(tpy)$_2^{2+}$ redox shuttle where k_{rec} represents the rate with no redox shuttle present (no RS) and k_{reg} represents the rate in the presence of the redox shuttle.

Table S6. Summary of fit parameters for target dyes **AB4**, **AB5**, **AB6** and **AB7** with the Co(N-tpy)$_2^{2+}$ redox shuttle where k_{rec} is the rate with without redox shuttle present (no RS) and k_{reg} represents the rate of the regeneration reaction. Device preparation including electrolyte solution components and TAS measurement details are stated in the manuscript under sections titled "TAS TiO2-Dye Film Preparation" and "TAS Measurements", respectively.

Figure S22. Spectral data for **AB4** with 0.1 M LiTFSI in MeCN without RS.

Figure S23. Spectral data for **AB4** with 0.1 M LiTFSI in MeCN with 0.25 M Co(N-tpy)$^{2+/3+}$.

Figure S24. Spectral data for **AB4** with 0.1 M LiTFSI in MeCN with 0.25 M Co(tpy)$^{2+/3+}$.

Figure S25. Spectral data for **AB5** with 0.1 M LiTFSI in MeCN.

Figure S26. Spectral data for **AB5** with 0.1 M LiTFSI in MeCN with 0.25 M Co(*N*-tpy)$^{2+/3+}$.

Figure S27. Spectral data for **AB5** with 0.1 M LiTFSI in MeCN with 0.25 M Co(tpy)$^{2+/3+}$.

Figure S29. Spectral data for **AB6** with 0.1 M LiTFSI in MeCN.

Figure S30. Spectral data for **AB6** with 0.1 M LiTFSI in MeCN with 0.25 M Co(N-tpy)$^{2+/3+}$.

Figure S31. Spectral data for **AB6** with 0.1 M LiTFSI in MeCN with 0.25 M Co(tpy)$^{2+/3+}$.

Figure S32. Spectral data for **AB7** with 0.1 M LiTFSI in MeCN.

Figure S33. Spectral data for **AB7** with 0.1 M LiTFSI in MeCN with 0.25 M Co(*N*-tpy)$^{2+/3+}$.

Figure S34. Spectral data for **AB7** with 0.1 M LiTFSI in MeCN with 0.25 M Co(tpy)$^{2+/3+}$.

Figure S35. Decay plots resulting from TAS for **AB4** without RS added, with Co(tpy)$_2^{3+/2+}$, and with Co(*N*-tpy)$_2^{3+/2+}$ RS.

Figure S36. Decay plots resulting from TAS for **AB5** without RS added, with Co(tpy)$_2^{3+/2+}$, and with Co(*N*-tpy)$_2^{3+/2+}$ RS.

Figure S37. Decay plots resulting from TAS for **AB6** without RS added, with Co(tpy)$_2^{3+/2+}$, and with Co(*N*-tpy)$_2^{3+/2+}$ RS.

Figure S38. Decay plots resulting from TAS for **AB7** without RS added, with Co(tpy)$_2^{3+/2+}$, and with Co(*N*-tpy)$_2^{3+/2+}$ RS.

Table S7. Summary TAS data for **AB4**, **AB5**, **AB6** and **AB7**.[a]**Table S8.** Dye molar absorptivities on film and dye loading studies for **AB4, AB5, AB6** and **AB7** averaged over three device sets.

Table S9. Summary of photovoltaic parameters for DSC devices prepared with dyes **AB4**, **AB5**, **AB6** and **AB7**.

Figure S39. *J-V* curves of **AB4**, **AB5**, **AB6** and **AB7** dyes with: top) Co(tpy)$_2^{3+/2+}$ and bottom) Co(*N*-tpy)$_2^{3+/2+}$ redox shuttles.

Figure S40. IPCE spectrum of **AB4**, **AB5**, **AB6** and **AB7** dyes with: top) Co(tpy)$_2^{3+/2+}$ and bottom) Co(*N*-tpy)$_2^{3+/2+}$ redox shuttles.

Figure S41. Small modulated photovoltage transient data of **AB4**, **AB5**, **AB6** and **AB7** dyes with: top) $Co(tpy)_2^{3+/2+}$ and bottom) $Co(N\text{-}tpy)_2^{3+/2+}$ redox shuttles.

Table S10. Electrochemical impedance spectroscopy data.

Figure S42. Nyquist (top) and Bode (bottom) plots resulting from electrochemical impedance spectroscopy for dyes with: left) $Co(tpy)_2^{3+/2+}$ and right) $Co(N\text{-}tpy)_2^{3+/2+}$ redox shuttles.

Figure S43. Relative value comparison with each halogenated dye across several interrogation techniques with $Co(tpy)_2^{3+/2+}$ as a RS. Note: the binding energy column is blank due to the redox shuttle not showing binding at a comparable geometry relative to $Co(N\text{-}tpy)_2^{3+/2+}$.

Figure S44. Relative value comparison with each halogenated dye across several interrogation techniques with $Co(N\text{-}tpy)_2^{3+/2+}$ as a RS with benchmark hydrogen terminated dye **AB4** included.

Figure S45. Relative value comparison with each halogenated dye across several interrogation techniques with $Co(tpy)_2^{3+/2+}$ (lighter shade) and $Co(N\text{-}tpy)_2^{3+/2+}$ (darker shade) as RSs with benchmark hydrogen terminated dye **AB4** included. Orange: electron transfer reaction from a RS to the oxidized dye measured by TAS (regeneration rate). Black: Electron lifetime measured via SMPVT. Red: electrochemical impendence spectroscopy charge transfer resistance at the TiO_2-dye interface with the electrolyte. Blue: power conversion efficiency of DSC devices.

1. Characterization Data

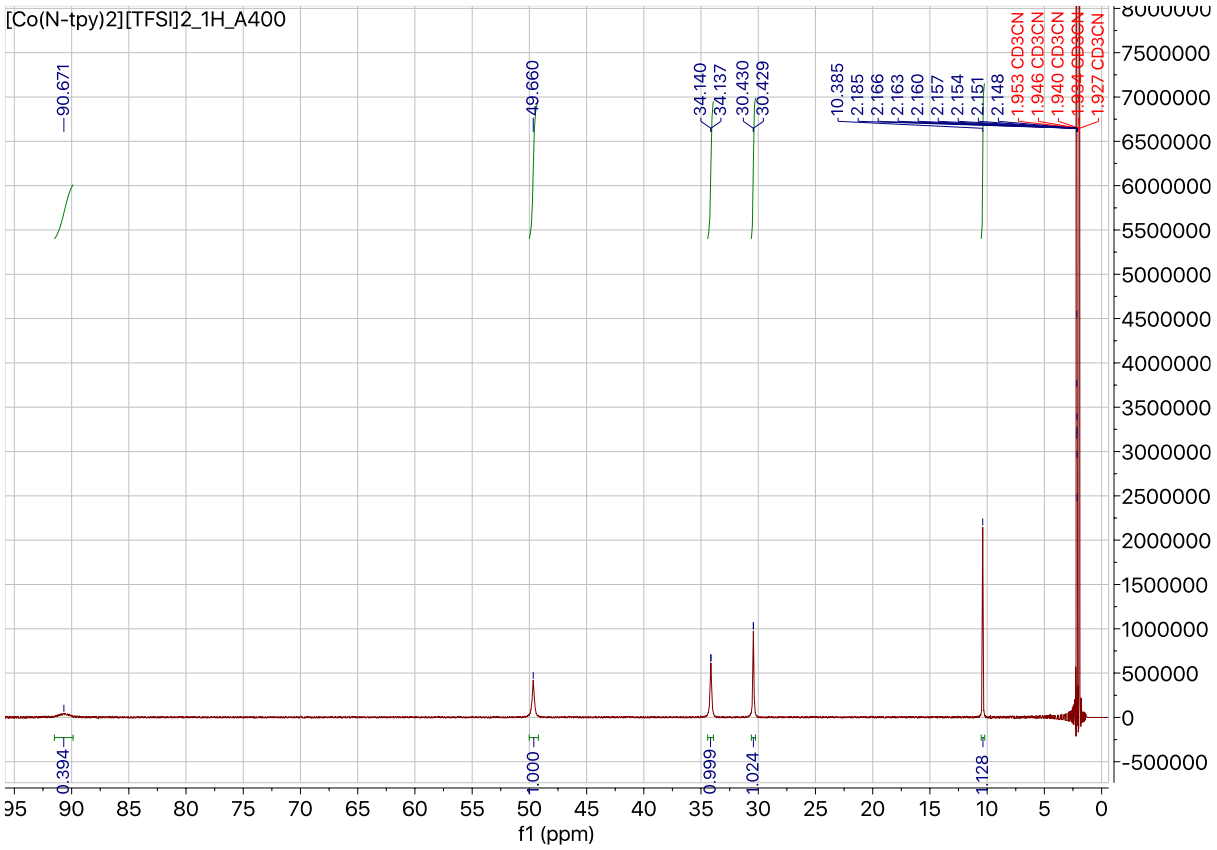

Figure S1. ^{1}H NMR for Co(*N*-tpy)$_2$[TFSI]$_2$ in CD_3CN at room temperature with a 400 MHz NMR.

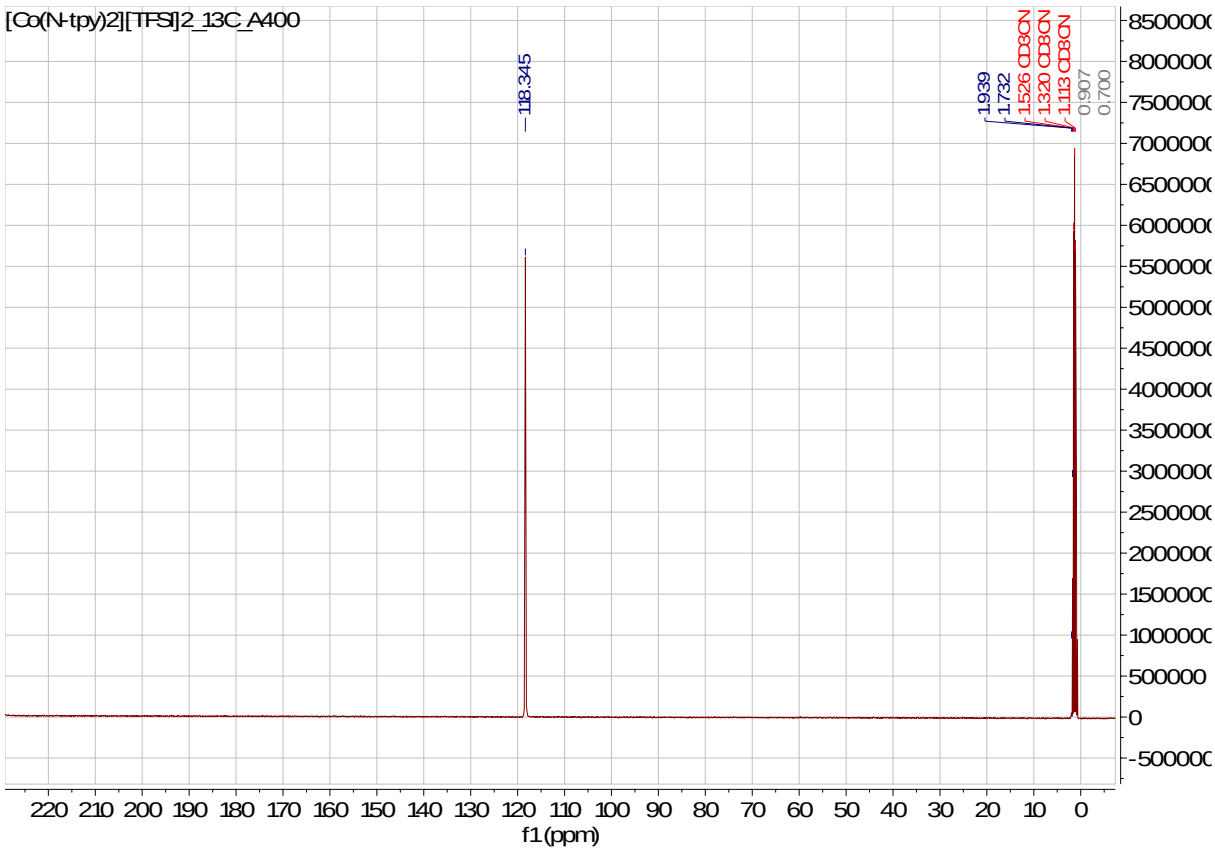

Figure S2. ^{13}C NMR for Co(*N*-tpy)$_2$[TFSI]$_2$ in CD_3CN at room temperature with a 400 MHz NMR where the signal is likely the TFSI carbon only due to the Co-complex of Co(*N*-tpy)$_2$[TFSI]$_2$ being paramagnetic.

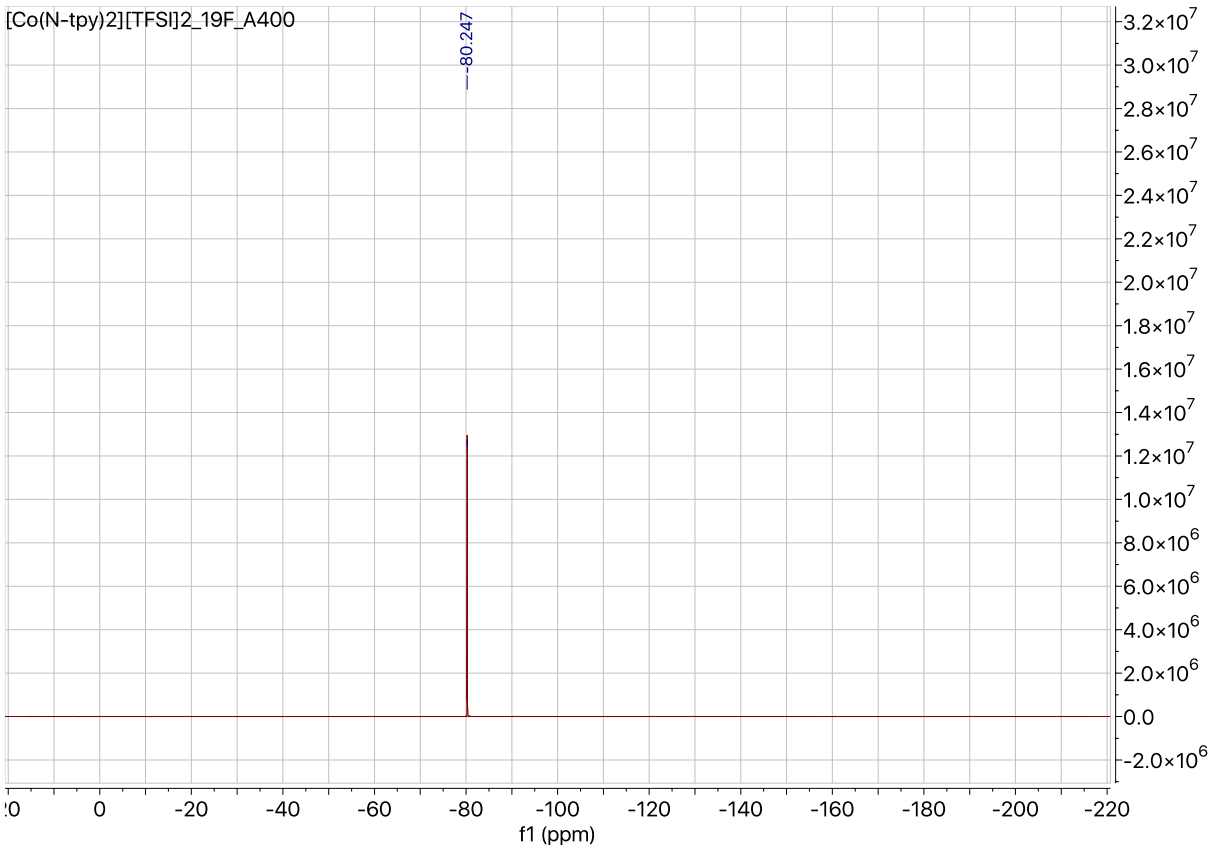

Figure S3. ^{19}F NMR for Co(*N*-tpy)$_2$[TFSI]$_2$ in CD_3CN at room temperature with a 400 MHz NMR.

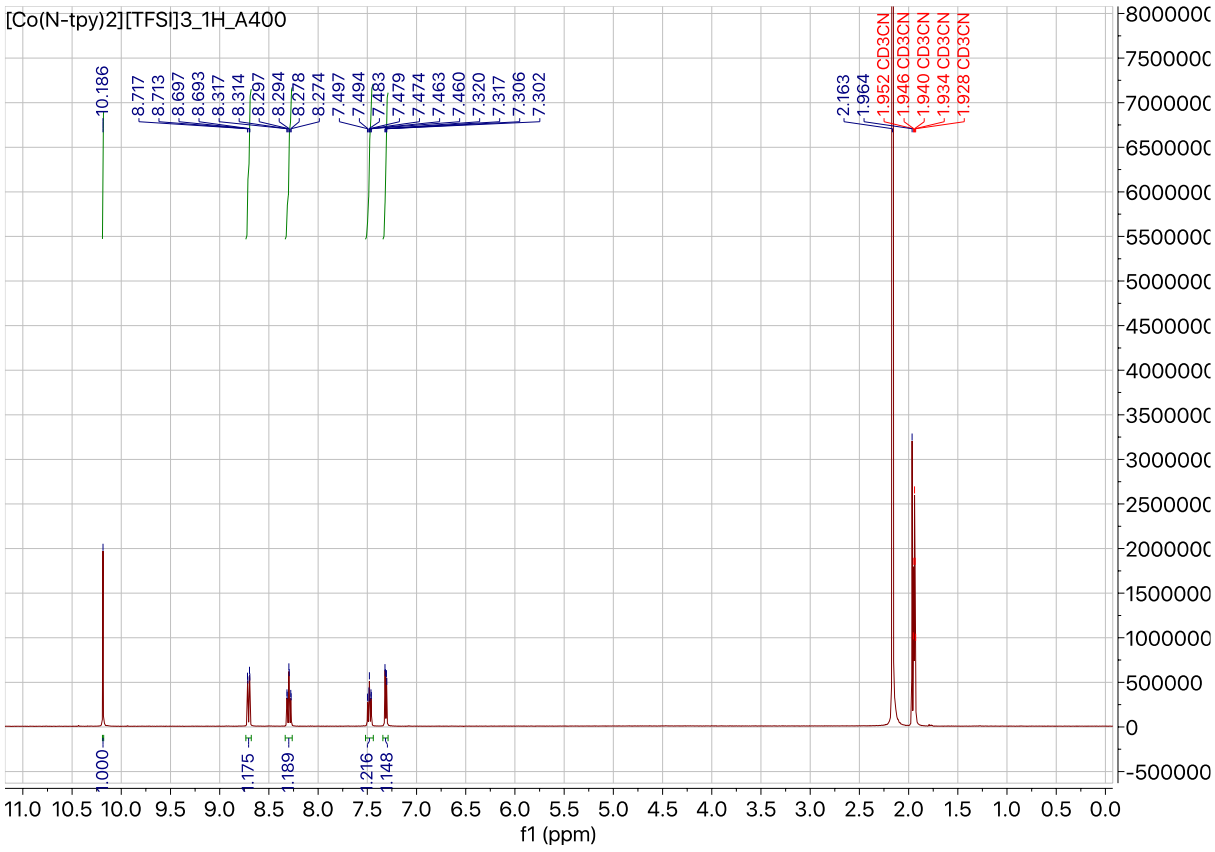

Figure S4. ^{1}H NMR for Co(*N*-tpy)$_2$[TFSI]$_3$ in CD_3CN at room temperature with a 400 MHz NMR.

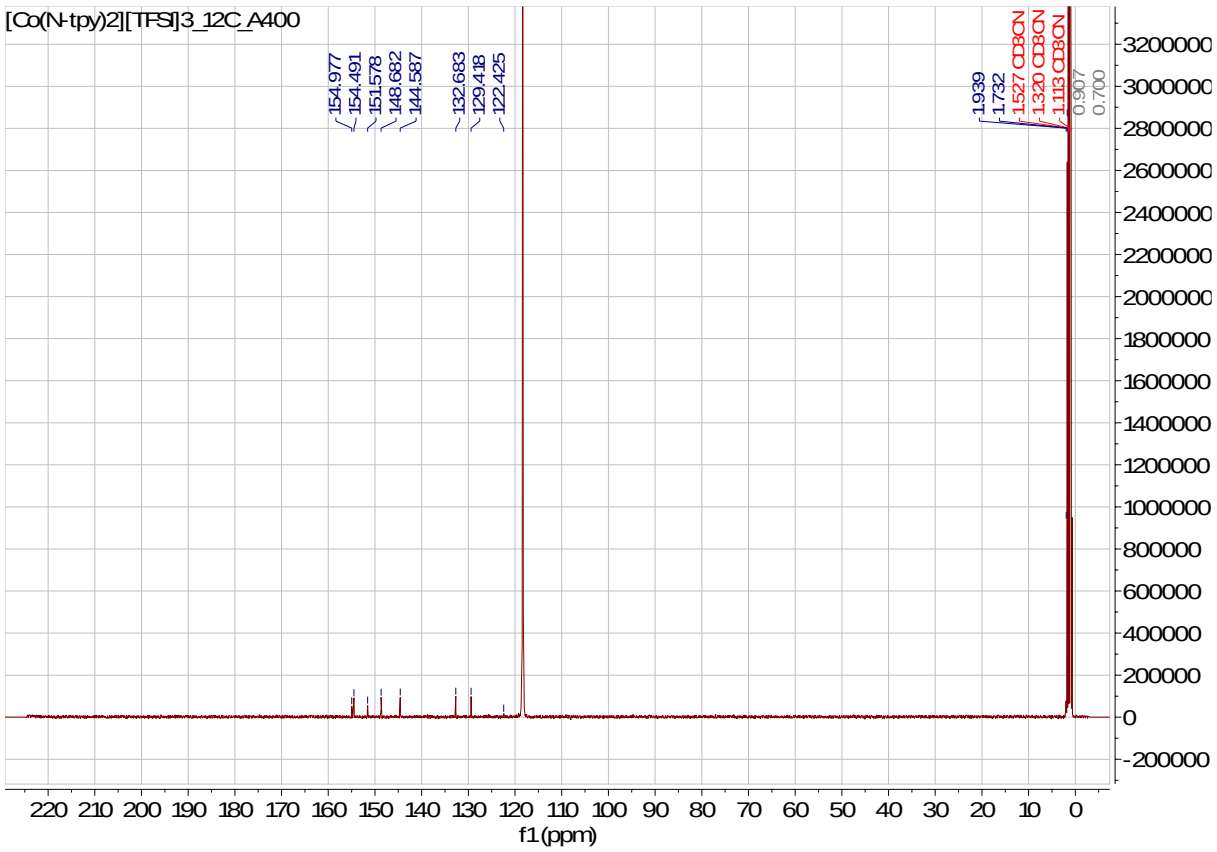

Figure S5. ^{13}C NMR for Co(*N*-tpy)$_2$[TFSI]$_3$ in CD_3CN at room temperature with a 400 MHz NMR.

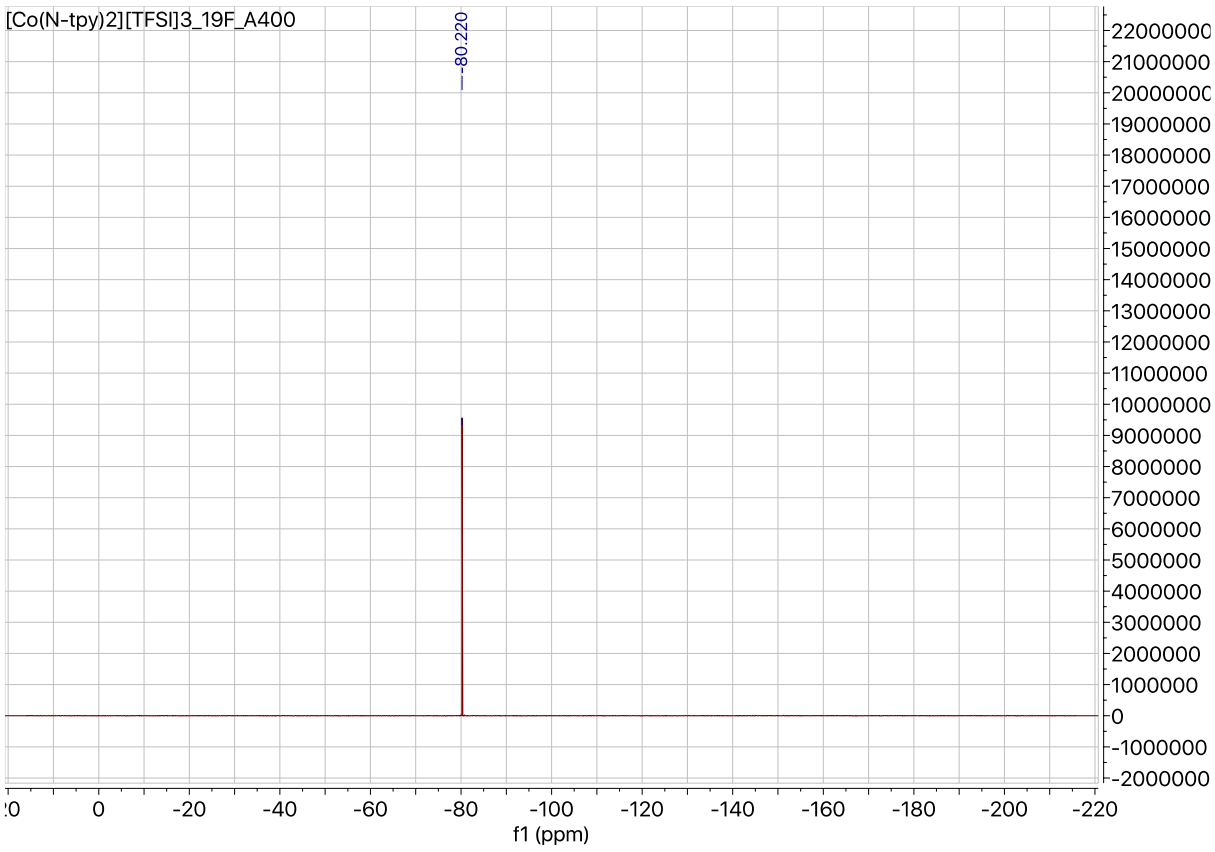

Figure S6. ^{19}F NMR for Co(*N*-tpy)$_2$[TFSI]$_3$ in CD_3CN at room temperature with a 400 MHz NMR.

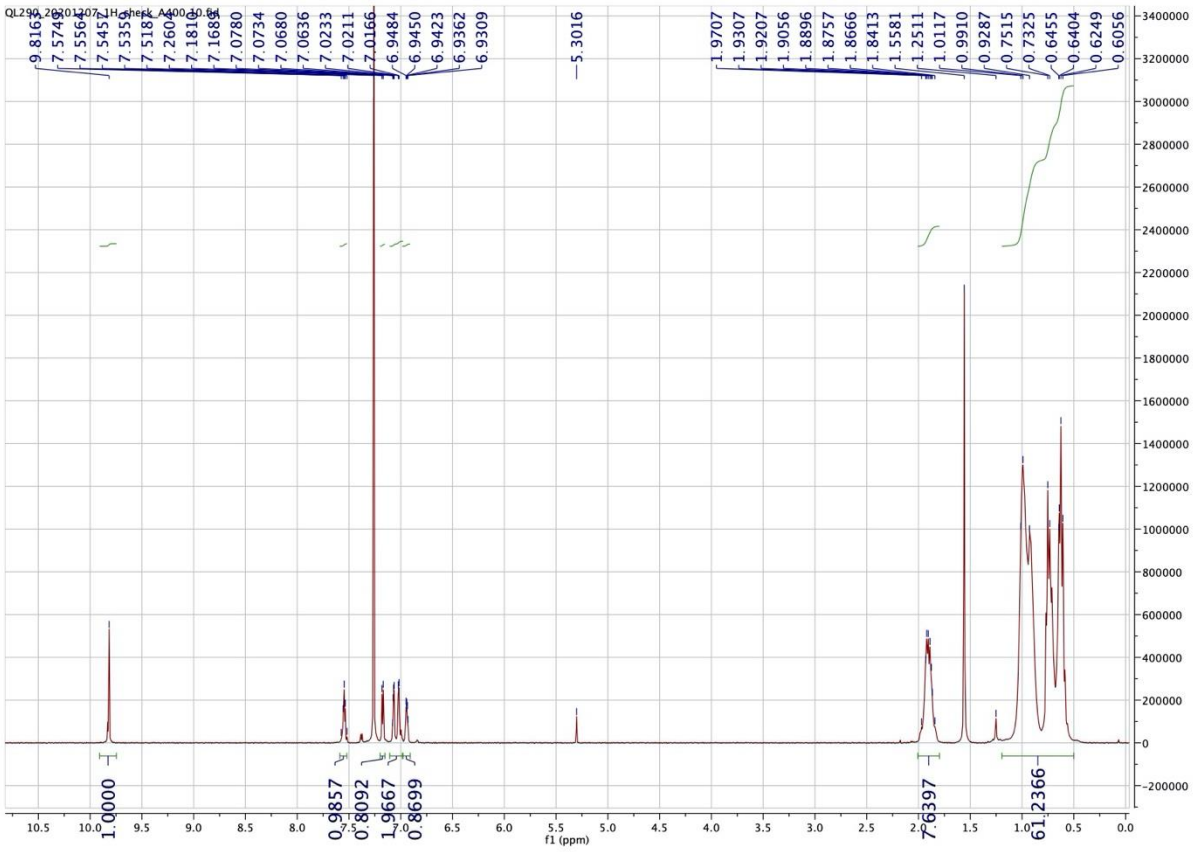

Figure S7. ^{1}H NMR for compound **3** in $CDCl_3$ at room temperature with a 400 MHz NMR.

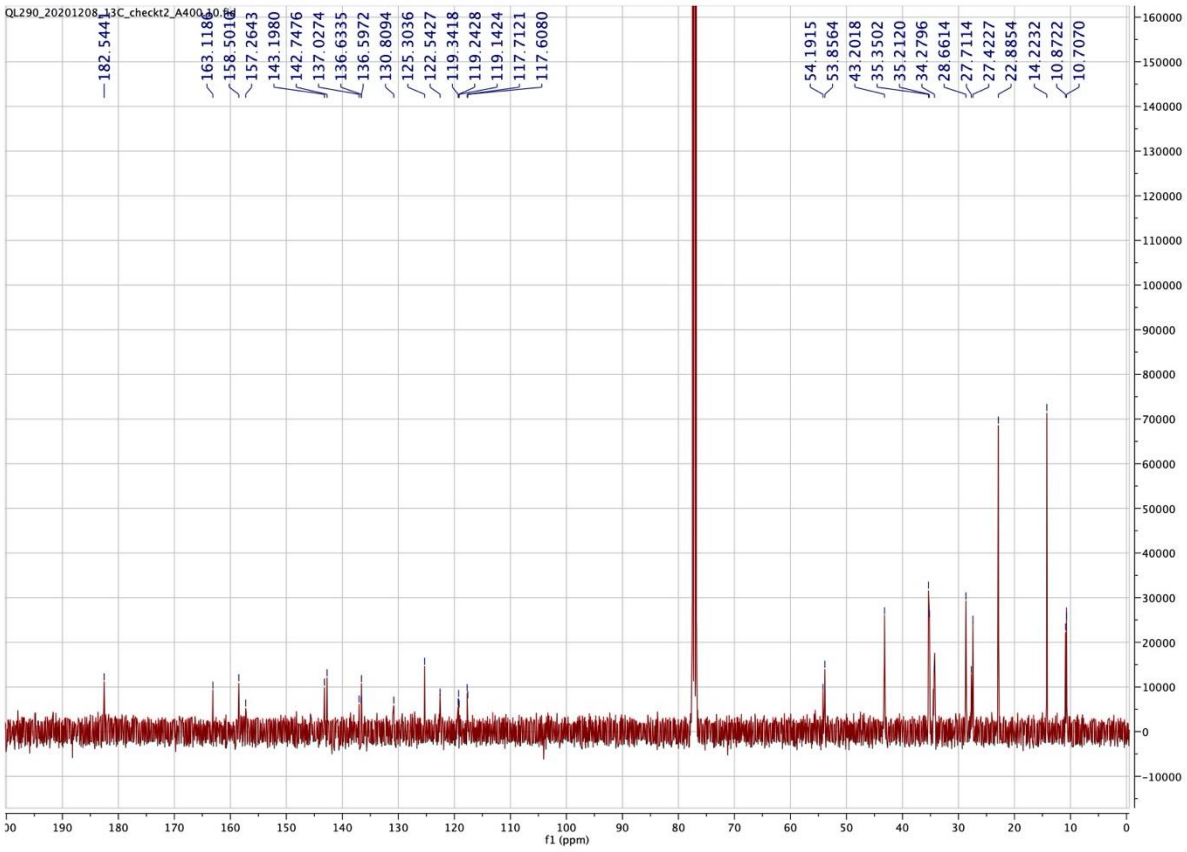

Figure S8. ^{13}C NMR for compound **3** in $CDCl_3$ at room temperature with a 400 MHz NMR.

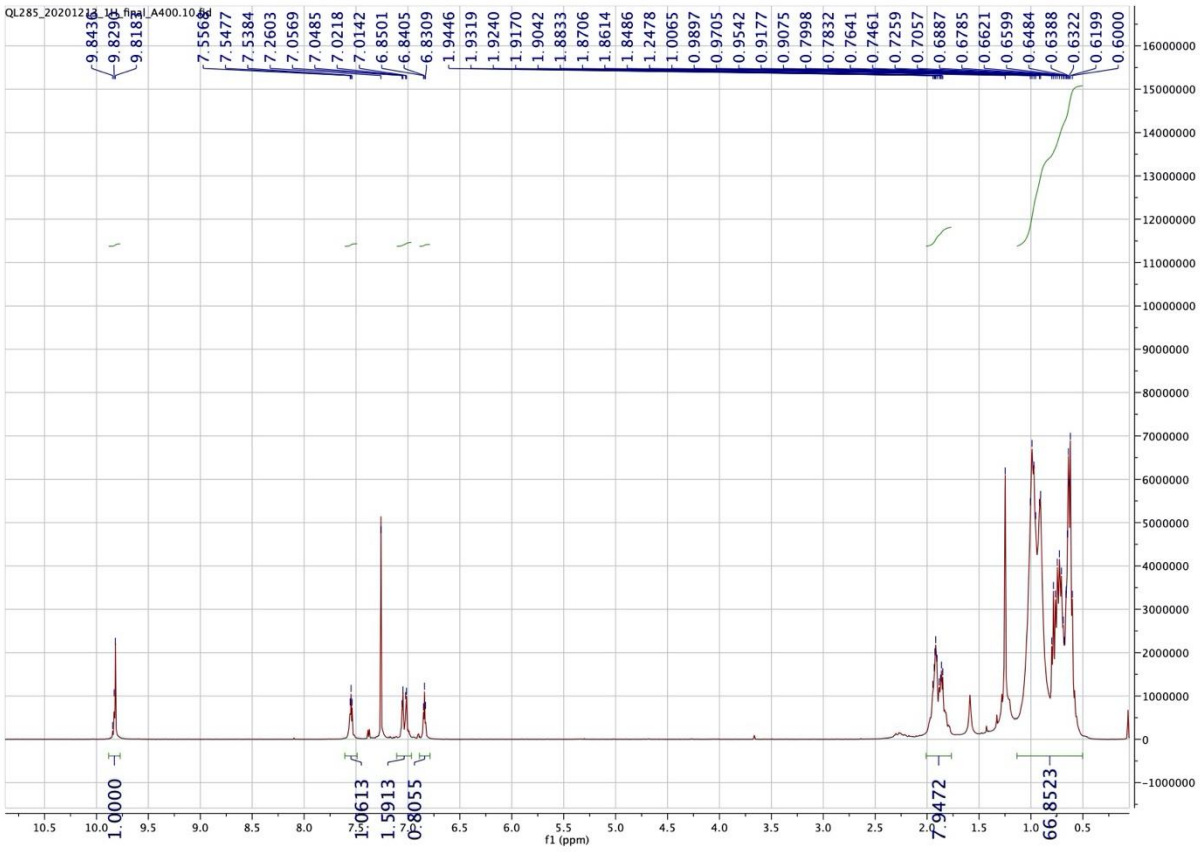

Figure S9. ^{1}H NMR for compound **4** in $CDCl_3$ at room temperature with a 400 MHz NMR.

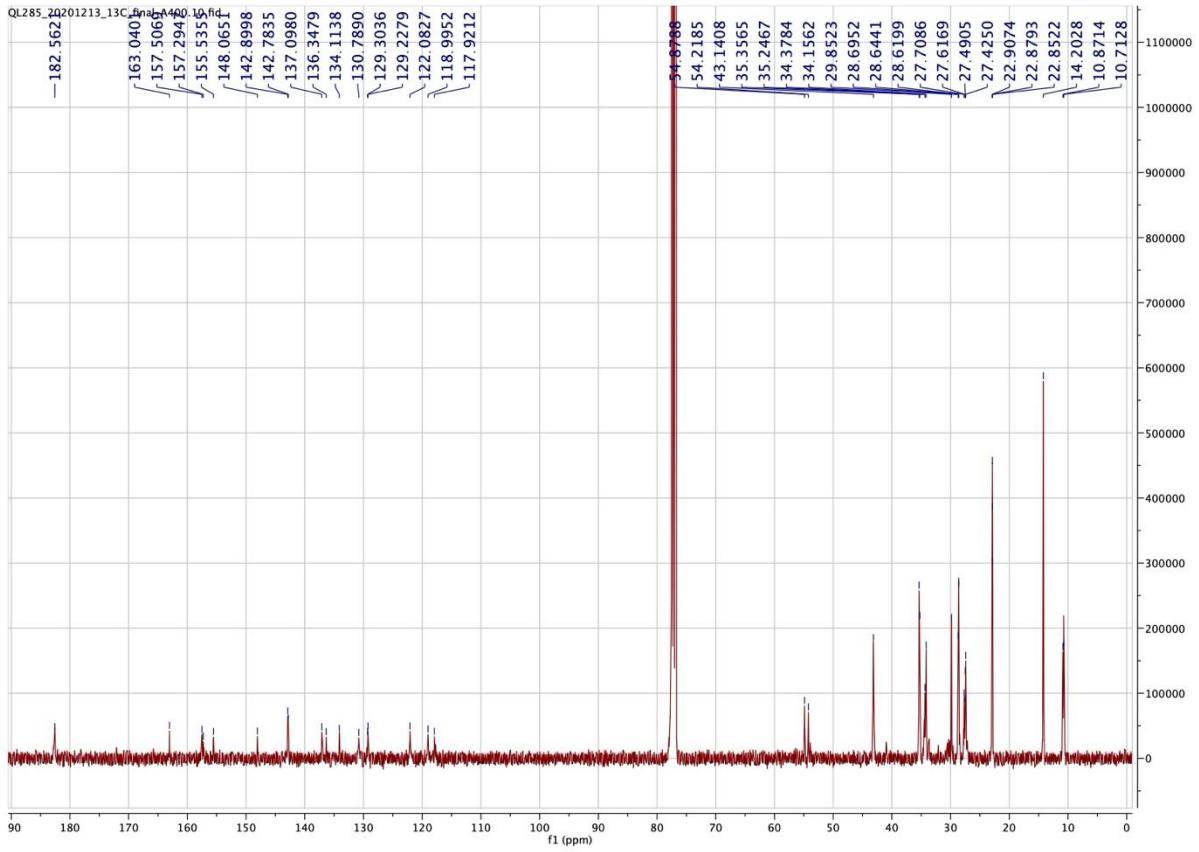

Figure S10. ^{13}C NMR for compound **4** in $CDCl_3$ at room temperature with a 400 MHz NMR.

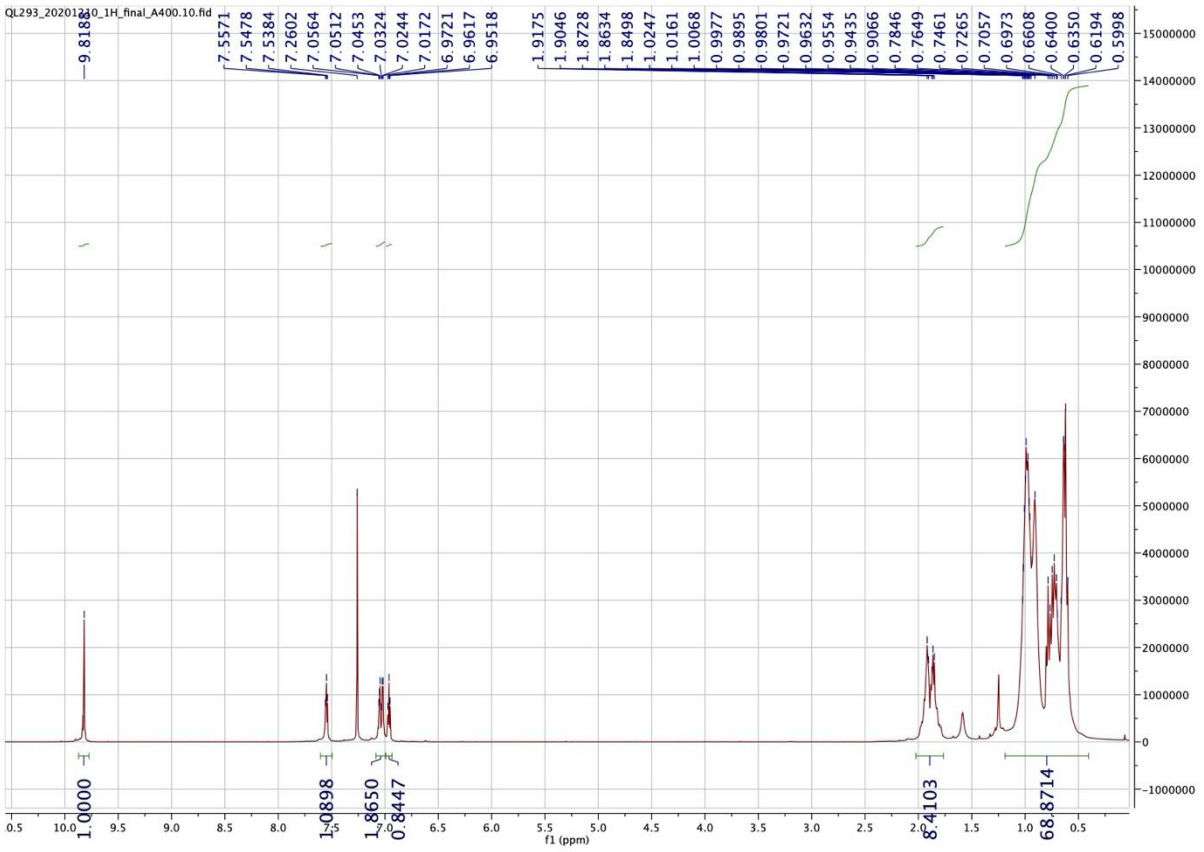

Figure S11. ^{1}H NMR for compound **5** in $CDCl_3$ at room temperature with a 400 MHz NMR.

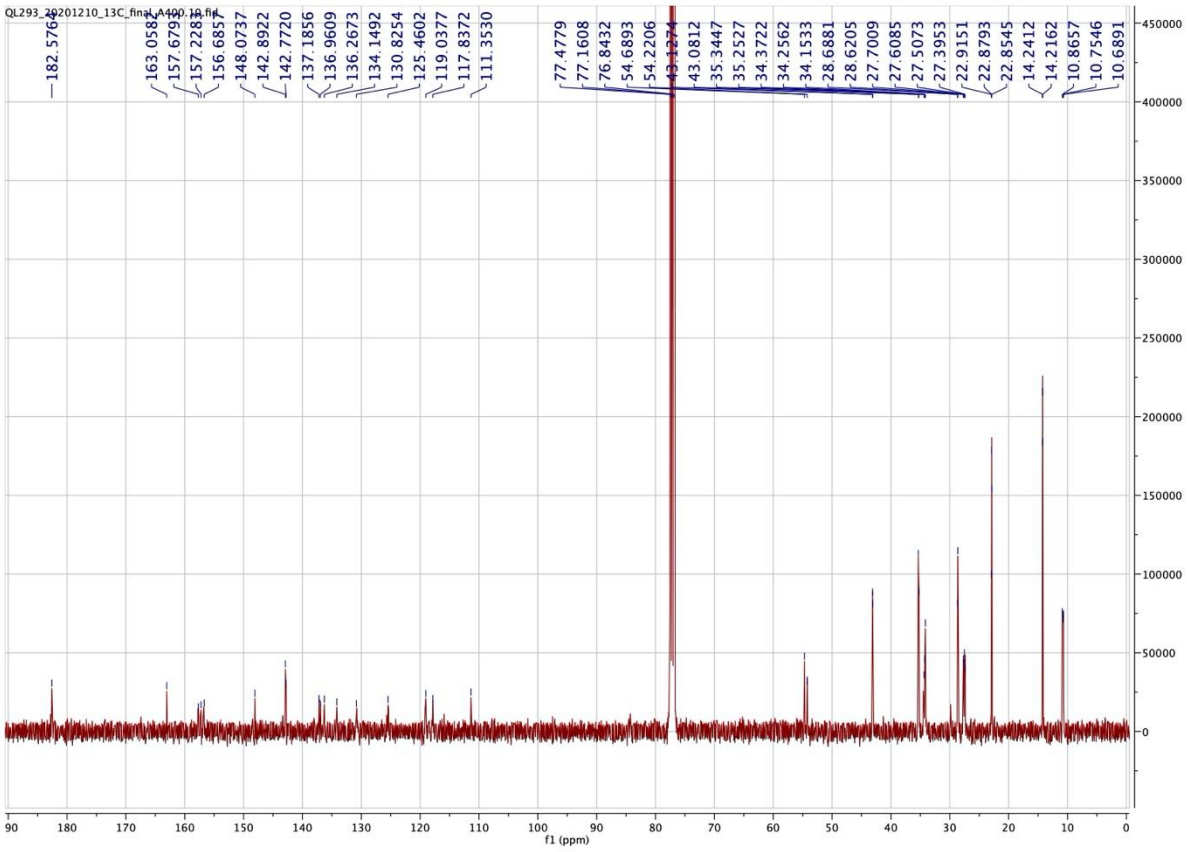

Figure S12. ^{13}C NMR for Compound 5 in $CDCl_3$ at room temperature with a 400 MHz NMR.

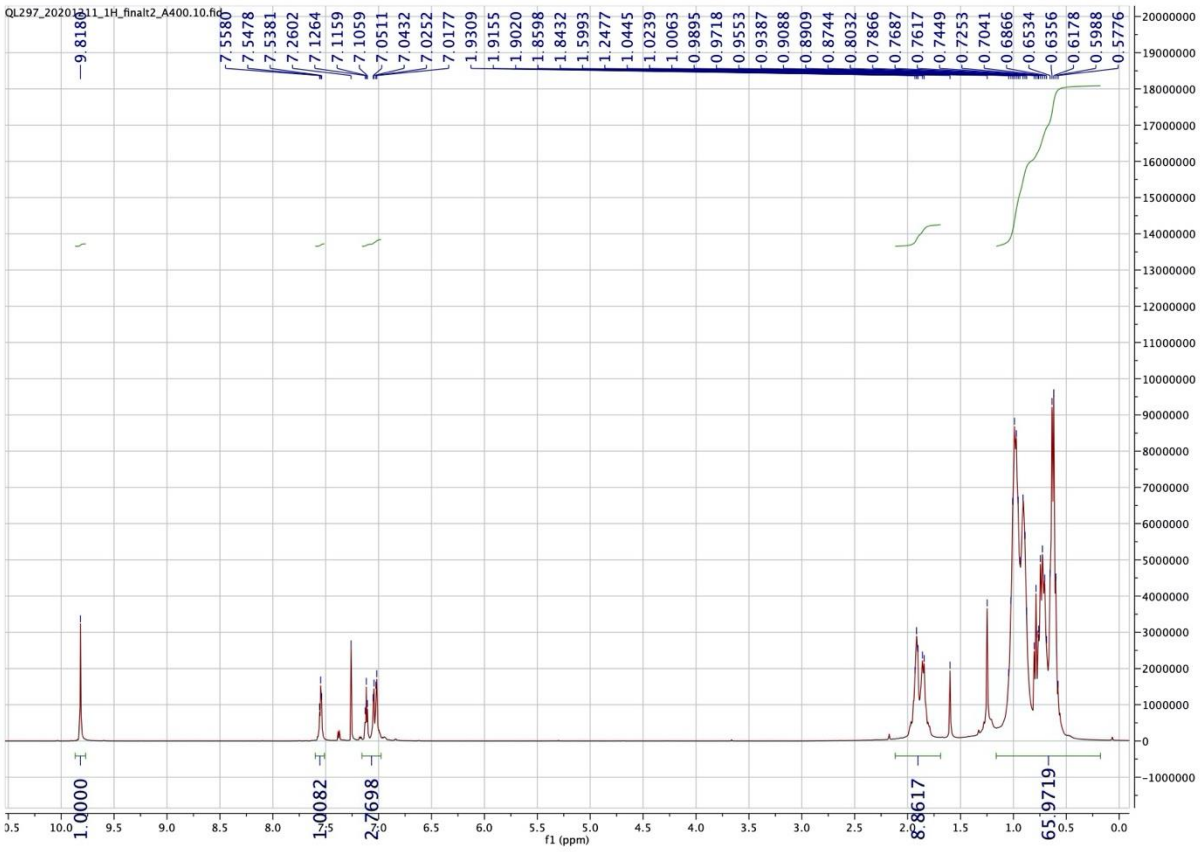

Figure S13. ^{1}H NMR for compound **6** in $CDCl_3$ at room temperature with a 400 MHz NMR.

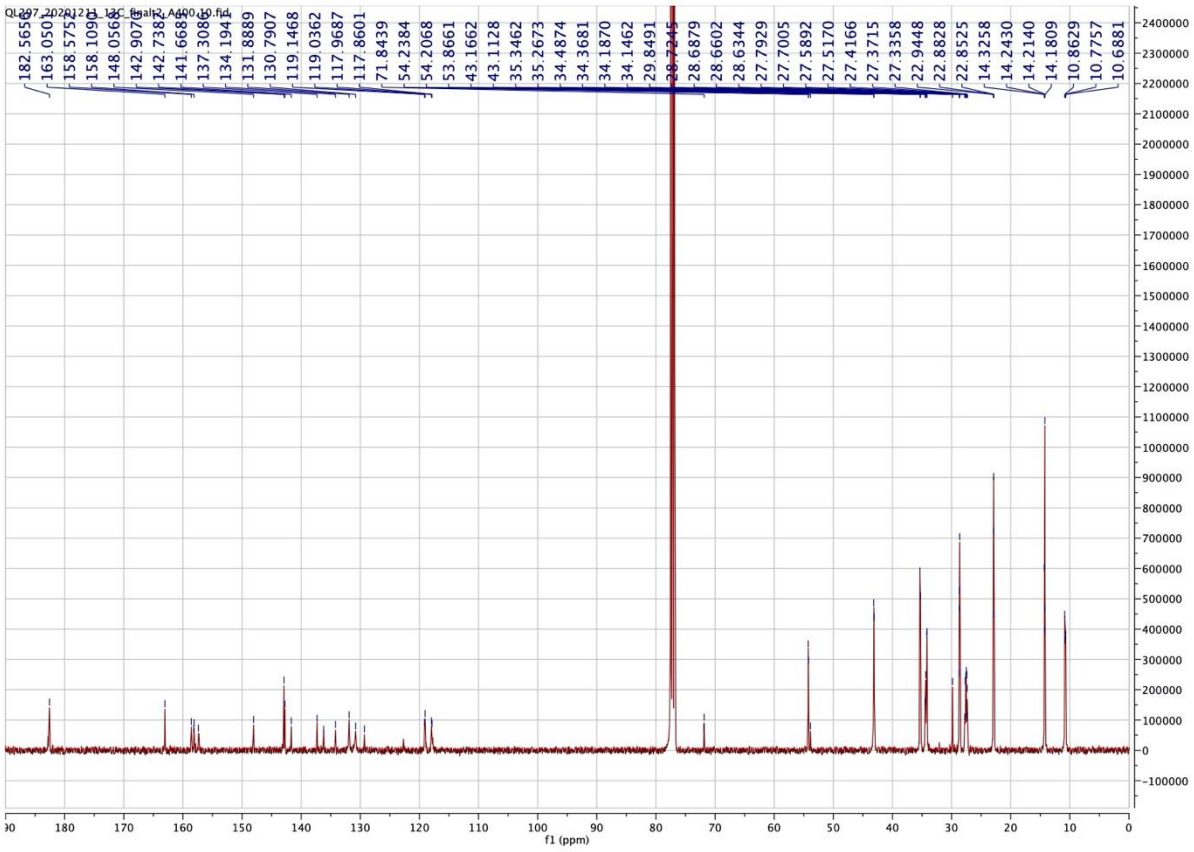

Figure S14. ^{13}C NMR for compound **6** in $CDCl_3$ at room temperature with a 400 MHz NMR.

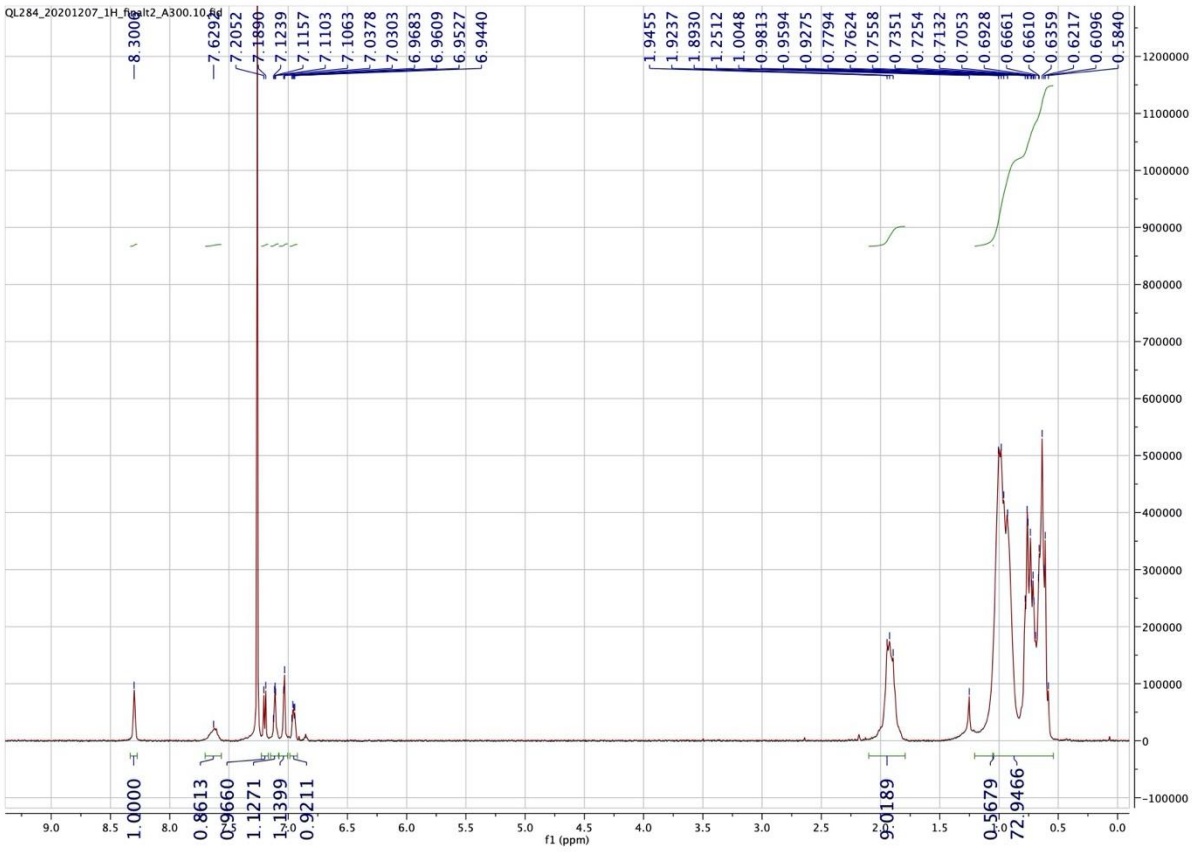

Figure S15. ^{1}H NMR for **AB4** in $CDCl_3$ at room temperature with a 300 MHz NMR.

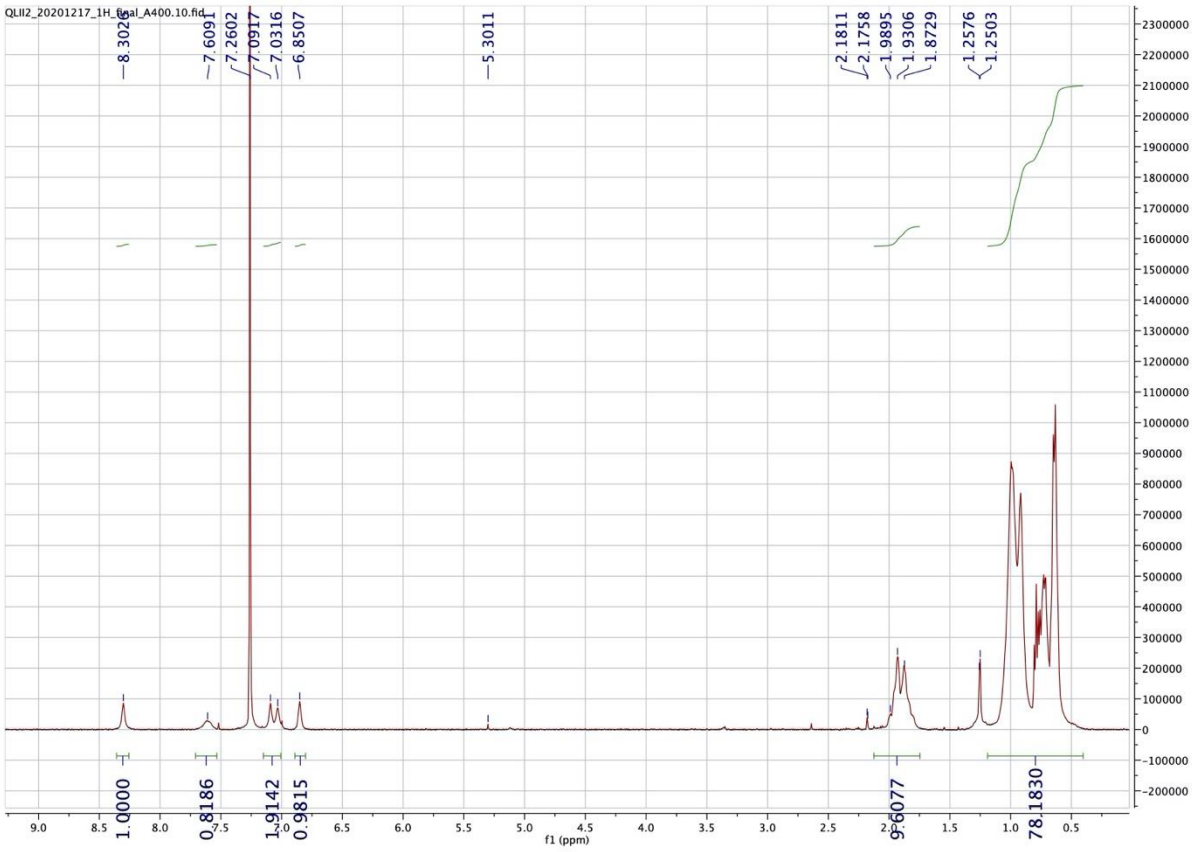

Figure S16. ^{1}H NMR for **AB5** in $CDCl_3$ at room temperature with a 400 MHz NMR.

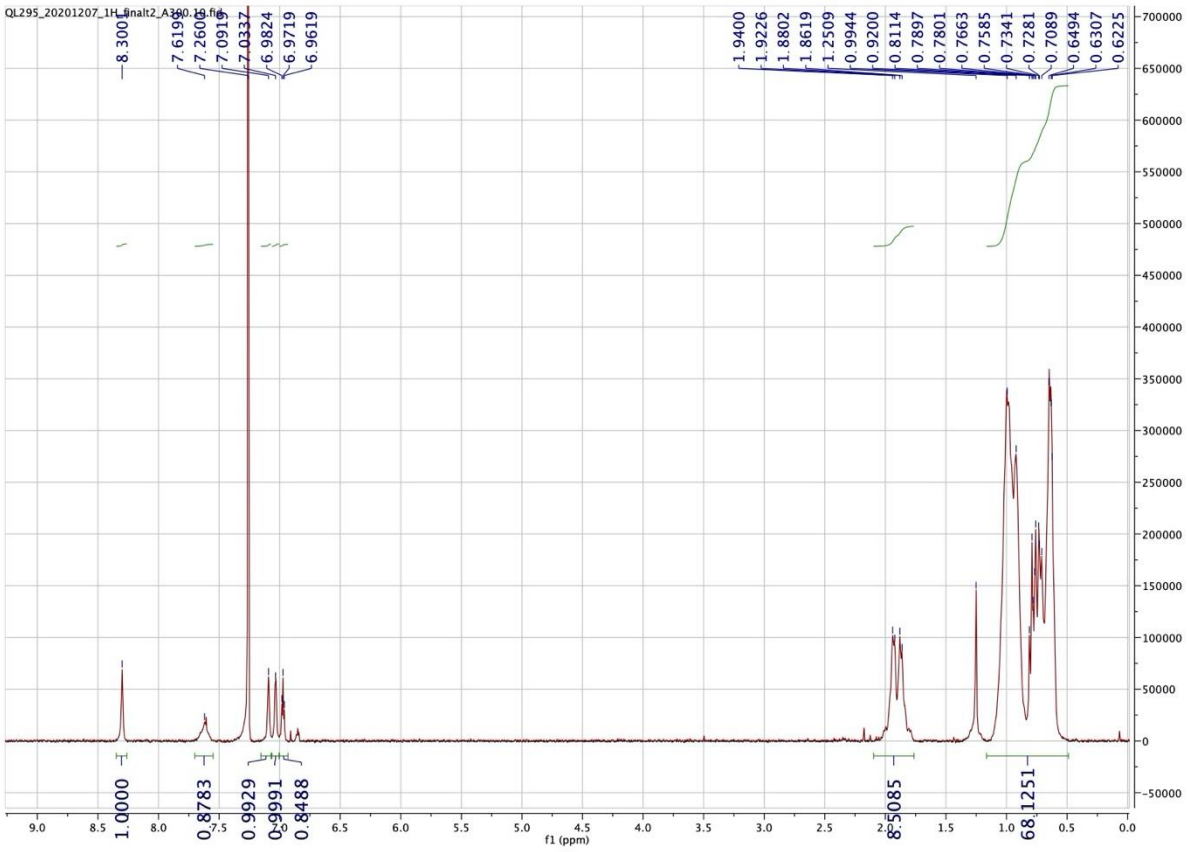

Figure S17. ^{1}H NMR for **AB6** in $CDCl_3$ at room temperature with a 300 MHz NMR.

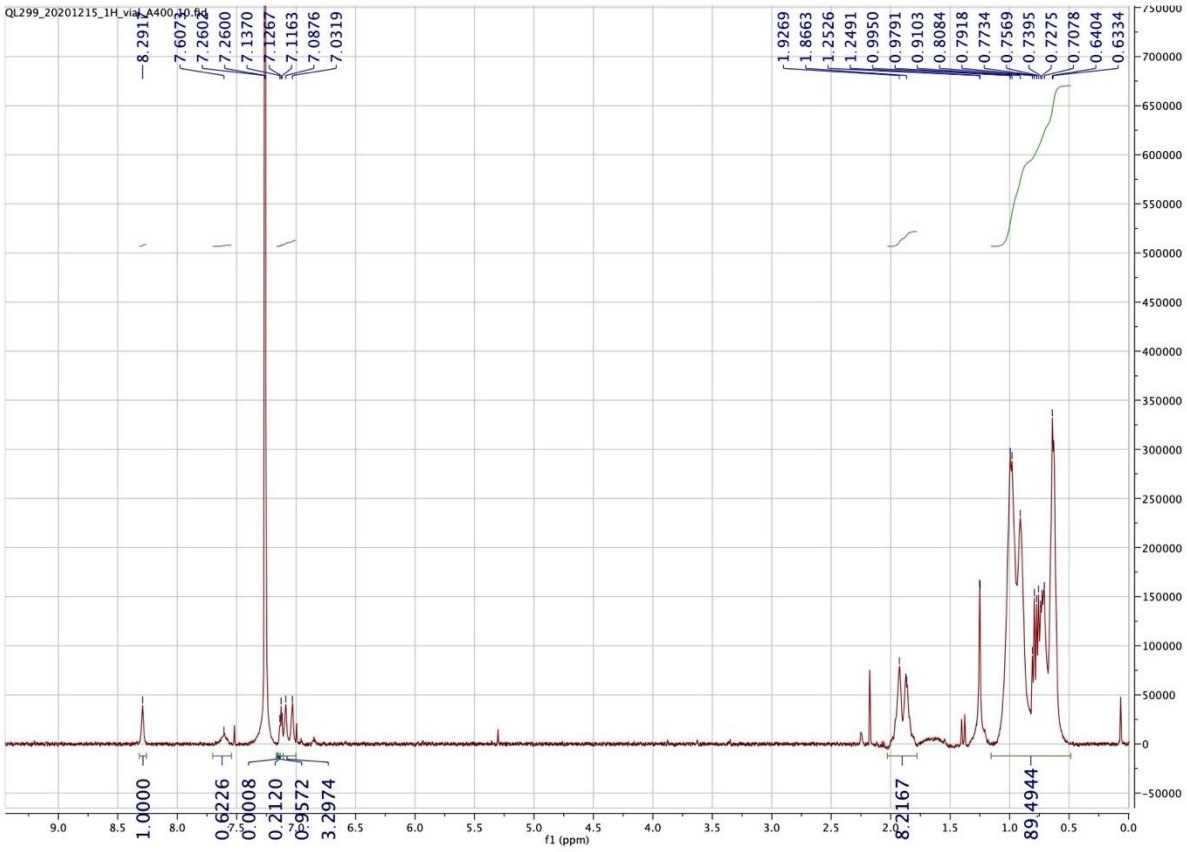

Figure S18. ^{1}H NMR for **AB7** in $CDCl_3$ at room temperature with a 400 MHz NMR.

2. Computational Results

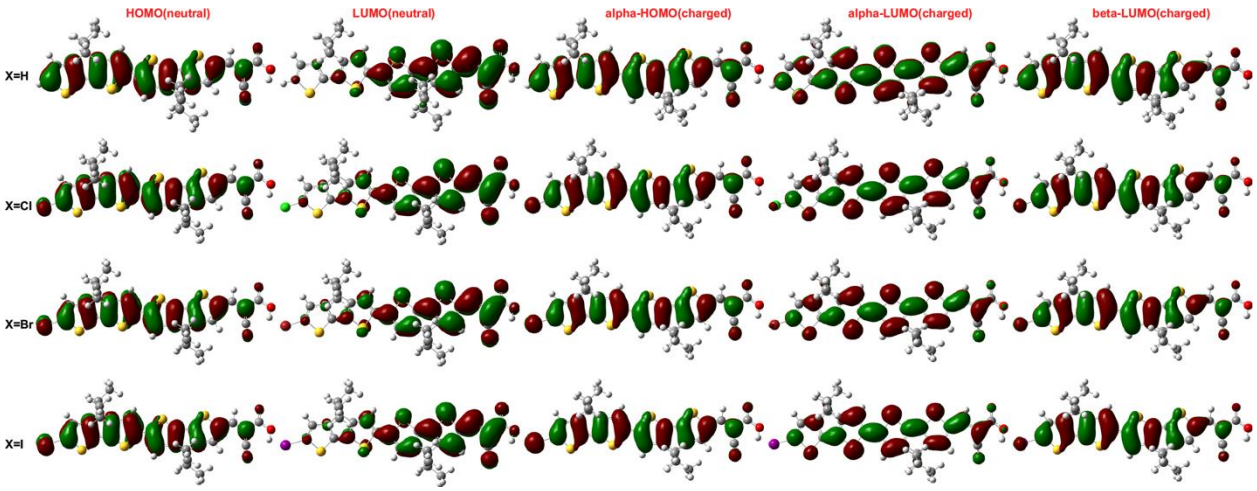

Figure S19. Molecular orbital (MO) diagrams of the neutral and positively charged dyes. The green and red surface represents the positive and negative signs of MO at isovalue = 0.02 a.u, respectively.

Table S1: Calculated charge transfer distance[234] due to excitation, the total amount of charge transfer, and wavelength associated with the excitation from the ground to the first singlet excited state (S_0-S_1) for the neutral and positively charged dyes.

Substituents (X)	D_{CT} (Å)		q_{CT} ($\|e^-\|$)		λ (nm)	
	Neutral	Charged	Neutral	Charged	Neutral	Charged
H	2.96	1.79	0.484	0.374	423.08	782.26
Cl	2.86	1.46	0.472	0.378	422.20	797.11
Br	2.87	1.36	0.473	0.387	423.00	800.92
I	2.88	1.23	0.477	0.401	424.50	805.66

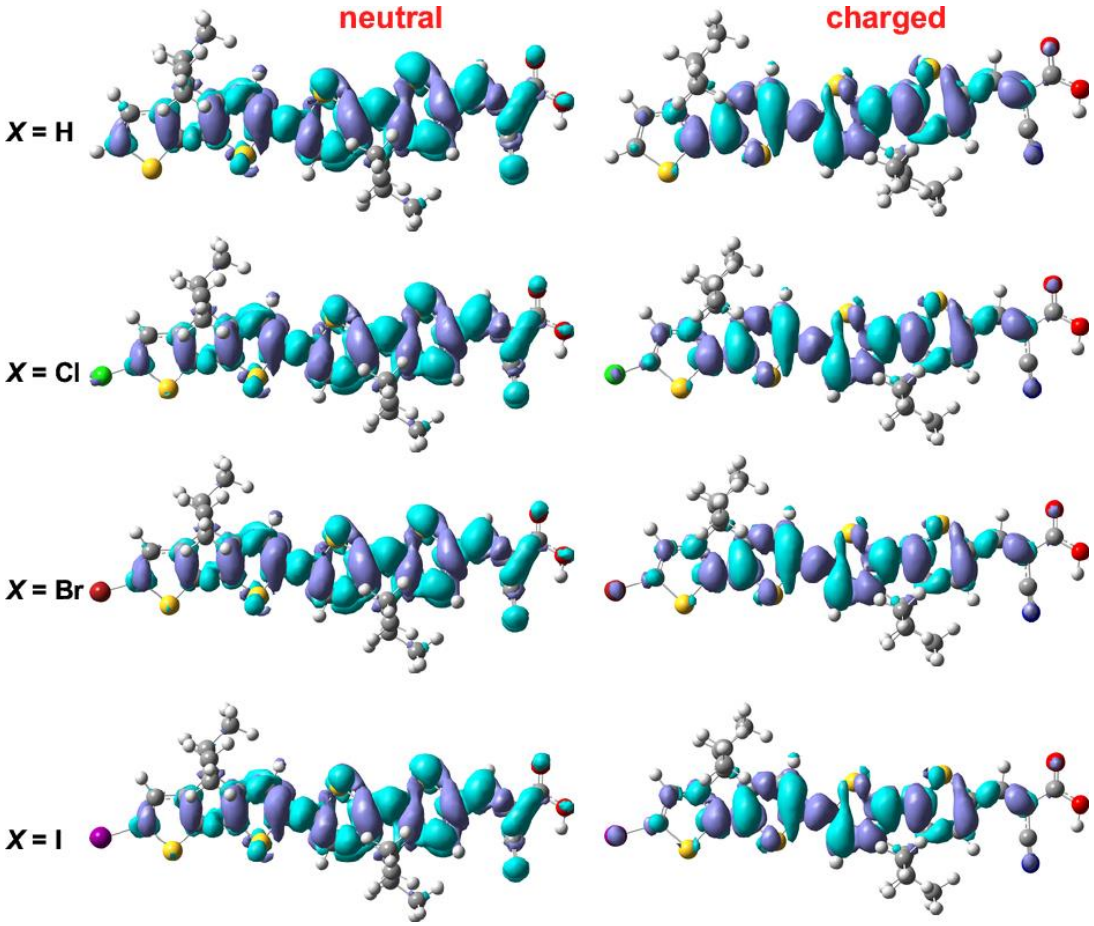

Figure S20. The total density difference ($\Delta\rho$) between the ground and first singlet excited state (S_0-S_1) of the neutral and positively charged dyes. The purple and blue-green surface represents the depletion (where electrons came from) and increment (where electrons went) of density due to excitation at isovalue=0.0005 a.u, respectively.

Table S2. Computed frontier molecular orbital energies, energy gap, optical gap and partial charges on the substituents for neutral and positively charged dyes.

Substituents (X)	HOMO (eV)		LUMO (eV)		HOMO-LUMO gap (eV)		Optical gap (eV) (S_0-S_1)		CM5 charges (e^-) on the substituents	
	Neutral	Charged	Neutral	Charged	Neutral	Charged	Neutral	Charged	Neutral	Charged
H	-6.82	-7.45	-1.27	-1.84	5.55	5.61	2.93	1.58	0.122	0.141
Cl	-6.87	-7.47	-1.28	-1.89	5.58	5.57	2.94	1.55	-0.069	-0.017

Br	-6.86	-7.47	-1.28	-1.90	5.58	5.57	2.93	1.55	-0.018	0.039
I	-6.85	-7.46	-1.28	-1.89	5.57	5.57	2.92	1.54	-0.0007	0.063

Table S3. Calculated optical properties of the neutral and charged dyes. The electronic transitions with orbital contributions, wavelength (λ) associated with that particular transition, and the oscillator strength (f) of the individual transitions. The orbital contributions of the charged dyes are not normalized.

Substituents (X)	Transitions	Orbital Contribution (%)		λ (nm)		f	
		Neutral	Charged	Neutral	Charged	Neutral	Charged
H	$S_0 \rightarrow S_1$	H → L 78%	H(β) → L(β) 150%	423.08	782.26	2.0776	0.3957
	$S_0 \rightarrow S_2$	H → L+1 53%	H(α) → L(α) 66%	312.29	543.31	0.0115	0.9012
	$S_0 \rightarrow S_3$	H-1 → L 42%	H(α) → L(α) 69%	280.37	523.61	0.0742	0.8279
Cl	$S_0 \rightarrow S_1$	H → L 78%	H(β) → L(β) 154%	422.20	797.11	2.1630	0.4410
	$S_0 \rightarrow S_2$	H → L+1 55%	H(α) → L(α) 75%	315.62	550.55	0.0197	1.0326
	$S_0 \rightarrow S_3$	H-1 → L 44%	H(α) → L(α) 62%	280.11	532.20	0.0647	0.7532
Br	$S_0 \rightarrow S_1$	H → L 78%	H(β) → L(β) 155%	422.95	800.92	2.1960	0.4643
	$S_0 \rightarrow S_2$	H → L+1 55%	H(α) → L(α) 76%	316.56	553.71	0.0234	1.0478
	$S_0 \rightarrow S_3$	H-1 → L 43%	H(α) → L(α) 62%	280.39	532.65	0.0660	0.7542
I	$S_0 \rightarrow S_1$	H → L 77%	H(β) → L(β) 155%	424.50	805.66	2.2386	0.4946

	$S_0 \rightarrow S_2$	H $\rightarrow$ L+1 55%	H(α) $\rightarrow$ L(α) 76%	317.69	557.74	0.0270	1.0516
	$S_0 \rightarrow S_3$	H$\rightarrow$ L+2 47%	H(α) $\rightarrow$ L(α) 63%	298.03	533.08	0.0003	0.7660

Table S4. Calculated binding energy between the redox-shuttles and different dyes, the distance between the dye substituents (*X*) and redox-shuttles, and the dihedral angle connecting the substituents with the redox-shuttles.

Redox-shuttle	Substituents (*X*)	Binding Energy (kcal/mole)		Distance (Å)		N-N-X-C dihedral (ϕ^0)	
		Neutral	Charged	Neutral	Charged	Neutral	Charged
Co(N-tpy)$_2$	H	-7.17	-7.27	2.34	2.28	-5.41	-1.20
	Cl	-6.37	-6.22	3.14	3.07	4.29	5.05
	Br	-7.69	-7.39	3.07	3.00	34.91	19.24
	I	-9.44	-9.30	3.07	3.00	29.58	16.27
Co(tpy)$_2$	H	-	-4.62	-	3.08	-	93.95
	Cl	-	-4.81	-	3.63	-	-30.86
	Br	-	-4.86	-	3.76	-	84.40
	I	-	-5.01	-	3.96	-	128.24

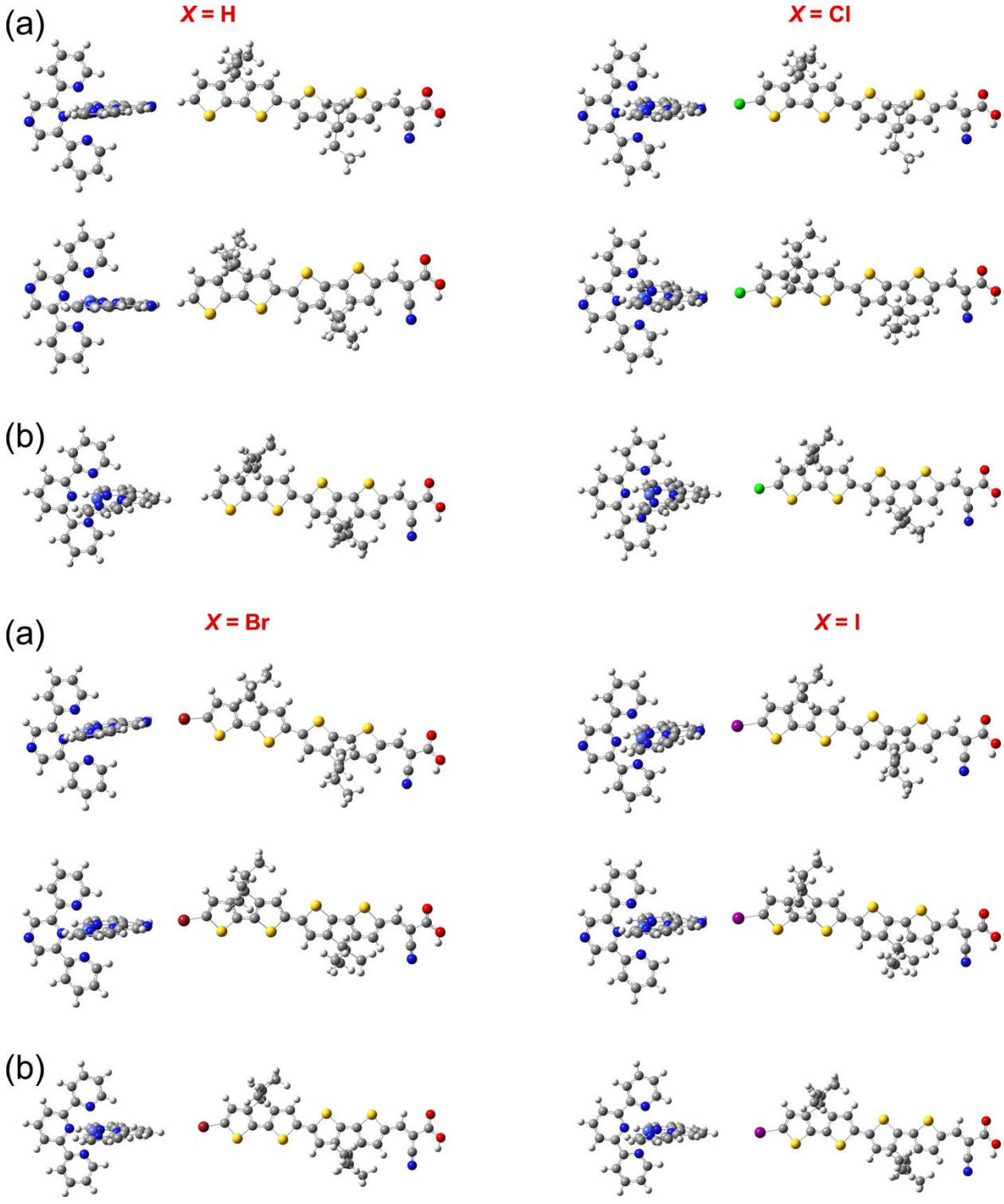
(a)
X = H
X = Cl
(b)
(a)
X = Br
X = I
(b)

Figure S21. Optimized geometries of the dyes with different redox shuttles. (a) Neutral (top) and charged (bottom) dyes with Co(*N*-tpy)$_2$ redox shuttle; and (b) charged dyes with Co(tpy)$_2$ redox shuttle.

3. Transient Absorption Spectroscopy

TAS device fabrication: TEC 10 glass was purchased from Hartford Glass. Once cut into 2x2 cm squares, the substrate was rinsed with water and acetone. The electrodes were comprised of a single 10 µm or 5 µm mesoporous TiO_2 layer (particle size, 30 nm, Dyenamo, DN-GPS-30TS) for iodine and cobalt cells, respectively. All the layers were screen printed from a Sefar screen (54/137–64W). Following the print, the substrate was heated for 7 minutes at 125 ^oC and the thickness was measured with a profilometer (Alpha-Step D-500 KLA Tencor). Once the layer was deposited, the substrate was then sintered with progressive heating from 125^oC (5-minute ramp from r.t., 5 minute hold) to 325 ^oC (15 minute ramp from 125^oC, 5 minute hold) to 375 ^oC (5 minute ramp from 325 ^oC, 5 minute hold) to 450 ^oC (5 minute ramp from 375 ^oC, 15 minute hold) to 500 ^oC (5 minute ramp from 450 ^oC, 15 minute hold) using a programmable furnace (Vulcan® 3-Series Model 3-550). The cooled electrode was prepared by immersing the TiO_2 film into the dye solution for 3 hours. The solution is 0.3 mM of dye in MeCN:*t*-BuOH:THF mixture (1:1:1) with a 20:1 CDCA:dye ratio unless otherwise indicated. The electrodes were washed with acetonitrile and the dried substrates were then partially sealed with a pre-cut semicircle of 25 µm thick hot melt film (Surlyn, Solaronix, "Meltonix 1170-25") and a thin glass cover slip by heating the system at 130 ^oC under 0.1 psi pressure for 30 seconds. Devices were completed by filling the cells with electrolyte solution by injecting it into the open portion of the coverslip with a micro syringe. The device is then sealed with a light-cured adhesive (Permabond UV6231) and curing under 450 nm light for 45 seconds. Iodine cells were light-soaked for 24 hours before measurements were taken.

Table S5. Summary of fit parameters for target dyes **AB4**, **AB5**, **AB6** and **AB7** with the $Co(tpy)_2^{2+}$ redox shuttle where k_{rec} represents the rate with no redox shuttle present (no RS) and k_{reg} represents the rate in the presence of the redox shuttle.

	τ_{ww} (μs)	β	Γ	τ_{obs} (μs)	k_{rec} *or* k_{reg} (s^{-1})	Φ (%)
AB4						
No RS	3.20	0.40	1.33	10.64	94,000	
$Co(tpy)_2^{2+}$	0.087	0.67	0.89	0.120	8.65e6	99.0
AB5						
No RS	2.80	0.40	1.33	9.30	108,000	
$Co(tpy)_2^{3+/2+}$	0.050	0.67	0.89	0.070	1.5e7	99.3
AB6						
No RS	5.80	0.50	1.00	11.60	86,000	
$Co(tpy)_2^{3+/2+}$	0.070	0.56	0.93	0.120	8.3e6	99.0
AB7						
No RS	4.80	0.47	1.16	11.90	84,000	
$Co(tpy)_2^{3+/2+}$	0.071	0.57	0.92	0.120	8.3e6	99.0

Table S6. Summary of fit parameters for target dyes **AB4**, **AB5**, **AB6** and **AB7** with the $Co(N\text{-}tpy)_2^{2+}$ redox shuttle where k_{rec} is the rate with without redox shuttle present (no RS) and k_{reg} represents the rate of the regeneration reaction. Device preparation including electrolyte solution components and TAS measurement details are stated in the manuscript under sections titled "TAS TiO2-Dye Film Preparation" and "TAS Measurements", respectively.

	τ_{ww}	β	Γ	τ_{obs} (μs)	k_{rec} *or* k_{reg} (s^{-1})	Φ (%)
AB4						

No RS	3.20	0.40	1.33	10.64	94.000	
Co(*N*-	2.50	0.57	0.92	4.04	242,000	72.0
AB5						
No RS	2.80	0.40	1.33	9.30	108.000	
Co(*N*-	1.60	0.57	0.92	2.60	385,000	84.4
AB6						
No RS	5.80	0.50	1.00	11.60	86.000	
Co(*N*-	1.50	0.51	0.98	2.90	345,000	80.0
AB7						
No RS	4.80	0.47	1.16	11.90	84.000	
Co(*N*-	3.40	0.57	0.92	5.50	182.000	68.4

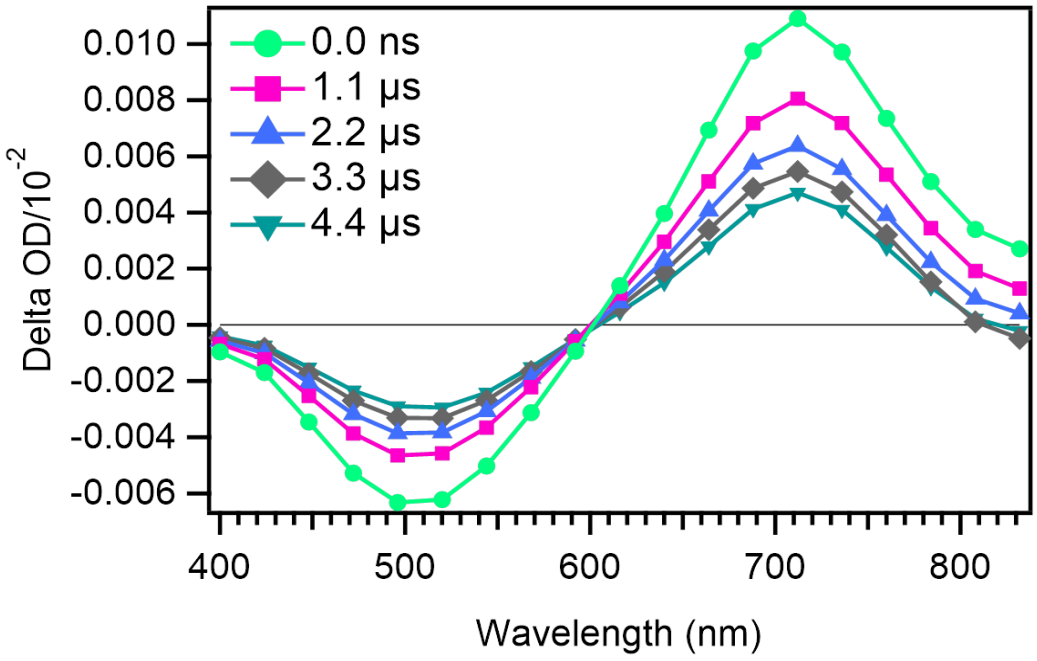

Figure S22. Spectral data for **AB4** with 0.1 M LiTFSI in MeCN without RS.

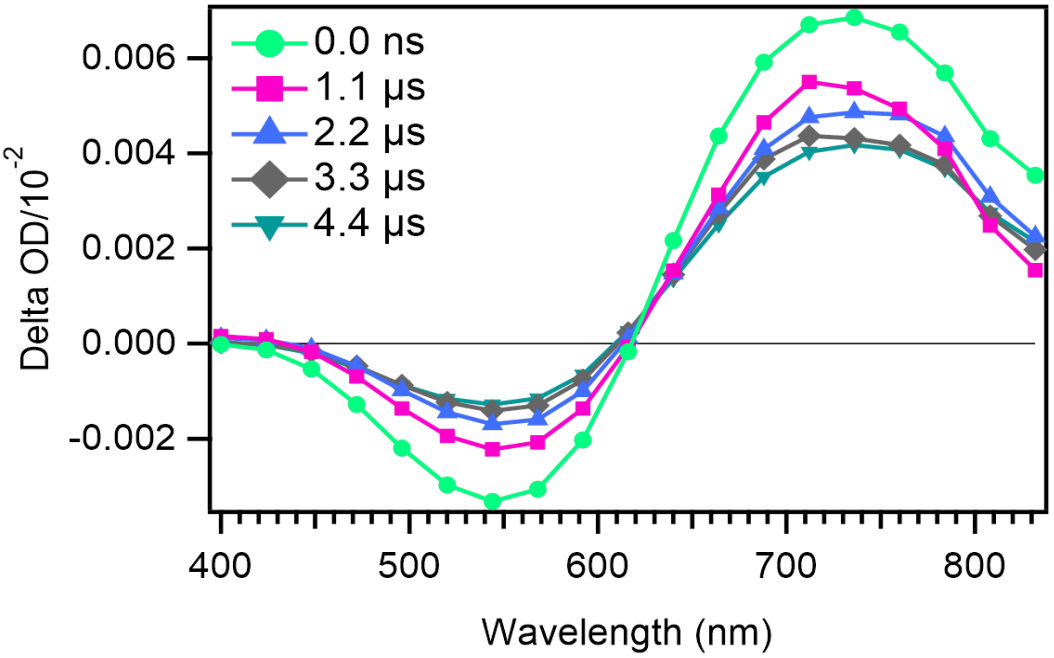

Figure S23. Spectral data for **AB4** with 0.1 M LiTFSI in MeCN with 0.25 M Co(*N*-tpy)$^{2+/3+}$.

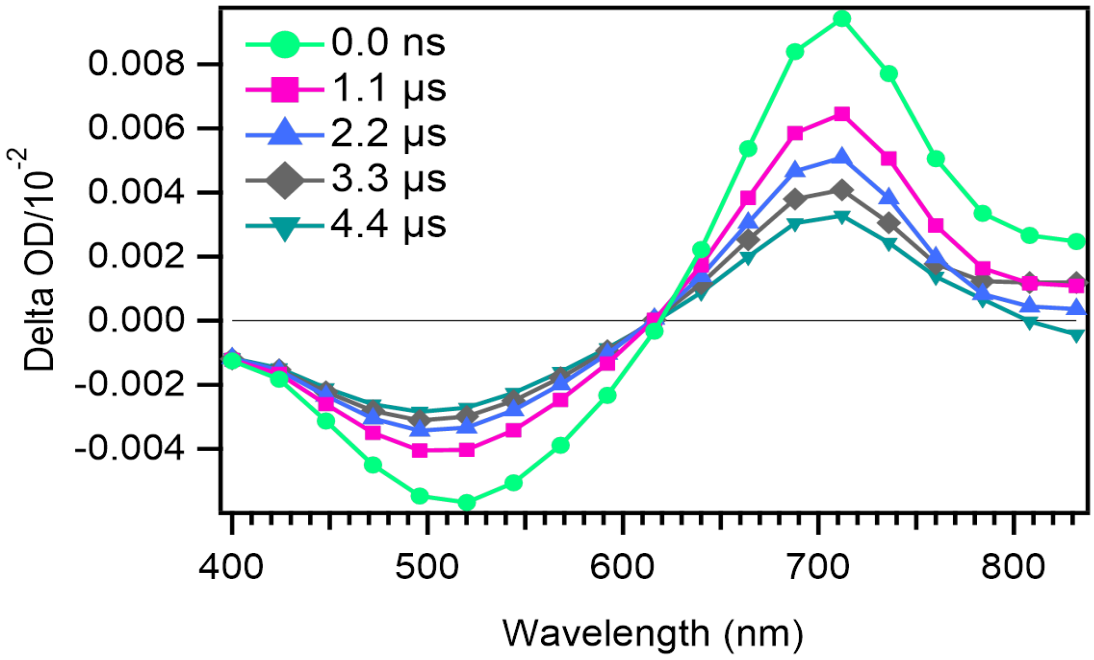

Figure S24. Spectral data for **AB4** with 0.1 M LiTFSI in MeCN with 0.25 M $Co(tpy)^{2+/3+}$.

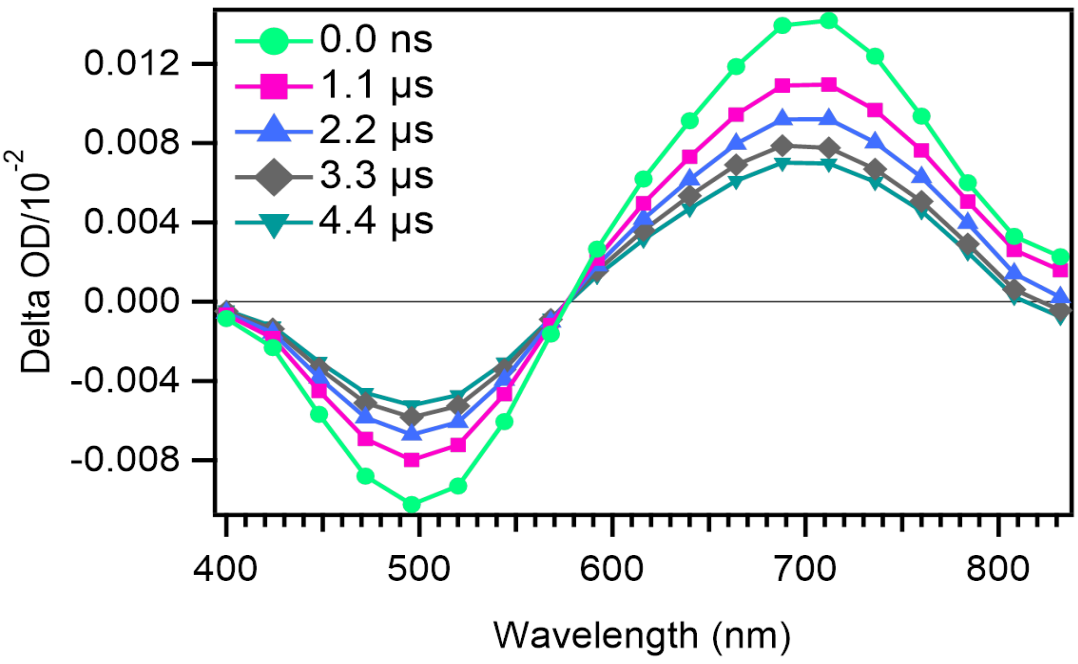

Figure S25. Spectral data for **AB5** with 0.1 M LiTFSI in MeCN.

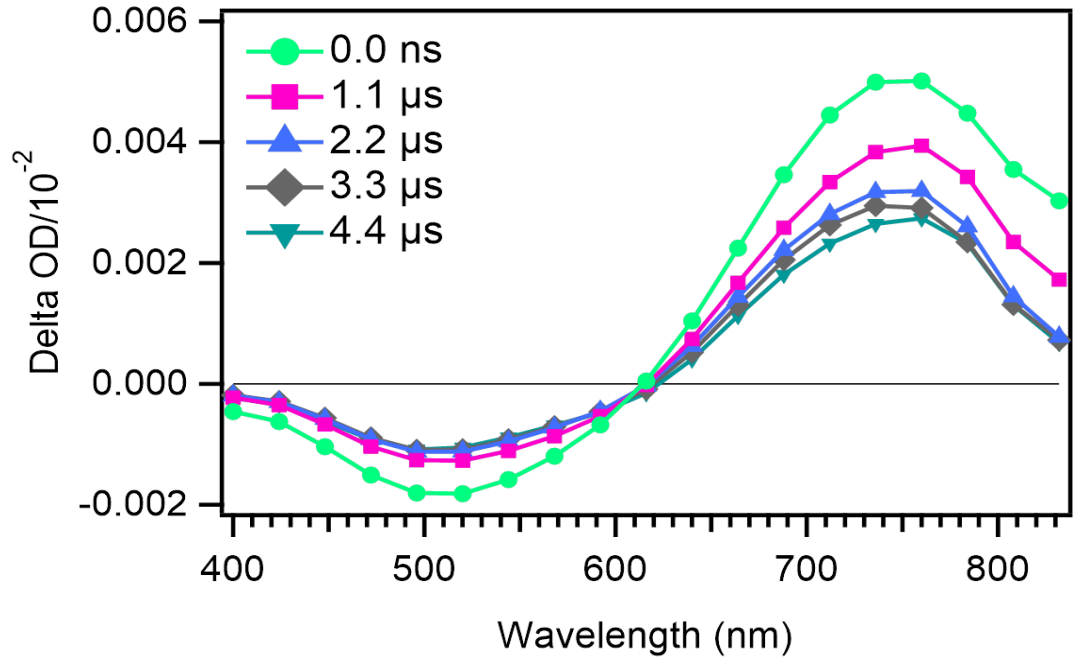

Figure S26. Spectral data for **AB5** with 0.1 M LiTFSI in MeCN with 0.25 M Co(*N*-tpy)$^{2+/3+}$.

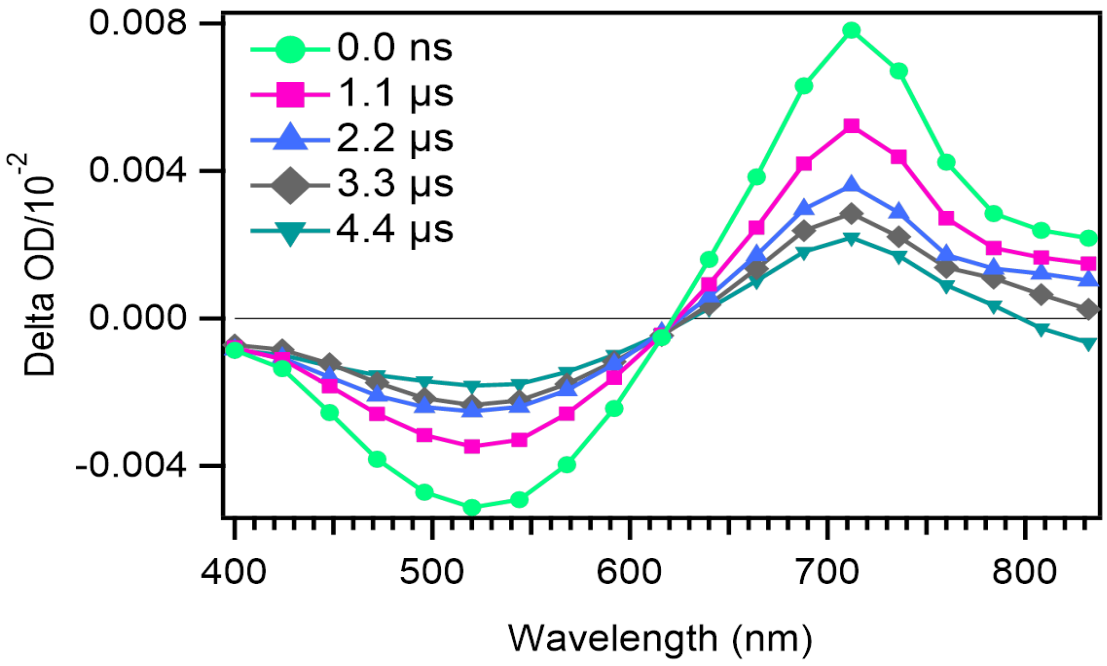

Figure S27. Spectral data for **AB5** with 0.1 M LiTFSI in MeCN with 0.25 M Co(tpy)$^{2+/3+}$.

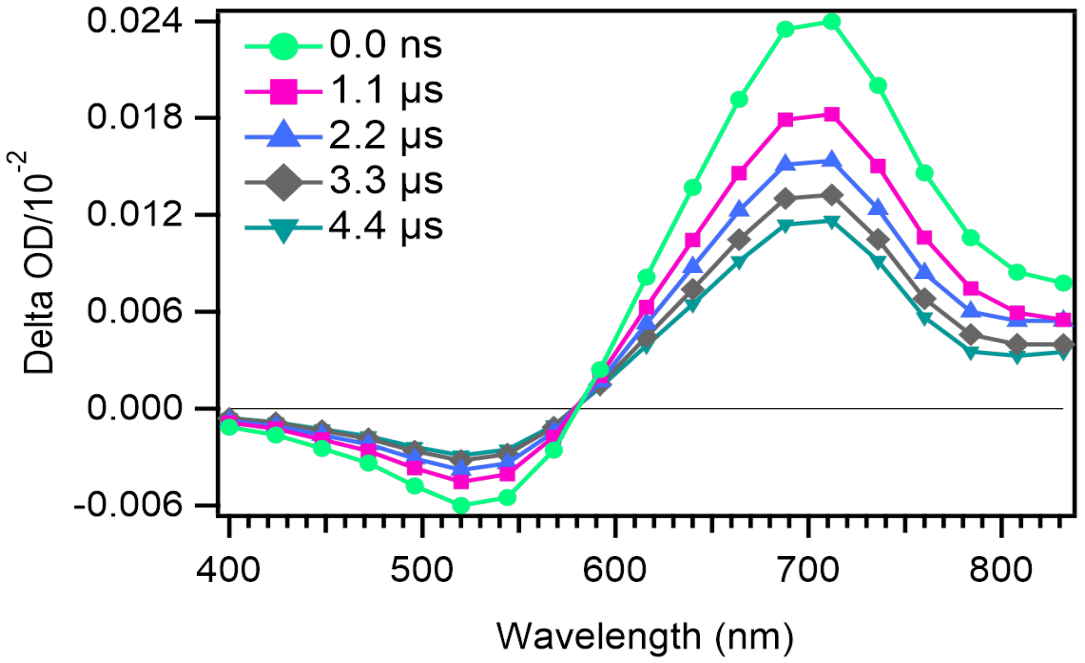

Figure S29. Spectral data for **AB6** with 0.1 M LiTFSI in MeCN.

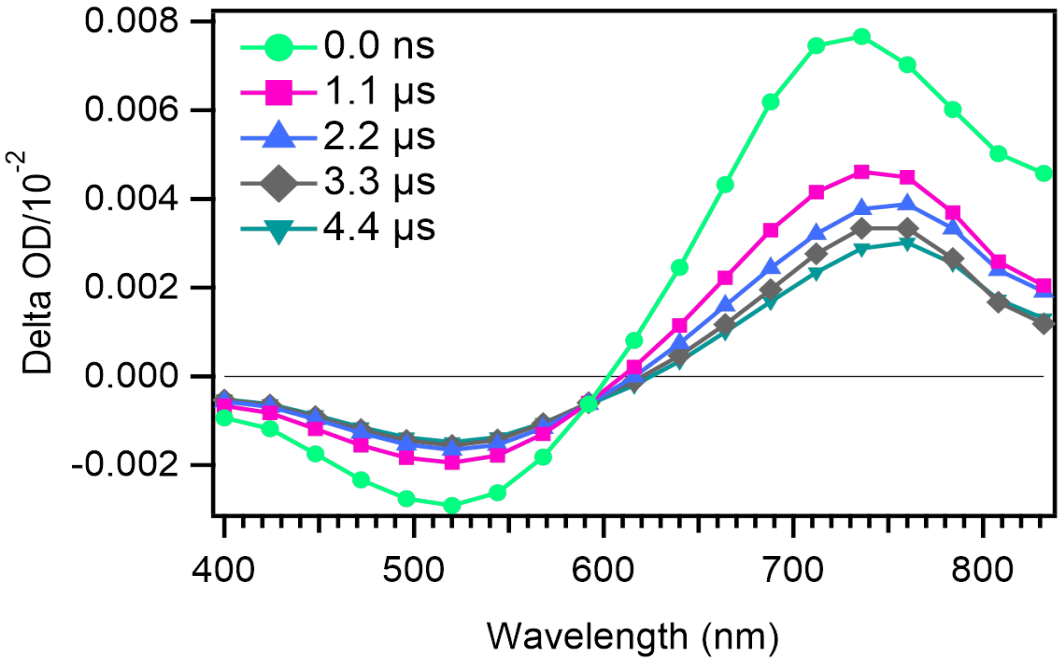

Figure S30. Spectral data for **AB6** with 0.1 M LiTFSI in MeCN with 0.25 M $Co(N\text{-}tpy)^{2+/3+}$.

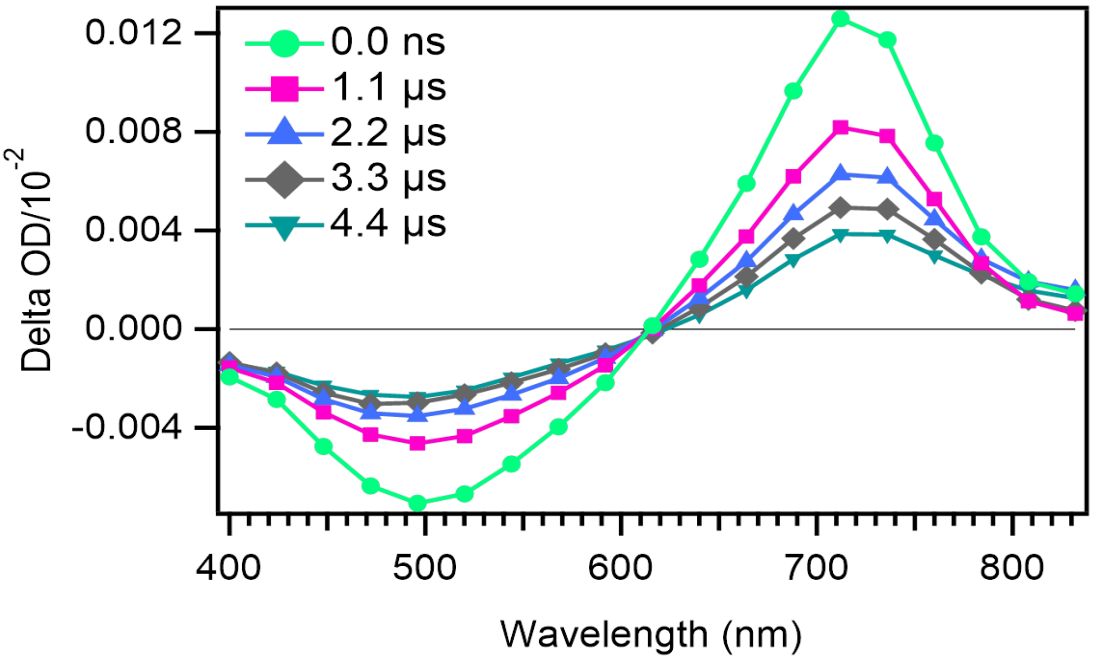

Figure S31. Spectral data for **AB6** with 0.1 M LiTFSI in MeCN with 0.25 M $Co(tpy)^{2+/3+}$.

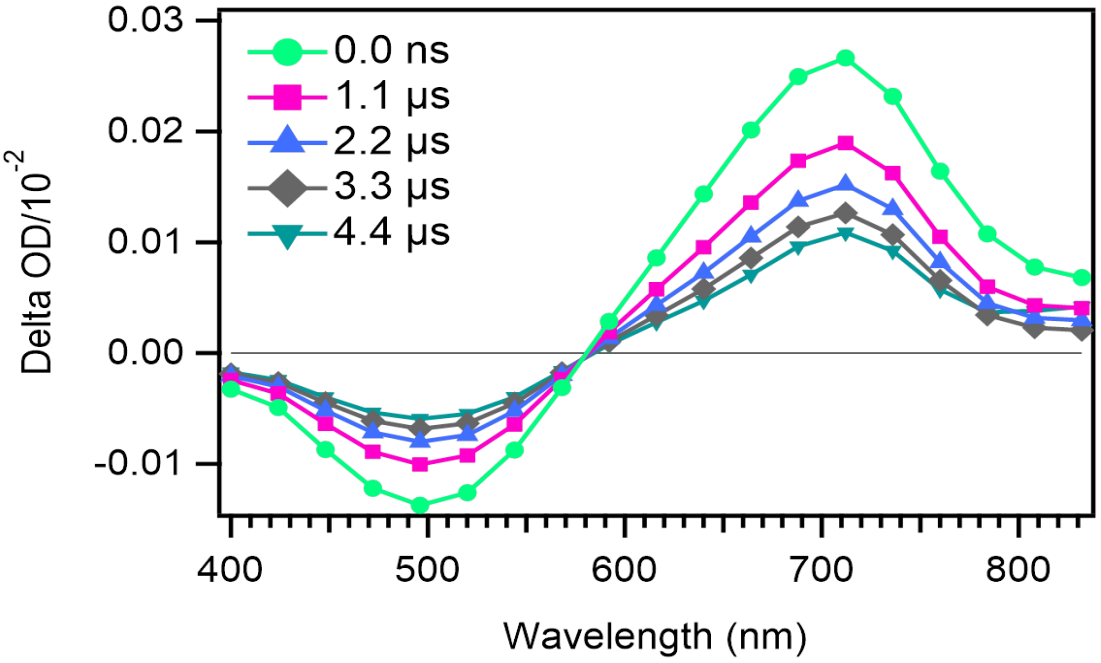

Figure S32. Spectral data for **AB7** with 0.1 M LiTFSI in MeCN.

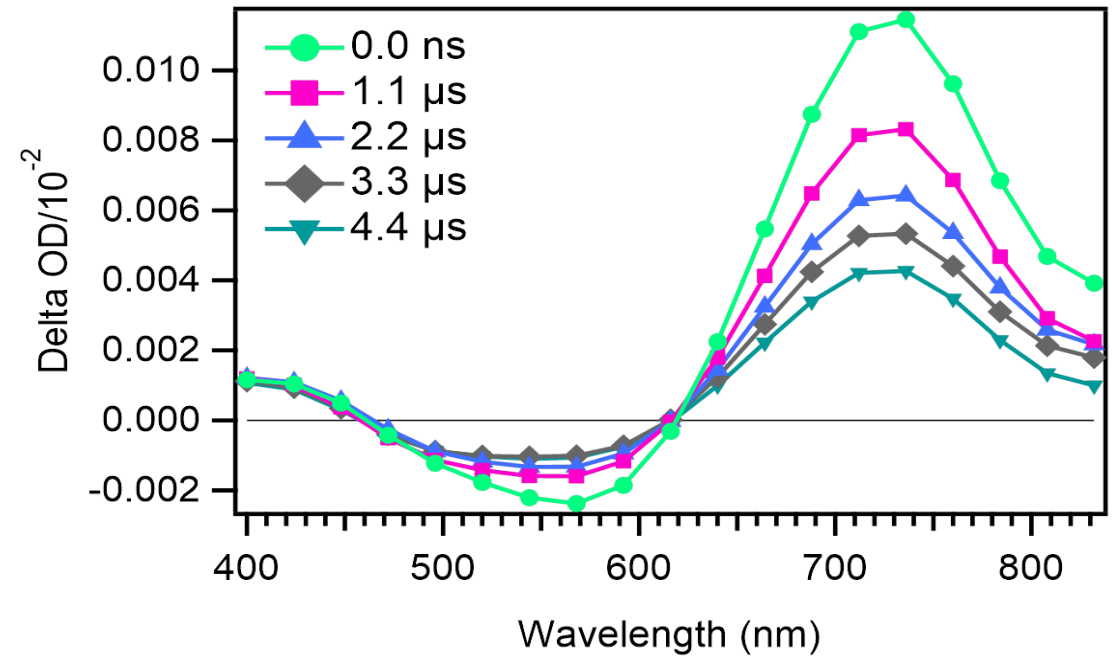

Figure S33. Spectral data for **AB7** with 0.1 M LiTFSI in MeCN with 0.25 M Co(*N*-tpy)$^{2+/3+}$.

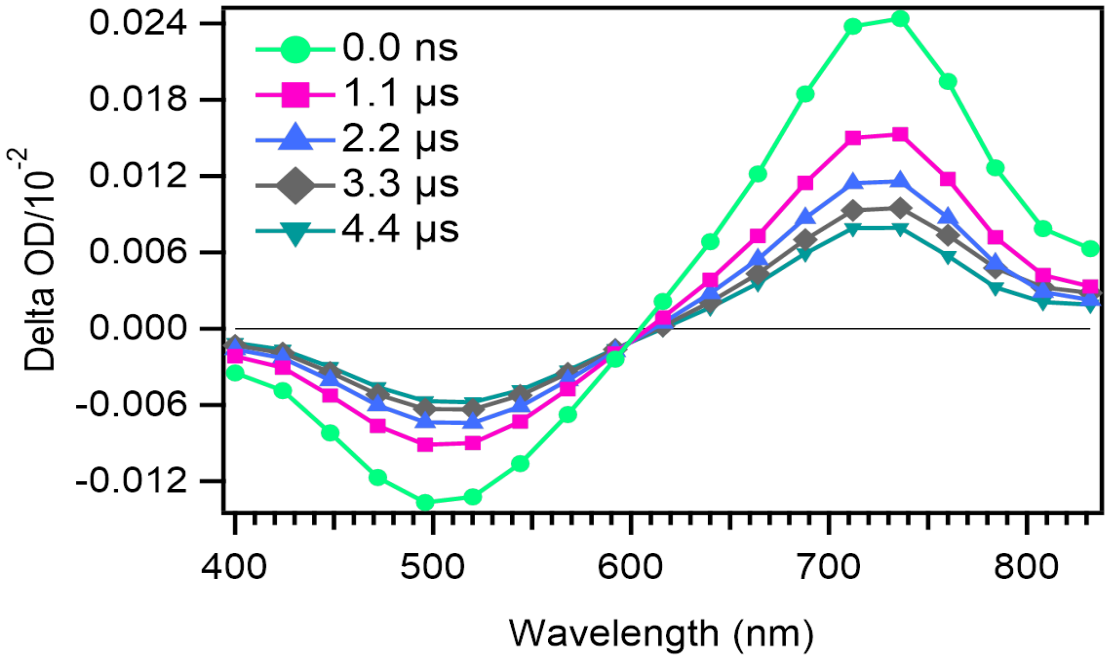

Figure S34. Spectral data for **AB7** with 0.1 M LiTFSI in MeCN with 0.25 M $Co(tpy)^{2+/3+}$.

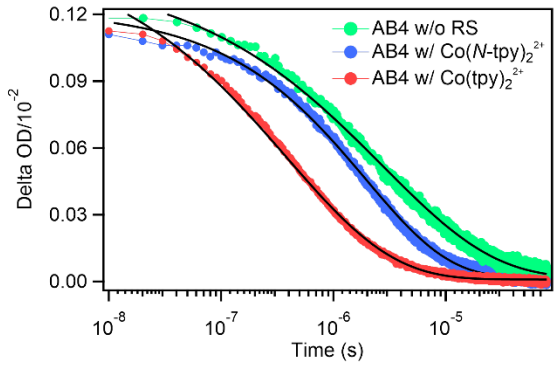

Figure S35. Decay plots resulting from TAS for **AB4** without RS added, with $Co(tpy)_2^{3+/2+}$, and with $Co(N\text{-tpy})_2^{3+/2+}$ RS.

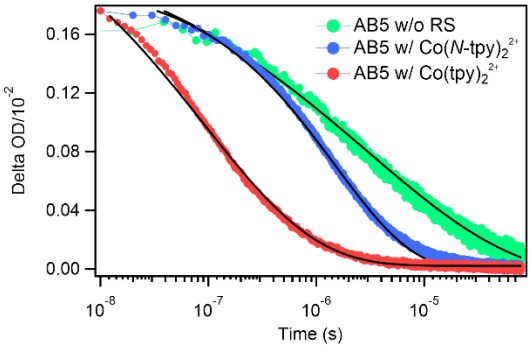

Figure S36. Decay plots resulting from TAS for **AB5** without RS added, with $Co(tpy)_2^{3+/2+}$, and with $Co(N\text{-}tpy)_2^{3+/2+}$ RS.

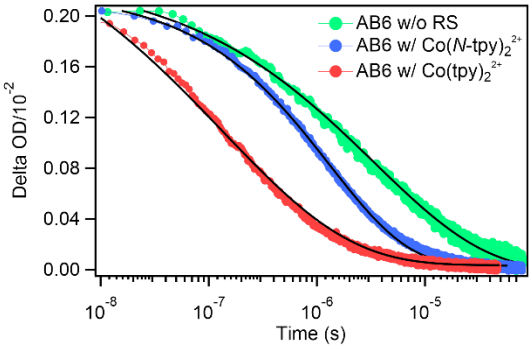

Figure S37. Decay plots resulting from TAS for **AB6** without RS added, with $Co(tpy)_2^{3+/2+}$, and with $Co(N\text{-}tpy)_2^{3+/2+}$ RS.

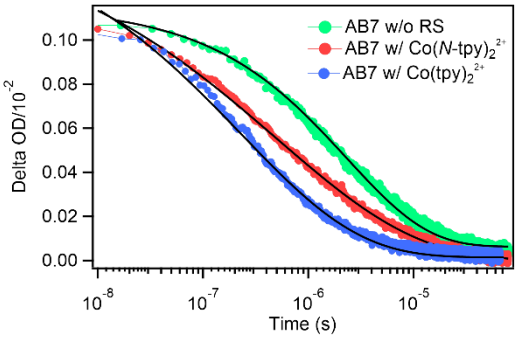

Figure S38. Decay plots resulting from TAS for **AB7** without RS added, with $Co(tpy)_2^{3+/2+}$, and with $Co(N\text{-tpy})_2^{3+/2+}$ RS.

Table S7. Summary TAS data for **AB4**, **AB5**, **AB6** and **AB7**.[a]

Dye	k_{reg} (s^{-1})	k_{rec} (s^{-1})	□ (%)
	$Co(N\text{-tpy})_2^{2+}$ as the RS		
AB4	2.42E+05	9.40E+04	72.0
AB5	5.85E+05	1.08E+05	84.4
AB6	3.45E+05	8.60E+04	80.0
AB7	1.82E+05	8.40E+04	68.4
	$Co(tpy)_2^{2+}$ as the RS		
AB4	8.65E+06	9.40E+04	99.0
AB5	1.70E+07	1.08E+05	99.4
AB6	8.30E+06	8.60E+04	99.0
AB7	8.30E+06	8.40E+04	99.0

[a] All measurements were taken under open-circuit conditions, with the pump power = <3.0 mJ/pulse and the probe wavelength set to 720 nm. Electrolyte with cobalt RS for both Co(tpy) and Co(N-tpy) comprised of 0.25M Co^{2+}, and 0.1 M LiTFSI.

4. DSC Device Data

Table S8. *Dye molar absorptivities on film and dye loading studies for* ***AB4, AB5, AB6*** *and* ***AB7*** *averaged over three device sets.*

Dye	ε_{max} ($M^{-1}cm^{-1}$)	Dye Loading Density (mol/cm^2)
AB4	19700	4.02×10^{-8}
AB5	21000	7.33×10^{-8}
AB6	28000	1.07×10^{-7}
AB7	28700	1.37×10^{-7}

The molar absorptivity values are in 0.01 M TBAOH/DMF solutions. Dye desorption studies were conducted as previously described.[235]

DSC device fabrication: DSC devices were fabricated as previously described.[236] For the photoanode, TEC 10 glass was used with 5 µm mesoporous TiO_2 layer (particle size, 30 nm, Dyenamo, DN-GPS-30TS). A 5.0 µm TiO_2 scattering layer (particle size, 100 nm, Solaronix R/SP) was also used. The sensitizing solution is 0.3 mM of dye in MeCN:*t*-BuOH:THF mixture (1:1:1) with a 20:1 CDCA:dye ratio. For the counter electrodes, TEC 7 FTO glass was used. Devices were characterized as previously described.[237]

Table S9. Summary of photovoltaic parameters for DSC devices prepared with dyes **AB4**, **AB5**, **AB6** and **AB7**.

Dye	V_{oc} (mV)	J_{sc} (mA cm^{-2})	FF (%)	PCE (%)

$Co(tpy)_2^{3+/2+}$				
AB 4	523	4.1	65	1.43
AB 5	558	4.7	71	1.90
AB 6	559	4.9	65	1.83
AB 7	573	6.3	67	2.45
$Co(N\text{-}tpy)_2^{3+/2+}$				
AB 4	700	2.2	66	1.00
AB 5	713	3.0	65	1.40
AB 6	732	3.0	69	1.50
AB 7	760	5.3	68	2.80

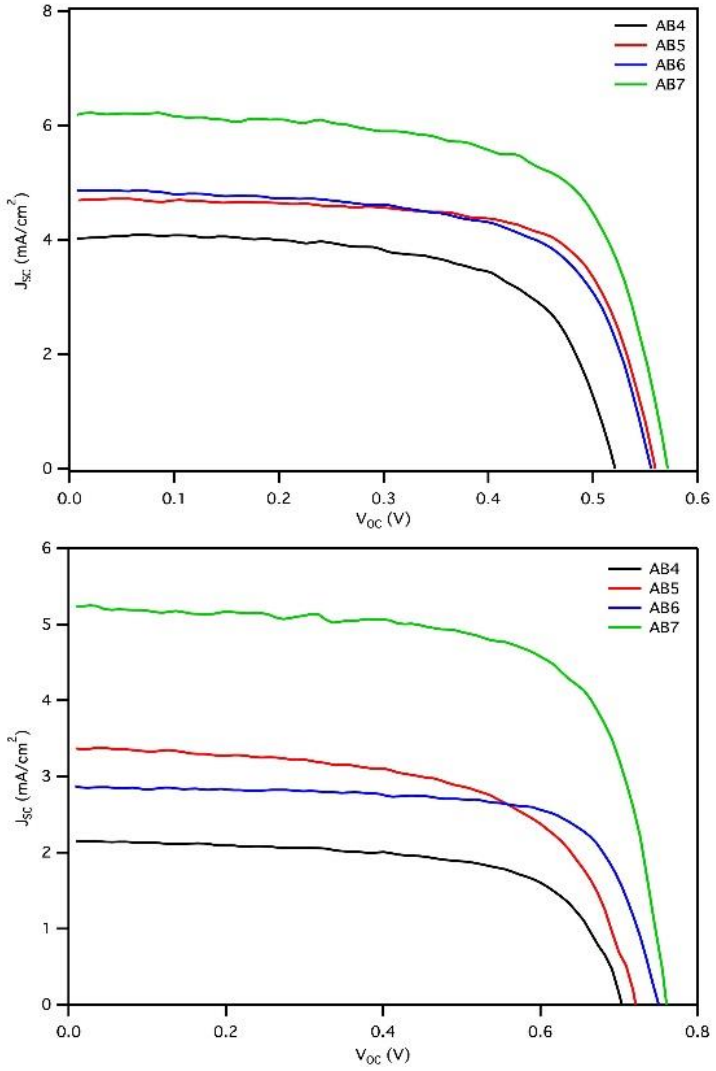

Figure S39. *J-V* curves of **AB4**, **AB5**, **AB6** and **AB7** dyes with: top) $Co(tpy)_2^{3+/2+}$ and bottom) $Co(N\text{-}tpy)_2^{3+/2+}$ redox shuttles.

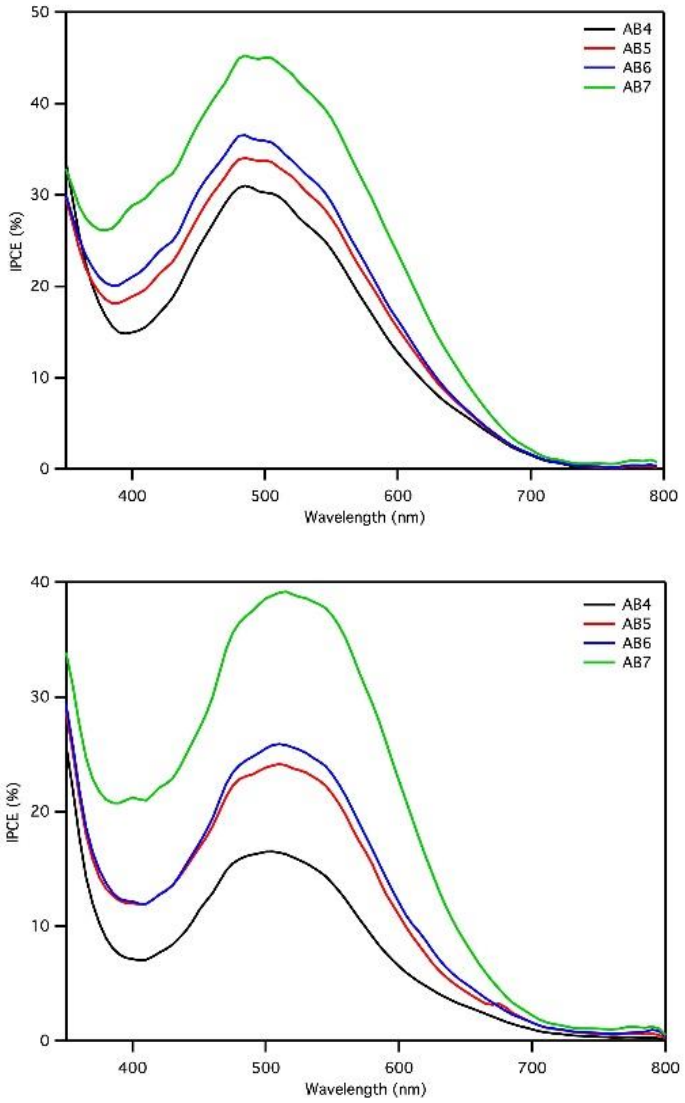

Figure S40. IPCE spectrum of **AB4**, **AB5**, **AB6** and **AB7** dyes with: top) $Co(tpy)_2^{3+/2+}$ and bottom) $Co(N\text{-}tpy)_2^{3+/2+}$ redox shuttles.

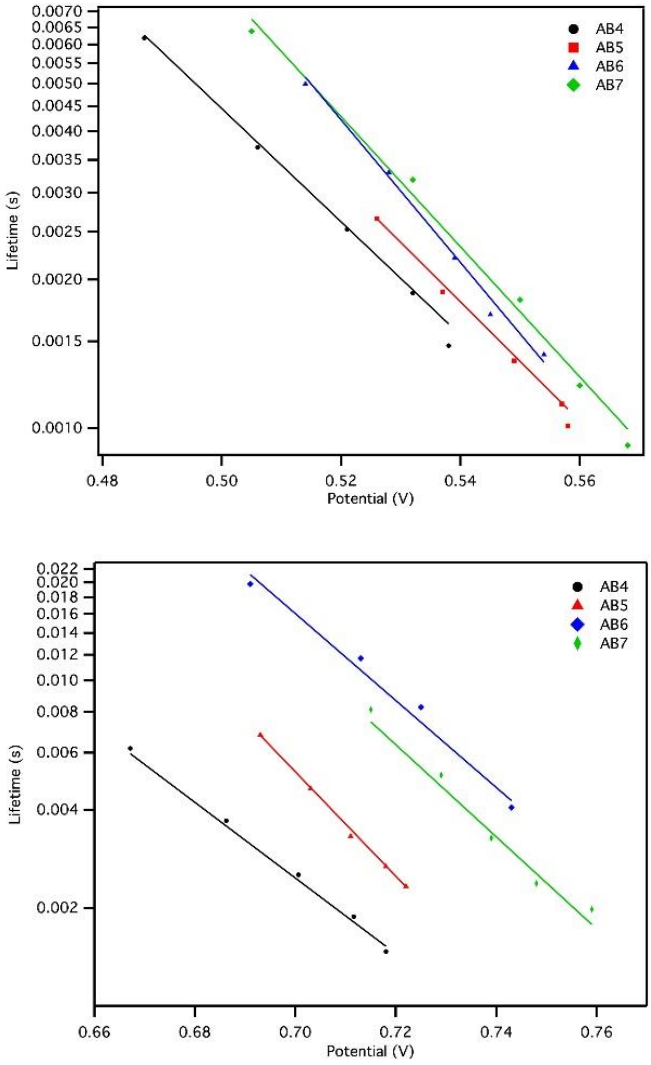

Figure S41. Small modulated photovoltage transient data of **AB4**, **AB5**, **AB6** and **AB7** dyes with: top) $Co(tpy)_2^{3+/2+}$ and bottom) $Co(N\text{-}tpy)_2^{3+/2+}$ redox shuttles.

Table S10. Electrochemical impedance spectroscopy data.

Dye	R_s (Ω)	R_{rec} (Ω)	C_μ (mF)	R_{CE} (Ω)	C_{CE} (mF)	η_{cc} (%)	τ_{TiO2} (ms)
$Co(tpy)_2^{3+/2+}$							
AB4	17.85	77.16	$2.00 \times 10^{-}$	18.13	$7.00 \times 10^{-}$	81	0.51
AB5	17.90	77.20	$2.00 \times 10^{-}$	18.10	$7.00 \times 10^{-}$	81	0.51
AB6	13.60	73.6	$2.00 \times 10^{-}$	13.70	$1.00 \times 10^{-}$	84	0.63
AB7	16.18	50.5	$2.30 \times 10^{-}$	12.00	$9.00 \times 10^{-}$	81	0.50
$Co(N\text{-}tpy)_2^{3+/2+}$							
AB4	11.20	132.80	$1.00 \times 10^{-}$	12.10	$1.70 \times 10^{-}$	92	2.00
AB5	10.70	193.00	$1.00 \times 10^{-}$	19.90	$1.00 \times 10^{-}$	91	1.00
AB6	9.70	159.30	$1.00 \times 10^{-}$	43.60	$4.00 \times 10^{-}$	79	1.26
AB7	12.50	76.85	$2.00 \times 10^{-}$	14.50	$9.00 \times 10^{-}$	84	0.50

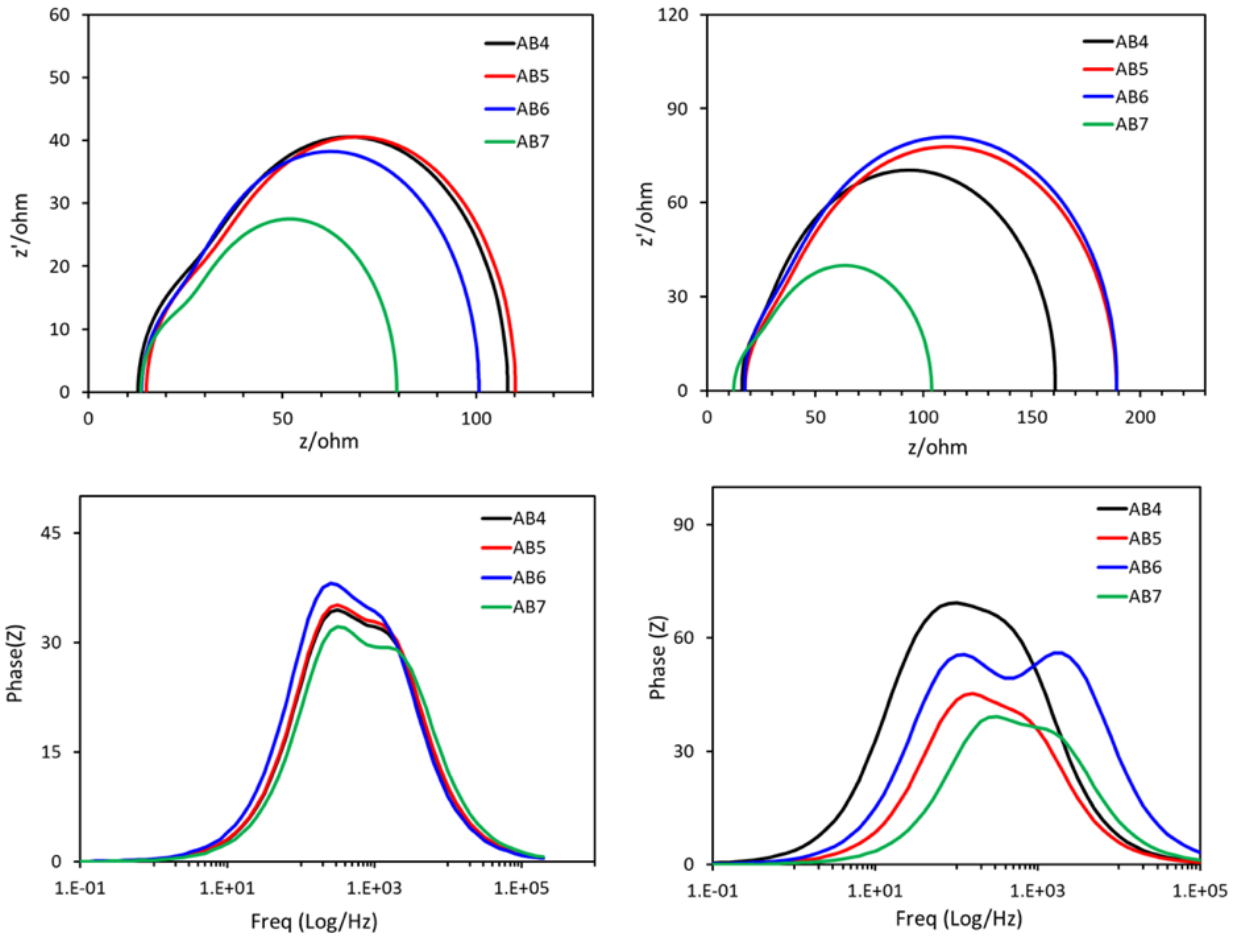

Figure S42. Nyquist (top) and Bode (bottom) plots resulting from electrochemical impedance spectroscopy for dyes with: left) $Co(tpy)_2^{3+/2+}$ and right) $Co(N\text{-}tpy)_2^{3+/2+}$ redox shuttles.

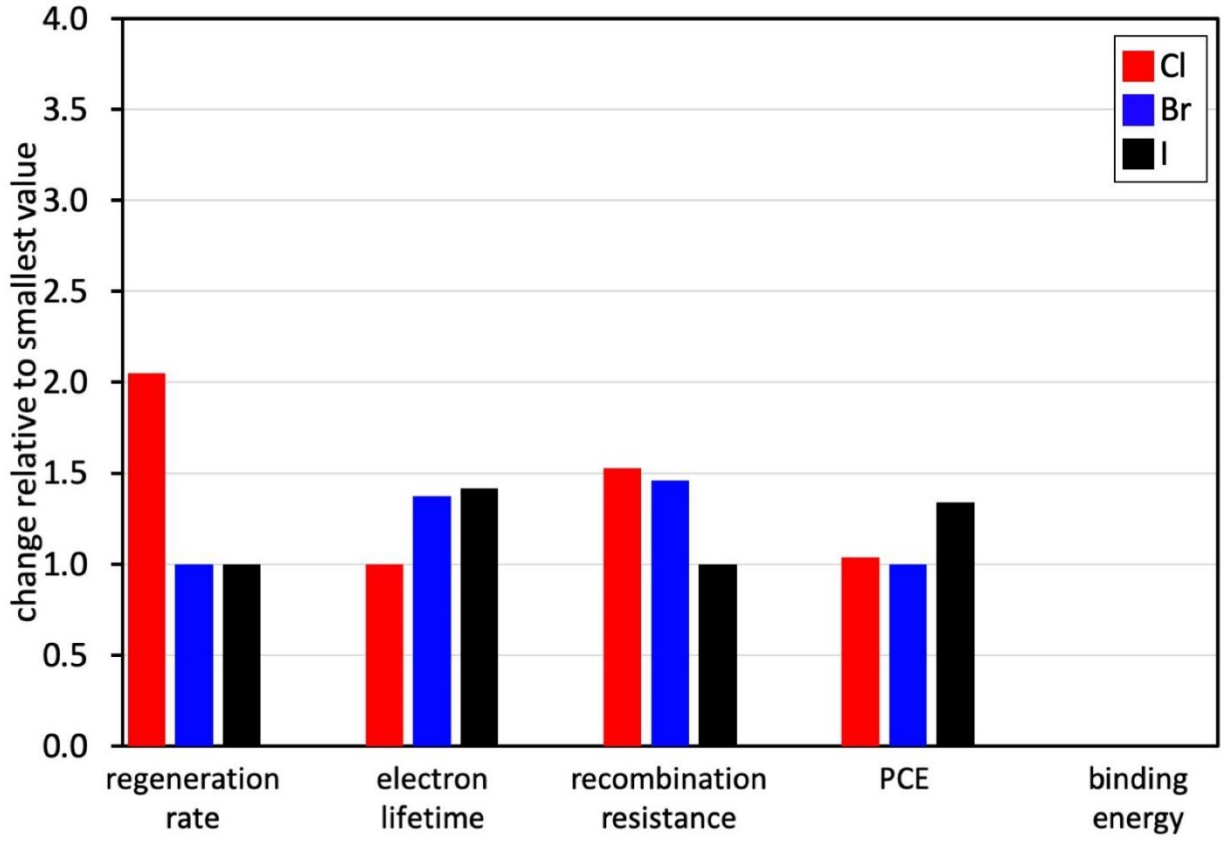

Figure S43. Relative value comparison with each halogenated dye across several interrogation techniques with $Co(tpy)_2^{3+/2+}$ as a RS. Note: the binding energy column is blank due to the redox shuttle not showing binding at a comparable geometry relative to $Co(N\text{-}tpy)_2^{3+/2+}$.

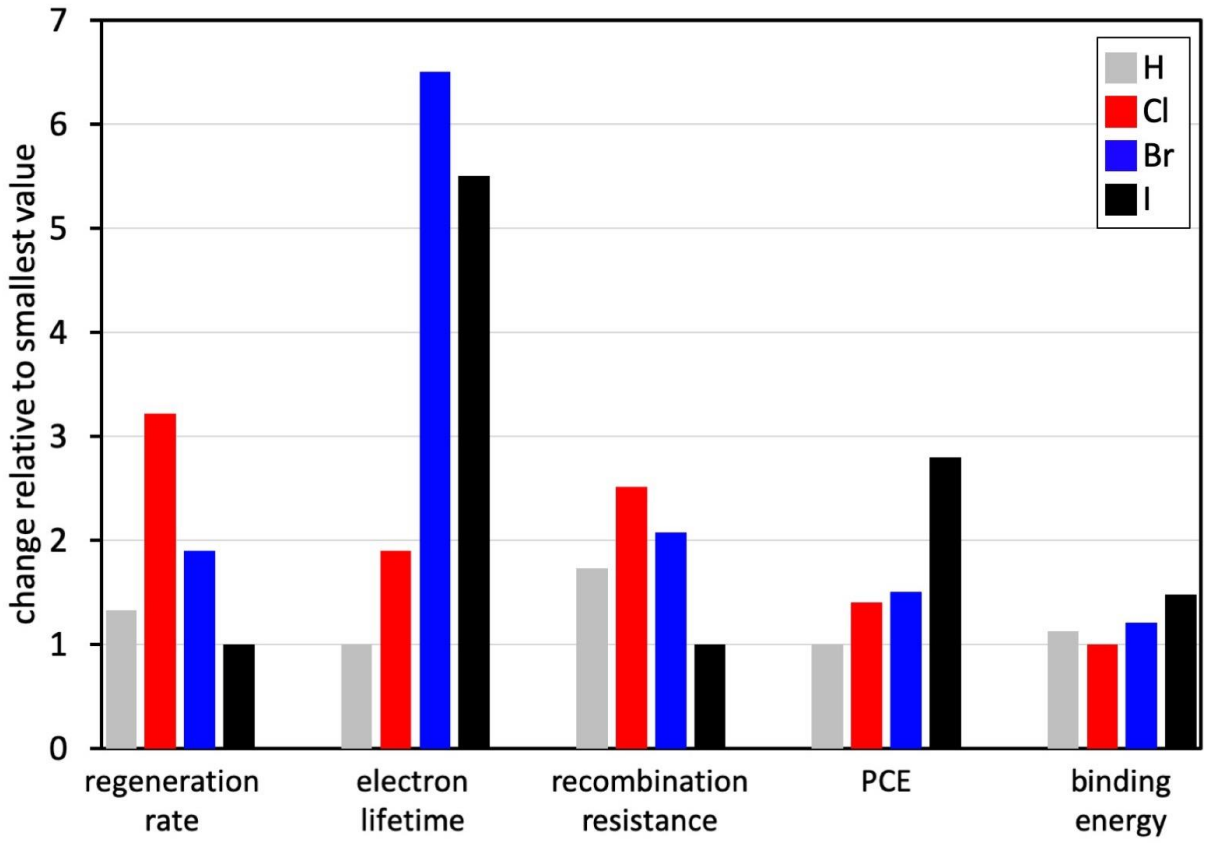

Figure S44. Relative value comparison with each halogenated dye across several interrogation techniques with Co(*N*-tpy)$_2^{3+/2+}$ as a RS with benchmark hydrogen terminated dye **AB4** included.

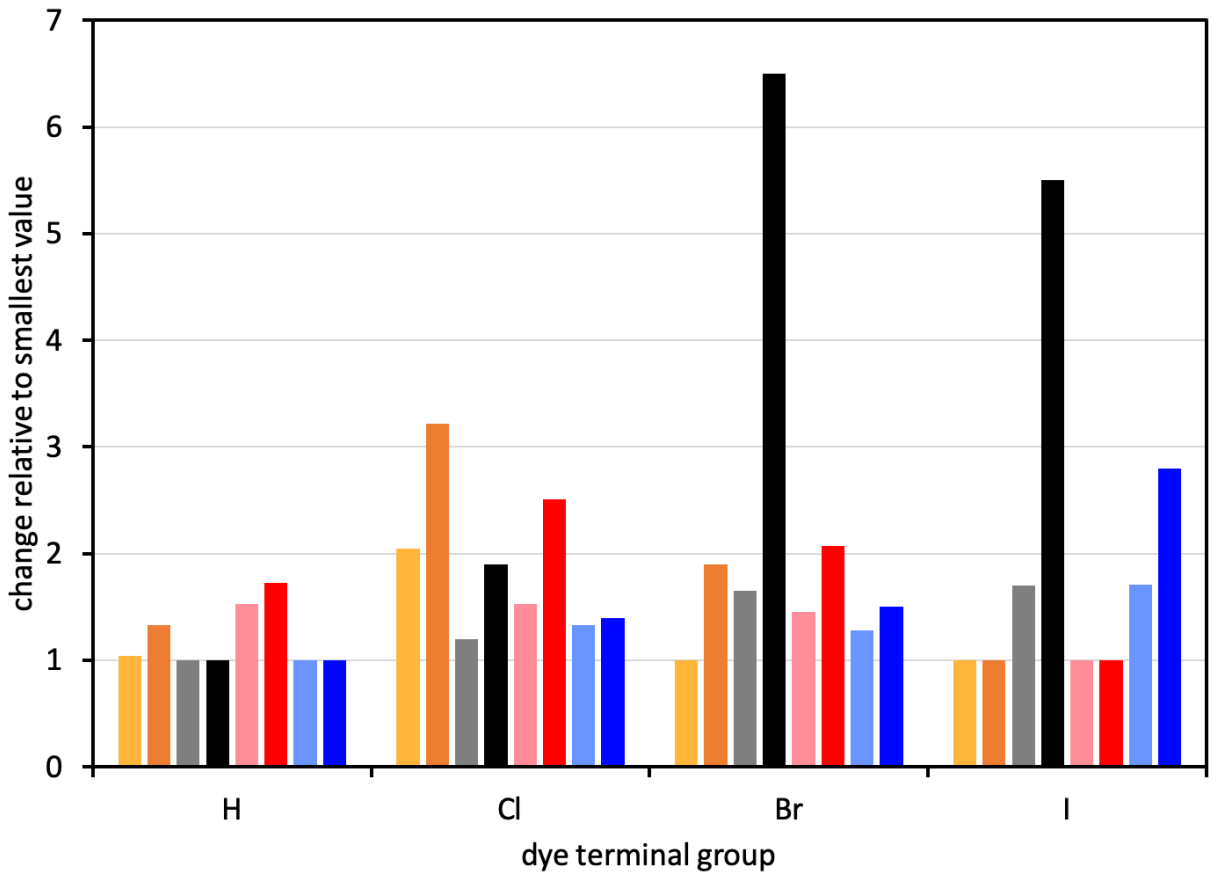

Figure S45. Relative value comparison with each halogenated dye across several interrogation techniques with $Co(tpy)_2^{3+/2+}$ (lighter shade) and $Co(N\text{-}tpy)_2^{3+/2+}$ (darker shade) as RSs with benchmark hydrogen terminated dye **AB4** included. Orange: electron transfer reaction from a RS to the oxidized dye measured by TAS (regeneration rate). Black: Electron lifetime measured via SMPVT. Red: electrochemical impendence spectroscopy charge transfer resistance at the TiO_2-dye interface with the electrolyte. Blue: power conversion efficiency of DSC devices.

Appendix II

Supporting Information for "LEWIS ACID−LEWIS BASE INTERACTIONS PROMOTE FAST INTERFACIAL ELECTRON TRANSFERS WITH A PYRIDINE-BASED DONOR DYE IN DYE-SENSITIZED SOLAR CELLS"

Dinesh Nugegoda,† Leigh Anna Hunt,† Anthony Devdass, Hammad Cheema, Ryan C. Fortenberry, Jonah W. Jurss,* Nathan I. Hammer,* and Jared H. Delcamp*

Department of Chemistry and Biochemistry, University of Mississippi, University, Mississippi 38677, United States

† These authors contributed equally.

*email: delcamp@olemiss.edu, nhammer@olemiss.edu, jwjurss@olemiss.edu

Table of Contents – Appendix II

1. Scheme S1. Synthetic scheme to the methyl ester derivative of **DN1 (DN1-ester)**.

Figure S1. CV of **DN1** in dichloromethane versus NHE.

Figure S2. CV of $[Co(PY5Me_2)(MeCN)]^{3+/2+}$ in MeCN.

Figure S3. UV−vis absorption spectra of $[Co(PY5Me_2)(MeCN)]^{3+}$ and $[Co(PY5Me_2)(MeCN)]^{2+}$ in MeCN.

Figure S4. Emission quenching study with **DN1** methyl ester and varying concentrations of $Co(PY5Me_2)$ in MeCN with photoexcitation at 507 nm.

Figure S5. Emission quenching study with DN1 ester and varying concentrations of $Co(bpy)_3$ in MeCN with photoexcitation at 507 nm.

Figure S6. Absorbance spectroelectrochemistry graphs for **DN1** (no bias), **DN1** with 1.01 V bias (red), and **DN1** with -1.35 V bias (black) in MeCN with 0.1 M electrolyte.

Figure S7. TAS data of **DN1** on TiO_2 with $[Co(bpy)_3]^{3+/2+}$.

Figure S8. TAS spectrum and decays resulting from photoexcited **DN1-ester** with added $[Co(PY5Me_2)(MeCN)]^{3+}$.

Figure S9. TAS data of **DN1-ester** in MeCN with $[Co(bpy)_3]^{3+}$.

Figure S10. TAS decays resulting from photoexcited **A1** on TiO_2 with no RS (gray), $[Co(PY5Me_2)(MeCN)]^{3+/2+}$ (red), and $[Co(bpy)_3]^{3+/2+}$ (blue).

Figure S11. TAS spectrum resulting from photoexcited **A1** on TiO_2 with no RS (top), $[Co(PY5Me_2)(MeCN)]^{3+/2+}$ (middle), and $[Co(bpy)_3]^{3+/2+}$ (bottom).

Figure S12. EIS circuit diagram, where R_s is the series resistance, R_{rec} is the recombination resistance of electrons in TiO_2 across the TiO_2–dye interface to an oxidized redox shuttle, C_μ is the chemical capacitance for charge accumulation in TiO_2, R_{CE} is the electron-transfer resistance at the counter electrode to an oxidized redox shuttle, and C_{CE} is the capacitance at the electrolyte-counter electrode interface

Figure S13. Nyquist (top) and Bode (bottom) plots of DN1 DSC devices.

Table S1. EIS data for DSC devices prepared with **DN1**

Figure S14. IPCE spectrum of **DN1** based DSC devices.

Figure S15. ^1H NMR (400 MHz, $CDCl_3$) of **2**.

Figure S16. $^{13}C\{^{1}H\}$ NMR (400 MHz, $CDCl_3$) of **2**.

Figure S17. ^{1}H NMR (400 MHz, $CDCl_3$) of **4.**

Figure S18. $^{13}C\{^{1}H\}$ NMR (400 MHz, $CDCl_3$) of **4.**

Figure S19.^{1}H NMR (400 MHz, $CDCl_3$) of **5.**

Figure S20. $^{13}C\{^{1}H\}$ NMR (400 MHz, $CDCl_3$) of **5.**

Figure S21. ^{1}H NMR (400 MHz, DMSO) of **DN1.**

Figure S22. ^{1}H NMR (400 MHz, $CDCl_3$) of **DN1 ester.**

Figure 23.^{13}C $\{^{1}H\}$ NMR (400 MHz, $CDCl_3$) of **DN1 ester.**

Figure S24. Stacked ^{1}H NMR (400 MHz, CD_3CN) of **DN1-ester** with $[Co(PY5Me_2)]^{2+}$ (upper) and **DN1 ester** only (below).

Figure S25. Stacked ^{1}H NMR (400 MHz, CD_3CN) of **DN1-ester** with $[Co(bpy)_3]^{2+}$ (top), $[Co(PY5Me_2)]^{2+}$ (middle), and **DN1-ester** only (below).

Figure S26. Stacked ^{1}H NMR (400 MHz, CD_3CN) of **DN1-ester** with varying ratios of $[Co(PY5Me_2)]^{2+}$.

Figure S27. Emission curves of **DN1-ester** with varied mole fractions of $[Co(PY5Me_2)(MeCN)]^{2+}$ (black lines) and at the same concentration of **DN1-ester** with no cobalt complex present (red dashed lines). Samples with the dye and cobalt complex were stirred for 1 hour at room temperature before data was collected.

Figure S28. Emission intensity ratios across a series of mole fractions of **DN1-ester** and $[Co(PY5Me_2)(MeCN)]^{2+}$. The total amount of analyte (dye + redox shuttle) was held constant at 1×10^{-5} M. I_0 is the emission intensity of the dye without any added redox shuttle at the corresponding mole fraction dye concentration.

1. Synthetic Scheme

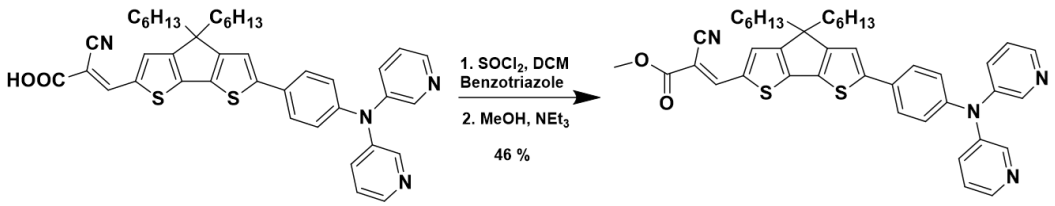

Scheme S1. Synthetic scheme to the methyl ester derivative of **DN1 (DN1-ester)**.

2. Optical and Electrochemical Properties

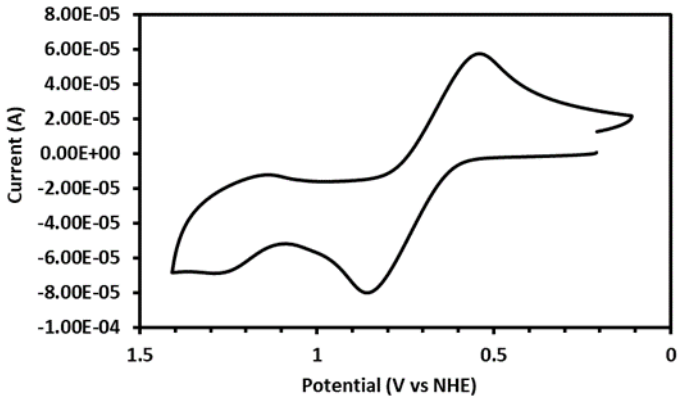

Figure S1. CV of **DN1** in dichloromethane versus NHE.

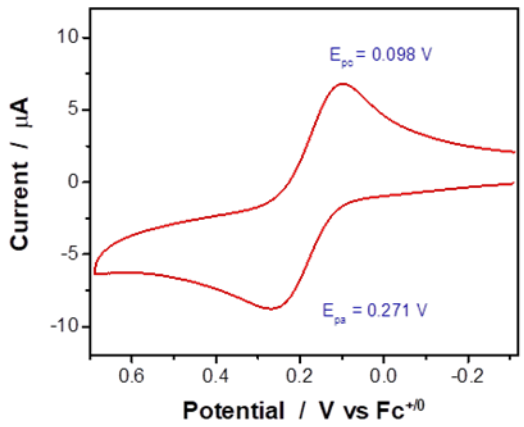

Figure S2. CV of $[Co(PY5Me_2)(MeCN)]^{3+/2+}$ in MeCN.

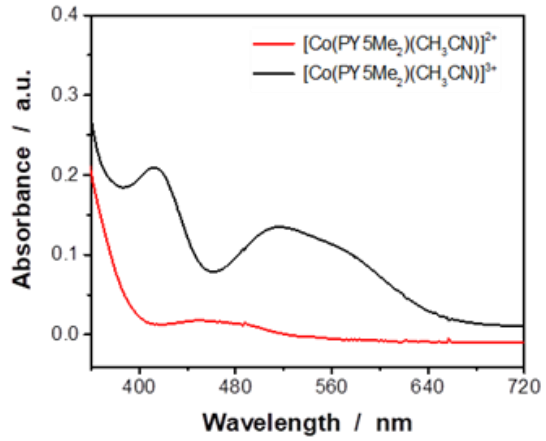

Figure S3. UV−vis absorption spectra of $[Co(PY5Me_2)(MeCN)]^{3+}$ and $[Co(PY5Me_2)(MeCN)]^{2+}$ in MeCN.

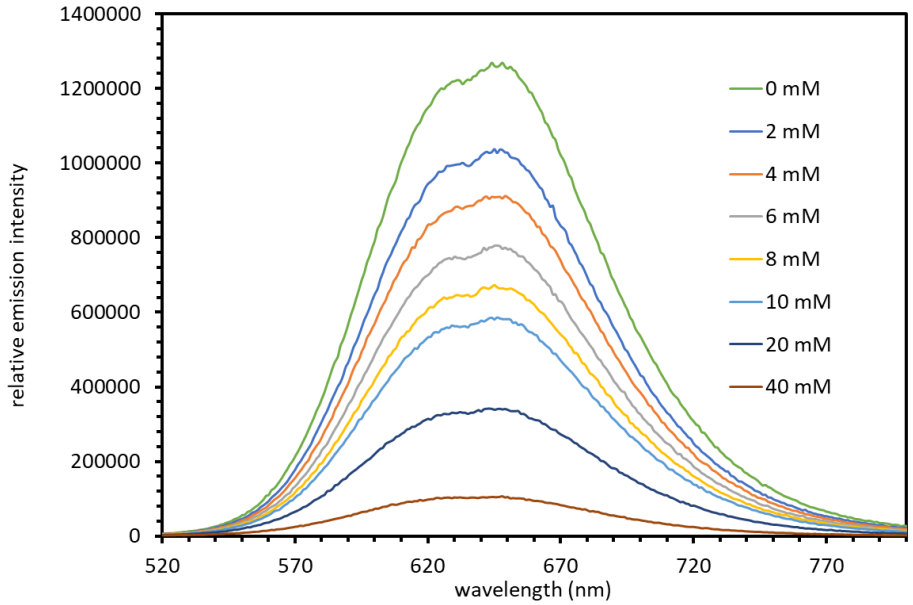

Figure S4. Emission quenching study with **DN1** methyl ester and varying concentrations of $Co(PY5Me_2)$ in MeCN with photoexcitation at 507 nm.

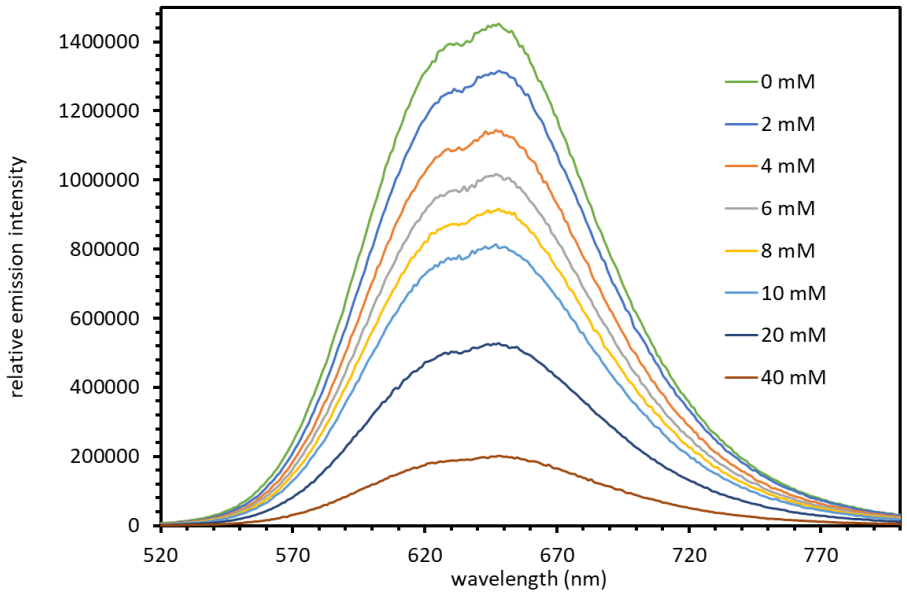

Figure S5. Emission quenching study with DN1 ester and varying concentrations of $Co(bpy)_3$ in MeCN with photoexcitation at 507 nm.

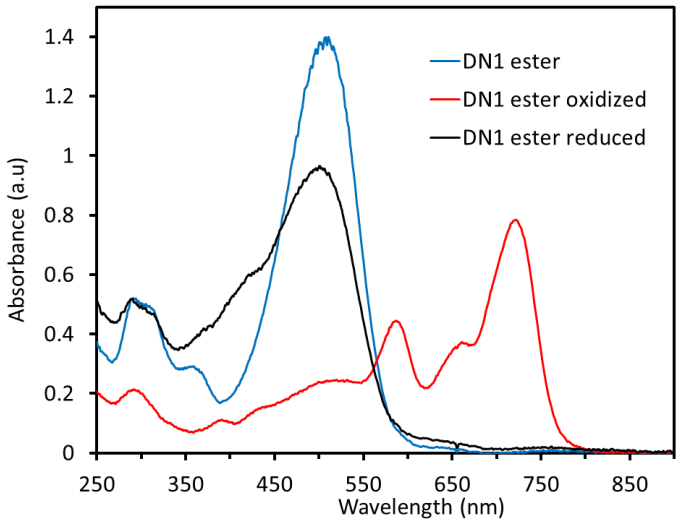

Figure S6. Absorbance spectroelectrochemistry graphs for **DN1** (no bias), **DN1** with 1.01 V bias (red), and **DN1** with -1.35 V bias (black) in MeCN with 0.1 M electrolyte.

3. Transient Absorption Spectroscopy Data

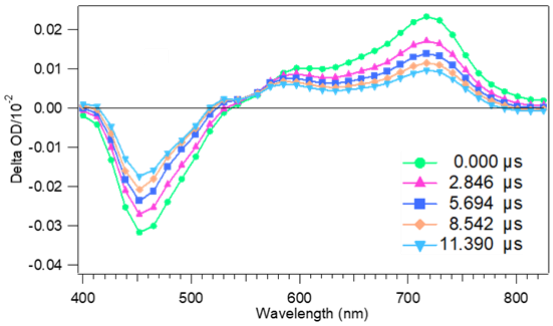

Figure S7. TAS data of **DN1** on TiO_2 with $[Co(bpy)_3]^{3+/2+}$.

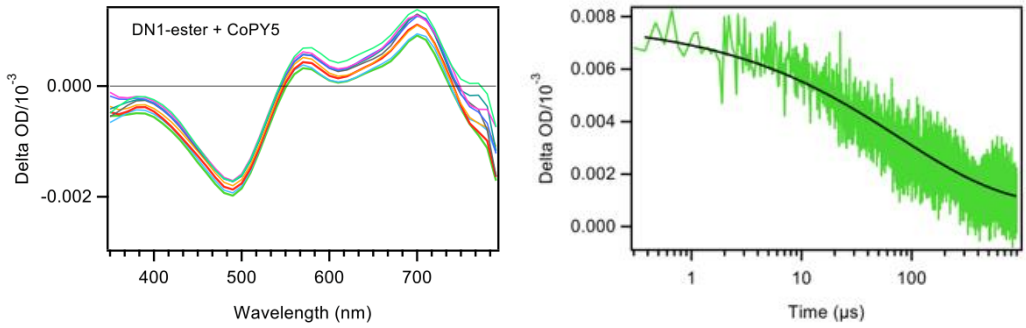

Figure S8. TAS spectrum and decays resulting from photoexcited **DN1-ester** with added $[Co(PY5Me_2)(MeCN)]^{3+}$.

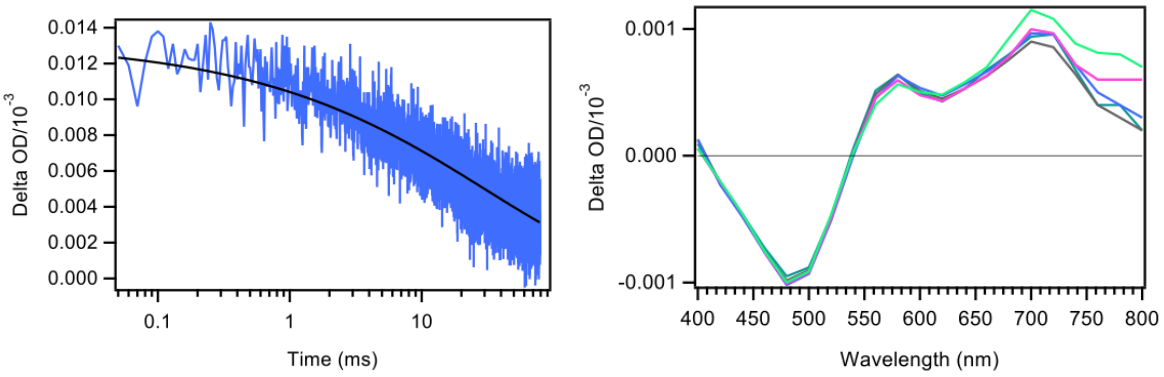

Figure S9. TAS data of **DN1-ester** in MeCN with $[Co(bpy)_3]^{3+}$.

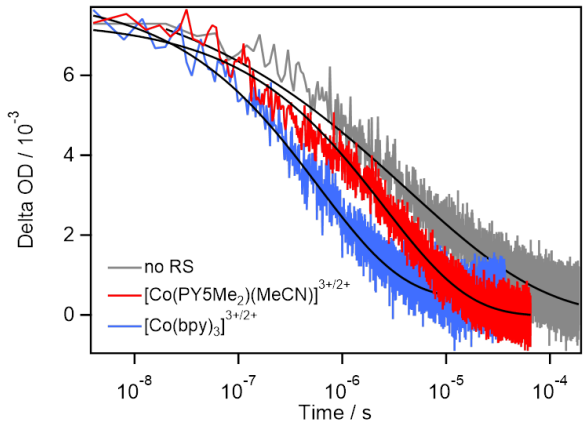

Figure S10. TAS decays resulting from photoexcited **A1** on TiO_2 with no RS (gray), $[Co(PY5Me_2)(MeCN)]^{3+/2+}$ (red), and $[Co(bpy)_3]^{3+/2+}$ (blue).

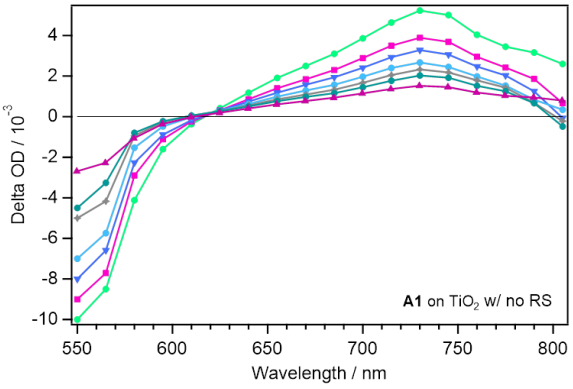

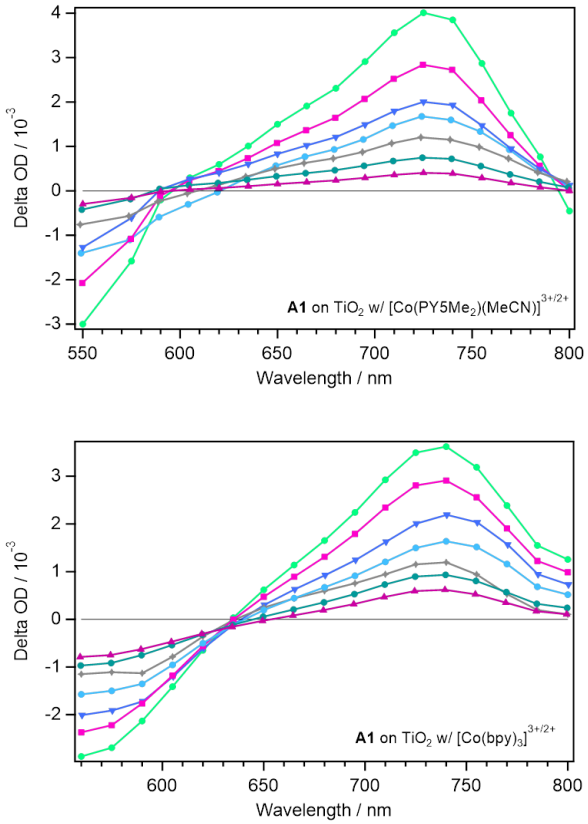

Figure S11. TAS spectrum resulting from photoexcited **A1** on TiO_2 with no RS (top), $[Co(PY5Me_2)(MeCN)]^{3+/2+}$ (middle), and $[Co(bpy)_3]^{3+/2+}$ (bottom).

4. DSC Device Data

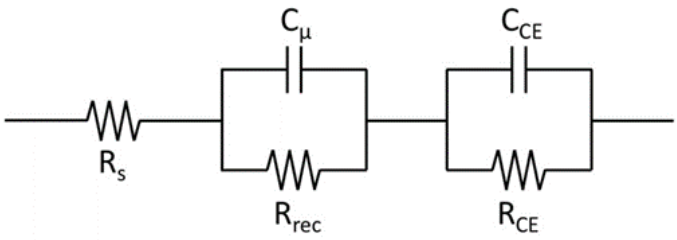

Figure S12. EIS circuit diagram, where R_s is the series resistance, R_{rec} is the recombination resistance of electrons in TiO_2 across the TiO_2–dye interface to an oxidized redox shuttle, C_μ is the chemical capacitance for charge accumulation in TiO_2, R_{CE} is the electron-transfer resistance at the counter electrode to an oxidized redox shuttle, and C_{CE} is the capacitance at the electrolyte-counter electrode interface.

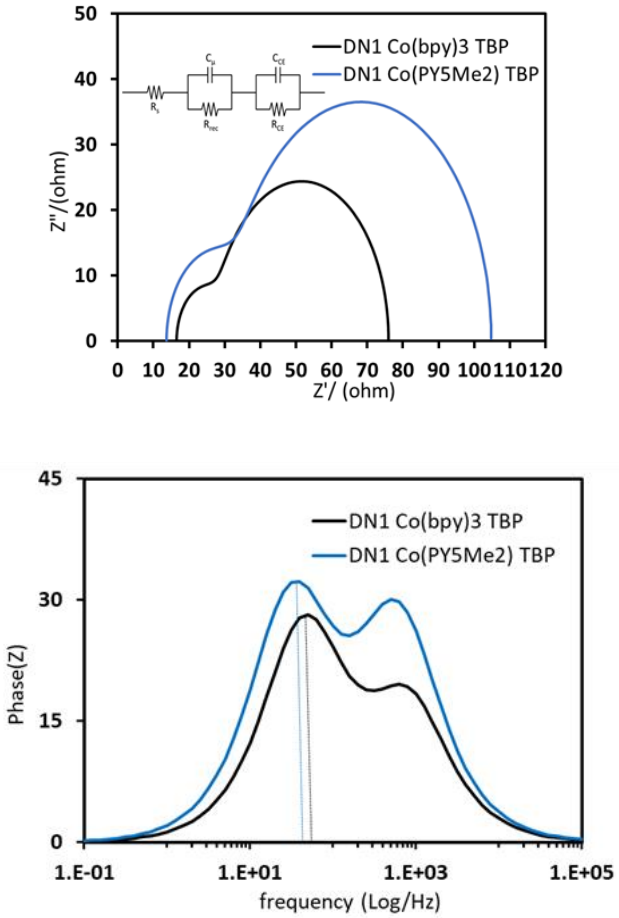

Figure S13. Nyquist (top) and Bode (bottom) plots of DN1 DSC devices.

Table S1. EIS data for DSC devices prepared with **DN1**

Redox Shuttle	R_s (Ω)	R_{rec} (Ω)	C_μ (mF)	R_{CE} (Ω)	C_{CE} (mF)	η_{cc} (%)	τ_{TiO_2} (ms)
$[Co(bpy)_3]^{3+/2+}$	14	48	7.8E-04	12	9.6E-06	80	3.2
$[Co(PY5Me_2)(MeCN)]^{3+/2+}$	14	71	3.5E-04	20	1.1E-05	78	4.0

The larger semicircle in the modified Nyquist plot represents the charge transfer resistance at the TiO_2-dye interface with the electrolyte (TiO_2-dye|electrolyte; R_{rec}). A desirable significantly higher charge transfer resistance across the TiO_2-dye interface to the RS is observed with $[Co(PY5Me_2)(MeCN)]^{3+/2+}$ when compared with $[Co(bpy)_3]^{3+/2+}$ via a fitted circuit (71 Ω versus 48 Ω). However, an undesirable higher charge transfer resistance is observed at the PEDOT counter electrode (R_{CE}) with $[Co(PY5Me_2)(MeCN)]^{3+/2+}$ when compared with $[Co(bpy)_3]^{3+/2+}$ (20 Ω versus 12 Ω). Charge collection efficiency (η_{cc}) was analyzed via the equation $\eta_{cc} = 1/(1 + (R_{CE}/R_{rec}))$[238] to understand the balance of these two resistances. The η_{cc} is observed to be slightly higher with $[Co(bpy)_3]^{3+/2+}$ at 80% versus 78% with $[Co(PY5Me_2)(MeCN)]^{3+/2+}$ which is a modest change. Electron lifetimes in TiO_2 are calculated from the Bode plot using the equation $\tau_{TiO_2} = 1/(2\pi f)$, τ_{TiO_2} is the lifetime of injected electrons in TiO_2 and f is the peak frequency for the lower frequency peak. The Bode plot shows a modest change of the electron lifetime in TiO_2 between the shuttles with a 3.2 ms lifetime for $[Co(bpy)_3]^{3+/2+}$ and 4.0 ms for $[Co(PY5Me_2)(MeCN)]^{3+/2+}$.

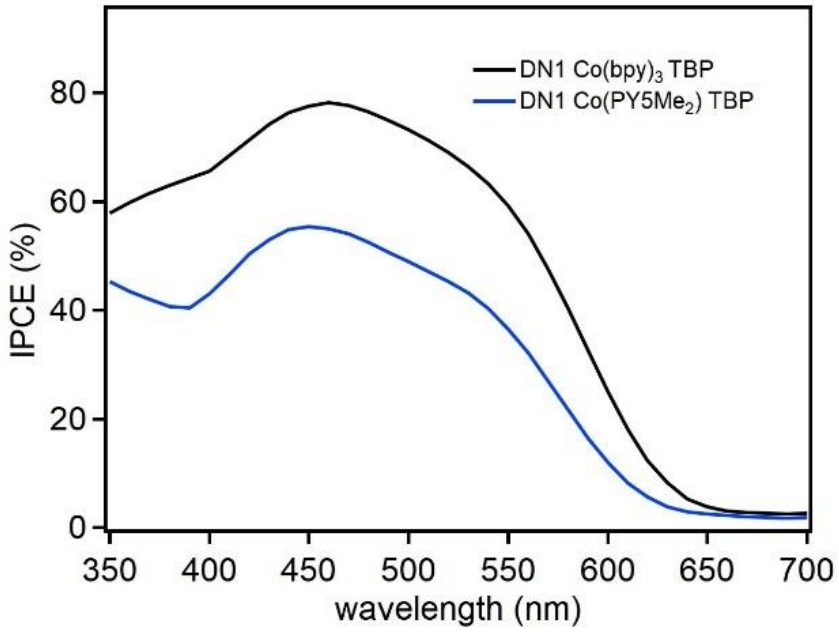

Figure S14. IPCE spectrum of **DN1** based DSC devices.

5. NMR Spectra

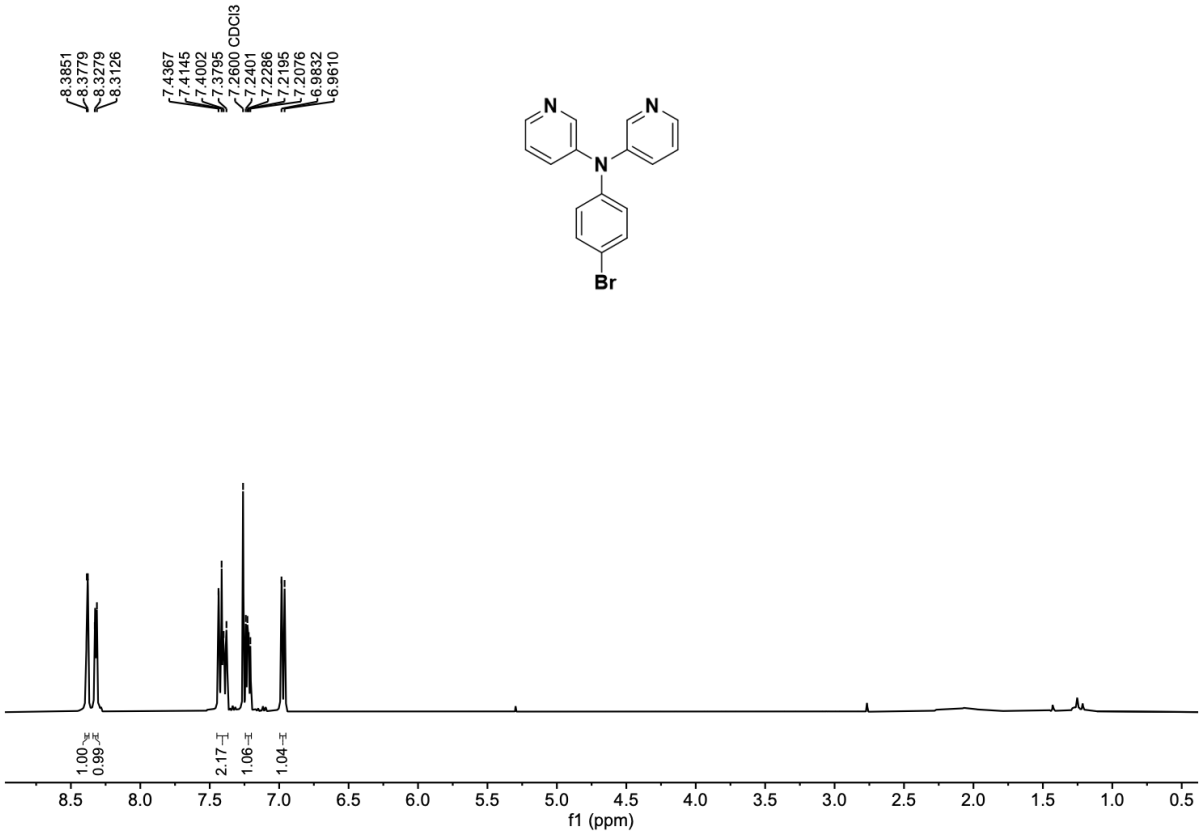

Figure S15. ^{1}H NMR (400 MHz, $CDCl_3$) of **2**.

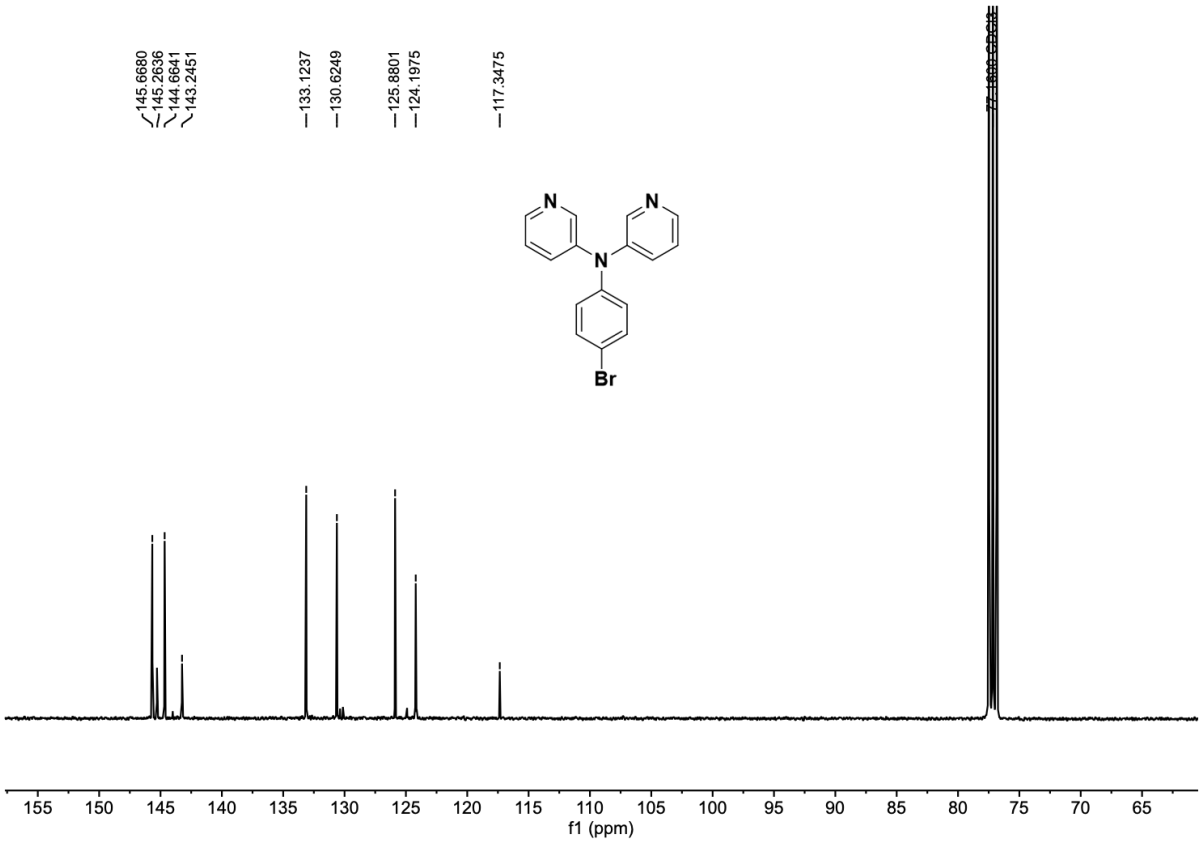

Figure S16. $^{13}C\{^{1}H\}$ NMR (400 MHz, $CDCl_3$) of **2**.

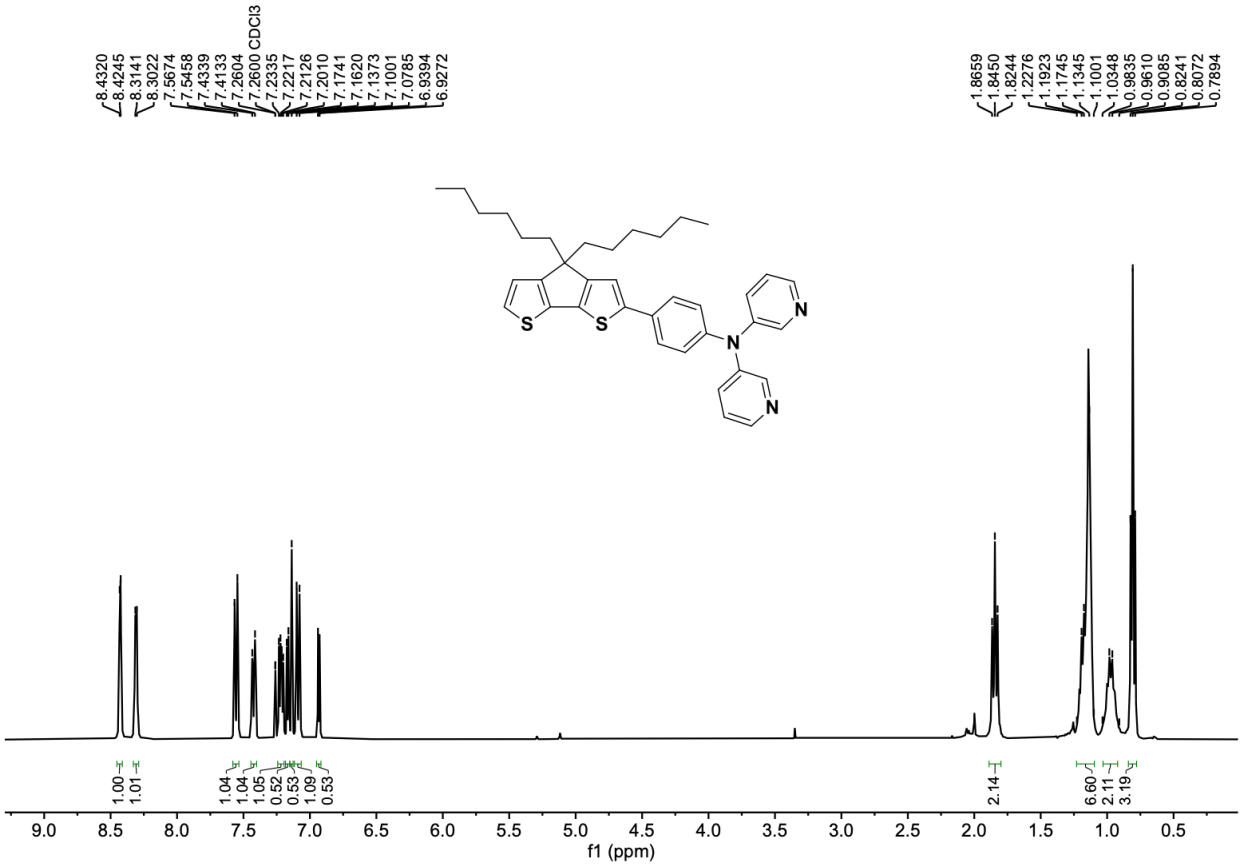

Figure S17. ^{1}H NMR (400 MHz, $CDCl_3$) of **4.**

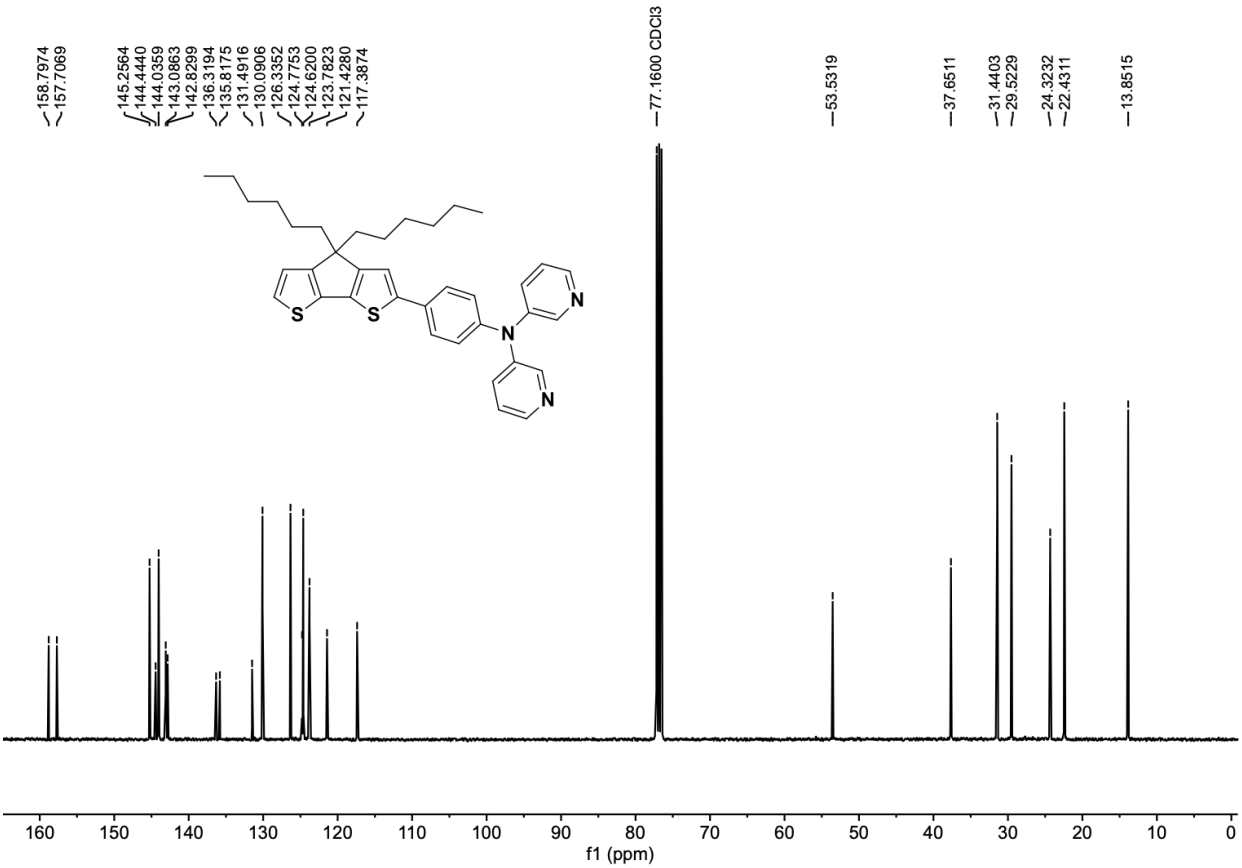

Figure S18. $^{13}C\{^{1}H\}$ NMR (400 MHz, $CDCl_3$) of **4.**

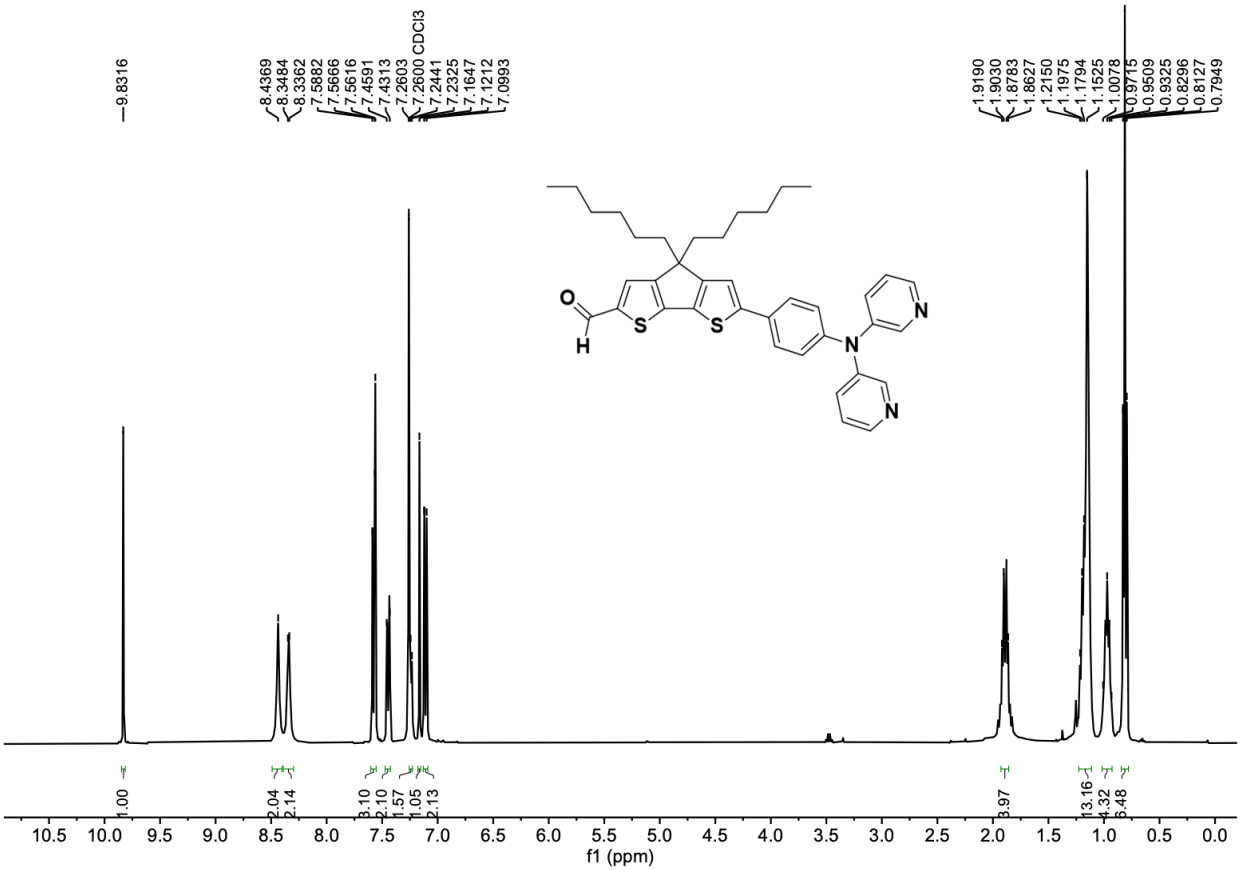

Figure S19.[1]H NMR (400 MHz, $CDCl_3$) of **5.**

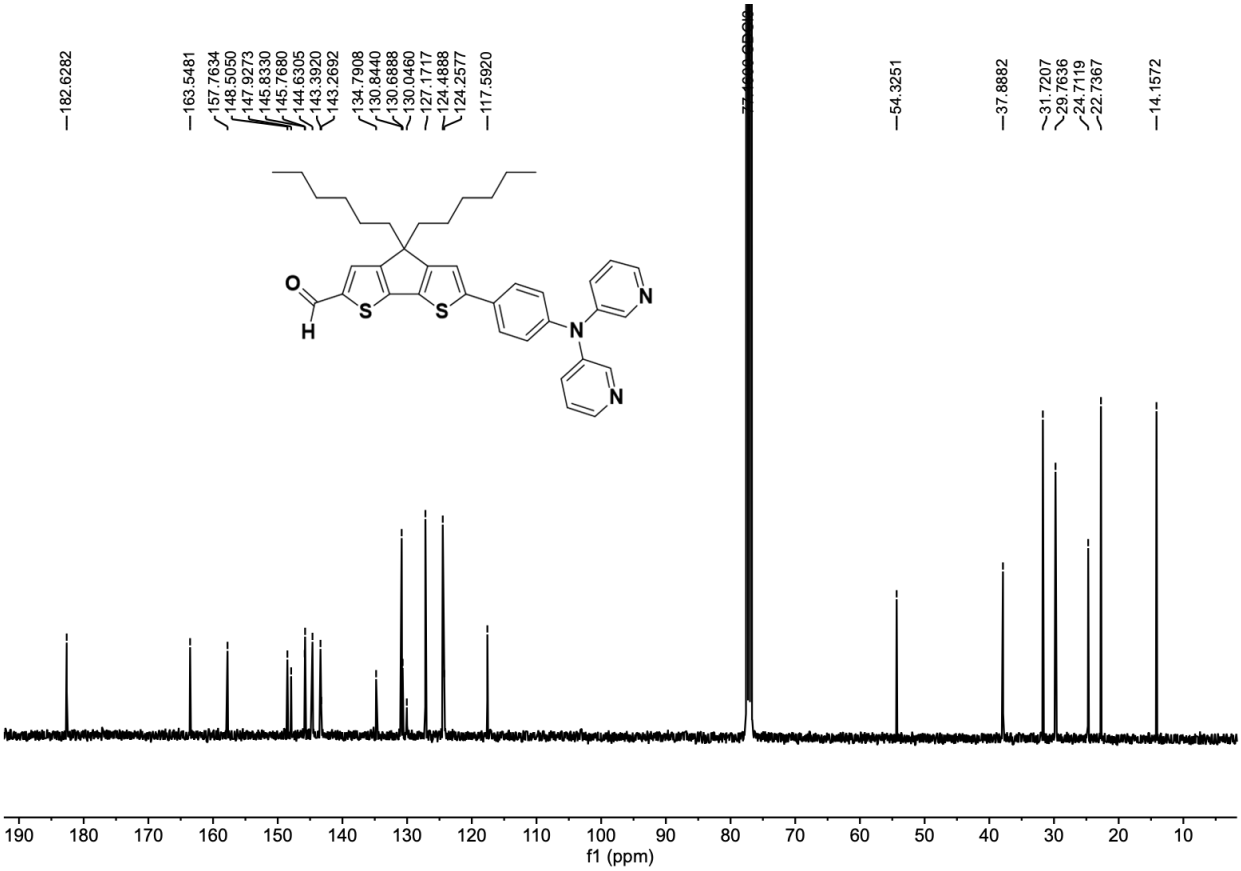

Figure S20. $^{13}C\{^{1}H\}$ NMR (400 MHz, $CDCl_3$) of **5.**

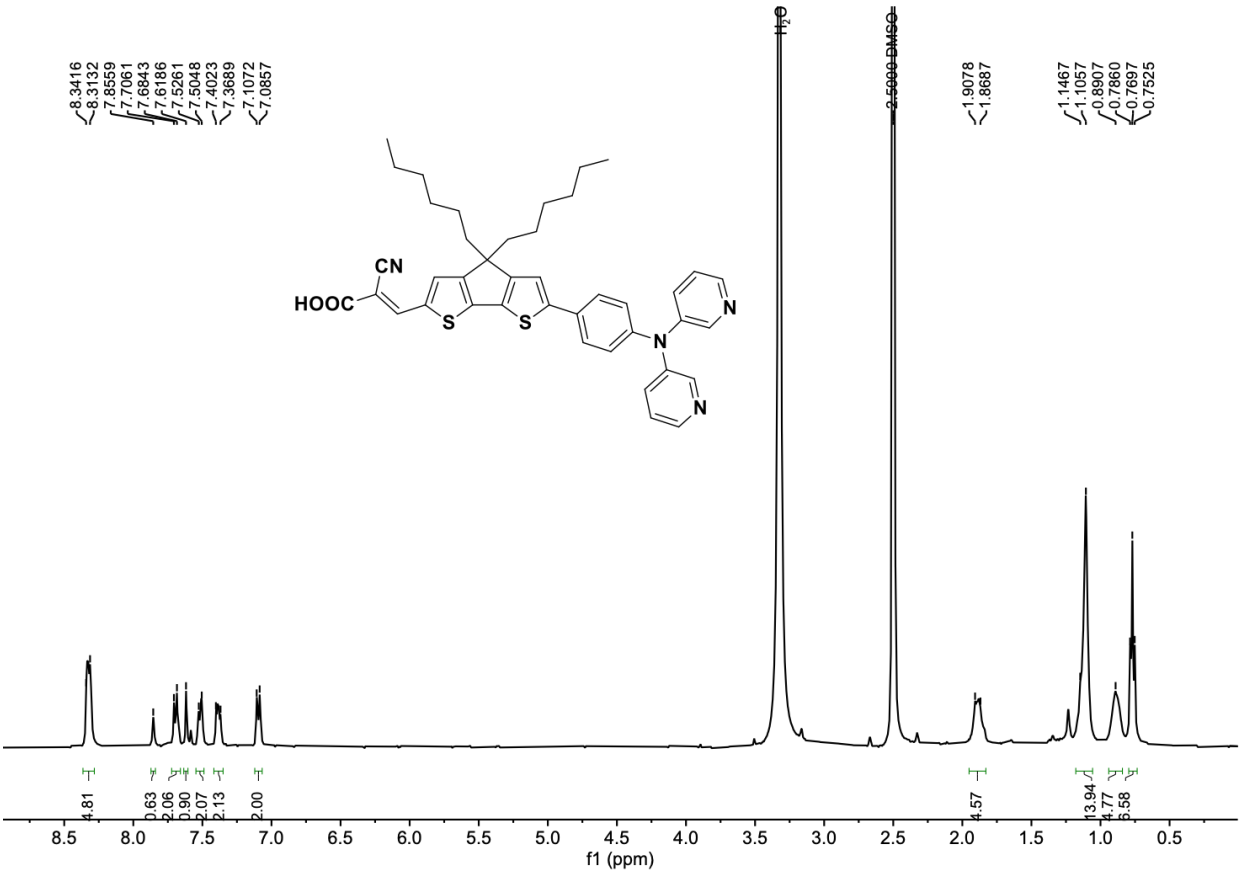

Figure S21. ^{1}H NMR (400 MHz, DMSO) of **DN1.**

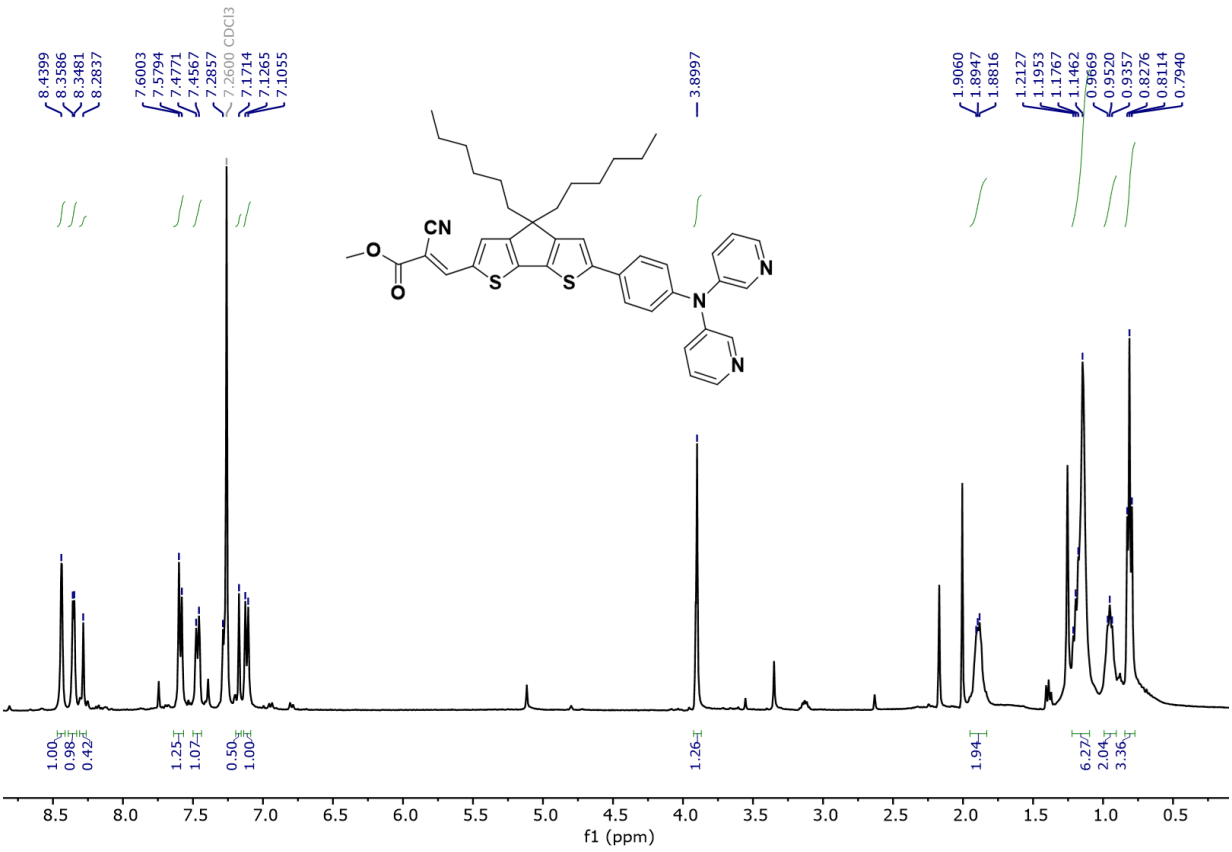

Figure S22. ^{1}H NMR (400 MHz, $CDCl_3$) of **DN1 ester.**

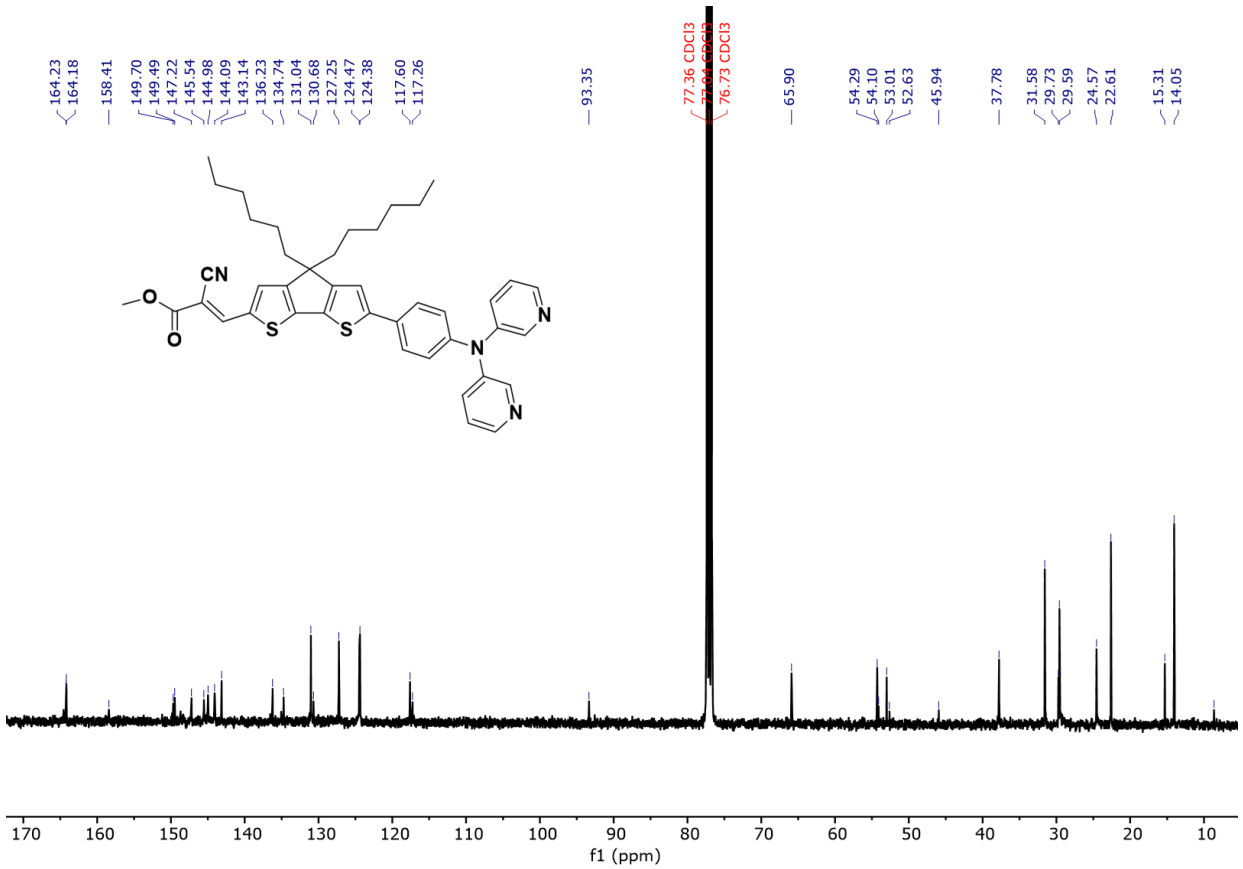

Figure 23. ^{13}C {^{1}H} NMR (400 MHz, $CDCl_3$) of **DN1 ester.**

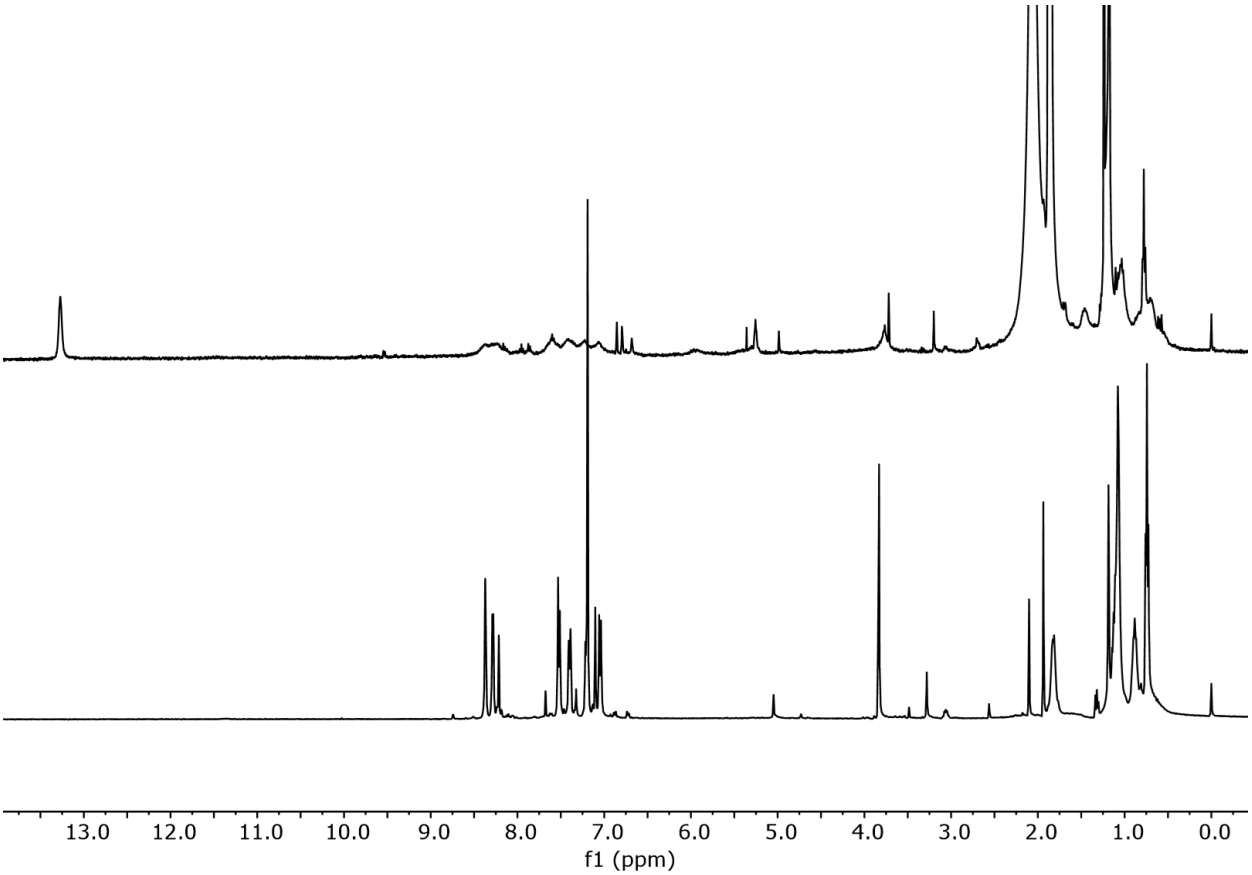

Figure S24. Stacked ^{1}H NMR (400 MHz, CD_3CN) of **DN1-ester** with $[Co(PY5Me_2)]^{2+}$ (upper) and **DN1 ester** only (below).

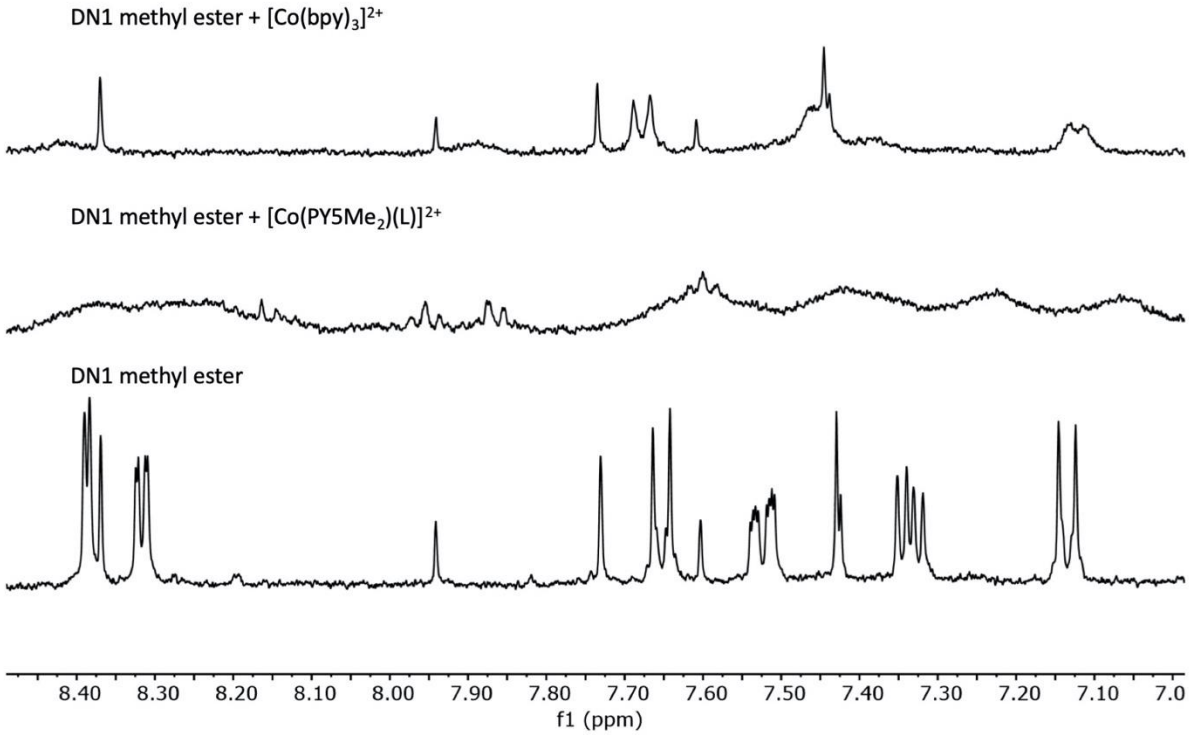

Figure S25. Stacked ^{1}H NMR (400 MHz, CD_3CN) of **DN1-ester** with $[Co(bpy)_3]^{2+}$ (top), $[Co(PY5Me_2)]^{2+}$ (middle), and **DN1-ester** only (below).

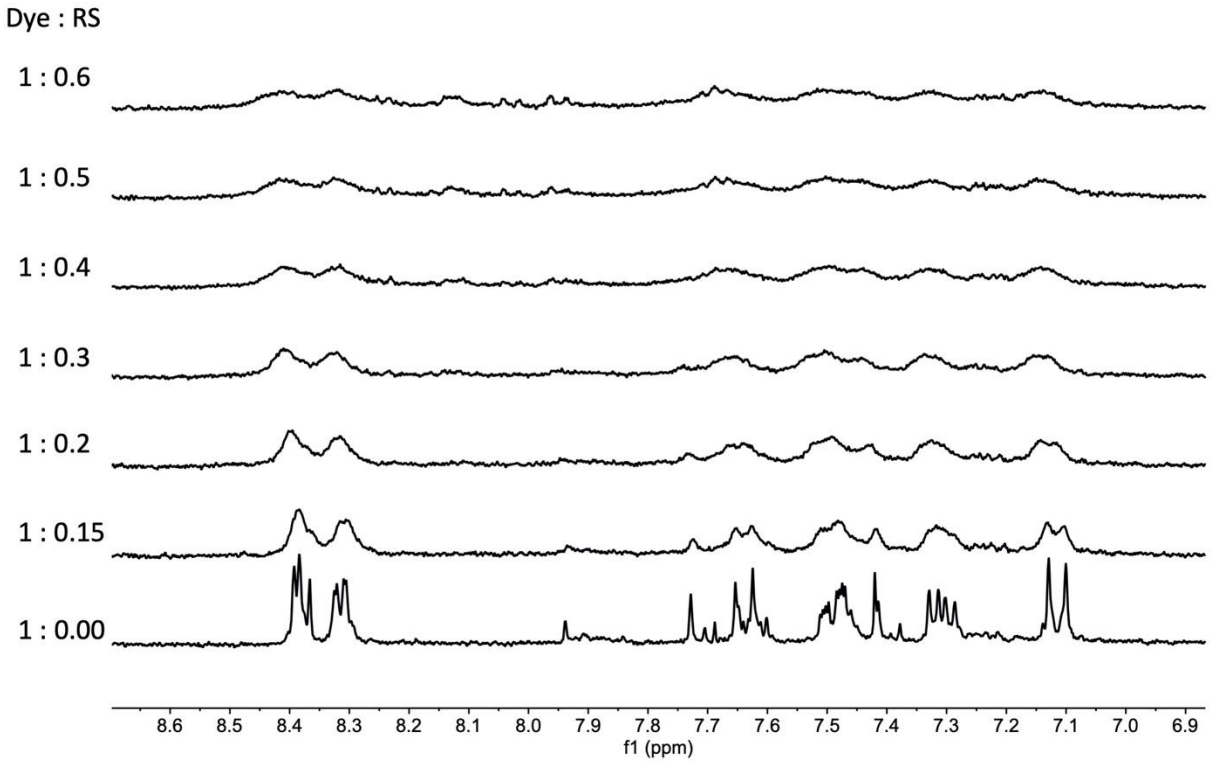

Figure S26. Stacked ^{1}H NMR (400 MHz, CD_3CN) of **DN1-ester** with varying ratios of $[Co(PY5Me_2)]^{2+}$.

Note S1. DN1-ester in CD_3CN has well-resolved peaks in the aromatic region of the ^{1}H NMR spectrum (Figures S24-S25). Upon addition of $[Co(PY5Me_2)(MeCN)]^{2+}$ to give a 1:1 dye:RS ratio, the aromatic peaks corresponding to the dye are observed to broaden and resemble a paramagnetic species in solution. This broadening is expected if the dye were to coordinate to a Co^{2+} metal center. Under identical conditions with added $[Co(bpy)_3]^{2+}$ in place of $[Co(PY5Me_2)(MeCN)]^{2+}$, many of the dye signals remain well resolved with some signals on the dye broadening or being suppressed, especially those of the pyridine rings. This suggests an interaction between the dye and both Co^{2+} RSs may be present with a stronger interaction with the $[Co(PY5Me_2)(MeCN)]^{2+}$ complex. The reason for the broadening of some signals with

$[Co(bpy)_3]^{2+}$ is not obvious from these studies. Notably, the computational data suggests a second binding point at the cyano group is possible with **DN1** and $[Co(PY5Me_2)(MeCN)]^{2+}$ which could explain the disappearance of this peak in the ^1H NMR spectrum.

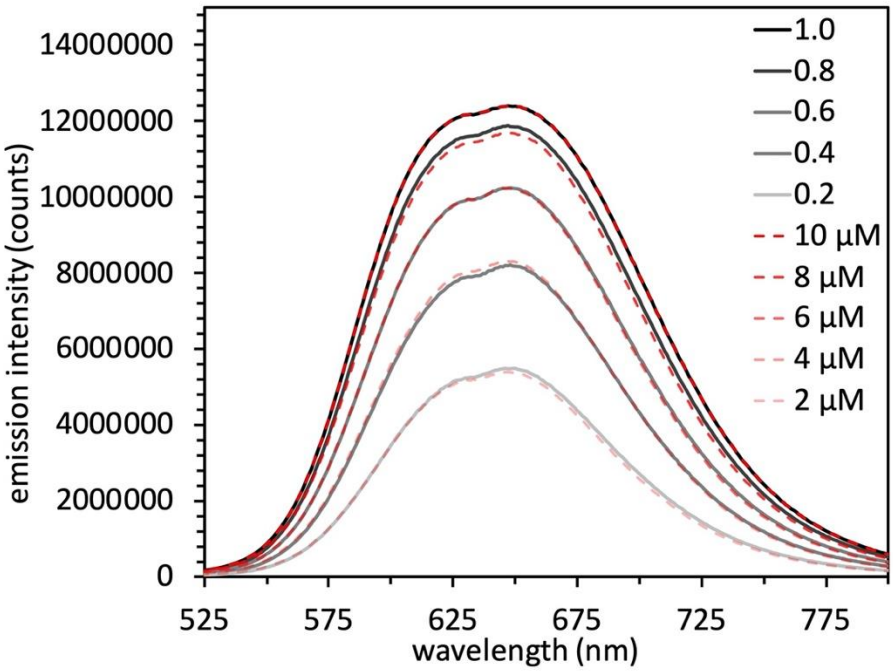

Figure S27. Emission curves of **DN1-ester** with varied mole fractions of $[Co(PY5Me_2)(MeCN)]^{2+}$ (black lines) and at the same concentration of **DN1-ester** with no cobalt complex present (red dashed lines). Samples with the dye and cobalt complex were stirred for 1 hour at room temperature before data was collected.

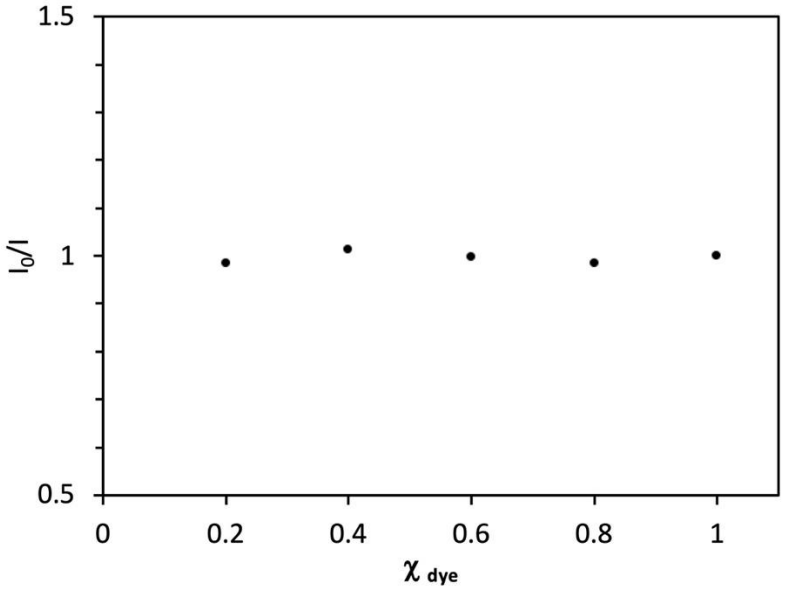

Figure S28. Emission intensity ratios across a series of mole fractions of **DN1-ester** and $[Co(PY5Me_2)(MeCN)]^{2+}$. The total amount of analyte (dye + redox shuttle) was held constant at 1×10^{-5} M. I_0 is the emission intensity of the dye without any added redox shuttle at the corresponding mole fraction dye concentration.

Appendix III

Supporting Information for "PREFERENTIAL DIRECTION OF ELECTRON TRANSFERS AT A DYE−METAL OXIDE INTERFACE WITH AN INSULATING FLUORINATED SELF-ASSEMBLED MONOLAYER AND MGO"

Leigh Anna Hunt, Roberta R. Rodrigues, Kayla Foell, Dinesh Nugegoda, Hammad Cheema,

Nathan I. Hammer,* and Jared H. Delcamp*

322 Coulter Hall, Department of Chemistry and Biochemistry, University of Mississippi, University, MS, 38677, USA

Table of Contents – Appendix I

1. **Figure S1**. TiO_2 absorption data with **B11** absorbed to 3.0 μm thick TiO_2 films with no additional treatment (black), a MgO insulating layer (red), and PFTS as an F-SAM treatment (blue).

2. **Figure S2.** Structure of **N719**.

3. **Figure S3.** *J-V* curves of **N719**/$Co(bpy)_3^{3+/2+}$ based devices with varying PFTS.

4. **Figure S4.** IPCE curves of **N719**/$Co(bpy)_3^{3+/2+}$ based devices with varying PFTS.

5. **Table S1.** Effect of varying PFTS on **N719**/$Co(bpy)_3^{3+/2+}$ DSC device performances.

6. **Figure S5.** *J-V* curves of **B11**/$Co(bpy)_3^{3+/2+}$ based devices with varying MgO amounts.

7. **Figure S6.** IPCE curves of **B11**/$Co(bpy)_3^{3+/2+}$ based devices with varying MgO amounts.

8. **Figure S7.** SMPVT measurements of **B11**/$Co(bpy)_3^{3+/2+}$ based devices with varying MgO amounts.

9. **Figure S8.** J-V curves of **B11**/$Co(bpy)_3^{3+/2+}$ based devices with varying MgO and PFTS amounts.

10. **Figure S9.** IPCE curves of **B11**/$Co(bpy)_3^{3+/2+}$ based devices with varying MgO and PFTS amounts.

11. **Figure S10.** SMPVT measurements of **B11**/$Co(bpy)_3^{3+/2+}$ based devices with varying MgO and PFTS amounts.

12. **Figure S11.** Charge extraction measurements plotted a capacitance versus open circuit voltage for **B11**/$Co(bpy)_3^{3+/2+}$ based devices with varying PFTS.

13. **Figure S12.** Charge extraction measurements plotted a capacitance versus open circuit voltage for **B11**/$Co(bpy)_3^{3+/2+}$ based devices with varying MgO amounts.

14. **Figure S13.** Charge extraction measurements plotted a capacitance versus open circuit voltage for **B11**/$Co(bpy)_3^{3+/2+}$ based devices with varying MgO and PFTS amounts.

15. **Figure S14.** Current dynamics studies for **B11**/$Co(bpy)_3^{3+/2+}$ devices treated with 0.025 M PFTS at varying sun intensities. The black lines are normalized to 1 sun intensity.

16. **Figure S15**. Current dynamics studies for **B11**/$Co(bpy)_3^{3+/2+}$ devices treated with 0.001 M $Mg(OMe)_2$ at varying sun intensities. The black lines are normalized to 1 sun intensity.

17. **Figure S16**. Current dynamics studies for **B11**/$Co(bpy)_3^{3+/2+}$ devices treated with no surface treatment at varying sun intensities. The black lines are normalized to 1 sun intensity.

1. Film Absorption Data

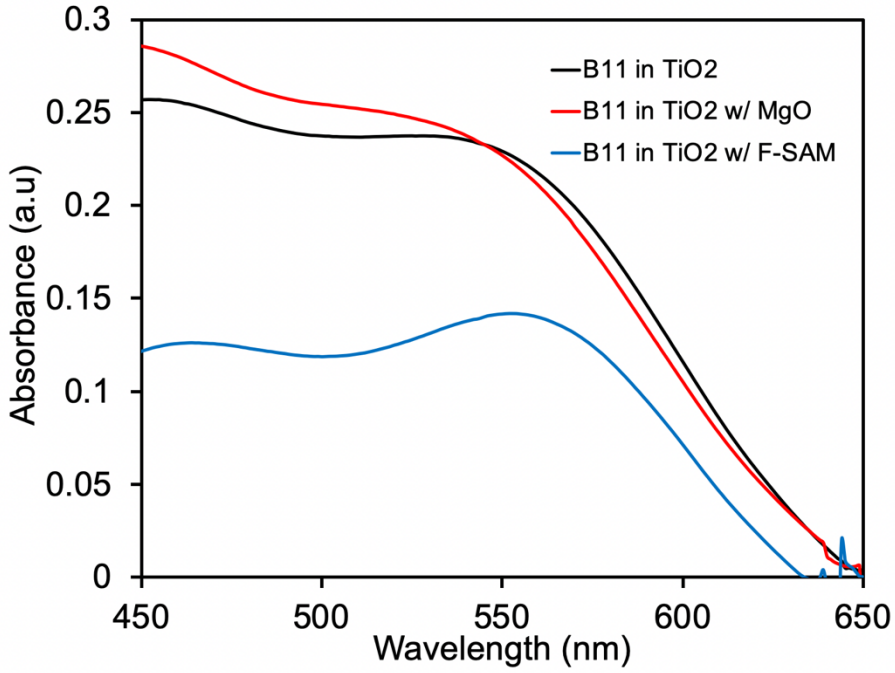

Figure S1. TiO_2 absorption data with **B11** absorbed to 3.0 µm thick TiO_2 films with no additional treatment (black), a MgO insulating layer (red), and PFTS as an F-SAM treatment (blue).

2. Additional DSC Device Data:

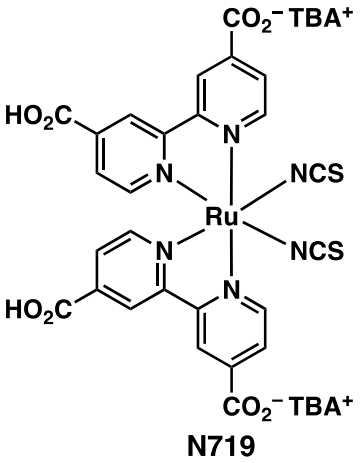

N719

Figure S2. Structure of **N719**.

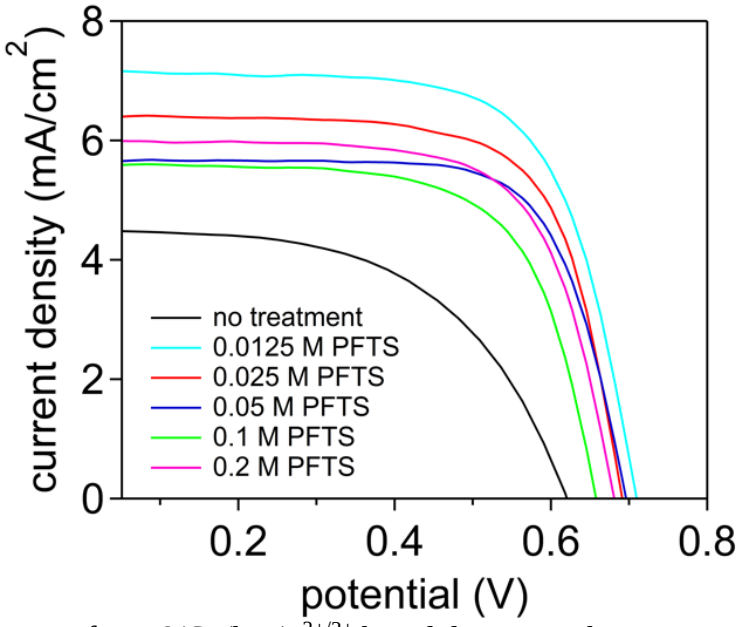

Figure S3. *J-V* curves of **N719**/Co(bpy)$_3^{3+/2+}$ based devices with varying PFTS.

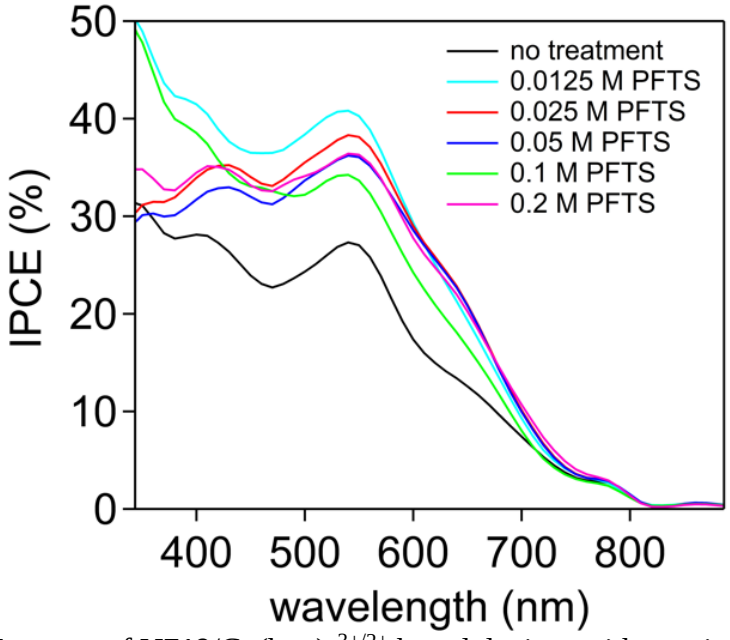

Figure S4. IPCE curves of **N719**/Co(bpy)$_3^{3+/2+}$ based devices with varying PFTS.

Table S1. Effect of varying PFTS on **N719**/Co(bpy)$_3^{3+/2+}$ DSC device performances.

Entry	PFTS	V_{oc} (mV)	J_{sc} (mA/cm^2)	FF	PCE (%)
1	None	615	4.53	0.56	1.58
2	0.0125 M	700	6.75	0.69	3.40
3	0.025 M	691	6.35	0.69	3.04
4	0.05 M	700	6.05	0.72	3.11
5	0.1 M	673	5.87	0.70	2.86
6	0.2 M	678	6.15	0.70	3.00

*Each entry is an average of at least 2 devices with a PCE standard deviation of $\leq \pm 0.3$.

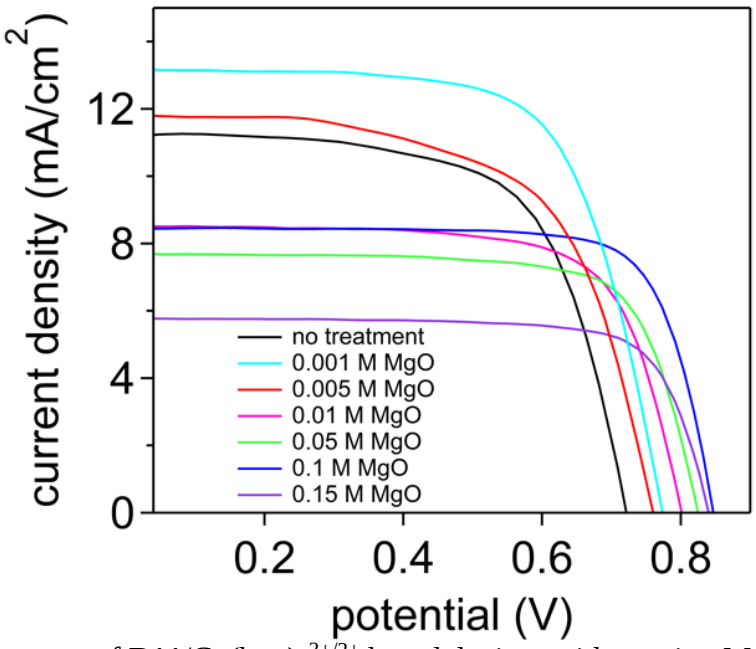

Figure S5. *J-V* curves of **B11**/Co(bpy)$_3^{3+/2+}$ based devices with varying MgO amounts.

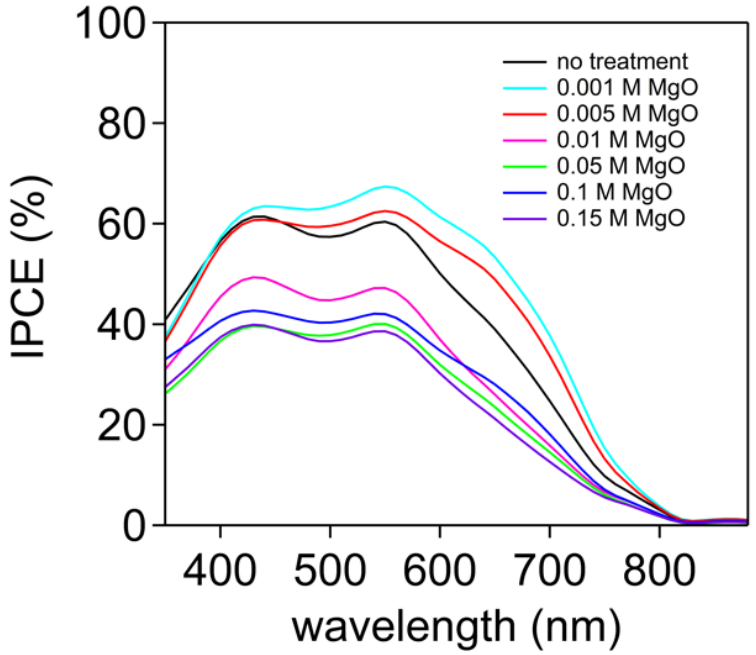

Figure S6. IPCE curves of **B11**/Co(bpy)$_3^{3+/2+}$ based devices with varying MgO amounts.

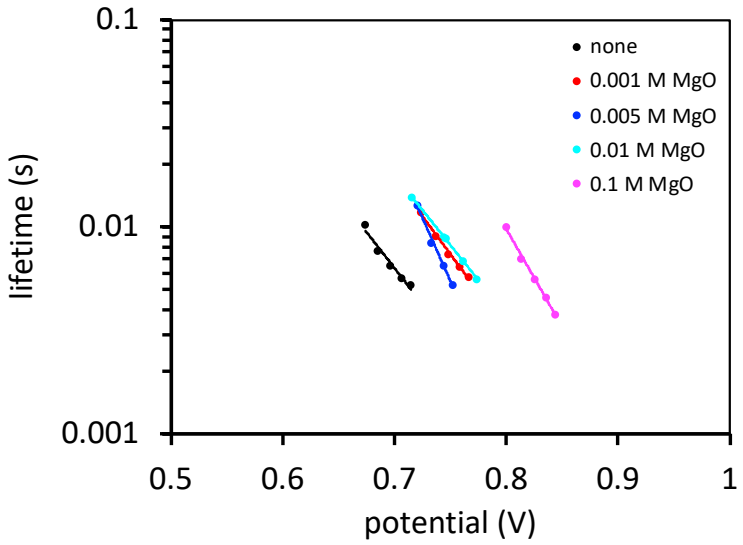

Figure S7. SMPVT measurements of **B11**/Co(bpy)$_3^{3+/2+}$ based devices with varying MgO amounts.

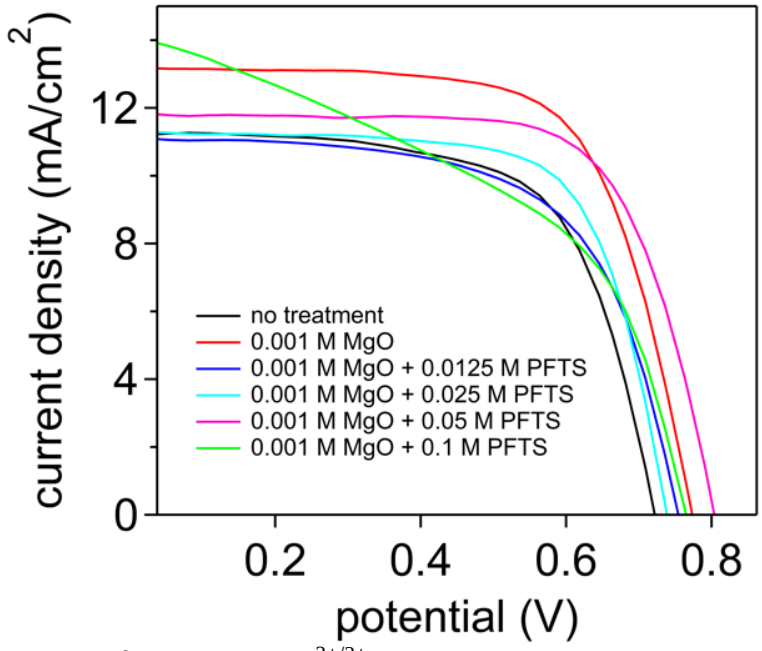

Figure S8. J-V curves of **B11**/Co(bpy)$_3^{3+/2+}$ based devices with varying MgO and PFTS amounts.

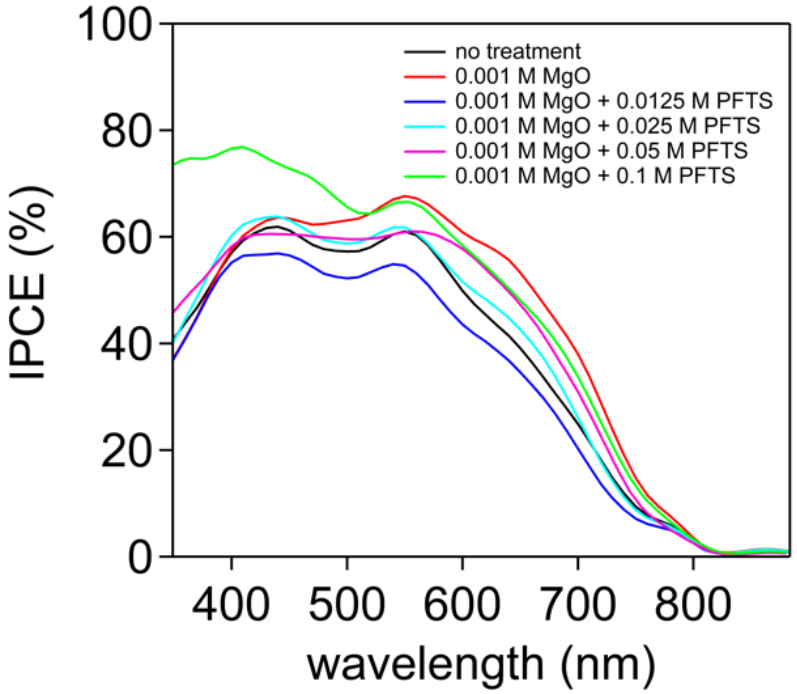

Figure S9. IPCE curves of **B11**/Co(bpy)$_3^{3+/2+}$ based devices with varying MgO and PFTS amounts.

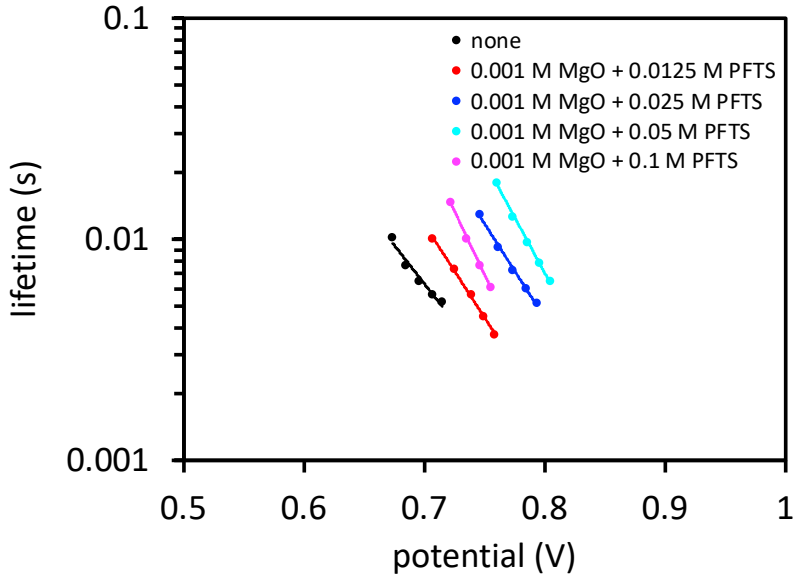

Figure S10. SMPVT measurements of **B11**/Co(bpy)$_3^{3+/2+}$ based devices with varying MgO and PFTS amounts.

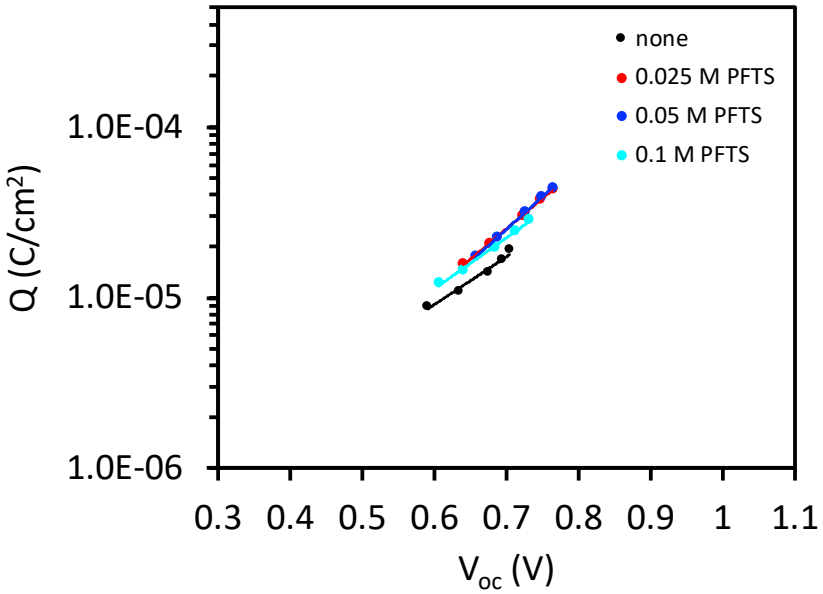

Figure S11. Charge extraction measurements plotted a capacitance versus open circuit voltage for **B11**/Co(bpy)$_3^{3+/2+}$ based devices with varying PFTS.

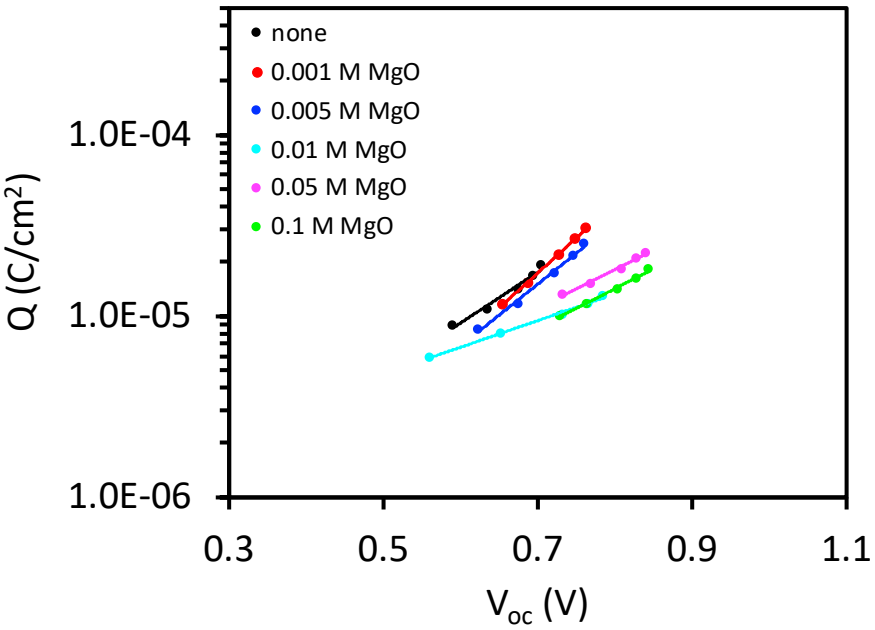

Figure S12. Charge extraction measurements plotted a capacitance versus open circuit voltage for **B11**/Co(bpy)$_3^{3+/2+}$ based devices with varying MgO amounts.

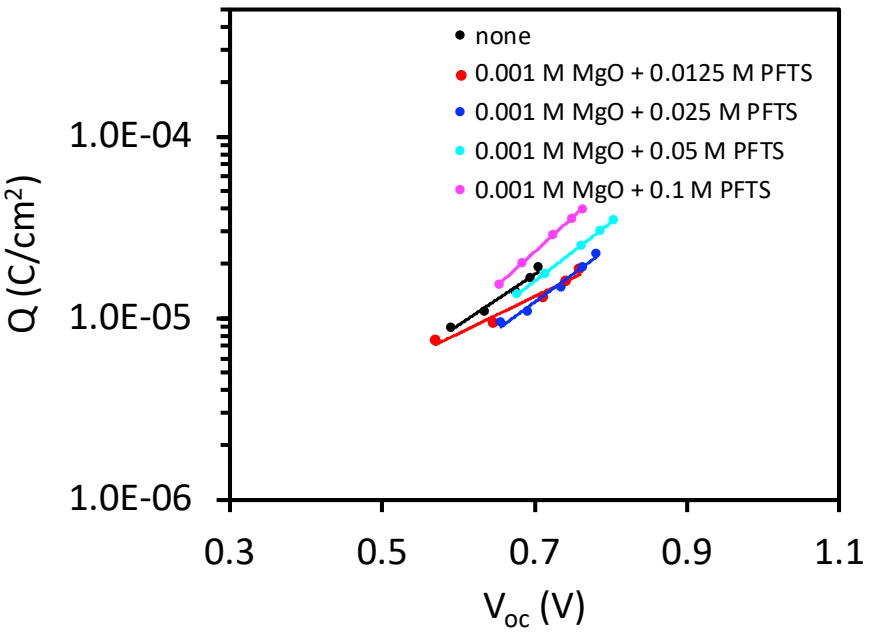

Figure S13. Charge extraction measurements plotted a capacitance versus open circuit voltage for **B11**/Co(bpy)$_3^{3+/2+}$ based devices with varying MgO and PFTS amounts.

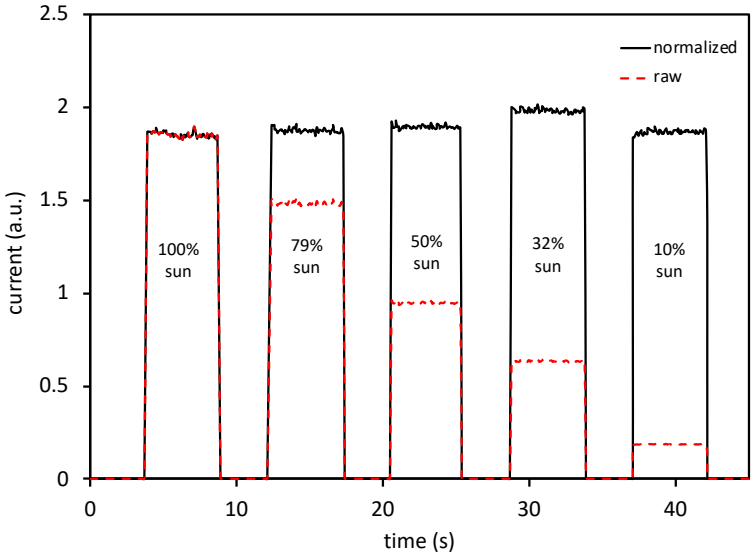

Figure S14. Current dynamics studies for **B11**/Co(bpy)$_3^{3+/2+}$ devices treated with 0.025 M PFTS at varying sun intensities. The black lines are normalized to 1 sun intensity.

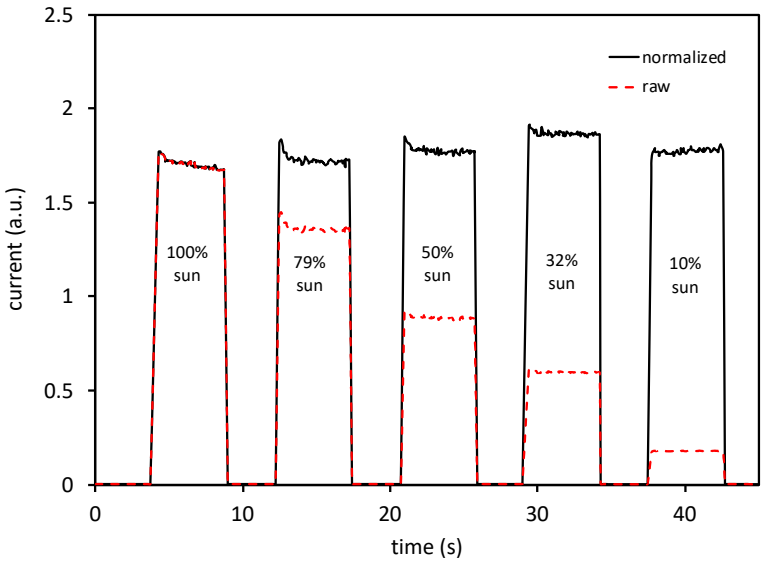

Figure S15. Current dynamics studies for **B11**/Co(bpy)$_3^{3+/2+}$ devices treated with 0.001 M Mg(OMe)$_2$ at varying sun intensities. The black lines are normalized to 1 sun intensity.

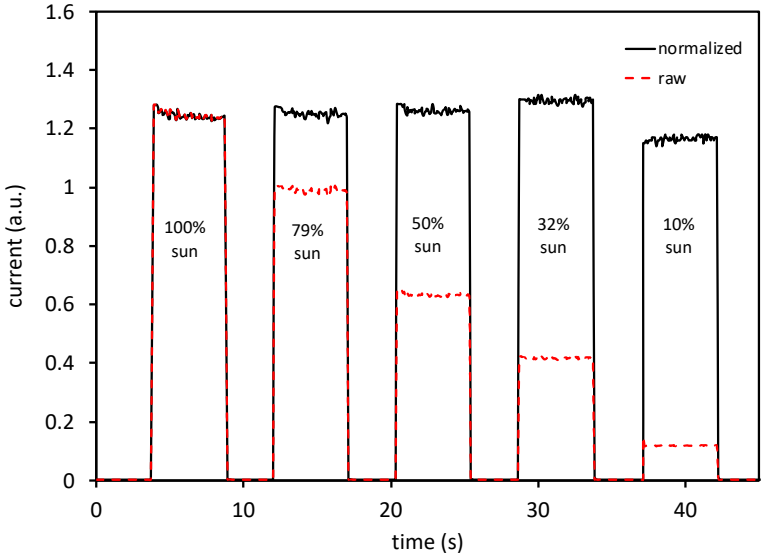

Figure S16. Current dynamics studies for **B11**/Co(bpy)$_3^{3+/2+}$ devices treated with no surface treatment at varying sun intensities. The black lines are normalized to 1 sun intensity.

3. Laser Spectroscopy

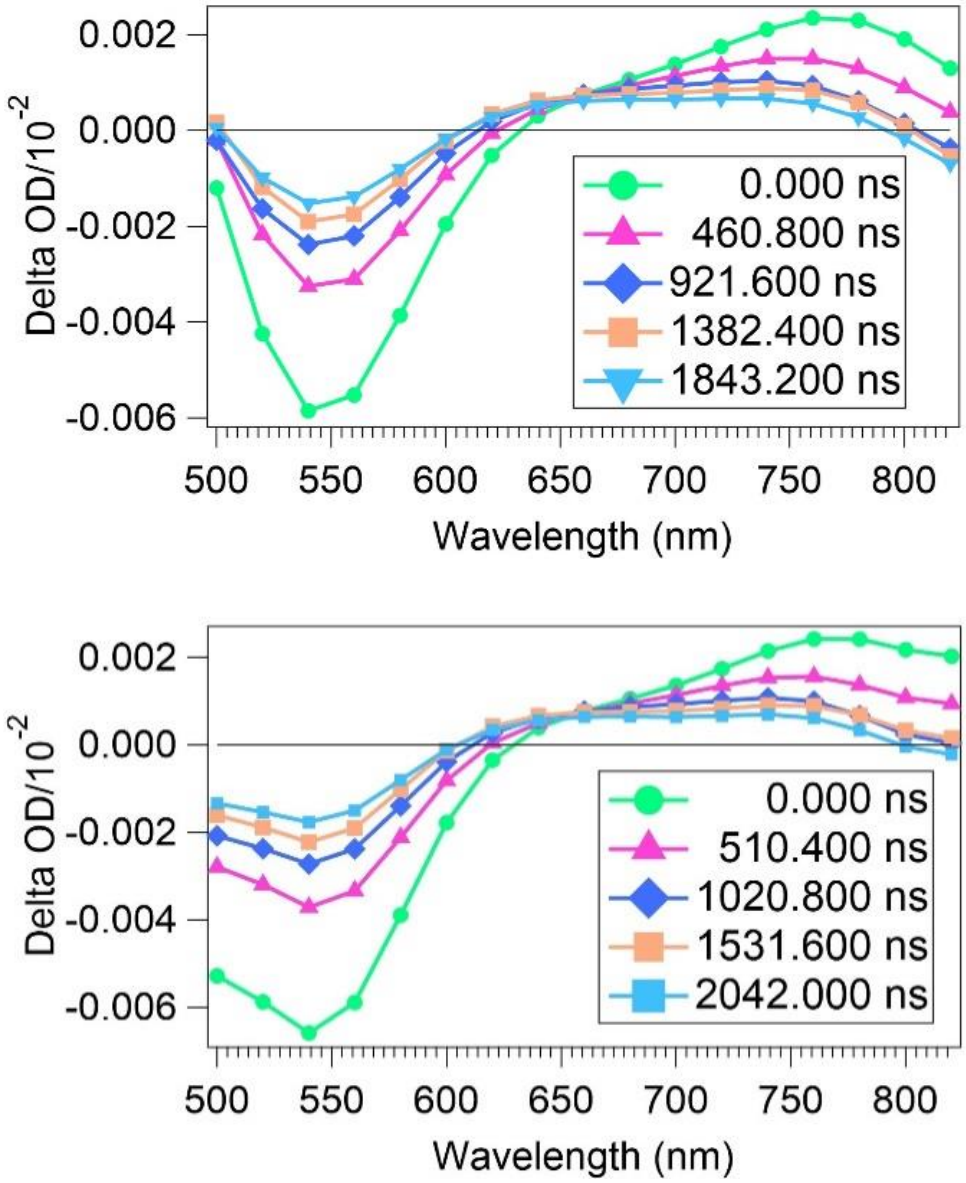

Figure S17. Spectral data for **B11**-sensitized TiO_2 devices with no insulator and a redox-inactive electrolyte (left) and no insulator with a full electrolyte containing $Co(bpy)_3^{3+/2+}$ (right).

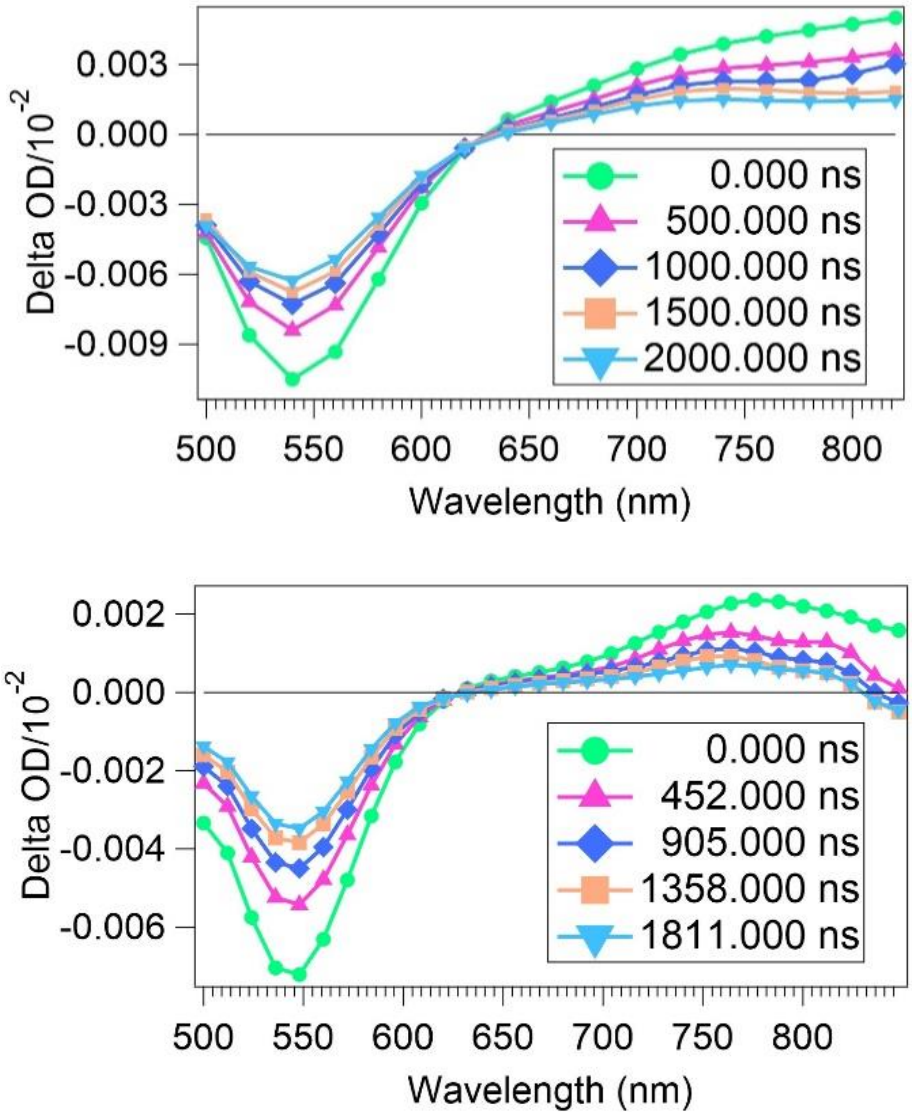

Figure S18. Spectral data for **B11**-sensitized TiO_2 devices with an MgO treatment and a redox-inactive electrolyte (left) and an MgO treatment with electrolyte containing $Co(bpy)_3^{3+/2+}$ (right).

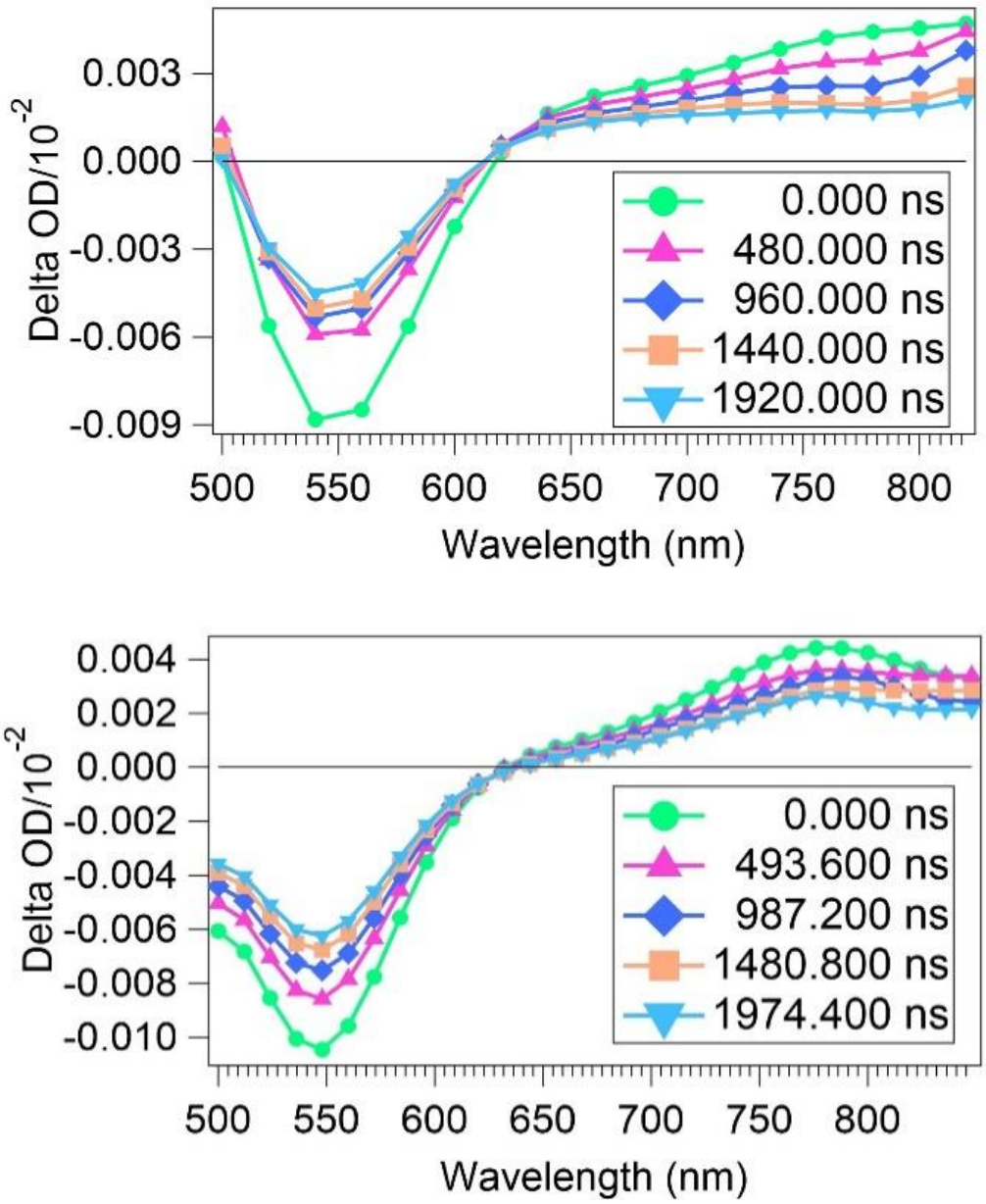

Figure S19. Spectral data for **B11**-sensitized TiO_2 devices with a PFTS treatment and a redox-inactive electrolyte (left) and a PFTS treatment with electrolyte containing $Co(bpy)_3^{3+/2+}$ (right).

4. Computational Results

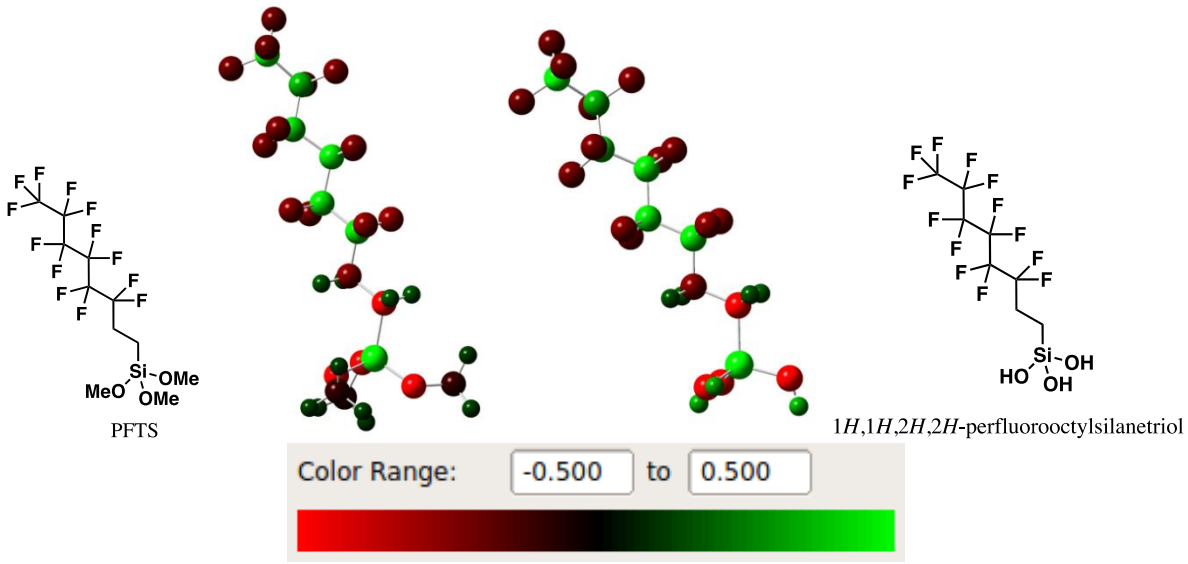

Figure S20. PFTS (left) and 1*H*,1*H*,2*H*,2*H*-perfluorooctylsilanetriol (right) with the atoms color coded for Mulliken charge at the atom.

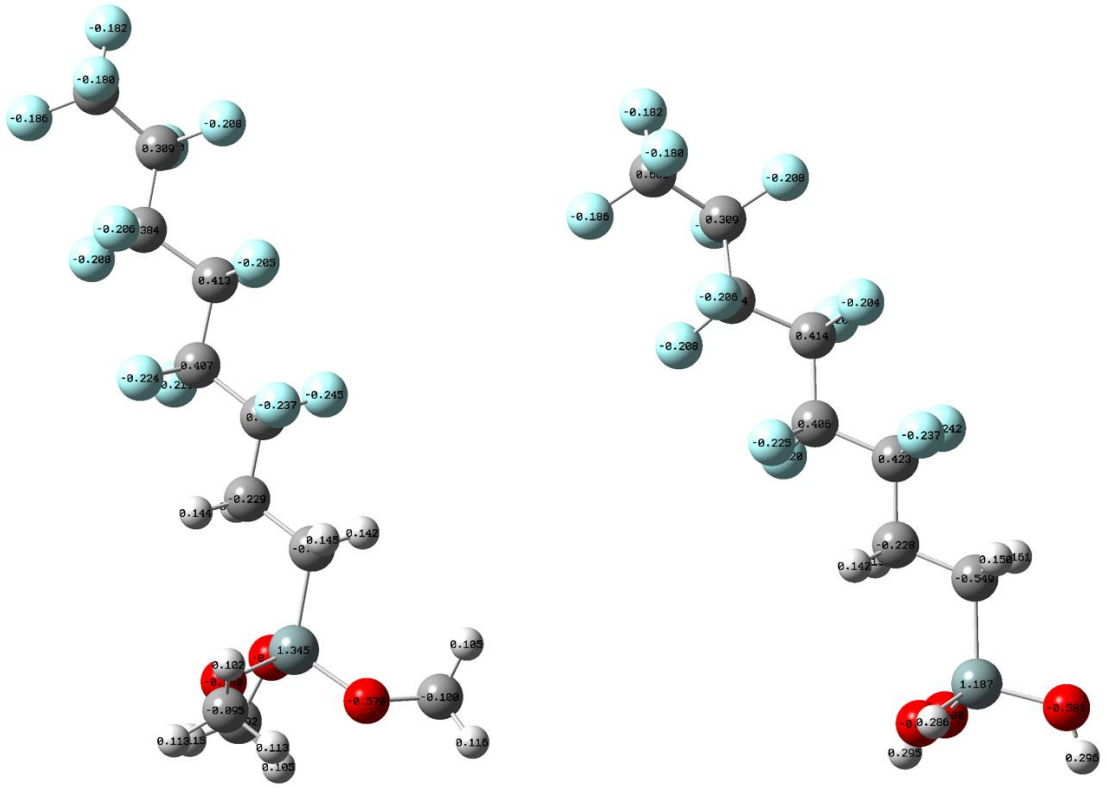

Figure S21. Mulliken charges at each atom of PFTS (left) and 1*H*,1*H*,2*H*,2*H*-perfluorooctylsilanetriol (right). Fluorine atoms range from –0.180 to –2.45, Si atoms are +1.187 to +1.345, and H atoms on the perfluorinated backbone range from +0.161 to +0.142 for each molecule. This shows a region of negative charge furthest from the surface, and a region of positive charge near the surface.

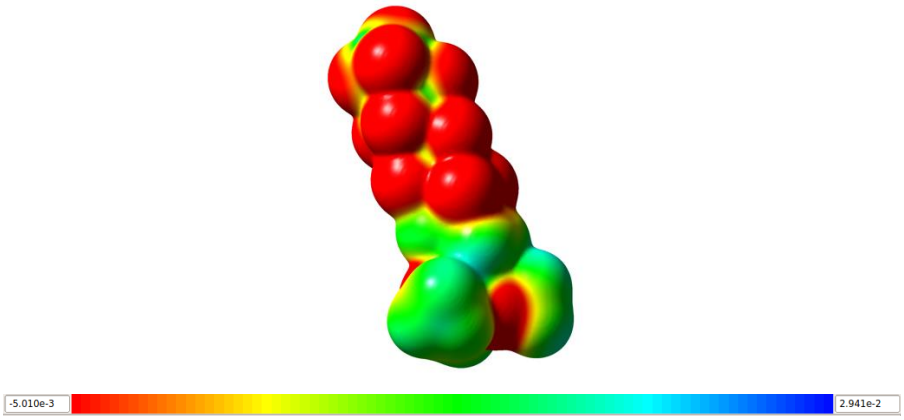

Figure S22. Molecular electrostatic potential map of PFTS.

XYZ Coordinates of molecules optimized at the B3LYP/6-311G (d,p) level of theory.

PFTS

Total energy: -2240.7853607 Hartees

Dipole: 1.45 D toward the Si atom.

C	3.37168400	-0.68748100	-0.43238100
C	2.13887600	0.08580700	0.06094000
C	0.84251000	-0.59194000	-0.34311200
C	-0.42514700	0.19563200	0.10035800
C	-1.78373600	-0.56623500	-0.05047000
C	-3.03576400	0.37516000	-0.01097000
C	-4.37437100	-0.37529800	0.28643700
C	-5.65761700	0.43665400	-0.06820500
F	-5.59957800	1.66530300	0.45723400
F	-5.80994500	0.53357400	-1.39019900
F	-6.72105600	-0.19595600	0.43756100
F	-4.41629900	-1.52662700	-0.42016600
F	-4.42500400	-0.66485300	1.60262800
F	-2.86457600	1.31191700	0.94726000
F	-3.14333700	0.99265800	-1.20892300
F	-1.80354300	-1.23130100	-1.22400800
F	-1.88378400	-1.45905100	0.95987700
F	-0.28717500	0.53106400	1.40744200
F	-0.47970600	1.34034900	-0.62832400
F	0.78215700	-0.73685300	-1.70060000
F	0.76156300	-1.84630700	0.19923600
Si	4.99006800	0.12777800	0.03277700
O	6.28482100	-0.77793600	-0.45239900
O	5.19187300	1.60226900	-0.66789900
O	4.91802200	0.35131600	1.66109700
C	6.59026400	-2.11378600	-0.07081900
C	5.75412800	1.89190100	-1.94373200
C	5.78819900	1.16978400	2.44050700
H	3.33559400	-0.79083300	-1.52153300
H	3.35297100	-1.70288200	-0.02355300
H	2.12380700	1.09802800	-0.35129000
H	2.15121500	0.17548500	1.14776000
H	5.85191700	-2.82036300	-0.46603500
H	6.63194300	-2.22018500	1.01831400
H	7.56740100	-2.36749700	-0.48476500
H	5.03439900	1.68537800	-2.74352100
H	6.65974700	1.30520400	-2.11925100
H	6.00347900	2.95404400	-1.96770900

H	5.36652100	1.24575000	3.44377300
H	5.87387700	2.17117300	2.00965000
H	6.78685000	0.72618300	2.51040200

Hydroxylated analogue of PFTS

Total energy: -2122.8649747 Hartees

Dipole: 1.59 D toward the Si atom.

C	-4.08282500	0.68209300	-0.25423500
C	-2.83769800	-0.15608800	0.07114500
C	-1.55139600	0.60199800	-0.20255500
C	-0.27359500	-0.24322200	0.07529000
C	1.07723400	0.54657400	0.06333900
C	2.33714200	-0.37348500	-0.08349800
C	3.67177900	0.31983300	0.34251300
C	4.95872100	-0.39779800	-0.16787500
F	4.91459300	-1.70438100	0.11525400
F	5.10091600	-0.24074700	-1.48521500
F	6.02087400	0.13735400	0.44194400
F	3.69815600	1.58449800	-0.13312400
F	3.73025700	0.35479500	1.68935800
F	2.18042500	-1.47611700	0.68124500
F	2.44012500	-0.75242500	-1.37724800
F	1.08184600	1.42137100	-0.96341600
F	1.17694100	1.23285800	1.22364000
F	-0.39938300	-0.82216600	1.29570800
F	-0.21606500	-1.22863800	-0.85771900
F	-1.50431300	1.00164000	-1.50816500
F	-1.47925500	1.72932400	0.56805500
Si	-5.67950400	-0.23245700	0.04233000
O	-6.87608400	0.84726300	-0.31213600
O	-5.80205600	-1.62512400	-0.85583700
O	-5.76135900	-0.75737000	1.60627500
H	-7.75680700	0.68100100	0.03182300
H	-5.96031500	-1.55211700	-1.79953500
H	-5.96000300	-1.68723700	1.73903700
H	-4.05287900	1.01151300	-1.29738600
H	-4.09231000	1.59004900	0.35556800
H	-2.81352600	-1.07049000	-0.52748700
H	-2.83734200	-0.45218900	1.12133200

Vita

Leigh Anna Hunt, Ph.D. Candidate
176 Coulter Hall · Oxford, MS 38655 · (662) 229-5993 · lahunt@go.olemiss.edu

Education

May 2022	**University of Mississippi** – *Oxford, MS* Doctor of Philosophy in Chemistry Research Advisor: Nathan I. Hammer
2011 – 2015	**University of Mississippi** – *Oxford, MS* Bachelor of Arts Degree Research Advisor: Nathan I. Hammer

Research Interests

Laser-based and time-resolved molecular spectroscopy, Charge transfer events at interfaces and in solution

Current research focuses on the spectroscopic characterization of photoinduced charge separation and electron transfer processes in heterogeneous environments that are of critical importance for efficient chemical and solar-to-electric energy conversion. Systems of interest include inorganic compounds for photocatalytic CO_2 reduction, artificial hydrogenases (metallopeptides) for H_2 evolution, and molecularly engineered sensitizer dyes and redox shuttles for dye-sensitized solar cell applications.

Research Experience

2016– Present **University of Mississippi**

1. Research – Photoinduced charge separation and electron transfer processes in heterogeneous environments
2. Experience
   - Nanosecond Transient Absorption Spectroscopy (nsTAS)
   - Nanosecond Pump-Pump-Probe Spectroscopy
   - Ultrafast Transient Absorption Spectroscopy (fsTAS)
   - Time-Resolved Infrared Absorption Spectroscopy (TRIR)
   - Time-Correlated Single Photon Counting (TCSPC)
   - UV/Vis Absorption Spectroscopy
   - Steady State and Time-Resolved Photoluminescence Spectroscopy
   - Raman Spectroscopy
   - Nd:YAG laser, Nd:YAG-pumped dye laser, optical parametric amplifier (OPA), laser optics, harmonic generation, etc.

Publications

16. **L.A. Hunt**, Sanjit Das, Dinesh Nugegoda, Robert W. Lamb, Matthew Figgins, Charles Edwin Webster, Nathan I. Hammer, Elizabeth T. Papish, and Jared H. Delcamp, "Ruthenium (II) Complexes of CNC Pincers and Bipyridine in the Photocatalytic CO_2 Reduction Reaction to CO using Visible Light: Catalysis, Kinetics, and Computational Insights," in preparation.
15. D. Nugegoda, **L.A. Hunt**, A. Devdass, J. Jurss, N. Hammer, and J. H. Delcamp. "Evidence of Interfacial Hydrogen Bonding Between a Hydrogen Bond Donating Redox Shuttle and a Dye with Lewis Basic Functionality at a Liquid-Solid Interface for Dye-sensitized Solar Cell Applications," submitted.
14. D. Nugegoda, S. Schwartz, S. Bhattacharya, **L.A. Hunt**, J. Jurss, N. Hammer, and J. H. Delcamp "Pi-stacking Promotes Rapid Interfacial Electron Transfer in Dye-Sensitized Solar Cells," in preparation.
13. Pallavi Prasad, **L.A. Hunt**, N. I. Hammer, and S. Chakraborty "A De-Novo Designed Cobalt Metallopeptide for H_2 Evolution: Slow Intermediate Deactivation Drives H_2 Evolution," in preparation.
12. Christine Curiac, **L.A. Hunt**, Nathan Hammer, and J. H. Delcamp, "Probing the Applicability of Marcus Inverted Region Models at Liquid-Solid Interfaces after Photoinduced Electron Transfer Reactions," in preparation.
11. J. Watson, R. Rodrigues, **L. A. Hunt**, N. I. Hammer, and J. H. Delcamp, "High efficiency Squaraine-Sensitized Dye-sensitized Solar Cells for Indoor Lighting Applications with Cu Redox Shuttles," in preparation.
10. Qing Li, **L.A. Hunt**, Ashley Williams, Hirunika Wijesinghe, Christine Curiac, Amala Dass, Nathan Hammer, and Jared Delcamp, "Dicyanobenzothiadiazole-based Dyes as Visible Light Absorbing Strong Photoinduced Oxidants with Long-Lived Excited States," in preparation.

9. Pallavi Prasad, **L.A. Hunt**, A. E. Williams, N. I Hammer, and S. Chakraborty, "A De Novo Designed Artificial Metallopeptide Hydrogenase: Insights into Photochemical Processes and the Role of Protonated Cys," ChemSusChem, in preparation.
8. **L.A. Hunt,** D. Nugegoda, A. Devdass, H. Cheema, J. Jurss, N. Hammer, and J. Delcamp, "Lewis Acid-Lewis Base Interactions Promote Fast Interfacial Electron Transfers with a Pyridine-Based Donor Dye in Dye-Sensitized Solar Cells," submitted (2021).
7. **L. A. Hunt**, R. Rodrigues, K. Foell, D. Nugegoda, H. Cheema, N. I. Hammer, and J. H. Delcamp, "Preferential Direction of Electron Transfers at a Dye-Metal Oxide Interface with an Insulating Fluorinated Self-Assembled Monolayer," Journal of Physical Chemistry C (2021).
6. **L. A. Hunt**, C. Curiac, M. A. Sabuj, Q. Li, A. Baumann, H. Cheema, Y. Zhang, N. Rai, N. I. Hammer, and J. H. Delcamp, "Probing Interfacial Halogen Bonding Effects with Halogenated Organic Dyes and a Lewis Base Decorated Transition Metal-Based Redox Shuttles at a Metal Oxide Interface in Dye-Sensitized Solar Cells," Journal of Physical Chemistry C (2021). DOI: 10.1021/acs.jpcc.1c05051 (link)
5. C. Curiac, R. Rodrigues, J. Watson, **L. A. Hunt**, A. Devdass, J. W. Jurss, N. I. Hammer, R. Fortenberry, and J. H. Delcamp, "Iron Redox Shuttles with Wide Optical Gap Dyes for High Voltage Dye-Sensitized Solar Cells," ChemSusChem, 14, 3084-3096 (2021). DOI: 10.1002/cssc.202100884 (link)
4. S. M. Parambath, A. E. Williams, **L .A. Hunt**, N. I Hammer, and S. Chakraborty, "A De Novo Designed Artificial Metallopeptide Hydrogenase: Insights into Photochemical Processes and the Role of Protonated Cys," ChemSusChem, 14, 2237-2246 (2021). DOI: 10.1002/cssc.202100122 (link)
3. P. R. Fontenot, B. Shan, B. Wang, S. Simpson, G. Ragunathan, A. F. Greene, A. Obanda, **L. A. Hunt**, N. I. Hammer, E. C. Webster, J. T. Mague, R. H. Schmehl, and J. P. Donahue, "Photocatalytic H2-Evolution by Homogeneous Molybdenum Sulfide Clusters Supported by Dithiocarbamate Ligands," Inorganic Chemistry, 58, 16458-16474 (2019). DOI: 10.1021/acs.inorgchem.9b02252 (link)
2. Y. Zhang, H. Cheema, L. McNamara, **L. A. Hunt**, N. I. Hammer, J. H. Delcamp, "Ullazine Donor-Pi bridge-Acceptor Organic Dyes for DSCs," Chemistry – A European Journal, 24, 5936 (2018). DOI: 10.1002/chem.201800030 (link)
1. H. Cheema, A. Peddapuram, R. E. Adams, L. McNamara, **L. A. Hunt**, N. Le, D. L. Watkins, N. I. Hammer, R. H. Schmehl, and J. H. Delcamp, "Molecular Engineering of NIR Absorbing Thienopyrazine Double Donor Double Acceptor Organic Dyes for DSCs," The Journal of Organic Chemistry, 82, 12038–12049 (2017). DOI: 10.1021/acs.joc.7b01750 (link)

Teaching & Mentorship Experience

2017 Teaching Assistant for General Chemistry Laboratories

- Responsible for grading and prelab lecture and educating students on proper lab safety and technique

2016 – Present — Teaching Assistant for Physical Chemistry Laboratories
- Responsible for grading and lecture of upper level physical chemistry labs that practiced essential thermodynamic and quantum mechanical experiments

2016 – Present — Guest Lecturer for upper level Physical Chemistry Courses
- Lectured undergraduate students on various topics within thermodynamics and quantum chemistry

2016 – Present — Graduate Student Mentor for the Hammer Research Group
- Ethan Lambert (B.S. Chemistry, Honors, current): ns TAS studies of back electron transfer in DSCs
- Nick Kruse (B.S. Chemistry, Physics, Honors, current): laser interactions of weakly-bound gas-phase negative ions
- Claudia Chambliss (B.A. Chemistry, Honors, current): Raman spectroscopy of ionic liquids

Presentations

Oral

3. **November 2021.** "Insights into Possible Halogen Bonding Effects in Dye Sensitized Solar Cells Studied via Nanosecond Transient Absorption Spectroscopy" Southeastern Regional Meeting of ACS, Birmingham, AL.
2. **August 2021.** "Mechanistic insights related to photocatalytic H_2 production from a de novo-designed artificial metallopeptide hydrogenase" ACS National Meeting, Atlanta, GA.
1. **July 2019.** "Determination of Dye Regeneration Efficiency in Dye Sensitized Solar Cells," Feeding and Powering the World 2019, Oxford, MS.

Poster

6. **November 2019.** "Advanced Spectroscopic Techniques for the Characterization of the Photophysical Properties of Emergent Molecular Optoelectronics," Center for Emergent Optoelectronics (CEMOs) Annual Meeting, Starkville, MS.
5. **July 2019.** "Fluorescence Lifetime Studies of Donor-π Bridge-Acceptor (D-π-A) Dyes for use in Dye-Sensitized Solar Cells," Feeding and Powering the World 2019, Oxford,

MS

4. **March 2019.** "Quantifying Environmental Influence on Interfacial Charge Transfer Kinetics Involving Organic Dyes Using Excited State Lifetimes and Transient Absorption Spectroscopy" 257th National Meeting of the American Chemical Society, Orlando, FL.
3. **July 2018.** "Fluorescence Lifetime Studies of Donor-π Bridge-Acceptor (D-π-A) Dyes for use in Dye-Sensitized Solar Cells," Feeding and Powering the World 2018, Oxford, MS.
2. **March 2018.** "Single Molecule Spectroscopic Studies of Squaraine-based Donor–Acceptor–Donor (D-A-D) dyes," 255th National Meeting of the American Chemical Society, New Orleans, LA.
1. **July 2017.** "Measuring Electron Injection Efficiencies for Optimization of Dye-Sensitized Solar Cells," Feeding and Powering the World 2017, Oxford, MS.

Professional Affiliations

2016 – Present	Member of National American Chemical Society
2016 – Present	Member of American Chemical Society Ole Miss Local Section
2020 – Present	Member of American Chemical Society Younger Chemists Committee
2021 – Present	President of Local Section Younger Chemists Committee